

SIMULATION OF FLOWING PLASMA DISCHARGES WITH APPLICATIONS TO
LASERS, FUEL CELLS, AND MICROTHRUSTERS

BY

RAMESH A. ARAKONI

B.Tech., Indian Institute of Technology, Madras, 2000

M.S., University of Illinois at Urbana-Champaign, 2003

DISSERTATION

Submitted in partial fulfillment of the requirements
for the degree of Doctor of Philosophy in Aerospace Engineering
in the Graduate College of the
University of Illinois at Urbana-Champaign, 2007

Urbana, Illinois

CERTIFICATE OF COMMITTEE APPROVAL

University of Illinois at Urbana-Champaign
Graduate College

August 23, 2007

We hereby recommend that the thesis by:

RAMESH A ARAKONI

Entitled:

**SIMULATION OF FLOWING PLASMA DISCHARGES WITH
APPLICATIONS TO LASERS, FUEL CELLS, AND MICROTHRUSTERS**

Be accepted in partial fulfillment of the requirements for the degree of:

Doctor of Philosophy

Signatures:



Director of Research - Dr. Mark J. Kushner

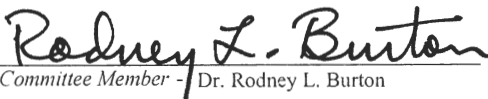


Head of Department - Dr. J Craig Dutton

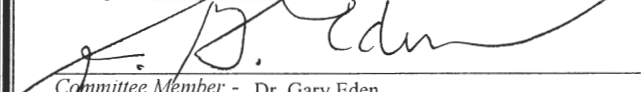
Committee on Final Examination*



Chairperson - Dr. Mark J. Kushner

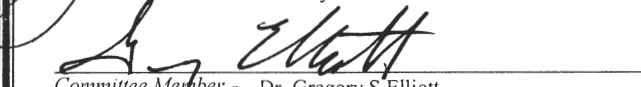


Committee Member - Dr. Rodney L. Burton



Committee Member - Dr. Gary Eden

Committee Member -



Committee Member - Dr. Gregory S Elliott

Committee Member -

* Required for doctoral degree but not for master's degree

ABSTRACT

Plasmas are gases composed of electrons, and ions, along with the neutral species, and are typically used in materials processing. In low-temperature plasmas, the electrons and heavy species are in thermal non-equilibrium, and hence the impact by energetic electrons in the discharge can be used to breakdown the feedstock gases into a desired product. Thermo-physical changes to the feedstock gas can also be used to alter the flow properties.

In this work, the plasma hydrodynamics is modeled using a 2-d unstructured-mesh based model to solve the Maxwell's equations and the transport equations. To parameterize over a larger operating space, a plug flow model (quasi 1d) was also used, especially for large reaction chemistries. A better understanding of the discharge and flow characteristics can be utilized in improving the operating efficiency of these devices. In this thesis we looked at the following problems:

Oxygen-iodine lasers are important from the perspective of defense applications, and in materials processing such as metal cutting. The excited iodine (I^*) (at 1.315 μm) are produced by transfer of energy between $O_2(^1\Delta)$ (a metastable species of oxygen) and I atoms, and the fraction of O_2 in the $^1\Delta$ state is important to the efficiency of the laser. The yield of $O_2(^1\Delta)$ is a function of energy deposition per O_2 in the discharge (He/ O_2 mixture), although it does not scale linearly with power at high powers due to dissociation of O_2 . Production of $O_2(^1\Delta)$ is efficient at electron temperatures (T_e) of 1-1.5 eV, and techniques to deposit power uniformly, additives to the discharge such as NO improves this efficiency by lowering the T_e . O atoms quench the I^* and hence their densities need to be controlled. The density of O atoms can be managed by adding small amounts of NO/ NO_2 which recoup O atoms through cyclic reactions. In general, the optical gain in the laser cavity can also be optimized using a

variety of parameters such as flow rates of NO/NO₂, and I₂ flow rate for a given power deposition.

Storage of H₂ is difficult, and hence an efficient and in-situ creation of H₂ in NH₃ plasmas is explored for use in portable fuel cells. We look at H₂ production in a microdischarge (MD) using NH₃ as a feedstock gas. Electron-impact reactions in the plasma and neutral chemistry in the afterglow regions are important sources of H and H₂. T_e is an important parameter affecting the dissociation of NH₃ especially at low concentrations of NH₃. In general, the conversion of NH₃ is efficient at lower speeds (higher residence time), and higher energy deposition per NH₃. A tradeoff exists between the energy required to create a H₂ molecule and number of H₂ molecules produced per NH₃.

Small satellites (few – 10s kgs) require μN – mNs of thrust for station keeping with nominal power requirements (few Watts) and MDs can be used as a source of thrust. In this work, a MD is used to deposit power to flowing Ar (at 10s Torr), and the changes to velocity, gas temperature, and thrust due to the discharge are studied. Parameterization based on flow and power deposition indicates a scaling based on energy deposition per Ar atom. Due to the large surface-to-volume ratio, low Reynolds numbers in these devices, the heat conduction to the walls and viscous losses play a significant part in the efficiency of operation. Operating conditions such as inlet pressure, nozzle length and its divergence angle can be optimized so as to increase the thrust due to the discharge.

ACKNOWLEDGEMENTS

I am most grateful to my advisor Prof. Mark J. Kushner for introducing me to the world of plasmas and providing me numerous opportunities to attend conferences and symposiums to deepen my technical knowledge and enhance my professional skills. The discussions with him in the research meetings have been instrumental in increasing my knowledge and understanding of not only plasmas, but also diverse topics in physics and engineering, and I hope to carry and improve on this throughout my career. I also thank him for his patience and guidance throughout the course of my PhD, and bailing me out at times when things were not going in the right direction!

I am grateful to the members of my committee – Prof. Gregory S. Elliott, Prof. Rodney L. Burton, and Prof. James G. Eden for their thoughtful comments and suggestions. Thanks are also due to J. J. Ewing of Ewing Technology Associates, Prof. Wayne Solomon and Dr. Carroll of CU Aerospace for their comments. I'd also like to acknowledge the support of the National Science Foundation and Air Force Office of Scientific Research.

I am grateful to the faculty at the Aerospace Engineering Department at the Indian Institute of Technology Madras for laying a strong foundation in technical skills, and guiding me to the path of higher education.

I would like to acknowledge the friendship and help of the past and present members of the Optical and Discharge Physics Group – Arvind, Pramod, Kapil, Vivek, Shane, Ananth, Ankur, Yang, Mingmei, Natalie, and Kelly. I'd like to acknowledge the staff at Dr. Kushner's office, Denise, Heidi, Katy, Linda, and Lisa at Iowa State University for all their

help and support. I'd also like to thank Staci Tankersley, Kendra Lindsey, and Sandee Moore for their help over the course of my study at UIUC.

7 years is a long time to spend on campus unless you have some great friends who make time whiz-by! Here's to you guys, you definitely made life easy! I hope we can be in touch long after graduation, no matter where our path leads us. I would like to acknowledge - school friends (Anand, Deepak, Harini, Jans, Jaya, Suddu), IIT friends (Rockalis, Aeros2zeros), my seniors (Arvind, Sameer, Sumant), the 1110 Stoughton gang (Jee, Prasanna, Kabab, BJB, Neeraj, Kaushik, Preeti, Chaitanya), Asha gang (Amit, Anurag, Dilipji, Jayandran, Jayashre, Lakshmi, Lalit, Nandita, Rekha, Rivi, Sunita, Vandana), Tae Kwon Do teachers (Mr. Hartman, Mr. Strle, Mr. Coch, Mr. Bubulka, Mr. Mohamed), the cricket gang (Amby, Band, Koo, Nayak, Pratik, Spandan, Viggi), the Potluckers gang (AK, Ashwin, Chans, Divya, Francis, Gowri, Hari, Hina, PK, Priya, Sathish, Shweta, Sumalya), the Mafia gang (Deepa, Kannan, Madhu, Savithri), the Coffee Room Gang (Allada, Ankur, Anu, Bhoj, Dev, Nikhil, Rahul, Steve, Vatsan, Vidya, Vishwa), the Boheme and Beaudelaire gang (Bandy, Benazir, Firoz, Jyoti, Misra, Pranaam, Ritu, Sachin, Saikat, Savitha, Srinii).

The support and encouragement of my parents and family has been invaluable throughout the many years of my education, especially towards the end of my PhD. I am deeply grateful to them for their unwavering and unconditional love, and hope I can fulfill their aspirations for me.

Salutations to the Supreme One whose grace is infinite, who creates, cares for, and destroys us and all the worlds at the end of time. Upon graduation, I hope to be able to continue seeking the Truth, knowing which, one can rid oneself of all Maya.

TABLE OF CONTENTS

CHAPTER 1. INTRODUCTION	1
1.1 Introduction to Plasmas.....	1
1.2 Applications of Plasmas.....	4
1.3 Modeling of Plasma Discharges	8
1.4 Summary	9
1.5 Figures.....	11
1.6 References.....	12
 CHAPTER 2. DESCRIPTION OF MODELS.....	 15
2.1 Introduction.....	15
2.2 GlobalKIN.....	15
2.3 nonPDPSIM	19
2.3.1 Mesh Generation and Discretization.....	20
2.3.2 Inputs to the Model	22
2.3.3 Solution of the Plasma Characteristics	23
2.3.4 Power Deposition.....	28
2.3.5 Neutral Fluid Transport.....	31
2.4 Figures.....	34
2.5 References.....	36
 CHAPTER 3. PRODUCTION OF O ₂ (¹ Δ) IN HE/O ₂ DISCHARGES FOR USE IN OXYGEN-IODINE LASERS.....	 37
3.1 Introduction.....	37
3.2 Description of the Reactor	41
3.3 Reaction Mechanism.....	42
3.4 O ₂ (¹ Δ) Scaling with Pressure, Composition: Inductively Coupled Plasma	45
3.5 O ₂ (¹ Δ) Scaling with Frequency and Power: Capacitively Coupled Plasma	50
3.6 Pressure Effects: Constant Energy per Molecule and Residence Time	53
3.7 Concluding Remarks.....	55
3.8 Figures.....	58
3.9 References.....	76
 CHAPTER 4. O ₂ (¹ Δ) PRODUCTION AND GAIN IN PLASMA PUMPED OXYGEN- IODINE LASERS: EFFECT OF NO AND NO ₂ ADDITIVES	 78
4.1 Introduction.....	78
4.2 Description of Reactor	80
4.3 Reaction Mechanism.....	81
4.4 Consequences of NO in the Inlet Flow	87
4.5 NO ₂ Injection	100
4.6 Concluding Remarks.....	102

4.7 Figures.....	104
4.8 References.....	120
CHAPTER 5. PRODUCTION OF H₂ IN Ar/NH₃ MICRODISCHARGES	121
5.1 Introduction.....	121
5.2 Reaction Mechanism.....	123
5.3 Scaling of Microdischarge Production of H ₂ : Plug Flow Modeling.....	128
5.4 Scaling of Microdischarge Production of H ₂ : 2-D Modeling	135
5.5 Concluding Remarks.....	140
5.6 Figures.....	142
5.7 References.....	156
CHAPTER 6. MICRODISCHARGES AS SOURCES OF THRUST FOR MICROTHRUSTERS.....	157
6.1 Introduction.....	157
6.2 Sandwich Microdischarge.....	160
6.3 Annular Microdischarges: Scaling with Power and Flow	169
6.4 Concluding Remarks.....	174
6.5 Figures.....	175
6.6 References.....	197
APPENDIX A: LIST OF REACTIONS FOR He/O₂ PLASMAS	199
A.1 References.....	208
APPENDIX B: LIST OF REACTIONS FOR He/O₂/NO/NO₂/I₂ PLASMAS.....	210
B.1 References	215
APPENDIX C: LIST OF REACTIONS FOR Ar/NH₃ PLASMAS	217
C.1 References	227
AUTHOR'S BIOGRAPHY	231

CHAPTER 1. INTRODUCTION

1.1 Introduction to Plasmas

Plasmas are gases in which there are charged particles such as electrons and ions, and excited neutral species (vibrational, rotational, electronic, and radicals) in addition to the neutral gas, and are sometimes referred to as the fourth state of matter. The density of electrons, n_e , degree of ionization (ratio of electron to neutral particle density, n_e/N), and the average energy of the electrons (electron temperature, T_e) can be used to characterize the plasmas in a broad sense. For example, the interstellar plasmas are at one end of the spectrum, with very low densities and temperatures. These plasmas make up nearly all of the matter in the universe. In the other end of the spectrum, one has the high-pressure arcs where the densities, and degree of ionization can be large ($n_e > 10^{15} \text{ cm}^{-3}$) and fusion devices where the electron temperatures are 100s – 1000s eV ($1 \text{ eV} \approx 11,593 \text{ K}$). This classification of plasmas based on density and temperature is shown in Fig. 1.1.

Glow discharges and arcs having number densities from $10^9 - 10^{15} \text{ cm}^{-3}$, and T_e ranging from 1 – 10 eV are the most common types of plasmas used in industrial and technological applications. In this dissertation, the focus is primarily on the applications of such glow discharges. For these discharges, the degree of ionization is small ($n_e/N \approx 10^{-6} - 10^{-5}$), and there is thermal non-equilibrium ($T_e \gg T_g$) between the electrons and heavy particles. The electrons have temperatures of a few eV (10,000s K), whereas the heavier particle temperatures range from 300 – 1,000 K.

Once the plasmas are formed they decay over time due to re-combination of the electrons and ions and by diffusion of charged species to the walls of the reactor. In the

steady state, a supply of power is required to offset the losses. The energy from the power source is coupled to the electrons in the plasma through direct (dc), capacitive (CCP), and/or inductive coupling (ICP) by the electric and/or magnetic fields produced by the power source. The electrons then transfer the energy to the neutral species through collisions thereby producing the excited and ionized states which can then be used in the desired application.

Due to the large difference in the masses of electrons and ions, the electrons typically oscillate about the ions which are relatively at rest. This gives rise to fundamental oscillations leading to fundamental length and time scales. The time scale is defined by the plasma frequency:

$$\omega_p = \sqrt{\frac{4\pi n_e e^2}{m_e}} \quad (1.1)$$

and the length scale is defined as the Debye length:

$$\lambda_D = \sqrt{\frac{kT_e}{4\pi n_e e^2}} \quad (1.2)$$

where n_e , m_e , and T_e are the electron density, mass and temperature, and e is the fundamental charge. As such, plasmas are electrically neutral at length scales larger than the Debye length, and time scales larger than the period of the plasma oscillation. In general, the charge-neutrality of plasmas is valid over the bulk of the plasma. However, this is not so near the electrodes, and dielectric surfaces for the following reason. The flux of electrons to

the walls is higher due to their larger velocities (mobilities). The electrons that strike the surface are adsorbed on the walls leading to the formation of a sheath region in the plasma. Thus, there is a net positive space charge and so the charge-neutrality is no longer valid in the sheath region. This build up of a net positive space charge causes a restoring force to develop which accelerates the positively charged ions into the walls, and the negatively charged species away from it. This restoring force is the ambipolar diffusion. The ambipolar diffusion coefficient D_a can be expressed as:

$$D_a = D \left(1 + \frac{T_e}{T_i} \right) \quad (1.3)$$

where the D is the diffusion in the bulk plasma (absence of ambipolar forces), and T_e and T_i are the electron and ion temperatures, respectively. Typically, the electron temperatures are a few eV, and the ion temperature is taken as the gas temperature T_g . Thus, the ambipolar diffusion can be nearly 50 – 100 times larger than the neutral diffusion. The assumption that T_g equals T_i is valid at pressures > 1 Torr where the ion-neutral collision frequency is large, leading to a thermalization of the energy.

For a “floating” or an ungrounded surface such as a dielectric material, the build-up of negative charge on the surface causes a “floating” potential to develop. The sheath potential accelerates the positive ions towards the walls. When the energetic ions strike the metal surfaces, they can release the bound electrons in the surface. These free “secondary electrons” are then accelerated by the electric field in the sheath and produce ionization in the bulk plasma. The source of the secondary electrons S is dependent on the ion flux and the surface:

$$S_j = \sum_i \Phi_i \gamma_{ij} \quad (1.4)$$

where S_j is the source of secondary electrons from the j^{th} surface, Φ_i is the flux of the i^{th} ion, and γ_{ij} is the secondary electron coefficient.

As such, the study of the dynamics and properties of the sheath is very important in applications such as materials processing and surface modification. This is because the surfaces are treated or modified by a combination of ion and neutral species fluxes, which are influenced by the characteristics of the sheath. For example, in a thin sheath, the ions are less collisional (as the time spent by the ion in the sheath is less than mean time between collisions), and hence the ions are very directional.

A complete description of the various physical processes occurring in plasmas is beyond the scope of this work. A comprehensive text on the physics of plasmas can be found in references 1 and 2.

1.2 Applications of Plasmas

The most common technological applications of plasmas include the plasma display panels, fluorescent lamps, and in semiconductor processing. In most applications of plasma, it is used as a medium to input energy and breakdown the feedstock into a required product, and/or excite the gas and use a property of the product to achieve the desired result.

For example, in plasma display panels [3,4], fluorescent lamps [5,6], and metal-halide lamps [7,8], the radiation from excited species is desired. The excited species are generated by electron-impact collisions. In plasma display panels, typical operating conditions are 100s

Torr, in mixtures of rare gases such as Ar/Xe. The emission from excimer species such as ArXe^* , Xe_2^* is used as a source of radiation, which is then converted to visible light in the phosphor coating.

In case of mercury vapor lamps for example, the emission from $\text{Hg}(6^3\text{P}_1)$ and $\text{Hg}(6^1\text{P}_1)$ is desired. In these applications, the efficiencies are typically governed by the fraction of the energy that is expended in producing these emitting states, which is a function of the plasma characteristics such as n_e , pressure, power density.

In semiconductor processing (typically at pressures of few – 10s mTorr), the most common use of plasmas is in etching of Si/SiO₂ (using Cl, Br and F containing gas mixtures) and deposition of thin films of metals (such as copper, tungsten) or dielectric materials (silicon-nitride films).[9,10] For example, in etching SiO₂, the plasma is used to breakdown a feedstock gas (such as C₄F₈) and create ions and neutral species. The ions are then accelerated towards the substrate by application of a bias, and these ions activate (increase reactivity) the surface sites on the wafer and/or physically etch away the material. Usually, an anisotropic etch is desired, which requires the incoming ions to be highly directional (usually perpendicular to the wafer). Due to this requirement the semiconductor plasmas are at low pressures where the mean free paths are larger. In the absence of collisions in the sheath, the direction of the ion flux is parallel to the applied electric field. The control over the ion energies, angular distributions, and plasma composition is vital in achieving the desired etch or deposition properties.

Plasmas can be used as a medium to increase reactivity or reduce activation energy, and can serve to augment or replace the equivalent chemical reactions. A common application is the spark plug in internal combustion engines. The discharge produced by the

spark plug produces a mix of reactive species leading to the ignition of the gas mixture. This principle of using plasma as a reactive medium is also being extended to other applications.

For example, production of $O_2(^1\Delta)$ (Singlet Delta of Oxygen, an electronically excited state) in mixtures of rare gas- O_2 is being studied in the context of Chemical Oxygen-Iodine Lasers (COILs) and a review of current literature can be found in Ref. 11. In conventional COIL, the $O_2(^1\Delta)$ is produced by liquid-phase chemical reactions involving volatile compounds such as H_2O_2 and Cl_2 gas. However, the robustness of a gas-phase COIL based on an electrical discharge has caught the attention of many, and will be discussed in chapters 3 and 4 of this dissertation.

Another example of plasmas as a medium for chemical reactions is in the enhancement of endothermic reactions such as in pyrolysis of NH_3 . [12] These reactions typically require elevated temperatures, whereas they can take place at lower temperatures in a plasma. For example, even at a temperature of 1500 K, the half-life of NH_3 for cracking is ≈ 0.7 s, whereas this process could happen in glow discharges at a much faster rate and at lower gas temperatures. The use of plasma in generation of H_2 by dissociation of NH_3 will be the focus of chapter 5 of this dissertation.

Research is also being carried out to apply these plasmas in other technological areas as well. Studies in flowing plasmas at relatively high pressures (> 10 s Torr) are being conducted for purposes such as sources of thrust [13,14], surface modification [15,16], and deposition [17]. Miniaturization of these plasma sources can also lead to a new generation of portable devices that can be used in tandem with conventional MEMS devices. [18]

In the case of microthrusters, the discharge is used as a means of adding energy and momentum to the flow, which is then used to enhance the thrust. These are similar in

operation to other electrothermal propulsion devices such as resistojets and arcjets. The coupling of the power deposition to the flow is important from the standpoint of efficiency (power required per unit thrust) and it is worthwhile to study the plasma dynamics in this regard. Chapter 6 of this dissertation explores the use of microdischarges as microthrusters.

While the etching and deposition in semiconductor plasmas are typically at very low pressures (10s mTorr) due to the requirement of anisotropy, higher pressures can be used in cases where the anisotropy (in ion fluxes) is not required. For example, Kikuchi et al [15] applied a rf plasma at atmospheric pressures for oxidation of a Si layer, and in generation of carbon nanotubes (both amorphous and graphitic). They used a He/O₂ plasma for oxidation of Si, and a discharge in pure CH₄ to develop the carbon nanotubes on a crystalline Si substrate. Lauer et al [16] used hollow-cathode microplasma in argon to modify the internal surface of a small-diameter polyethylene tube, so that it could be made bio- and hemato-compatible.

Plasmas can be used in mitigating the effects of shock in high speed aerodynamics, and a review of current research in this regard can be found in [19]. A discharge in the leading edge of a bluff body can be used to increase the shock stand-off distance, which reduces the gas temperature that the surface is exposed to. The reduction in shock strength also reduces the overall drag coefficient. Plasma based actuators are also being studied [20] with the goal of controlling the flow in the boundary layers of control surfaces of an aircraft. The plasma actuator operates as a dielectric-barrier discharge, and the uni-directional momentum of the charged particles is used to infuse momentum in the boundary-layer of the flow. This can then be used in controlling and delaying the onset of boundary-layer separation.

1.3 Modeling of Plasma Discharges

Building and operating plasma reactors from the standpoint of diagnostics is expensive owing to their complexity and cost of operation. Also, the shortening of product cycles (in semiconductor manufacturing, for instance), implies that a good understanding of the physical processes that govern these plasmas is essential for efficient and fast product development. In this regard, modeling of these plasma reactors is a very useful tool to understand the processes and in identifying the key mechanisms and pathways, and can be especially useful when used in conjunction with experimental results. Advances in plasma modeling have been useful not only in understanding the process, but have also been useful in designing the plasma reactors.

A variety of numerical methods have been developed to deal with the diverse physical processes that take place in plasmas. They range from global plasma models (quasi 1-d) to full 3-d simulations based on fluid- and/or particle-type models.

Ahedo et al [21] studied the 1-d plasma flow in a Hall thruster, and accounted for the interactions between the electrostatic, thermal, and kinetic effects. Carman and Mildren [22] modeled a short-pulse dielectric barrier discharge in xenon to study the plasma kinetics. They assumed the variation along the plate to be minimal and focused on the axial region between the parallel plates of the discharge. They used a local field approximation (assumption of quasi-neutrality). Stafford and Kushner [23] used a global model to study the production of $O_2(^1\Delta)$ in He/O₂ discharges for use in Oxygen-Iodine lasers.

Passchier and Goedheer [24] developed one of the first 2-d models, and used it to study an rf discharge in Ar. They used drift-diffusion approximation for the transport of

charged species, and semi-implicit solutions of the Poisson's equation. Kothnur and Raja [25] modeled a dc microhollow cathode discharge in He at high pressures (100s Torr). They used a self-consistent fluid model for the transport equations. Hammond et al [26] developed a fully conservative numerical algorithm to study low-temperature rf discharges at low pressures. They proposed an efficient algorithm to discretize electron fluxes, which was more accurate than the Scharfetter-Gummel [27] fluxes. Yang et al [28] studied rf discharges in Xe to improve the luminous efficiency in plasma display panels. They proposed two kinds of cell designs using 2-d numerical calculations. Nam and Economou [29] modeled miniature ($d \approx 0.5$ cm) ICPs in Ar at pressures of few 100s mTorr. Their results closely matched with experimental results of Hopwood et al [30].

Three-dimensional simulations are not so common owing to the computational complexity. Cai and Boyd [31] computed the plume flows from a cluster of four Hall thrusters using hybrid particle-fluid method. They used a direct simulation Monte Carlo (DSMC) method to track collisions of heavy particles, and Particle-in-Cell (PIC) methods to track the transport of ions in electric fields. Kushner [32] studied the asymmetries due to 3-D effect of gas pumping in a high plasma density ICP at low pressures.

1.4 Summary

The organization of this thesis is as follows. The descriptions of the models used in this study are described in detail in Ch. 2. A quasi- 1-d model *GlobalKIN* is used in exploring the parameter space in detail, and the 2-d modeling platform *nonPDPSIM* is used to look at the spatial effects which cannot otherwise be captured in 1-d models. The various

modules such as electron transport and energy, conservation of charged species, and neutral fluid dynamics are discussed in detail.

Chapters 3 and 4 deal with the production of $O_2(^1\Delta)$ and $I(^2P_{1/2})$ in the context of electrical Oxygen-Iodine Lasers. In Ch. 3, the scaling of $O_2(^1\Delta)$ production in ICP and CCP discharges in mixtures of He/ O_2 will be discussed. Parameterization with power, pressure, and composition will be explored with the goal of increasing the yield of $O_2(^1\Delta)$. The reaction chemistry is identical to that used in Ref. 23, and will be summarized. In Ch. 4, the effects of additives such as NO to the discharge, and NO_2 and I_2 in the afterglow are discussed in the context of Oxygen-Iodine lasers. The reaction mechanism due to addition of NO, NO_2 , and I_2 species will be discussed. $O_2(^1\Delta)$ and $I(^2P_{1/2})$ production in the presence of NO additives, and the effects of gas composition in the densities of important species are studied. Parameterization based on power and pressure is also carried out using *GlobalKIN*.

In Ch. 5, the generation of H_2 in discharges of Ar/ NH_3 mixtures will be discussed, with the goal of maximizing the H_2 flux per unit power, and the utilization of NH_3 . The reaction chemistry will be discussed in detail, with emphasis on the dissociation of NH_3 in the discharge and the subsequent neutral chemistry. Parameterization based on flow rate, gas composition, and power density will be discussed.

In Chapter 6, microdischarges in Ar are studied in the context of microthrusters. Different classes of microdischarges are studied, and the effects of geometry such as the length of the nozzle, and divergence angle on the plasma and flow characteristics are also studied. Parameterization based on power and pressure is carried out, and the enhancement of thrust due to the discharge is reported.

1.5 Figures

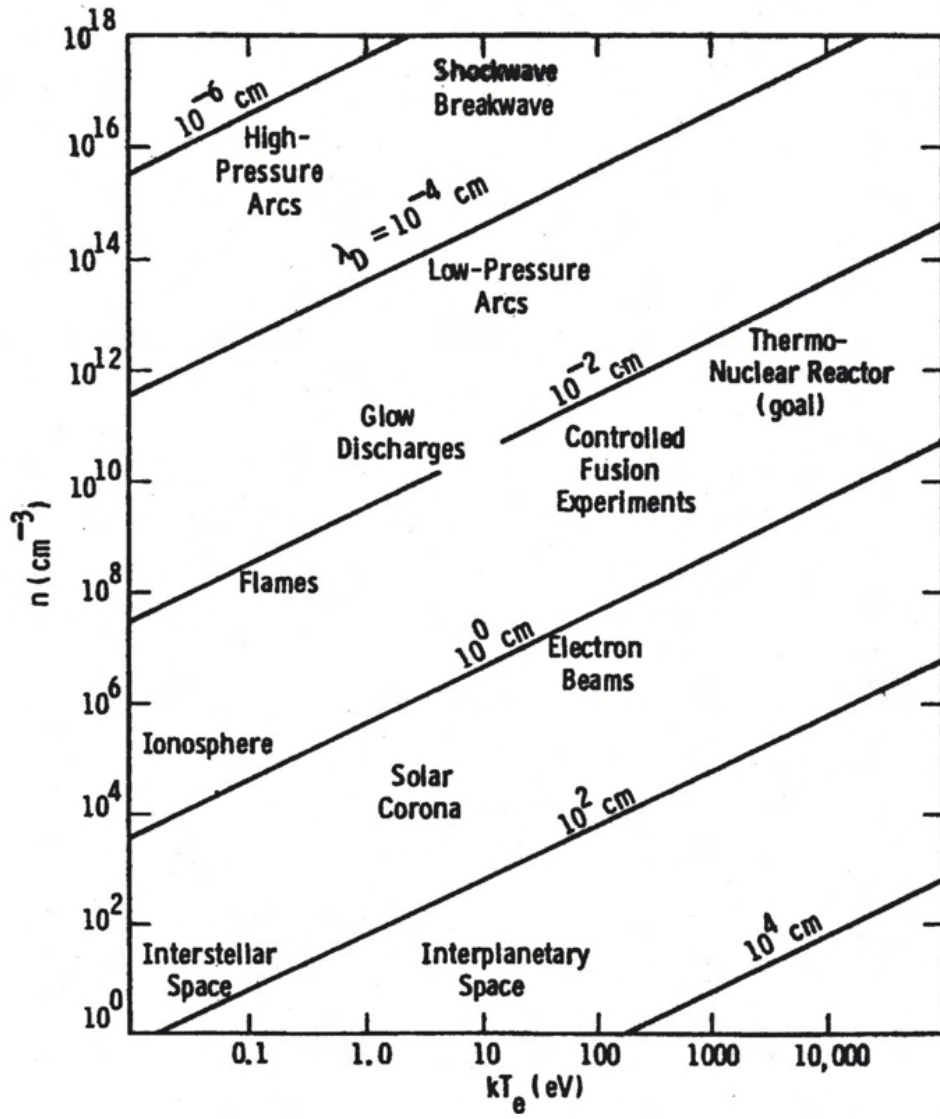


Fig. 1.1 Classification of plasmas based on density and temperature of electrons.

1.6 References

1. M. A. Lieberman and A. J. Lichtenberg, *Principles of Plasma Discharges and Materials Processing* (John Wiley & Sons, NY, 1994).
2. M. Mitchner and C. H. Kruger, Jr., *Partially Ionized Gases* (John Wiley & Sons, NY, 1992).
3. A. Sobel, *Sci. Am.* **278**, 70 (1998).
4. S. Rauf and M. J. Kushner, *J. Appl. Phys.* **85**, 3460 (1999); S. Rauf and M. J. Kushner, *J. Appl. Phys.* **85**, 3470 (1999).
5. J. M. Anderson, *US Patent* 3,500,118 (1970).
6. G. G. Lister, J. E. Lawler, W. P. Lapatovich and V. A. Godyak, *Rev. Mod. Phys.* **76**, 541 (2004).
7. W. M. Keefe and Z. K. Krasko, *US Patent* 4,709,184 (1987).
8. B. Lay, R. S. Moss, S. Rauf and M. J. Kushner, *Plasma Sources Sci. Tech.* **12**, 8 (2003).
9. D. B. Graves, *IEEE Trans. Plasma Sci.* **22**, 31 (1994).
10. M. Armacost *et al*, *IBM J. Res. Dev.* **43**, 39 (1999).
11. A. A. Ionin, I. V. Kochetov, A. P. Napartovich and N. N. Yuryshev, *J. Phys. D: Appl. Phys.* **40**, R25 (2007).
12. R. d'Agostino, F. Cramarossa, S. De Benedictis and G. Ferraro, *Plasma Chem. Plasma Proc.* **1** 19 (1981).
13. H. Horisawa and I. Kimura, "Very Low-Power DC Plasma Jet Microthrusters", AIAA 2001-3791.
14. J. Slough, S. Andreason, T. Ziemba and J. J. Ewing, "Micro-discharge Micro-thruster", AIAA 2005-4074.

15. T. Kikuchi, Y. Hasegawa and H. Shirai, *J. Phys. D: Appl. Phys.* **37**, 1537 (2004).
16. J. L. Lauer *et al*, *J. Appl. Phys.* **96**, 4539 (2004).
17. R. M. Sankaran and K. P. Giapis, *J. Appl. Phys.* **92**, 2406 (2002).
18. J. Hopwood, O. Minayeva and Y. Yin, *J. Vac. Sci. Tech. B* **18**, 2446 (2000).
19. P. Bletzinger, B. N. Ganguly, D. Van Wie and A. Garscadden, *J. Phys. D: Appl. Phys.* **38**, 33 (2005).
20. C. L. Enloe, T. E. McLaughlin, R. D. Van Dyken and J. C. Fischer, “Plasma Structure in the aerodynamic plasma actuator”, *42nd AIAA Aerospace Sciences Meeting and Exhibit (Reno, Nevada, USA)* (2004).
21. E. Ahedo, P. Martínez-Cerezo and M. Martínez-Sánchez, *Phys. Plasmas* **8**, 3058 (2001).
22. R. J. Carman and R. P. Mildren, *J. Phys. D: Appl. Phys.* **36**, 19 (2003).
23. D. S. Stafford and M. J. Kushner, *J. Appl. Phys.* **96**, 2451 (2004).
24. J. D. P. Passchier and W. J. Goedheer, *J. Appl. Phys.* **74**, 3744 (1993).
25. P. S. Kothnur and L. L. Raja, *J. Appl. Phys.* **97**, 043305 (2005).
26. E. P. Hammond, K. Mahesh and P. Moin, *J. Comp. Phys.* **176**, 402 (2002).
27. D. L. Scharfetter and H. K. Gummel, *IEEE Trans. Electron Devices* **ED-16**, 64 (1969).
28. S. S. Yang, H. C. Kim, S. W. Ko and J. K. Lee, *IEEE Trans. Plasma Science* **31**, 596 (2003).
29. S. K. Nam and D. J. Economou, *J. Appl. Phys.* **95**, 2272 (2004).
30. J. Hopwood, O. Minayeva and Y. Yin, *J. Vac. Sci. Technol. B* **18**, 2446 (2000).
31. C. Cai and I. D. Boyd, “3D Simulation of Plume Flows from a Cluster of Plasma Thrusters”, *36th AIAA Plasmadynamics and Lasers Conference (Toronto, Ontario, Canada)* (2005).

32. M. J. Kushner, J. Appl. Phys. **82**, 5312 (1997).

CHAPTER 2. DESCRIPTION OF MODELS

2.1 Introduction

In this chapter, the models used in this study (2-dimensional, and global or quasi 1-d model) are described in detail. The global model (GlobalKIN) when used as a plug flow model is a quasi 1-d model that addresses the problem from a global perspective of mass, momentum, and energy transfer. It computes volume-averaged quantities and can be used to quickly analyze important reactions and explore the parameter space in detail. The 2-dimensional platform is a more comprehensive modeling platform and consists of various sub-models that cater to various physical aspects of the problem. It can be broken down into the following sub-models: a Boltzmann solver to give electron energy distributions and its moments, Poisson's equation solver that computes the electric potential taking into account surface and volume charges, electron Monte Carlo transport module to compute electron energy distributions using a particle simulation approach, species transport using Scharfetter-Gummel fluxes, and neutral transport using Navier-Stokes equations coupled with reaction kinetics. Each of the sub-models will be explained in detail in the subsequent sections.

2.2 GlobalKIN

GlobalKIN is a volume averaged, global kinetics model for plasma chemistry which, in plug flow mode, resolves axial transport. GlobalKIN consists of a volume averaged plasma chemistry module, a surface kinetics module and an electron energy transport module. The plasma chemistry module provides the time rate of change of species based on gas phase chemistry and surface reactions. T_e and average gas temperature, T_g , are also solved for by integrating their respective conservation equations. Assuming a linear axial

flow, transport to radial surfaces is included by using a diffusion length. The surface-kinetics module employs a surface site-balance model which provides surface reaction coefficients used in the volumetric model. The electron energy transport module consists of a solution to Boltzmann's equation for the electron energy distribution (EED) which provides electron impact rate coefficients based on the EEDs and fundamental cross-sections. The resulting rate equations are integrated in time using a stiff ordinary differential equation solver. By simultaneously calculating the axial speed of the flow based on constant pressure, change in enthalpy, species densities and gas temperature, and the integration in time is mapped to axial position.

The time rate of change of species is determined by the continuity equation:

$$\frac{dN_i}{dt} = W_i + S_i - \frac{N_i}{T_g} \frac{dT_g}{dt} \quad (2.1)$$

$$\frac{dN_i^\pm}{dt} = W_i + S_i + \vec{\nabla} \cdot (D_{a,i} \vec{\nabla} N_i) \quad (2.2)$$

$$W_i = -\vec{\nabla} \cdot \left(-\gamma_i D_i \vec{\nabla} N_i + \sum \gamma_i f_{ji} D_j \vec{\nabla} N_j \right) \quad (2.3)$$

where N_i and N_i^\pm are the densities of the i^{th} neutral and charged species, D_i and $D_{a,i}$ are the diffusion and ambipolar diffusion coefficients, W_i is the radial diffusive flux, γ_i is the relative sticking coefficient on the wall, f_{ji} is the return fraction of the species i from the wall due to the flux of the j^{th} species, S_i is the source of species i due to reactions, and T_g is the gas temperature. The diffusivities are calculated from Lennard-Jones potentials and are calculated for each species as a function of the local gas composition. The ambipolar

diffusion arises due to difference in mobility between the electrons and ions and act in a way to restrict the mobility of electrons and enhance the mobility of ions. These are calculated based on the instantaneous relative mobility (between ions and electrons) and diffusivities. The gradients are replaced by a diffusion length Λ , over which the densities go to zero, and typically this value is the diameter of the tube or a characteristic length. The rates of reactions are obtained from Arrhenius expressions for the heavy particle reactions, and from the electron energy distribution (EED) for the electron impact reactions.

In low temperature plasma at relatively high pressures (> 1 Torr) which is the case in this work, the ions and neutrals are in near thermal equilibrium due to the collisions, and hence the temperature of the ions is the same as the neutral gas temperature. Thus, the temperature calculations (for the heavy particles) can be described by a single equation with contributions to gas heating from inelastic collisions with electrons, heat of reactions, and conduction to the walls. The electrons can be accelerated quickly in electric fields and can attain high velocities. Hence, the electron temperature can be quite different from neutral gas temperature, and has to be treated separately.

$$\begin{aligned} \frac{d}{dt}(NC_p T_g) = \sum_i \frac{3}{2} n_e v_{mi} \frac{2m_e}{M} k_B (T_e - T_g) + \sum_j n_e k_j N_j \Delta \varepsilon \\ - \sum_j \Delta H_j + \frac{K}{\Lambda^2} (T_w - T_g) - \frac{d}{dt} \left(\frac{1}{2} M_w N v_x^2 \right) \end{aligned} \quad (2.4)$$

$$\frac{d}{dt} \left(\frac{3}{2} n_e k_B T_e \right) = \vec{j} \cdot \vec{E} - \vec{\nabla} \cdot \vec{q}_e - \sum_i \frac{3}{2} v_{mi} \frac{2m_e}{M_i} k_B (T_e - T_g) - \sum_j n_e k_j N_j \Delta \varepsilon_j \quad (2.5)$$

$$\vec{q}_e = \frac{5}{2} \vec{\Gamma}_e k_B T_e - \lambda_e \vec{\nabla} (k_B T_e) \quad (2.6)$$

$$\vec{\Gamma}_e = \mu_e q_e n_e \vec{E} - D_e \vec{\nabla} n_e \quad (2.7)$$

$$\lambda_e = \frac{5}{2} \frac{n_e k_B T_e}{m_e \nu_{m,avg}} \quad (2.8)$$

$$D_e = \frac{k_B T_e}{m_e \nu_{m,avg}} \quad (2.9)$$

where N is the neutral gas density, C_p and T_g are the specific heat and temperature of the gas, n_e , m_e , T_e are the electron density, mass and temperature, ν_{mi} is the momentum transfer collision frequency between electrons and the i^{th} species, k_B is the Boltzmann's constant, M_i is the ion mass, k_j , N_j , and $\Delta \varepsilon_j$ are the rate constant, density of colliding partner, and energy loss for the j^{th} electron impact reaction, ΔH_j is the enthalpy of the j^{th} heavy-particle reaction, K is the average thermal conductivity, Λ is the diffusion length, M_w is the average mass, and v_x is the flow velocity. The $j.E$ term in the electron energy equation represents the power deposited by the electric fields and is specified as an input to the problem. q_e is the electron energy flux and is composed of the convection and conduction parts. The Γ_e is the electron flux (drift-diffusion) used for the convection term, and the λ_e is the coefficient of electron conduction.

The electron energy distribution and the rates of reactions (calculated by convolving the EED with cross-sections for reactions) are generated by solving Boltzmann's equations for the EED using the two-term spherical harmonic expansion.[5] These are calculated as a function of the given E/N values, and as a function of distance as the composition of the gas changes along the axis of the discharge due to reactions between various species.

The transport of neutral species are accounted for by introducing an axial velocity v_z that is solved for using conditions such as initial velocity or mass flow rate taking into account changes in density (due to reactions) and temperature (due to heat of reactions).

$$\frac{dv_z}{dt} = -\frac{v_z}{\rho} \frac{d\rho}{dt}, \quad (2.10)$$

where the density (ρ) is obtained from average molecular weight M_w and number density N .

In plug flow mode, only the axial convection is included, and the axial diffusion is ignored. However, the radial diffusion terms are included using the diffusion length Λ .

The variables (N_i , T_g , T_e , n_e , v_z) are normalized and solved simultaneously using an Ordinary Differential Equation (ODE) solver using libraries available from Lawrence Livermore National Labs.[6] The solution is then marched in time and space (using the axial velocity) and the solution to these quantities is obtained as a function of distance. The Boltzmann solver is called at frequent intervals along the tube to take into account the changes in mole fractions of the species, especially in regions of power deposition. Downstream of the discharge region, the Boltzmann solver is called less frequently as the electron energies and densities are negligible.

Dirichlet and Neumann boundary conditions are prescribed at the inlet and outlet, respectively. Since the mass flow rate is handled conservatively, it automatically adjusts the velocities such that there is no net change in mass at the axial locations. At each axial location, the charge conservation is automatically maintained by the ambipolar fluxes.

2.3 nonPDPSIM

nonPDPSIM is the 2-d model that solves for the plasma potential (Poisson's equation), densities of species, gas and electron temperatures, neutral flow velocities in a consistent manner taking into account surface reactions, secondary electron emissions, photoelectric and thermoelectric emissions (if any). Unstructured triangulated meshes are

used to capture the computational domain in sufficient detail with varying degrees of refinement so as to ease computational burden. Apart from the Boltzmann solver for the equilibrium EEDs, the non-equilibrium nature of the EEDs (especially near cathode surfaces) are handled using an electron Monte Carlo technique applied on a Cartesian mesh that has been superimposed on the unstructured mesh. This can resolve temporal and spatial variations of the plasma and the neutral gas properties. Power deposition using Inductive Coupling and/or Capacitive Coupling is calculated consistently along with the rest of the discharge.

2.3.1 Mesh Generation and Discretization

The unstructured triangular meshes were generated offline using a commercial mesh generator (SkyMesh, produced by SkyBlue systems). The inputs to this were the coordinates of the nodes, the connectivity of the geometrical edges, and the boundary conditions such as material identity of the faces, edges, and nodes. Other details included the zone number and whether the geometrical entity was part of the boundary or not. The zone number was used to specify different initial conditions such as pressure and temperature in different parts of the plasma and was useful in cases where the inlet pressure was higher than the outlet pressure, simulating a typical flowfield in a nozzle. Refinement zones are applied so as to have a very fine mesh near the regions where the gradients of physical quantities are likely to be high with a progressively coarser mesh towards the outlet of the reactor. A typical mesh used in this study is shown in Fig 2.1 with the boundaries of the refinement zones highlighted. This particular mesh was used in the simulation of microthrusters and the fine mesh is in the region near the electrodes. The Finite Volume Method (FVM) was used

to discretize the partial differential equations arising from the modeling of the plasma and hydrodynamics. The vertex centered approach was used to construct the finite volumes. Thus, the vertices (or the nodes) formed the center of the volume, and the boundaries of the volume were constructed by joining the perpendicular bisectors of the edges between the nodes and their neighbors as shown in Fig 2.2. The FVM formulation automatically conserves the fluxes of quantities provided there are no obtuse-angled triangles. The mathematical formulation of operators such as gradients, Laplacian are shown below:

$$\bar{\nabla} \phi_i = \frac{1}{N} \sum_{j=1}^N \left(\frac{\phi_j - \phi_i}{l_{i,j}} (\cos \theta_{ij} \hat{i} + \sin \theta_{ij} \hat{j}) \right) \quad (2.11)$$

$$\bar{\nabla} \cdot \vec{\phi}_i = \frac{1}{V_i} \sum_{j=1}^N (\vec{\phi}_{ij} \Delta S_{ij}) \quad (2.12)$$

$$\nabla^2 \phi = \frac{1}{V_i} \sum_{j=1}^N \left(\frac{\phi_j - \phi_i}{l_{ij}} \Delta S_{ij} \right) \quad (2.13)$$

where, ϕ_i and ϕ_j refer to the values of the quantity ϕ for the i^{th} node and its j^{th} neighbor. The terms l_{ij} , θ_{ij} , ΔS_{ij} and ϕ_{ij} refer to the distance, angle, surface area and value of the quantity ϕ at the interface between the i^{th} node and its j^{th} neighbor. N is the number of neighbors for the node. The value of ϕ_{ij} is determined by the method used to determine the flux (upwind for fluid quantities, Scharfetter-Gummel in case of charged particles). The surface area ΔS_{ij} is calculated appropriately depending on whether the mesh is in Cartesian or cylindrical-polar co-ordinates.

2.3.2 Inputs to the Model

The inputs to the model include the global conditions such as pressure, temperature, flow rates, and mole fractions of the various species included. Material properties include thermal and electrical conductivities, designation of dielectric and metal surfaces, designation of nozzle and pump materials, and secondary electron and thermoelectric emission coefficients. The power deposition could be specified by indicating a voltage on the metal surfaces, or as a power that has to be deposited into the plasma. In case of Inductively Coupled Plasmas, the power to be coupled to the plasma is input and an initial value of the voltage is mentioned.

The species to be included are mentioned along with their initial mole fractions in the discharge. The charged species are scaled along with the initial electron density which is typically set to a value of $1/1000^{\text{th}}$ of the expected steady state value. The mole fractions of each of the species coming into the discharge through the nozzle(s) are also mentioned.

The coupling between the various modules can be adjusted by setting the frequency at which they are called. The times when the modules such as Boltzmann, Monte Carlo, Navier-Stokes, and Surface are called are included in the input file.

The inputs to the Monte Carlo module include the extents of the Cartesian mesh, the number of particles to simulate, and the number of energy bins. For the Boltzmann module, the number of E/Ns for which the electron impact rates are calculated is tabulated.

The reaction mechanism includes the various electron impact reactions, ion-ion and ion-neutral reactions, and other heavy particle reactions. The rates are calculated from the Boltzmann/Monte Carlo module for the electron impact reactions, and using Arrhenius type calculations for heavy particle reactions. The cross-sections for electron impact reactions are

tabulated for various electron energies and interpolated for values of electron energy that lie in-between. The rate constants and cross-sections are included from articles that have been previously published in peer-reviewed journals. The mechanisms used in this work are included in Appendices A – C.

2.3.3 Solution of the Plasma Characteristics

The plasma potential and the densities of the charged species are linked together in the core of the model that solves the Poisson's equation for the plasma potential using volumetric and surface charge densities.

$$-\vec{\nabla} \cdot \epsilon \vec{\nabla} \Phi = \sum_j (N_j q_j) + \rho_s \quad (2.14)$$

$$\frac{\partial N_i}{\partial t} = -\vec{\nabla} \cdot \vec{\phi}_i + S_i \quad (2.15)$$

$$\frac{\partial \rho_s}{\partial t} = -\sigma_i \vec{\nabla} \cdot q_i \vec{\phi}_i (1 + \gamma_i) - \vec{\nabla} \cdot \sigma (-\vec{\nabla} \Phi), \quad (2.16)$$

where ϵ , Φ , ρ_s , and σ are the electrical permittivity, plasma potential, surface charge, and conductivity of the material, respectively. The N_j , q_j , ϕ_j , S_j , and γ_j refer to the number density, charge, flux, rate of production, and secondary emission coefficient of the j^{th} charged species. The charged particles were transported by using Scharfetter-Gummel fluxes.[7] This method has advantages over drift-diffusion in that it can handle sharp gradients in densities, and provides stable solutions. In this method, the flux between node i and neighbor j ϕ_{ij} is given by:

$$\bar{\phi}_{ij} = \alpha \bar{D} \left(\frac{n_j - n_i \exp(\alpha_{ij} \Delta x_{ij})}{1 - \exp(\alpha_{ij} \Delta x_{ij})} \right) \quad (2.17)$$

where, n_i and n_j are the charged particle density, and α_{ij} is given by:

$$\alpha_{ij} = \frac{q}{|q|} \frac{\bar{\mu} \vec{E}_{ij}}{\bar{D}}, \quad (2.18)$$

where D and μ are the average diffusion and mobilities.

$$\bar{D} = \frac{D_i + D_j}{2}, \quad \bar{\mu} = \frac{\mu_i + \mu_j}{2} \quad (2.19)$$

The system of equations (2.14 – 2.16) are solved simultaneously for the Φ_i , N_{ik} , and $\rho_{s,i}$ where the subscript i refers to the node number, and subscript k refers to the k^{th} charged species. The equations are normalized (to improve the matrix conditioning), linearized and solved using an iterative Newton method using numerically calculated Jacobian terms. For example, the Poisson's equation can be written as:

$$F_1(t) = -\vec{\nabla} \cdot \epsilon \vec{\nabla} \Phi - \sum_j N_j q_j - \rho_s = 0, \quad (2.20)$$

and the time-marching is achieved by using an implicit scheme:

$$F_1(t + \Delta t) = F_1(t) + \frac{\partial F_1}{\partial X_j} \Delta X_j(t + \Delta t) = 0, \quad (2.21)$$

where the Jacobian terms are obtained by perturbing the independent variables such as Φ_i , Φ_j , $N_{i,k}$, $N_{j,k}$, and $\rho_{s,i}$ and $\rho_{s,j}$ and calculating the change in F_1 due to the changes in each of the independent variables. Thus, one can construct the matrix equation:

$$\left[\frac{\partial F_i}{\partial X_j} \right] \Delta X_j = -F_1(t), \quad (2.22)$$

with i representing the cumulative index for each node and equation (Poisson's, charge continuity, or surface charge), and j representing the cumulative index for each node and independent variable. The matrix that arises due to the above equation is a sparse matrix and sparse matrix techniques are used to reduce storage and aid in the solution. The matrix was solved iteratively using bi-conjugate gradient method with incomplete LU factorization using numerical packages such as *dslucs*, *dslugm* obtained from the SLAP Sparse Matrix Library [8] or *sparskit* [9]. The L_∞ norm was used as the method to calculate residue and the matrix solution was iteratively solved until the residue was less than a pre-defined value. The initial guess for the independent variables were chosen to be:

$$\Delta X_{i,0} = (X_i(t) - X_i(t - \Delta t_0)) \frac{\Delta t}{\Delta t_0}, \quad (2.23)$$

where $\Delta X_{i,0}$ is the starting guess, and Δt_0 is the previous timestep.

The number of iterations required to solve the matrix equation for the prior timesteps were kept track of and used to automatically increase or decrease the timesteps used. For example, the timestep was increased by a pre-defined factor if the number of iterations in the 20 prior timesteps was less than a pre-defined number of iterations. These were used so as to minimize the number of times the matrix was re-built.

Once the timestep is completed, the transport properties (mobilities, diffusivities) and reaction rates are calculated again based on the current values of the variables. This is done so as to have tight coupling between the various physical processes. Updates to other quantities (such as T_e , neutral densities) are done depending on the input that specifies the frequency at which they need to be updated.

The electron energy equation that governs the T_e is the same as Eq. 2.5, except that in this case the gradients are calculated consistently (as opposed to using diffusion lengths in the global model). The solution is achieved using a Successive Over Relaxation (SOR) method. SOR is an iterative method used for solving elliptic equations. The discretization in space of the the Eq. 2.5 leads to:

$$\frac{\partial T_{e,i}}{\partial t} = f(T_{e,i}) + \alpha T_{e,i} + \gamma \sum_{j=1}^N T_{e,j}, \quad (2.24)$$

which can further be discretized in time as:

$$T_{e,i}^{n,k+1} = \frac{T_{e,i}^{n,k} + f(T_{e,i}^{n,k}) + \gamma \Delta t \sum_{j=1}^N T_{e,j}^{n,k}}{1 - \alpha \Delta t}, \quad (2.25)$$

where $T_{e,i}^{n,k}$ is the value of T_e at the i^{th} node during the k^{th} iteration. The function $f(T_{e,i})$ contains the information for energy loss through collisions, and energy gain due to power deposition. The values α and γ contain the information for geometrical factors due to the gradient and Laplacian calculations for electron diffusion, conduction, and convection, and the summation from 1 to N is for the neighbors of the node i . The SOR is implemented using the equation below:

$$T_{e,i}^{n,k+1} = \beta \left(\frac{T_{e,i}^{n,k} + f(T_{e,i}^{n,k}) + \gamma \Delta t \sum_{j=1}^N T_{e,j}^{n,k}}{1 - \alpha \Delta t} \right) + (1 - \beta) T_{e,i}^{n,k}, \quad (2.26)$$

where β is the “over-relaxation” parameter and a value of 1.7 was used in our calculations. Typically, any value > 1 can be used as the relaxation parameter, and values of 1.7 -1.8 lead to faster convergence. This over-relaxation implies that the latest $(k+1^{\text{th}})$ value of T_e is given more weightage than the k^{th} value. The value of Δt is the same as used in the Poisson’s equation. The T_e is said to have converged when the relative difference between the values of T_e for any two successive iterations for all the nodes is less than a pre-defined tolerance.

The solution to the Boltzmann equation is the same as used in the global model, and it computes the electron-impact rates for the reactions based on the EED and the collision cross-section. In addition to the Boltzmann module, the Monte Carlo approach is used to capture the high-energy tail of the EED, which can be important in regions of non-equilibrium. In the Monte Carlo approach, pseudo-particles are released from a source location (typically surfaces of cathodes, thermoelectric emission points on the metal) with a

fixed starting energy (velocity) in random directions and tracked as they drift in the electric fields. As they move in the Monte Carlo domain, the collisions are tracked, and the statistics such as number density and the energy are collected at each discretized spatial location. The electrons are tracked until they leave the Monte Carlo region or until they are thermalized ($E < 0.9 E_0$). The sources due to these Monte Carlo electrons are then included along with those of the bulk electrons in a consistent manner.

2.3.4 Power Deposition

The power deposition to the plasma is by either through capacitive coupling or through inductive coupling. In capacitive coupling, the powered electrodes deposit power into the plasma through the formation of sheaths where the ions and secondary electrons are accelerated and transfer power through collisions. A voltage is applied to the electrode through the means of a circuit, and depending on the current flowing through the electrode, the voltage is changed. Basic circuit elements such as a resistor, capacitor, and an inductor can be attached, and the voltage that appears on the electrode is given by:

$$V(t) = V_0 - I(t)R(t) - L \frac{dI}{dt} - \int \frac{I}{C} dt , \quad (2.27)$$

The charge separation in the sheath causes an electric field to be setup and the power deposited into the plasma is given by:

$$P = \int_V \vec{j} \cdot \vec{E} dV , \quad (2.28)$$

where j is the current density (due to flux of both electrons and ions), and E is the electric field and the integration is over the volume of the plasma. In terms of the inputs, one could either specify a voltage and let the power be calculated automatically, or specify a power to be deposited and let the voltage fluctuate. The fixed power deposition is achieved by monitoring the power deposited on a time-averaged basis, and normalizing the voltage so as to deposit the required power. Thus, if P_{in} and P_{act} are the desired and actual power deposition, then the voltages could be adjusted by the relation:

$$V_0(t+1) = V_0(t) \sqrt{\frac{P_{in}}{P_{act}}} . \quad (2.29)$$

This normalization is regulated so that the relative changes to the voltages are no more than a few %. Since we are mostly looking at steady-state results, the ramifications of the regulation and normalization are not very important. The time interval used for the averaging process is an input parameter and can be used to modulate the power.

Inductive Coupling of the power deposition is achieved by the electromagnetic coupling of the current in the coils to the plasma. The coils are setup in a way that the currents have azimuthal symmetry. The solution of the electric fields is addressed by solving the frequency domain form of the Maxwell's equation.

$$\nabla^2 E_\theta - \mu_0 \varepsilon \frac{\partial^2 E_\theta}{\partial t^2} = \mu_0 \sigma \frac{\partial E_\theta}{\partial t} + \mu_0 \frac{\partial J_\theta}{\partial t} , \quad (2.30)$$

where the electric field and the currents are assumed to be of the form:

$$E_{\theta}(\vec{r}, t) = E_0(\vec{r}) \exp(i\omega t), \quad (2.31)$$

$$J_{\theta}(\vec{r}, t) = J_0(\vec{r}) \exp(i\omega t), \quad (2.32)$$

and the wave equation can be reduced to the form:

$$\nabla^2 E_0 + \mu_0 \varepsilon \omega^2 E_0 = i\omega \mu_0 \sigma E_0 + i\omega \mu_0 J_0, \quad (2.33)$$

where μ_0 and ε are the magnetic permeability of free space and electric permittivity, J_0 and ω are the amplitude and frequency of the current in the coils, and σ is the conductivity of the plasma. The wave equation is discretized and solved using the SOR method as follows:

$$E_{0,i} \left(-\sum_{j=1}^N \frac{\Delta S_{ij}}{l_{ij} V_i} + \mu_0 \varepsilon \omega^2 - i\omega \mu_0 \sigma \right) = -\sum_{j=1}^N \frac{\Delta S_{ij} E_{0,j}}{l_{ij} V_i} + i\mu_0 \omega J_{0,i}, \quad (2.34)$$

$$E_{0,i}^{n+1} = \beta \left(\frac{\sum_{j=1}^N \frac{\Delta S_{ij} E_{0,j} - i\mu_0 \omega J_{0,i}}{l_{ij} V_i}}{\sum_{j=1}^N \frac{\Delta S_{ij}}{l_{ij} V_i} - (\mu_0 \varepsilon \omega^2 - i\omega \mu_0 \sigma)} \right) + (1 - \beta) E_{0,i}^n. \quad (2.35)$$

The subscripts i and j refer to a node and its neighbors, and the superscripts n and $n+1$ refer to the iteration numbers. The geometrical factors ΔS_{ij} , l_{ij} , and V_i are the same as those used in the SOR for the T_e calculation. A value of 1.7 was used as the over-relaxation parameter β , and the criterion for convergence was similar to that of the T_e equation. The current in the coil J_0 was normalized so as to deposit the required power which was calculated as:

$$P_{act} = \frac{1}{2} \int_V \sigma \vec{E} \cdot \vec{E} dV \quad (2.36)$$

2.3.5 Neutral Fluid Transport

The neutral fluid transport (mass, momentum, energy) was handled using the compressible Navier-Stokes equations. For the Navier-Stokes equations, the fluid was thought to be a homogeneous entity. The individual species transport was addressed separately utilizing the advective flow fields obtained by solving the Navier-Stokes equations. The equations solved were:

$$\frac{\partial \rho}{\partial t} = -\vec{\nabla} \cdot \rho \vec{V} + S \quad (2.37)$$

$$\frac{\partial \rho \vec{V}}{\partial t} + \vec{\nabla} \cdot (\rho \vec{V} \vec{V}) = -\vec{\nabla} P + \mu \vec{\nabla}^2 \vec{V} + \sum_{ions} q_i \vec{E}_i (N_i - S_i m_i \mu_i) \quad (2.38)$$

$$\begin{aligned} \frac{\partial \rho C_p T_g}{\partial t} + \vec{\nabla} \cdot (\rho C_p T_g \vec{V}) &= \vec{\nabla} \cdot (k \vec{\nabla} T_g) + P(\vec{\nabla} \cdot \vec{V}) \\ &- \sum_{reactions} R_i \Delta H_i + \sum_{ions} \vec{j} \cdot \vec{E} + \mu(\vec{\nabla} \vec{V}) \cdot (\vec{\nabla} \vec{V}) \end{aligned} \quad (2.39)$$

where ρ , V , T_g are the density, velocity and temperature of the gas, S are the sources due to the inlets and outlets, P is the static pressure (calculated from equation of state), μ is the viscosity, q_i , N_i , S_i , m_i , μ_i , and j_i are the charge, number density, source, mass, mobility, and current density of the i^{th} ion, C_p and k are the average specific heat and conductivity of the gas, R_i and ΔH_i are the rate and enthalpy of the i^{th} reaction, and E is the electric field. The solution to these equations was by direct integration with implicit Jacobian terms. For example, the continuity equation can be written as:

$$G_1(t) = \frac{\partial \rho}{\partial t} = -\vec{\nabla} \cdot \vec{V}, \quad (2.40)$$

and integrating ρ implicitly in time, we get:

$$\rho(t + \Delta t) = \rho(t) + G_1(t + \Delta t)\Delta t. \quad (2.41)$$

Now, $\Delta\rho$ can be written as:

$$\Delta\rho = \left(G_1(t) + \frac{\partial G_1}{\partial X_j} \Delta X_j \right) \Delta t, \quad (2.42)$$

where the differentiation in time has been replaced by differentiation with respect to the independent variables. The ΔX_j represents the perturbation in variables such as ρ , ρu , ρv , and T_g for the nodes and their neighbors. Finally, the entire system (all the equations, for all the nodes) can be assembled into a matrix which can be represented as follows:

$$\left[\frac{1}{\Delta t} [I] - \left[\frac{\partial G_i}{\partial X_j} \right] \right] \{ \Delta X_j \} = \{ G_i \}, \quad (2.43)$$

where $[I]$ is an identity-matrix of appropriate dimension, the index i is cumulative over all the equations (continuity, x- and y- momentum, gas temperature) and nodes, and the index j is for all the independent variables for all the nodes. The solution of the matrix equation is identical to the methods used for solution of plasma parameters.

The transport of individual species was addressed by superimposing the advection flow speed along with the diffusion, and taking into account the reactions between the species. These are done in a time-splicing manner wherein during the updates of the neutral species, the charged species densities are assumed to be constant. The neutral fluid transport includes source terms from gas-phase and surface reactions (if any).

$$\frac{\partial N_i}{\partial t} = -\vec{\nabla} \cdot (\vec{v}N_i + D_i N \vec{\nabla}(\chi_i)) + S_i \quad (2.44)$$

In the above equation, χ_i represents the mole fraction of the i^{th} neutral species, N_i is the density of the i^{th} species and N is the total density. The term S_i represents source terms due to surface and gas-phase reactions. The integration of this equation is carried out using an SOR method.

2.4 Figures

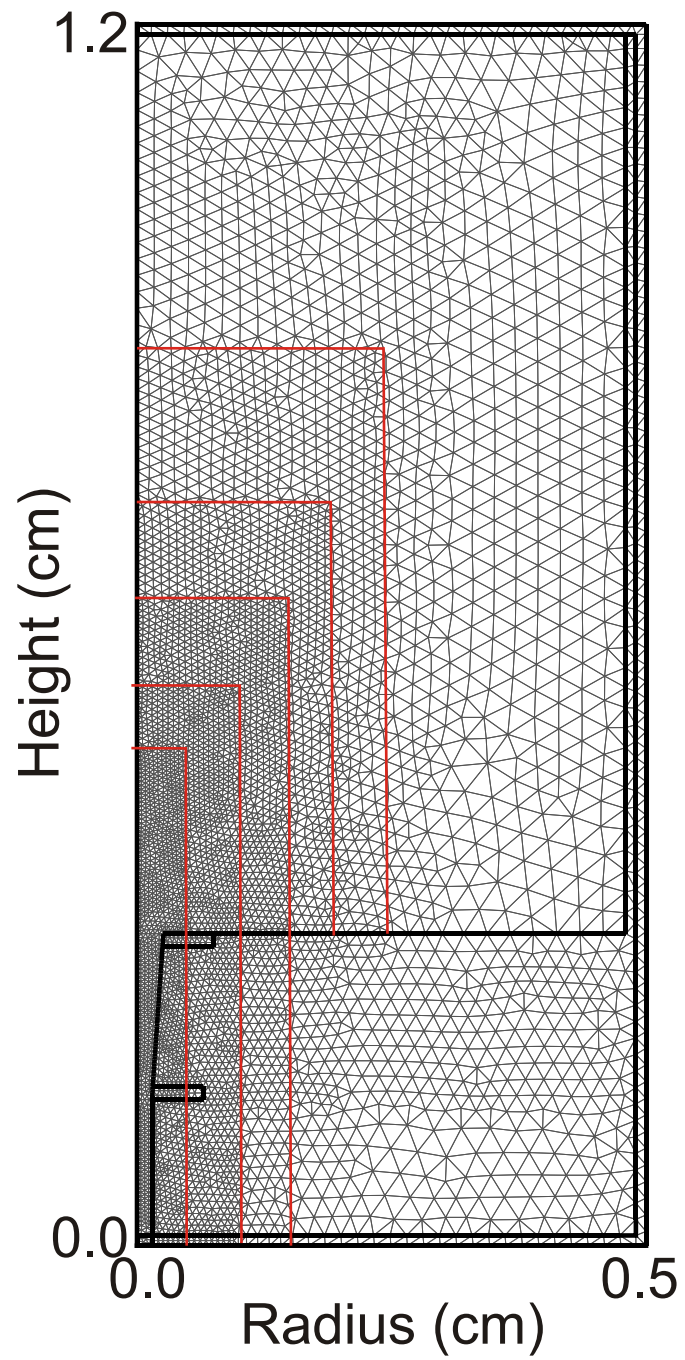


Fig. 2.1 An example of a mesh showing the refinement regions.

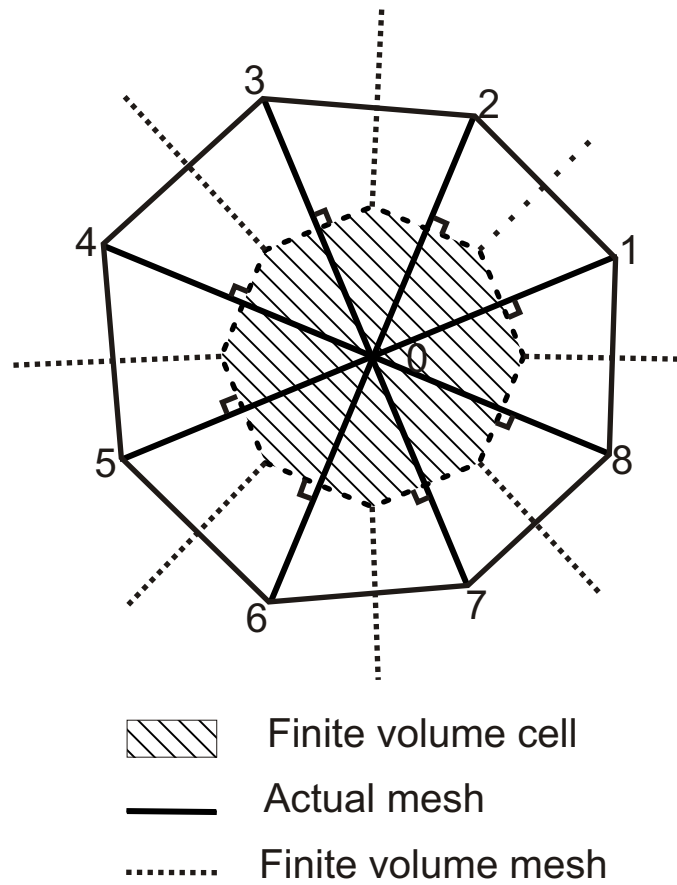


Fig. 2.2 Schematic of the mesh and the control volume.

2.5 References

1. H. W. Ellis *et al*, At. Data Nuc. Data Tab. **17**, 177 (1976).
2. H. W. Ellis *et al*, At. Data Nuc. Data Tab. **22**, 179 (1978).
3. H. W. Ellis *et al*, At. Data Nuc. Data Tab. **31**, 113 (1984).
4. H. W. Ellis *et al*, At. Data Nuc. Data Tab. **60**, 37 (1995).
5. S. D. Rockwood, Phys. Rev. A **8**, 2348 (1973).
6. P. N. Brown, G. D. Bryne and A. C. Hindmarsh, SIAM J. Sci. Stat. Comp. **10**, 1038 (1989).
7. D. L. Scharfetter and H. K. Gummel, IEEE Trans. Electron Dev. **16**, 64 (1969).
8. SLAP Sparse Matrix Library, <http://www.netlib.org>
9. Y. Saad, Department of Computer Science Engineering, University of Minnesota.

CHAPTER 3. PRODUCTION OF $O_2(^1\Delta)$ IN He/ O_2 DISCHARGES FOR USE IN OXYGEN-IODINE LASERS

3.1 Introduction

Chemical oxygen-iodine lasers (COIL) are being investigated due to its high efficiency and potential for multikilowatt cw operation.[1-6] COILs have applications in missile-defense and processing of metals due to their near-infrared wavelength (absorbed in metals), and in remote metal processing due to their ease of transport using optical fibers.[7]

In conventional COILs, the Singlet Delta Oxygen (SDO, $O_2(^1\Delta)$) required to pump the atomic iodine $I(^2P_{3/2})$ to the excited level $I(^2P_{1/2})$ is generated by a liquid-phase chemical reaction between Cl_2 in a basic solution of H_2O_2 . [1] While these produce the SDO efficiently, a few drawbacks exist when scaling these to large powers, or while using these for continuous-wave (cw) operation. For example, storage of hydrogen peroxide or Cl_2 is cumbersome and can be a safety hazard. Also, the reaction between Cl_2 and H_2O_2 is highly exothermic and hence active measures are required to control the temperature. As a result of these issues, researchers are moving towards a discharge produced SDO for use in a COIL.

Recently, gas-phase generation of SDO in discharges containing mixtures of rare-gas/ O_2 are being studied.[8,9] Gas-phase generation of $O_2(^1\Delta)$ eliminates the need to carry or store dangerous chemicals and enables re-cycling of the feedstock gases which reduces the system mass. However, the yields of $O_2(^1\Delta)$ (fraction of O_2 molecules in the SDO state) are not as high compared to the $\approx 70\%$ yield (Ref. 10) possible in liquid-phase generators. Hence, recent studies have focused on ways to improve the yields of $O_2(^1\Delta)$ in the discharge.

The yield of SDO influences the laser power as it determines the density of the upper level state of iodine $I(^2P_{1/2})$. Fujii et al [2] reported that the yield of SDO should be $> 15\%$ so as to achieve a ratio of densities of $I(^2P_{1/2})$ to $I(^2P_{3/2}) > 0.5$ which enables population inversion for laser oscillation. Hon et al [11] conducted heuristic studies to relate the ratio of densities $O_2(^1\Delta)$ and O_2 to the gain in the laser cavity. They reported that threshold ratio of densities of $O_2(^1\Delta)$ to O_2 required for positive gain depended on the cavity temperature as follows:

$$Y_{th} = \frac{[O_2(^1\Delta)]}{[O_2]} = \frac{1}{1+1.5\exp(401/T_{cav})}, \quad (3.1)$$

where Y_{th} is the threshold yield of $O_2(^1\Delta)$ required, and T_{cav} is the gas temperature in the cavity in K. This gave a threshold yield of ≈ 0.15 at 297 K.

Measurements of $O_2(^1\Delta)$ yield have been reported in discharges in O_2 . One of the first estimate of yield of $O_2(^1\Delta)$ was reported by Foner and Hudson.[12] They noticed higher than expected densities of O_2^+ in a pure oxygen discharge, and attributed it to the presence of the metastables $O_2(^1\Delta)$. They reported that around 10 – 20 % of the oxygen molecules were in the $^1\Delta_g$ state. Cook and Miller [13] produced $O_2(^1\Delta)$ with yields of 7% in O_2 , and 3.5% in NO_2 , and 0.5% in CO_2 in microwave excited discharges. For discharges in gases other than O_2 , their data validated their hypothesis that the SDO was produced directly from the feedstock gases, and not by the excitation of the ground state oxygen formed by dissociation. Bernard and Pchelkin [14] developed a ratiometric system for accurately determining SDO content in a low-pressure gas sample, and achieved a SDO yield of 11% in a microwave discharge that was used to calibrate their measurements.

Some of the recent studies have focused on the mechanism of formation of $O_2(^1\Delta)$ in an oxygen discharge and have tried successfully in tailoring the discharge parameters such as reduced electric field (E/N) and electron temperature (T_e) towards producing the SDO efficiently.

Hill [15] developed a controlled avalanche discharge in an attempt to increase the yields of SDO using non-self-sustaining plasmas. His use of power modulation (short, high-voltage spike, followed by a smaller voltage to sustain the plasma) helped achieve SDO yield of 16%. A yield of $\approx 16\%$ (measurement of $O_2(^1\Delta)$ and $O_2(^1\Sigma)$) was also reported by Verdeyen et al [16] using an rf discharge. Ionin et al [17] studied electron-beam sustained discharges in O_2/Ar mixtures with CO or H_2 as additives, and were able to sustain these discharges at high specific input energies. Based on reaction kinetics, they predicted yields of SDO in such non-self-sustaining discharges to be as high as 40% in room temperatures. Hicks et al [18] studied non-self-sustained discharges in He- O_2 mixtures at high pressures (120 Torr) using a pulser technique where the ionization was produced by short, high-repetition-rate pulses at high voltages, and the current was sustained using a dc discharge (operated in a direction perpendicular to the pulser) between pulses. While the yields of SDO (calculated using emission from $O_2(^1\Sigma) \rightarrow O_2$) were not very high ($\approx 2 - 4\%$), expansion to Mach 3 in a supersonic nozzle reduced their static temperature so that the threshold yields (Eq. 3.1) were lower. Thus, they achieved gain in the laser cavity.

In recent years, modeling of these discharges with emphasis on the kinetics and flow properties has also contributed in understanding the important pathways to formation and destruction of SDO.

Napartovich et al [19] modeled the kinetics of the O₂ discharge and suggested a more detailed study including individual electronic-vibrational states. Based on cross-sections of ground state O₂, they predicted that the fractional power spent in producing SDO maximized at an E/N \approx 8.7 Td (1 Townsend = 10⁻¹⁷ V-cm²). The predicted yield was as high as 43% for this value of E/N. This estimate was higher because they used the inlet values of mole fractions as opposed to those in the discharge. Inclusion of superelastic collisions (de-excitation by electrons) and assuming a 30% initial concentration of SDO in the discharge, the predicted yield came down to \approx 0.21. They also studied the yields of SDO in Ar/O₂ and He/O₂ mixtures and predicted that SDO content in Ar/O₂ mixtures was likely to be higher due to a better discharge efficiency. Stafford and Kushner [20] modeled rf discharges in flowing He/O₂ plasmas using a global plasma kinetics model and studied the scaling of SDO production with emphasis on energy deposition per O₂ molecule in the discharge. They predicted that peak yields could be as high as 0.3 at energy deposition of 5 – 8 eV per oxygen molecule. They also predicted that dissociation of O₂ molecules and gas heating would reduce SDO yields at higher powers. Stafford and Kushner [21] studied the effects of axial transport using a 1-d plasma kinetics model and attributed the experimentally observed plasma glow (both up- and down- stream) due to electron diffusion and capacitive coupling to the power source. They predicted that yields exceeding 50% was possible using a pulsed discharge combined with a continuous-wave (cw) discharge.

In this chapter, results from a 2-d model of the He/O₂ discharge are reported. The model used for this study is nonPDPSIM, and is explained in detail in Ch. 2. The spatial variations in the discharge (in axial and radial directions) are studied along with the flow and scaling issues. The focus will be on methods to improve the yields of O₂(¹ Δ) in discharges

containing He/O₂ mixtures at few – 10s Torr in both Inductively Coupled (ICP) and Capacitively Coupled Plasmas (CCP). Parameterization based on power, pressure, and mole fraction of O₂ was conducted to study the scaling and spatial variations of the plasma and flow characteristics, and the effect that they have on the O₂(¹Δ) yields.

3.2 Description of the Reactor

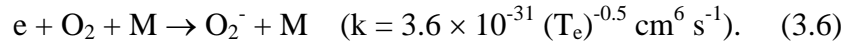
The geometries of the reactors used in this chapter are shown in Figs. 3.1(a) and 3.1(b). The reactor is a constant diameter (6 cm) tube with a length of 60 cm. A mixture of He/O₂ at pressures of few – 10s Torr and flow rate of few std. liters per minute (slpm) is introduced at the inlet. This corresponds to an axial velocity of $\approx 896 \text{ cm s}^{-1}$ at 3 Torr and 6 slpm, and represents a residence time of 67 ms. The length of the tube is sufficient to capture the post-discharge region in sufficient detail. The gas temperature at the inlet is 300 K, and the velocity is constant across the tube. The axial gradients are assumed to be 0 at the outlet. The plasma is surrounded by quartz and metal electrodes which are kept at a constant temperature of 300 K. In reality, the material surrounding the plasma is actively cooled using a water jacket. Controlling the gas temperature is necessary to improve the yield of SDO (Eq. 3.1).

The power is coupled to the plasma either inductively using the coils (Fig. 3.1(a)) or capacitively using the ring electrodes (Fig. 3.1(b)) and is varied from 40 - 100s W. In case of the ICP, a 5-turn coil operating at 5 MHz delivers the power to the plasma. The power is assumed to be coupled to the plasma without losses to the dielectric materials such as the quartz tube and the surrounding air. For the CCP discharges using ring electrodes, the frequencies are varied from 10 – 27 MHz.

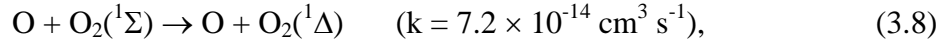
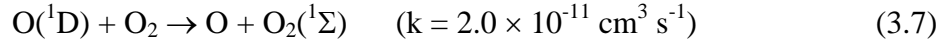
3.3 Reaction Mechanism

The complete set of reactions used in the model is shown in Appendix A. The species considered for the model include ground state neutrals: He, O, O₂, and O₃; vibrational and electronic states: He(²S), O₂(v), O₂(¹Δ), O₂(¹Σ), O(¹D), and O(¹S); and ions He⁺, O⁺, O₂⁺, O⁻, O₂⁻, and O₃⁻. The species He(²P) is included for energy loss calculations for the electrons, but it is lumped along with He(²S). The O₂(v) represents the total of the first four vibrational levels of O₂. The mechanism is discussed below with emphasis on SDO generation.

In the upstream regions of the discharge, most of the oxygen is in the form of O₂ molecules. The main electron impact reactions on O₂ are:

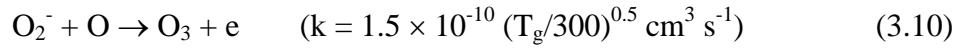
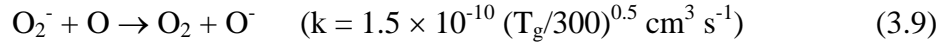


Most of the O₂(¹Δ) is formed by electron impact (Eq. 3.2) and the rate of this reaction is maximum at T_e between 1 and 1.5 eV. The dissociation reactions (Eq. 3.3, 3.4) produce significant amounts of O in the discharge. For example, about 1 atom of O is produced for every O₂(¹Δ) produced. O(¹D) is formed both by dissociation of O₂ and by excitation of O atoms by electron impact. The O(¹D) can react with other O₂ molecules forming O₂(¹Σ) in the process.



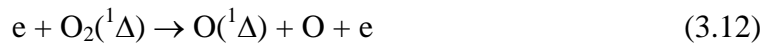
where k is the rate constant at 300 K.

Three body reactions (Eq. 3.6) lead to formation of significant amounts of O_2^- ions which then charge exchange with O atoms to form O^- ions and O_3 .



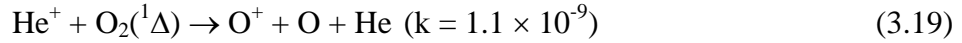
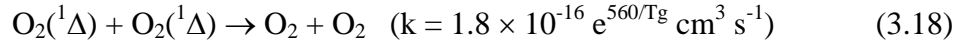
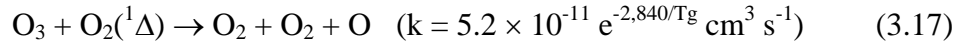
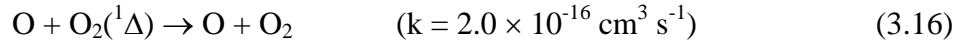
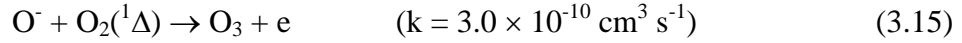
Both O^- and O_2^- react with $\text{O}_2(^1\Delta)$ with a rate constant of 3.0×10^{-10} , and $2.0 \times 10^{-10} \text{ cm}^3 \text{ s}^{-1}$, respectively. At a pressure of 3 Torr, the negative ion densities are $\approx 3 - 4 \times 10^{10} \text{ cm}^{-3}$, which gives a lifetime few 10^{th} s of a second for $\text{O}_2(^1\Delta)$ consumption. At higher pressures, the rates of 3-body reactions such as those leading to the formation of O_2^- are larger, and hence the consumption of $\text{O}_2(^1\Delta)$ by this pathway is larger. Hence, the density of O_2^- needs to be monitored for their effect on quenching of $\text{O}_2(^1\Delta)$.

As the density of $\text{O}_2(^1\Delta)$ builds up, superelastic collisions and Penning reactions can consume $\text{O}_2(^1\Delta)$.

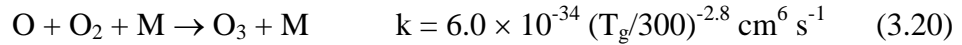




Other consumption pathways for $O_2(^1\Delta)$ include heavy particle reactions such as reaction with O^- , O , O_3 , $O_2(^1\Delta)$ and Penning ionizations by He^+ ions.



O_3 is formed mainly by reactions such as Eq. 3.15, and by 3-body recombinations.



In general, these 3-body reactions gain prominence as the pressure increases. Dominant quenchers of O_3 are $O_2(^1\Sigma)$, $O(^1D)$, and $O(^1S)$ at temperatures closer to room temperature. At much higher temperatures (not typical in these discharges) O_3 can decompose to O and O_2 .

Of all the positive ions, O_2^+ has the least ionization potential and hence its density is the maximum (due to charge exchange). The O_2^+ re-combines dissociatively leading to more O atoms, and is also a source of heating. The ions in general act as storehouses of energy and can transmit the electronic energy to other species (charge-exchange). A

basic surface reaction mechanism is included as part of the mechanism. All the ions that

reach the quartz/metal surface get neutralized and return to the plasma as the corresponding neutral species. The de-excitation of $O_2(^1\Delta)$ to O_2 by the walls has a probability of 10^{-5} or less [22] and this value was used as the sticking coefficient. Thus, of all the $O_2(^1\Delta)$ flux reaching the surface, 10^{-5} of that flux would stick to the walls and be returned to the plasma as O_2 .

3.4 $O_2(^1\Delta)$ Scaling with Pressure, Composition: Inductively Coupled Plasma

The azimuthal electric field (E_θ), power density, T_e , n_e , and the positive ion density are shown for base case conditions of 3 Torr, 6 slpm flow of 70/30 mixture of He/ O_2 , and 40 W power deposition in the ICP reactor in Fig. 3.2. The E_θ is maximum at a location adjacent to the central coil and is zero along the axis (due to the boundary condition). The skin depth in the electrodes is not resolved and the electric fields inside the coils are assumed to be zero. In our model, we assume that all of the power is coupled to the plasma. However, in reality there will be losses due to the small but finite conductivity (σ) of the dielectric materials such as quartz. The power deposition peaks in a region where the overlap between the plasma conductivity (proportional to n_e) and E_θ is maximum. Shielding of the electric field by the electrons (Debye shielding) in the plasma prevents the diffusion of E_θ , which in turn reduces the diffusion of power deposition into the plasma. The T_e is 2.6 eV near the peak power deposition region and ≈ 1.5 eV near the edge of the plasma. T_e is an important parameter in the production of $O_2(^1\Delta)$ in the discharge, and efforts to reduce the T_e to an optimum value (between 1 and 1.5 depending on the mole fractions of He and O_2) can improve the yields of $O_2(^1\Delta)$. [21]

The total positive ion density is $\approx 1.5 \times 10^{11} \text{ cm}^{-3}$, which is nearly twice that of the n_e at $8 \times 10^{10} \text{ cm}^{-3}$. The negative ions such as O^- , O_2^- , and O_3^- account for the difference between the positive ions and the electron density. The O^- ions form the largest fraction of the negative ions as O_2^- charge exchange with O to form O^- ions. The O^- ions react with $\text{O}_2(^1\Delta)$ and $\text{O}_2(^1\Sigma)$ to form O_3 and hence the O^- and other negative ions reduce the yields of $\text{O}_2(^1\Delta)$. Ion-ion re-combinations decrease the densities of the ions before they are convected by the flow. Ions can also lose their charge to the walls. Hence, the ions and electrons do not diffuse downstream.

The gas temperature, velocity, and densities of neutral species such as O , O_2 , $\text{O}_2(^1\Delta)$ are shown in Fig. 3.3 for base case conditions. The gas temperature increases by 53 K in the discharge due to resistive Joule heating ($\vec{j} \cdot \vec{E}$) and by dissociative reactions. The gas is cooled by expansion and due to heat loss to the walls (held constant at 300 K). The neutral gas velocity is roughly constant along the discharge although it increases slightly in the discharge due to expansion of the hot gas.

The density of O_2 is maximum in the region upstream of the discharge, and it decreases due to gas heating and conversion of O_2 to other species such as O , and $\text{O}_2(^1\Delta)$. The oxygen atoms are formed by dissociation reactions due to electron impact (Eq. 3.3 and 3.4) and this is unique to the discharge produced SDO (as opposed to the chemically produced SDO). The density of O peaks in the discharge region where the power deposition is maximum. In the downstream region, re-association reactions decrease the density of O atoms.

The $\text{O}_2(^1\Delta)$ is formed mainly in the discharge by electron impact reactions. Once the $\text{O}_2(^1\Delta)$ has been produced, its density does not diminish as the gas flows downstream. This is

due to a long radiative lifetime (few – 10s minutes) of $O_2(^1\Delta)$, and a small wall de-activation rate[22]. Also, at these pressures, quenching by O_3 is small due to small densities of O_3 (typically $< 10^{13} \text{ cm}^{-3}$ at 40 W deposition). The conversion of species such as $O(^1D)$ and $O_2(^1\Sigma)$ to $O_2(^1\Delta)$ by collisions with O and O_2 and cooling of the gas increases the density of $O_2(^1\Delta)$ downstream of the discharge.

For these conditions, the yield of $O_2(^1\Delta)$ calculated as:

$$Y = \frac{[O_2(^1\Delta)] + [O_2(^1\Sigma)]}{[O_2] + 0.5[O] + 1.5[O_3] + [O_2(^1\Delta)] + [O_2(^1\Sigma)]} \quad (3.21)$$

is $\approx 6.6 \%$ which is lower than the threshold yield (Eq. 3.1) required for a lasing gain at these temperatures.

Scaling these discharges to higher pressures can cause the localization of the plasma, and power deposition. The effect of pressure on the discharge characteristics such as power deposition, n_e , T_e , and density of O are shown in Fig. 3.4, and 3.5, respectively. For a given total power, the peak power density increases with pressure, and the peak electron density reduces. At higher pressures, the collision frequency increases and mean-free-path decreases. Hence, the electrons transfer energy to neutrals before they diffuse, leading to a localized discharge. Hence, for a given total power deposition, the power densities increase with pressure.

If the pressure is increased while keeping the coil frequency fixed, then the average energy of electrons (T_e) is lower due to higher rate of collisions leading to thermalization of electrons. The decrease in T_e results in an increase in production of O atoms through

dissociation of O₂. For example, reduction in T_e from 2.2 to 2.0 results in an increase in dissociation by 6.5% in the discharge. However, the O atoms re-associate at a faster rate with pressure and hence they have higher densities in the discharge and lower densities downstream of the discharge.

The peak values of charged species such as n_e , total positive, and negative ion densities are shown in Fig. 3.6 as a function of pressure and composition. Ion densities are in general lower at higher pressures. This is because of 2 reasons. At higher pressures, there is a reduction in the rate of ionization due to a lower T_e , hence reducing the production of positive ions. Also, the electron-ion and ion-ion re-combination through 3-body processes occur at a faster rate at higher pressures, hence increasing their consumption.

In general, the effect of composition on the densities was smaller than the effect of pressure. At higher O₂ mole fractions, electron densities are lower mainly due to attachment leading to formation of O₂⁻ ions, and by dissociative attachment leading to formation of O⁻ ions. However, when the discharge is low in O₂ content, the primary loss mechanisms for the electrons are formation of electronically excited states of He and He⁺ ions which can Penning ionize other species, leading to higher n_e and positive ion densities.

The effect of pressure on the neutral flow characteristics such as T_g , densities of O, O₂(¹Δ), O₂(¹Σ), O₃, and yield of O₂(¹Δ) are shown along the axis of the discharge in Fig. 3.7 for a discharge at 3 Torr, 40 W, and 30% O₂. At higher pressures, for the same flow rate (6000 sccm) and power, the power deposition per molecule is the same, although the residence time of the gas in the discharge is larger. Also, the power is dissipated in dissociation and other processes that lead to the production of excited neutral species which lead to gas heating. In the discharge, the production of O and O₂(¹Δ) scales with the

pressure. Downstream of the discharge, the effects of pressure such as: production of O_3 by 3-body collisions (Eq. 3.20) leading to a non-linear increase in O_3 , and re-association of O can be observed. O_3 is also a quencher of $O_2(^1\Delta)$ (Eq. 3.17) and hence the density of $O_2(^1\Delta)$ decreases in the afterglow especially at higher pressures. At lower pressures (< 10 Torr) this effect is almost negligible. Thus, at higher pressures the yield of $O_2(^1\Delta)$ is $\approx 6 - 7\%$ near the discharge, but reduces as the gas flows downstream.

The neutral flow characteristics including T_g , densities of O, $O_2(^1\Delta)$, O_3 , $O_2(^1\Sigma)$ and yield of $O_2(^1\Delta)$ are shown along the axis of the discharge in Fig. 3.8 for 3 Torr, 40 W as a function of composition. The gas temperature profile was biased to the downstream direction due to the convection of the hot gas. For a given power, the gas heating was not significantly dependent on the composition of the gas. Gas heating is caused by Joule heating ($\vec{j} \cdot \vec{E}$) or by Frank-Condon heating (conversion of potential energy in electronic states to translational energy) and while the increase in O_2 mole fraction causes an increase in Frank-Condon heating, the $\vec{j} \cdot \vec{E}$ term is lower due to the lower ion densities, thus conserving the total due to both of these terms.

The density of $O_2(^1\Delta)$ increased along the length of the discharge. In the afterglow region, conversion of $O_2(^1\Sigma)$ to $O_2(^1\Delta)$ and reduction of gas temperature caused an increase in its density. Note that the yield remains almost a constant in the afterglow. At larger mole fractions of O_2 , the $O_2(^1\Delta)$ increased, although the corresponding yield was lower. While a high yield of $O_2(^1\Delta)$ is necessary for a positive gain in the laser cavity, the number density of $O_2(^1\Delta)$ is also equally important when one needs to scale the output from the laser. Thus, methods that maintain the yield of $O_2(^1\Delta)$ at higher pressures are required to scale the laser

output. The O_3 was formed primarily in the afterglow region by 3-body recombination of O with species such as O_2 and $O_2(v)$. These 3-body processes occur rapidly at higher pressures, and since O_3 is also a quencher of $O_2(^1\Delta)$ (at elevated temperatures), there is a need to control the production of O_3 by controlling the densities of O.

3.5 $O_2(^1\Delta)$ Scaling with Frequency and Power: Capacitively Coupled Plasma

The reactor used in modeling the CCP discharge is shown in Fig. 3.1(b). The COILs are replaced by ring electrodes that are operated at radio frequencies (5 - 25 MHz) coupling the power capacitively to the discharge. The plasma characteristics for the base case of 3 Torr, 70/30 mixture of He/ O_2 flowed at 6 slpm, and 40 W CCP at 25 MHz is shown in Fig. 3.9. In the CCP discharge, the power deposition was spread over a larger volume leading to a more uniform n_e . As a result of uniformity, the peak n_e was much lower than the corresponding value for the ICP discharge.

In general, electron densities in CCP type discharges are lower than ICP discharges. This is because, the electric fields are perpendicular to the wall surfaces in CCPs (they are azimuthal in ICPs) typically, and hence the acceleration of the electrons/ions is directed towards the walls. The T_e is uniform throughout the bulk plasma, and is slightly higher near the electrodes where the n_e is smaller.

The T_g , densities of O, O_3 and $O_2(^1\Delta)$ are shown in Fig. 3.10 for the base case conditions (3 Torr, 25 MHz CCP at 40 W, 6 slpm of 70/30 He/ O_2 flow). As in the ICP case, the gas temperature profile is biased toward the downstream electrode owing to convection of neutral gas. The temperature is higher near the electrodes due to slightly higher power deposition in the sheath region. The neutral density profiles are similar to that of the ICP

discharge, although the magnitudes are different. The $O_2(^1\Delta)$ densities are lower for the CCP discharge due to lower peak electron densities and the slightly higher (by a few tenths of an eV) T_e in the CCP. Losses due to ion acceleration into the sheath reduce the net power available in the discharge and hence contribute to the lower yields in the CCP as compared to the ICP discharge. The O densities decrease downstream of the discharge due to recombination reactions producing O_3 and O_2 .

The effect of the frequency of the CCP discharge on the operating conditions of the plasma such as n_e , T_e , E/N , and power deposition are shown in Fig. 3.11 for conditions of 3 Torr, 40 W, and a composition of 70/30 He/ O_2 . The uniformity of the power density improved as the frequency was increased from 5 to 20 MHz and consequently, for a fixed power, the peak power densities reduced from 0.64 to 0.2 W-cm⁻³. The reduced electric field (E/N) is also uniform at higher frequencies, although it is slightly higher in the bulk discharge. The peak T_e came down from 4 to 3 eV, while the T_e in the bulk plasma was marginally higher.

The effect of frequency on the neutral densities is shown in Fig. 3.12 for the same conditions. The gas temperature is not significantly altered by the frequency, and is not shown. The density of $O_2(^1\Delta)$ increased by nearly 18 % when the frequency was increased from 5 to 20 MHz and this is attributed to the increase in n_e and the reduction in peak T_e resulting in an increase of rate of $O_2(^1\Delta)$ production. Higher frequencies also reduce the losses in the sheath, thus improving the yield for a given power deposition.

The scaling of the discharge with respect to power deposition was studied by keeping the pressure and flow rate as constant and varying the power deposited. There was no significant spatial variation in the plasma with increase in power. The plasma properties

such as electron and ion densities, and electron temperature are shown along the axis of the discharge as a function of power in Fig. 3.13. The T_e decreases by about 0.1 eV in the bulk plasma as the power is increased from 40 to 120 W which is favorable for $O_2(^1\Delta)$ production. The electron and positive-ion density increased linearly with power deposition, whereas the positive ions scaled sub-linearly with power deposition. The negative ions were almost independent of the power deposition. This is because the production of negative ions is mainly by a 3-body process (Eq. 3.6) leading to O_2^- , and to a smaller extent by dissociative attachment leading to formation of O^- . With increase in power maintaining the same pressure, even though the electron densities are higher, the rarefaction of the neutral gas at higher temperatures (shown in Fig. 3.14) reduces the density of neutral species thereby reducing the production rates of negative ions. The neutral gas temperature and densities are shown in Fig. 3.14 as a function of power, and the normalized values are shown in Fig. 3.15. The densities of excited neutral species are normalized by dividing by the total power deposited, and the gas temperature is normalized by calculating the increase in gas temperature (from 300 K) per unit power. If all processes in the plasma are linear with power deposition, then the normalized quantities should be identical as a function of power. However, this is not the case especially for T_g . Gas heating (as shown by ΔT_{gas}) is super-linear with power deposition due to a combination of 2 factors. The T_e is slightly lower at higher power deposition resulting in a larger fraction of energy spent in producing vibrational states and dissociation which results in gas heating. Even a change of 0.1 eV in T_e can increase dissociation by 6-10%. Also, the ion-ion re-combinations also contribute to gas heating though this effect is smaller due to the small fraction of ions in the discharge. The O densities are linearly dependent on power although the peak O densities are observed

downstream as the power is increased. This is due to the rarefaction of gas at higher temperatures. Once the gas cools downstream, the densities increase. The $O_2(^1\Delta)$ density is better at higher power deposition levels (within the range of power deposition studied) due to higher conversion rates of $O_2(^1\Sigma)$ to $O_2(^1\Delta)$ due to collisional de-activation by O atoms. O_3 production scaled with power density although it was very sensitive to gas temperature and varied significantly along the tube. At higher gas temperatures, the formation rate of O_3 suffers as it is formed by 3-body reactions. As such O_3 is detrimental as it quenches $O_2(^1\Delta)$ and hence its density needs to be kept in control.

3.6 Pressure Effects: Constant Energy per Molecule and Residence Time

The effects of the pressure on the discharge characteristics and the kinetics of the reaction chemistry were studied while maintaining the energy deposition per O_2 molecule and the residence time. The residence time and eV/ O_2 molecule are maintained a constant so as to isolate the effects of 3-body reactions. The residence time is a measure of how much time is spent by the gas in the discharge region and is calculated based on the flow velocity and the length of the tube. As the pressure is increased, the mass flow rate must be increased proportionately so as to maintain the same velocity. To maintain the same energy deposition per O_2 molecule for the increased mass flow rate, the power must also be increased proportionately.

The spatial variations of the power and electron density are shown as a function of pressure while scaling the conditions from the base case of 3 Torr, 40 W, 6 slpm to 40 Torr, 533 W, 80 slpm and are shown in Fig. 3.16. At high pressures the discharge is slightly biased toward the downstream electrode, whereas at low pressures, the discharge was

uniformly distributed over both the electrodes. This is because of a combination of factors. The E/N is higher near the downstream electrode than the upstream electrode due to gas being hotter (leading to lower N) near the downstream region. In a region that has higher E/N , the electrons gain more energy between collisions and hence have better ionization efficiency. Hence, the discharge is favored in a region that has the highest E/N , and consequently, the downstream electrode sustains much of the plasma for a given power. The neutral gas is hotter in the region adjacent to the downstream electrode due to the fact that it would have already passed through a region in which power deposition has occurred. Thus, at higher pressures, the discharge becomes asymmetric with respect to the electrodes due to convection of the hot gas towards the downstream electrode.

The T_e , electron and ion densities along the axis are shown in Fig. 3.17 for the above cases with constant eV per molecule and residence time. Note that the values on the axis are only representative of the general trends, and not the peak values. Increasing the pressure decreases the T_e as the electron-neutral collision increases thereby transferring their energy to the neutrals at a faster rate. At a lower T_e , the fractional power used in ionizing reactions is reduced, and it is reflected in the smaller proportional increase in the positive ion density as the pressure and power are scaled. The T_e decreases from 2.0 to 1.5 eV as the pressure is increased from 3 to 40 Torr. Thus, the positive ion density only increased from 1.6 to $4.1 \times 10^{10} \text{ cm}^{-3}$ as the pressure, power, and flow rate are scaled by a factor of 13.3. The loss of ions is also accelerated at high pressures by three-body electron-ion re-combinations. The formation of negative ions suffers at high temperatures due to a reduction in densities of the third body. The negative ion densities are higher in the upstream region where the neutral gas density is much higher, and the T_e is lower, which increases the rate of attaching

reactions. In general, the extent (along the axis of the discharge) of the electron and ion densities reduces with increase in pressure due to the increased rates of re-combination reactions at higher pressures.

The effect of the pressure scaling on the neutral densities is shown in Fig. 3.18. The gas temperature and the densities of O and $O_2(^1\Delta)$ are normalized so as to make comparisons with regards to scaling. The gas temperature is normalized by calculating the increase in temperature (from 300 K) per unit power deposited in the plasma. The densities are normalized by dividing by pressure. At high pressures, the per capita increase in temperature is slightly smaller. At higher pressures, the peak gas temperatures occur at downstream locations compared to the low pressure cases. This is because of transition from a symmetric (with respect to electrodes) to an asymmetric discharge where the bulk of the power deposition occurs near the downstream electrode. The peak per-capita production of $O_2(^1\Delta)$ is comparable, whereas the O densities do not scale with pressure due to re-association of O atoms downstream resulting in production of O_3 and O_2 molecules. At higher pressures, the O atoms produced in the discharge are rapidly consumed downstream as they re-associate to form O_3 and O_2 . The $O_2(^1\Sigma)$ density does not increase proportionately to the pressure as it is converted to $O_2(^1\Delta)$ rapidly by reactions with O atoms. O_3 is formed in significant quantities upstream of the discharge and in the afterglow when the temperatures are not very high, and can be a significant quencher of $O_2(^1\Delta)$.

3.7 Concluding Remarks

The production of $O_2(^1\Delta)$ for use in Oxygen-Iodine Lasers was investigated in discharges in mixtures of He/ O_2 . $O_2(^1\Delta)$ is a long-living metastable species of O_2 which does

not get deactivated by collisions with the wall, and hence it can be flowed down a tube without significant losses. The predominant formation pathway for $\text{O}_2(^1\Delta)$ was by electron-impact on O_2 . The rate of this reaction is optimal at low T_e (1.5 eV) whereas the self-sustaining value of T_e is typically 2.5 – 3.0 eV.

In ICPs, the power deposition is contained and maximum near the coils. This is because the overlap of the electron density and the electric fields (which ultimately determines power deposition) is maximum in this region. Increasing the pressure for the same power caused a reduction in peak densities of ions and electrons due to increase in rates of ion-ion and electron-ion re-combination reactions. The increase in O_2 content led to increase in densities of negative ions due to attachment of electrons and a decrease in electron and positive ion density. Larger mole fractions of O_2 led to larger $\text{O}_2(^1\Delta)$ density, but the corresponding yield was lower.

The CCP discharges in general had lower electron densities due to a more uniform power deposition. The losses in the sheath (by ion fluxes) led to marginally lower yields of $\text{O}_2(^1\Delta)$ compared to the ICP discharges. However, the ICP discharge assumed that the power was fully coupled into the plasma (without losses to other materials). As the frequency was increased from 5 – 20 MHz, the power deposition and electron density were more uniform. The T_e was slightly lower at higher frequencies, and hence increased the yield of $\text{O}_2(^1\Delta)$. The discharge scaled with power deposition for the constant pressure. There was no significant change to the mode of the discharge, and only a marginal increase in gas heating (increase per unit power) was observed.

With increase in pressure, the discharge became more localized, leading to higher power densities and gas temperatures. At higher pressures, the T_e was lower and a larger

portion of the power was being expended in dissociation or excitation reactions producing large amounts of O and $O_2(^1\Delta)$. While the $O_2(^1\Delta)$ densities in the discharge were much higher, they were rapidly quenched downstream of the discharge, leading to a lower yield at the exit of the reactor.

3.8 Figures

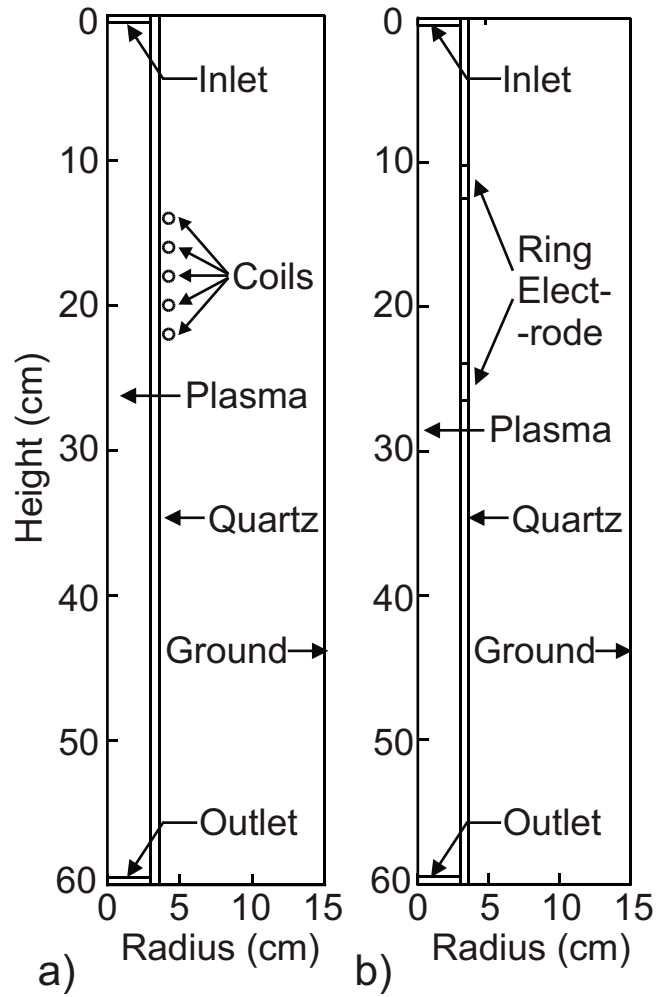


Fig. 3.1 Geometries of the reactor used: a) Inductively Coupled Plasma, b) Capacitively Coupled Plasma.

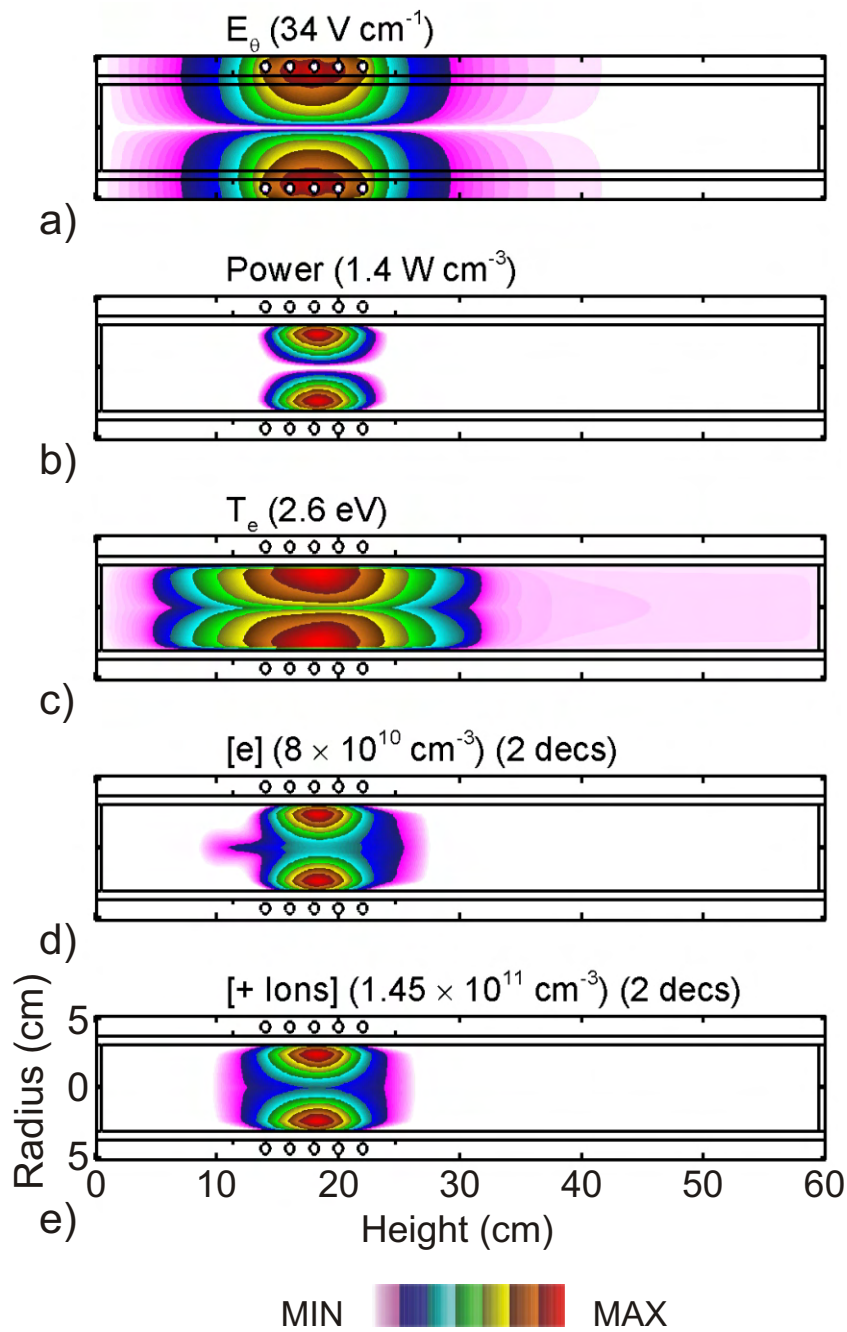


Fig. 3.2 Plasma characteristics such as: a) Azimuthal Electric field, b) Power Density, c) Electron Temperature, d) Electron Density, and e) Positive Ion Density for a 3 Torr, 40 W ICP with a 70/30 He/O₂ mixture. The electron and ion densities are plotted on a 2 decade log scale, and the others are plotted on a linear scale from 0 to maximum.

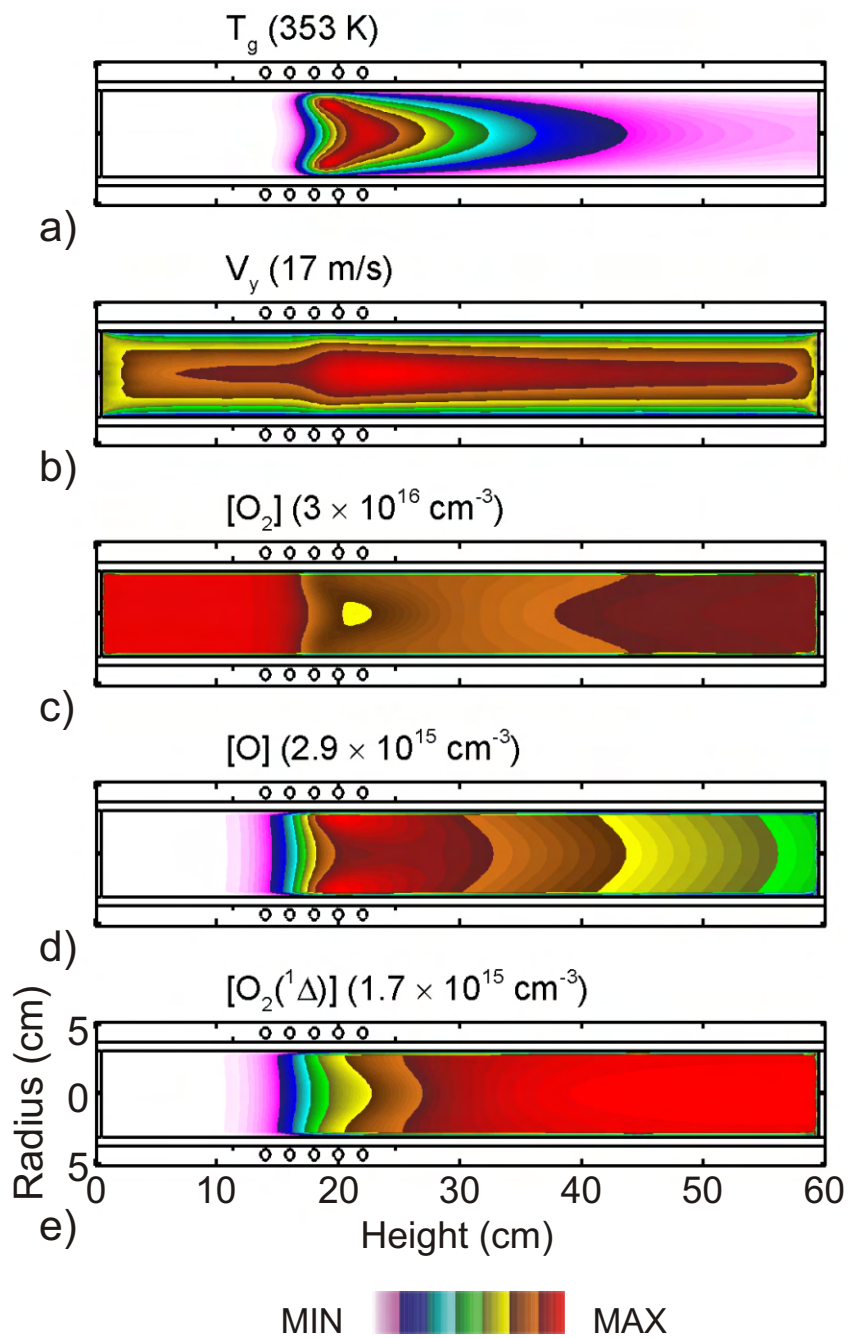


Fig. 3.3 Neutral flow characteristics such as: a) Gas Temperature, b) Axial Velocity, c) O_2 Density, d) O Density, and e) $O_2(^1\Delta)$ Density for a 3 Torr, 40 W ICP with a He/ O_2 mixture of 70/30. The contours are plotted on a linear scale from 0 to maximum.

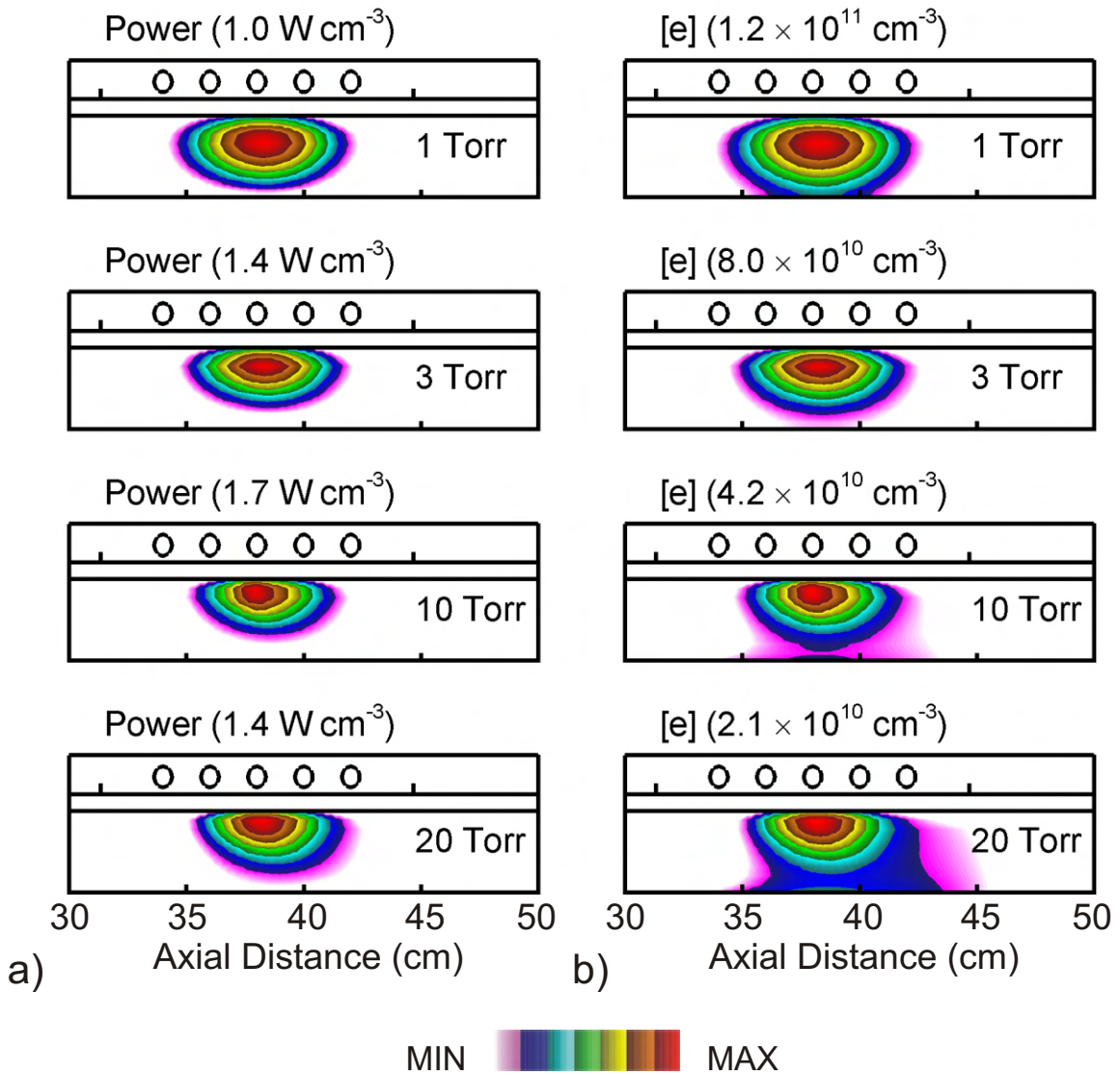


Fig. 3.4 a) Power Density, and b) Electron Density, as a function of Pressure for 40 W ICP with a 70/30 He/O₂ mixture. The contours are plotted on a 2 decade log scale.

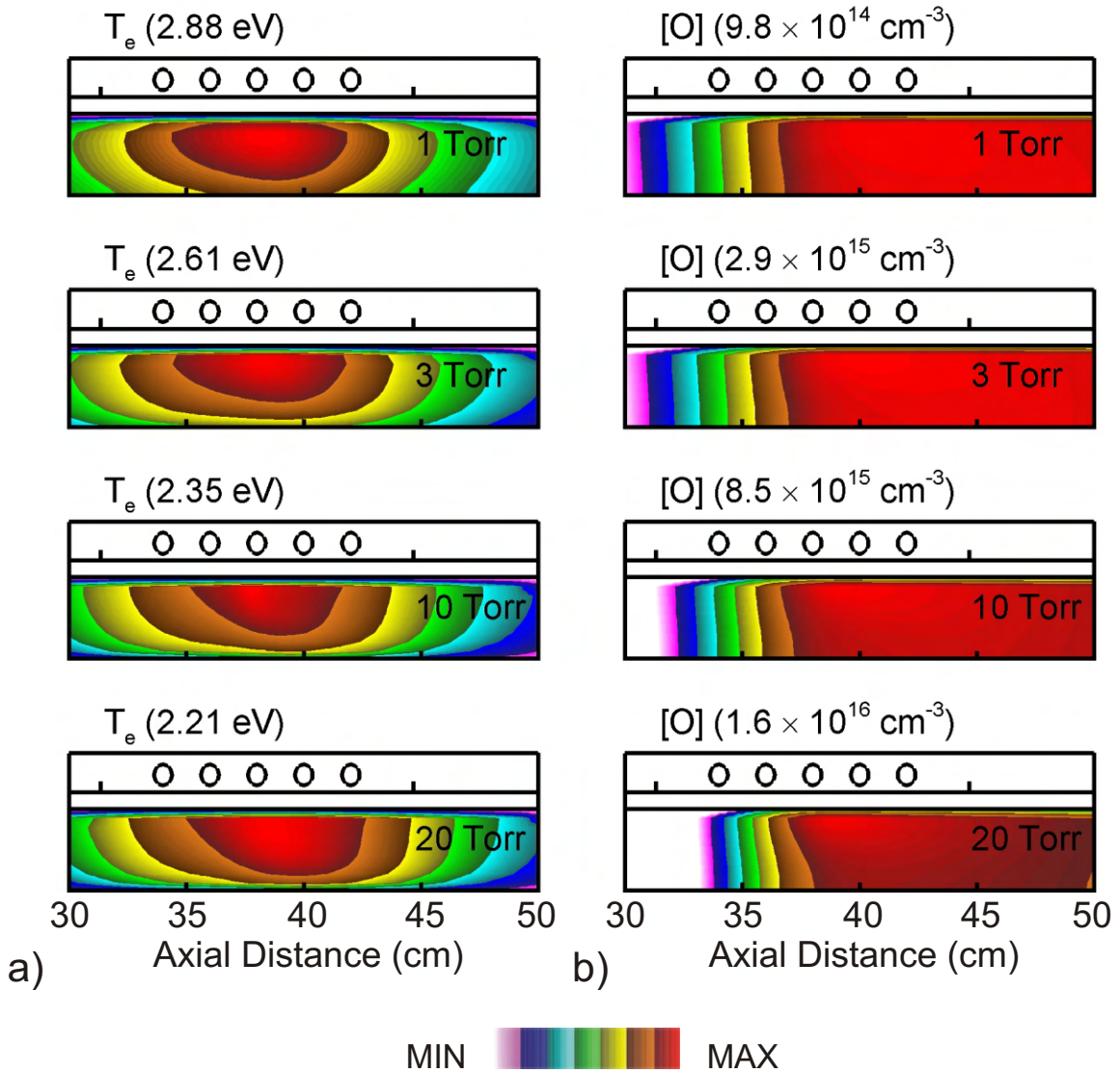


Fig. 3.5 a) Electron Temperature, and b) O Density, as a function of Pressure for 40 W ICP with a 70/30 He/O₂ mixture. The contours are plotted on a linear scale from 0 to maximum.

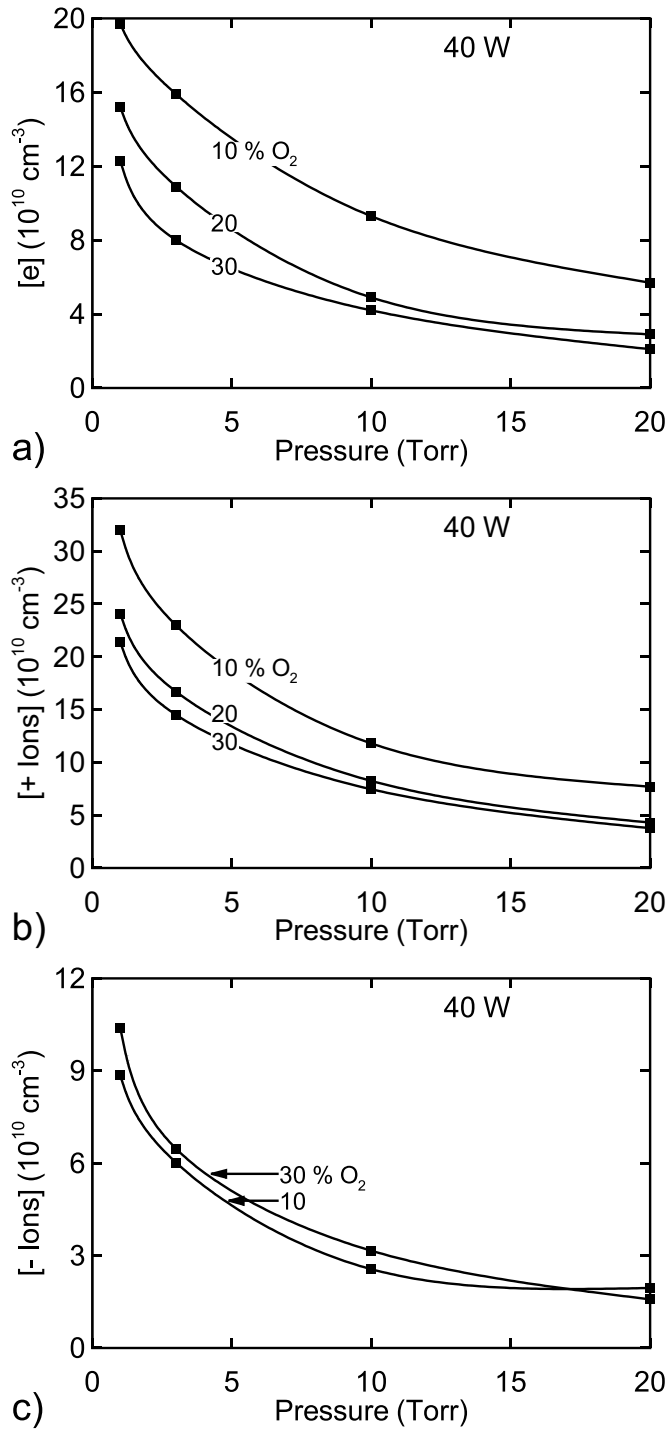


Fig. 3.6 Dependence of a) Electron Density, b) Positive Ion Density, and c) Negative Ion Density on Pressure and composition of He/ O_2 for 40 W ICP. The peak values in the discharge region are reported.

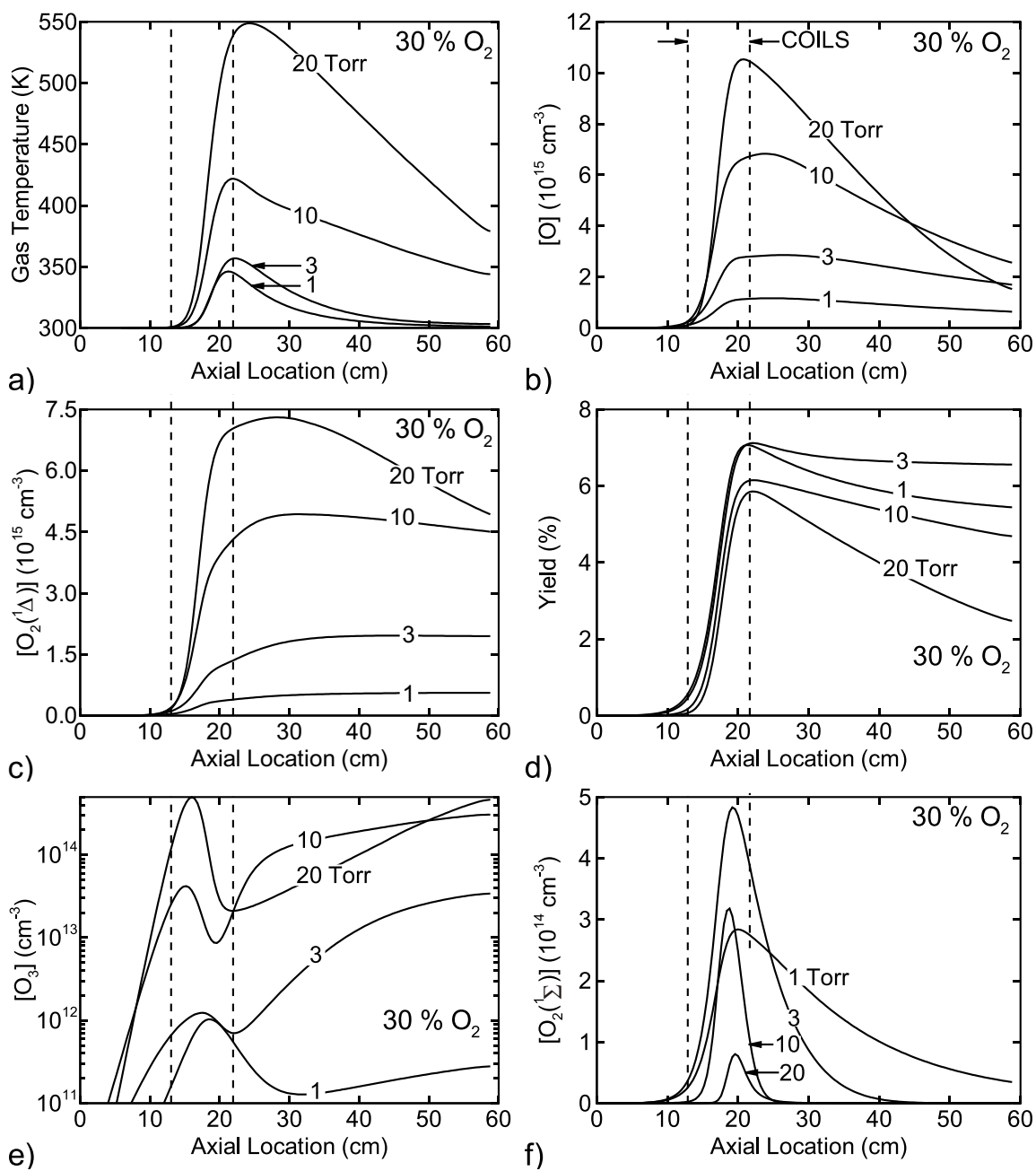


Fig. 3.7 a) Gas Temperature, b) [O], c) [O₂(¹Δ)], d) Yield, e) O₃, and f) O₂(¹Σ) along the axis of the tube for 40 W ICP as a function of pressure.

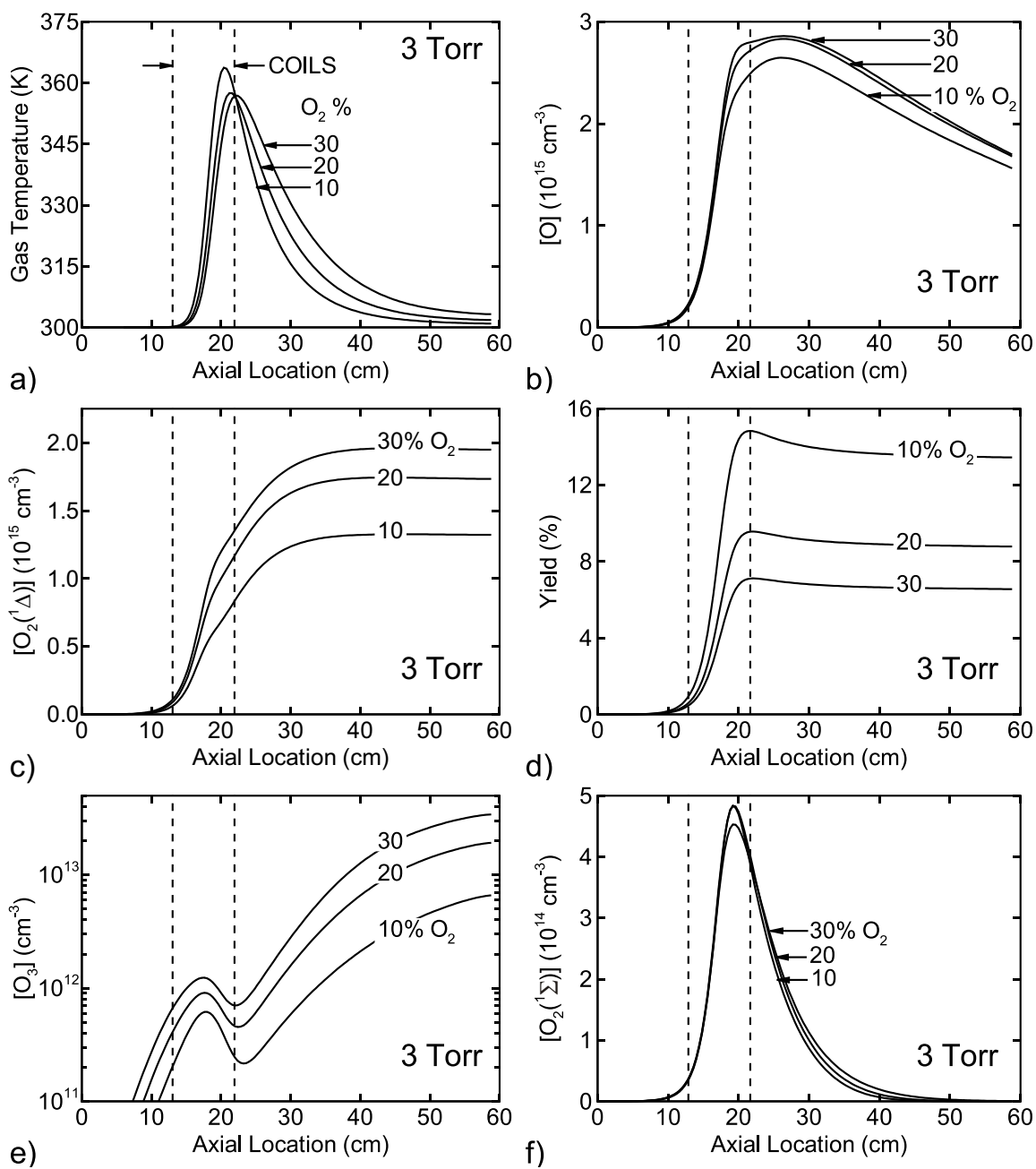


Fig. 3.8 a) Gas Temperature, b) [O], c) [O₂(¹Δ)], d) Yield, e) O₃, and f) O₂(¹Σ) along the axis of the tube for 3 Torr, 40 W ICP as a function of composition.

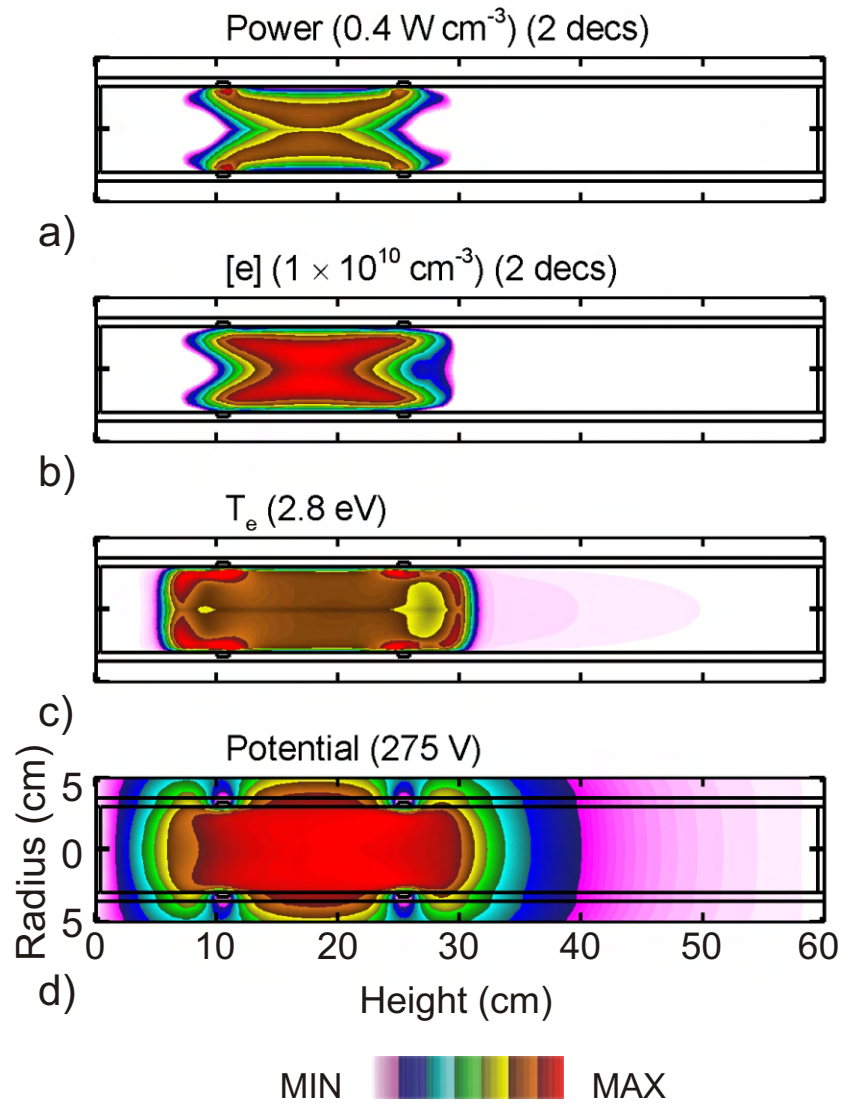


Fig. 3.9 Plasma characteristics such as: a) Power Density, b) Electron Density, c) Electron Temperature, and d) Plasma Potential for a 3 Torr, 40 W CCP with with a 70/30 He/O₂ mixture. The electron and power densities are plotted on a 2 decade log scale, and the rest are plotted on a linear scale from 0 to maximum.

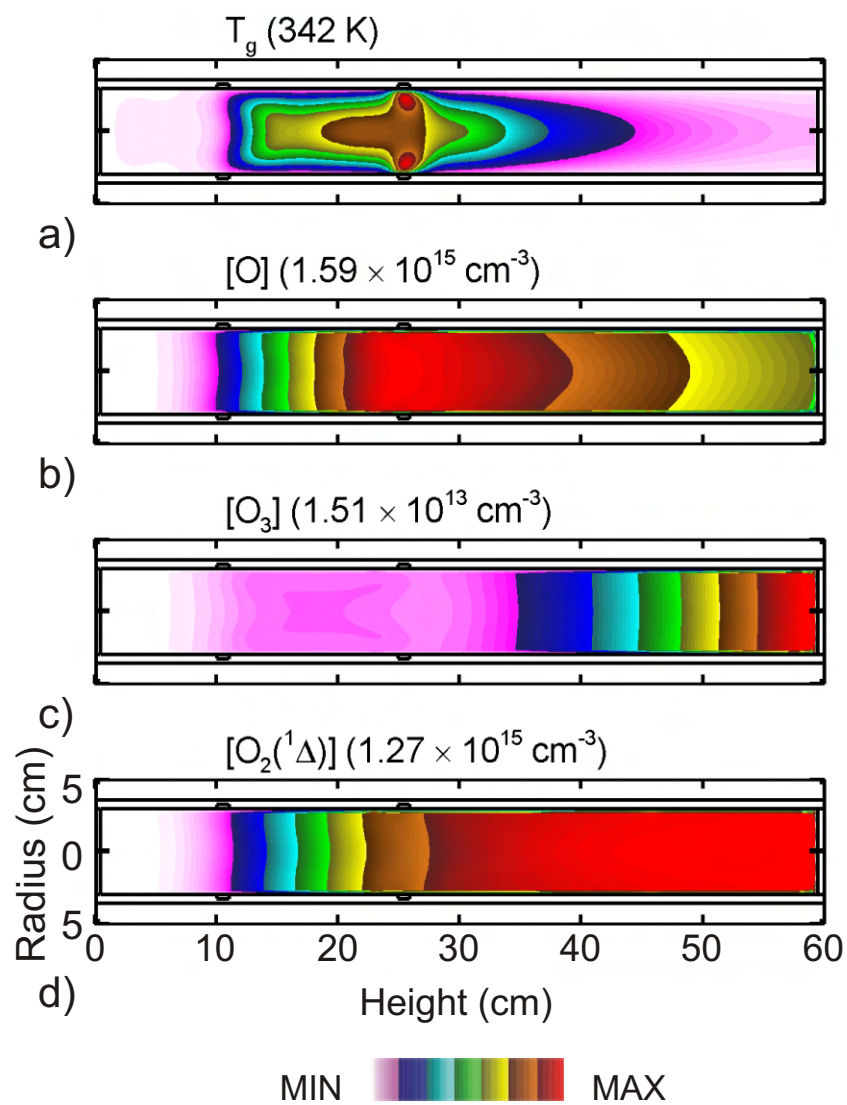


Fig. 3.10 Neutral flow characteristics such as: a) Gas Temperature, b) O_2 Density, c) O Density, and e) $O_2(^1\Delta)$ Density for a 3 Torr, 40 W ICP with a 70/30 He/ O_2 mixture. The contours are plotted on a linear scale.

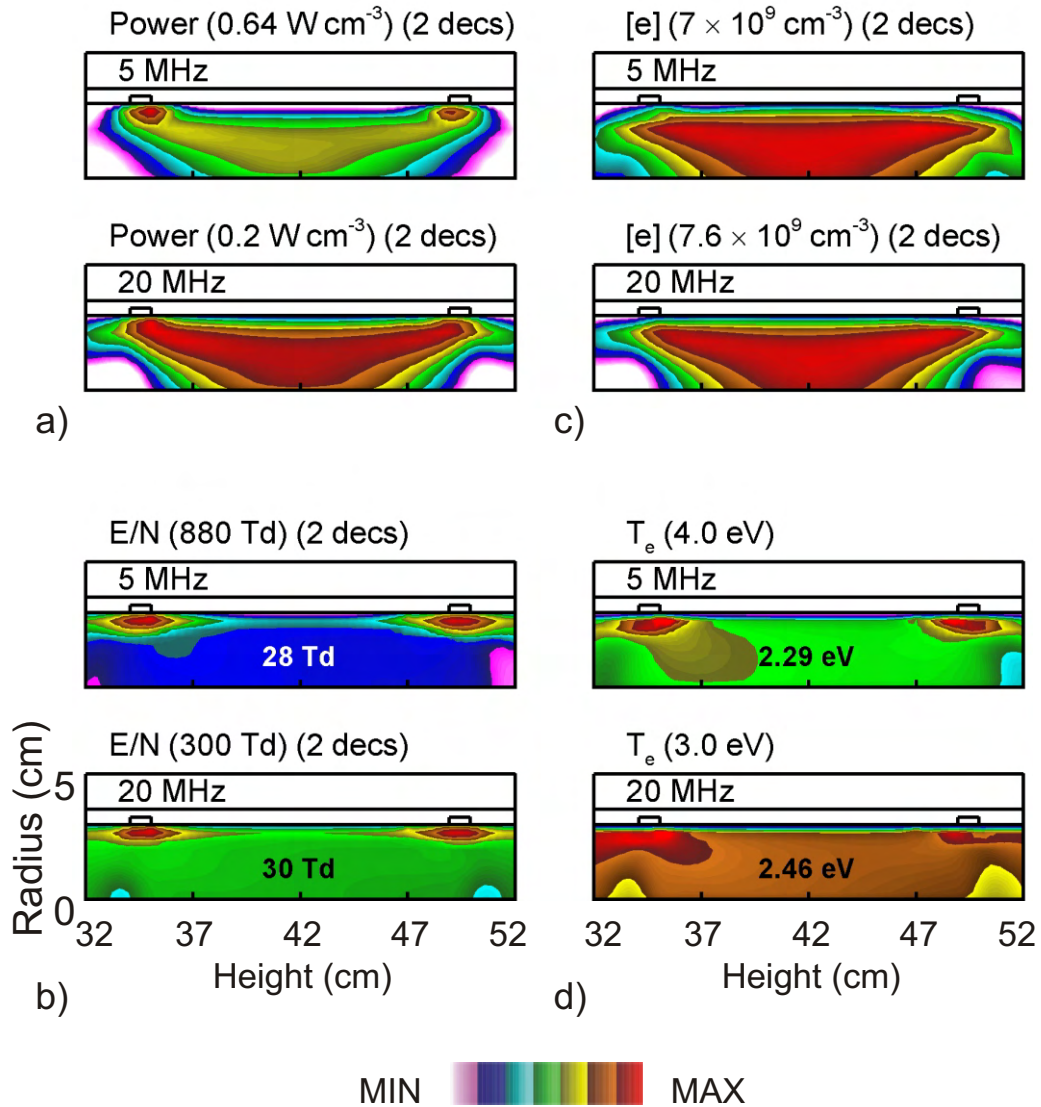


Fig. 3.11 Plasma characteristics such as: a) Power Deposition, b) E/N, c) Electron Density, and d) Electron Temperature as a function of CCP frequency for 3 Torr, 40 W CCP with a 70/30 He/O₂ mixture. The contours are plotted on a 2-decade log scale except for T_e which is linear.

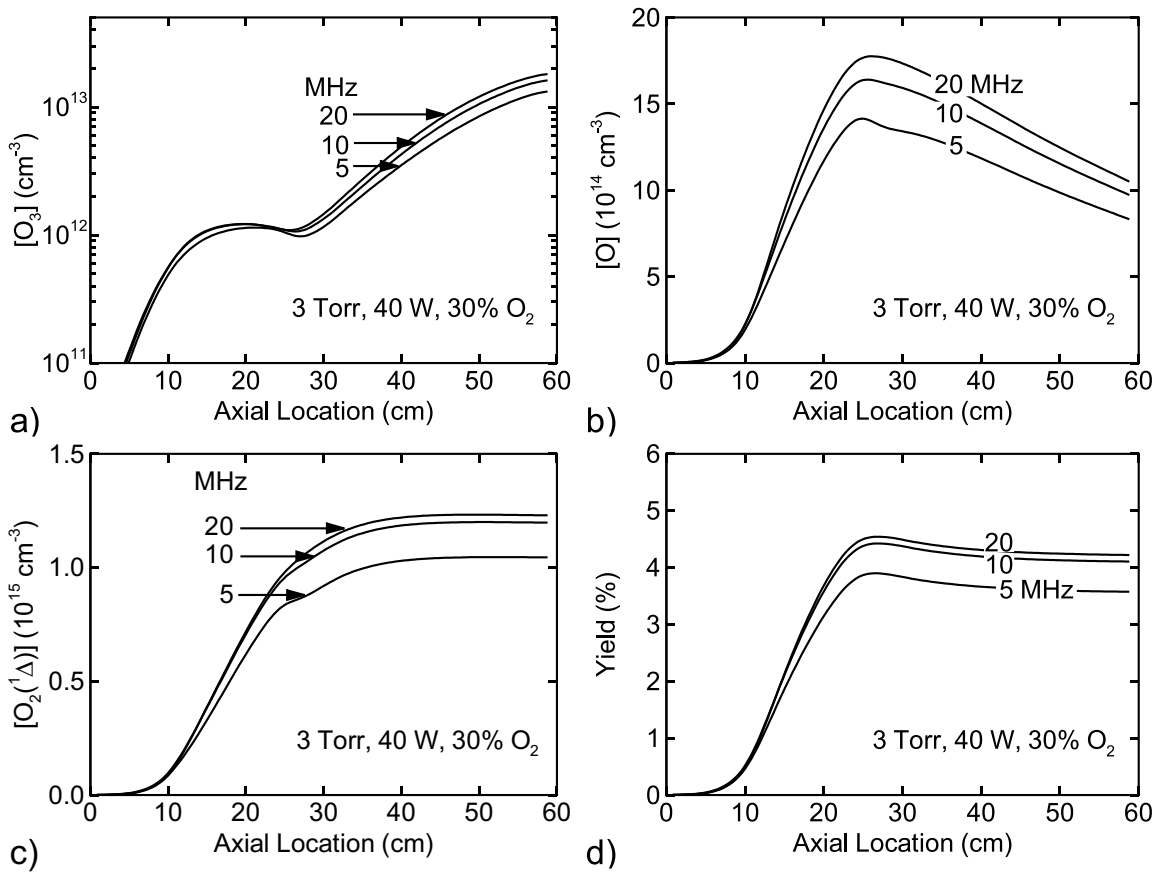


Fig. 3.12 Neutral densities along the axis: a) O₃, b) O, c) O₂(¹Δ), and d) Yield as a function of CCP frequency for 3 Torr, 40 W CCP with 70/30 He/O₂ mixture.

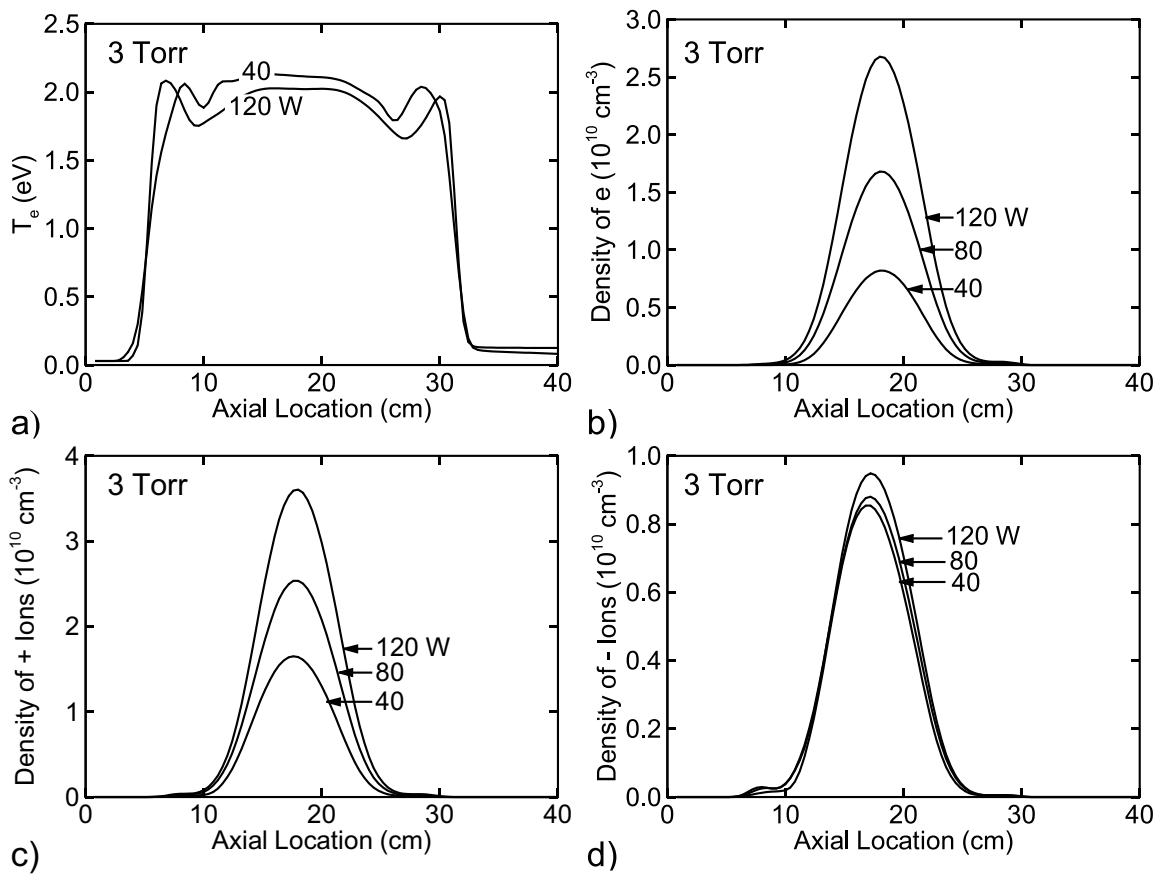


Fig. 3.13 Plasma properties along the axis: a) Electron Temperature, b) Electron Density, c) Positive Ion Density, and d) Negative Ion Density as a function of power for a 3 Torr, 25 MHz CCP with a 70/30 He/O₂ mixture.

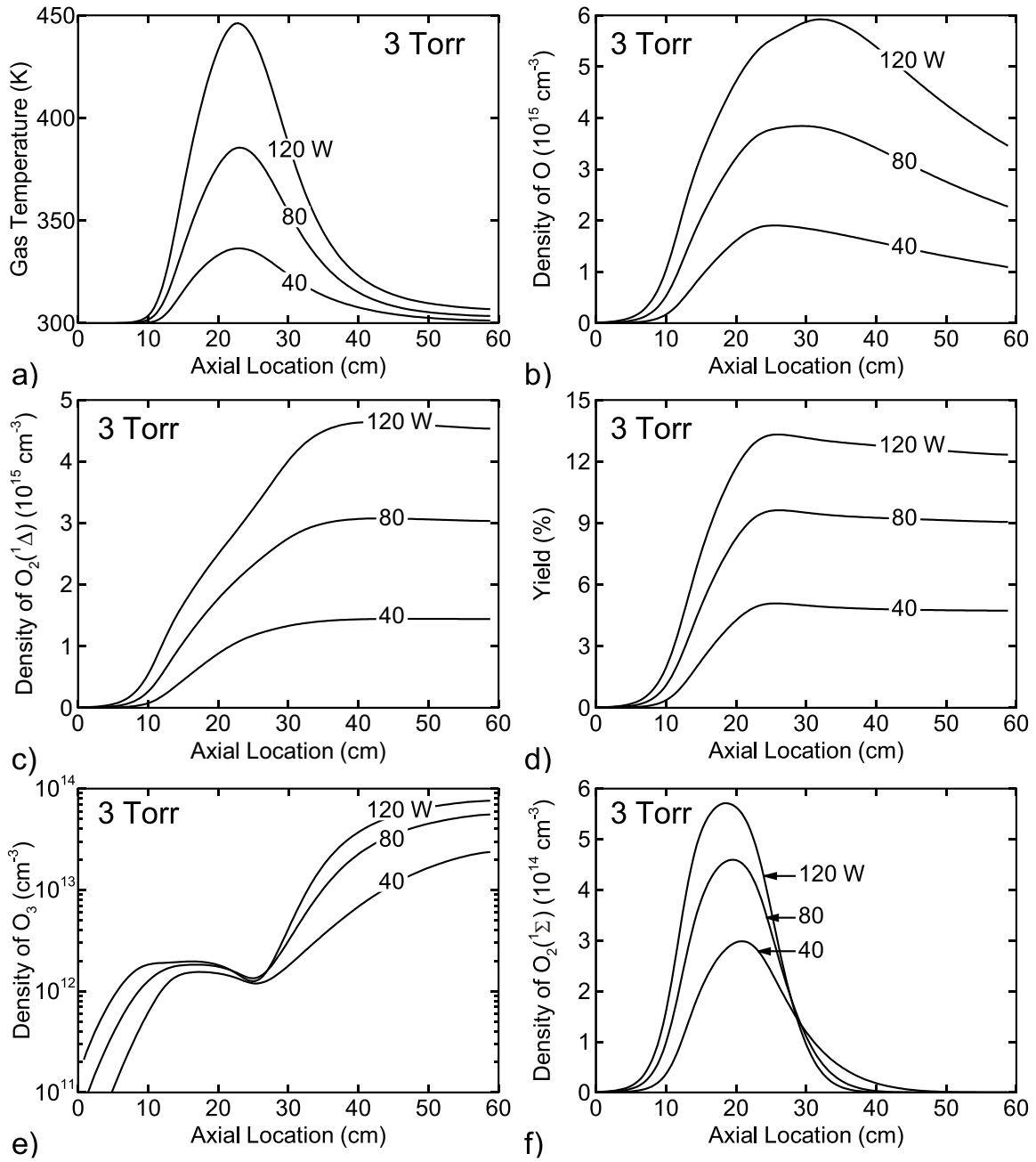


Fig. 3.14 Neutral fluid properties while varying power: a) T_{gas} , b) Density of O, c) Density of O₂(¹Δ), d) Yield of O₂(¹Δ), e) Density of O₃, and f) Density of O₂(¹Σ) for a 3 Torr, 25 MHz CCP with a 70/30 He/O₂ mixture.

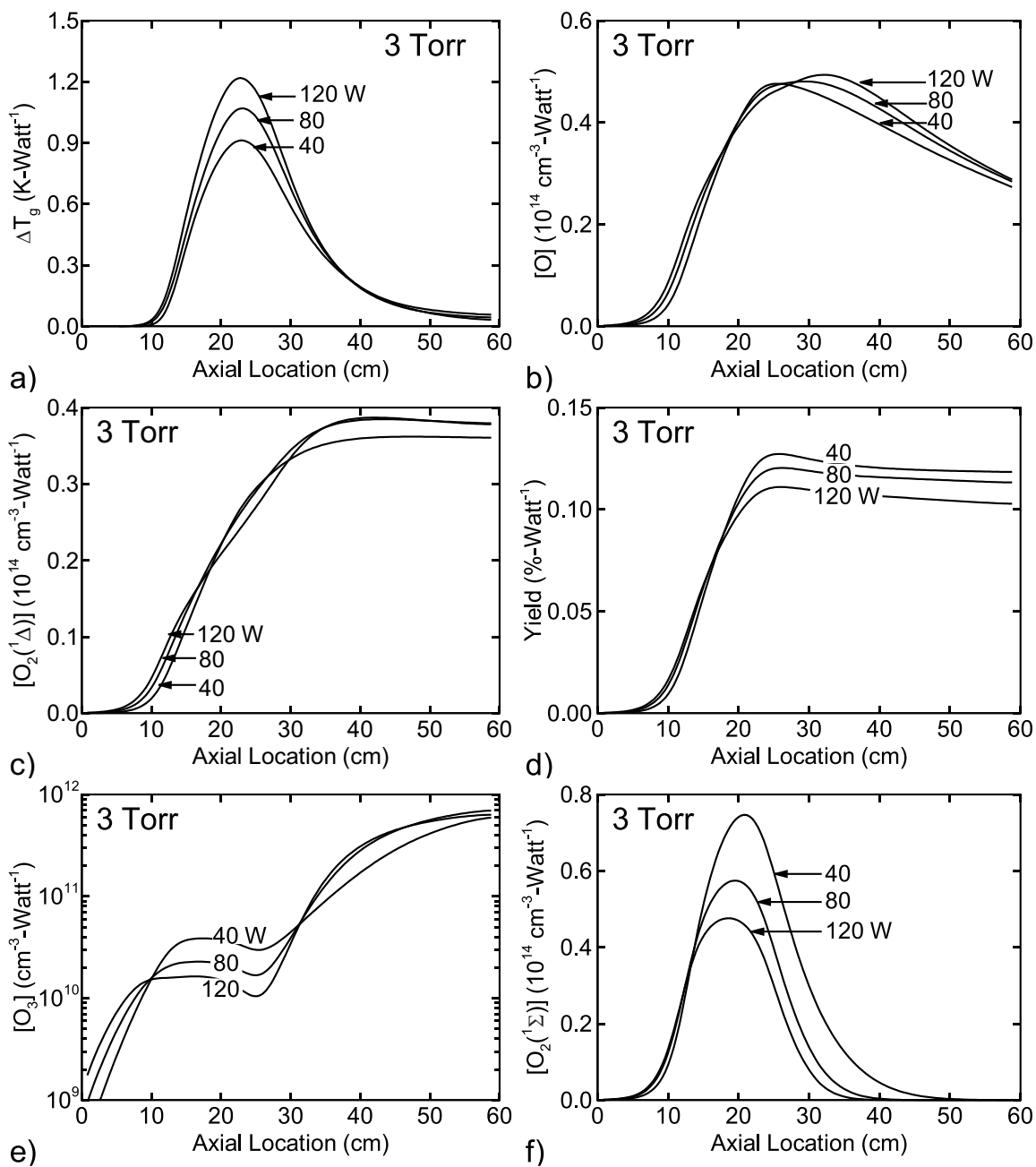


Fig. 3.15 Neutral fluid properties normalized for power: a) ΔT_{gas} , b) Density of O, c) Density of $\text{O}_2(^1\Delta)$, d) Yield per unit power, e) Density of O_3 , and e) Density of $\text{O}_2(^1\Sigma)$ per unit power for 3 Torr, 25 MHz CCP with a 70/30 He/ O_2 mixture.

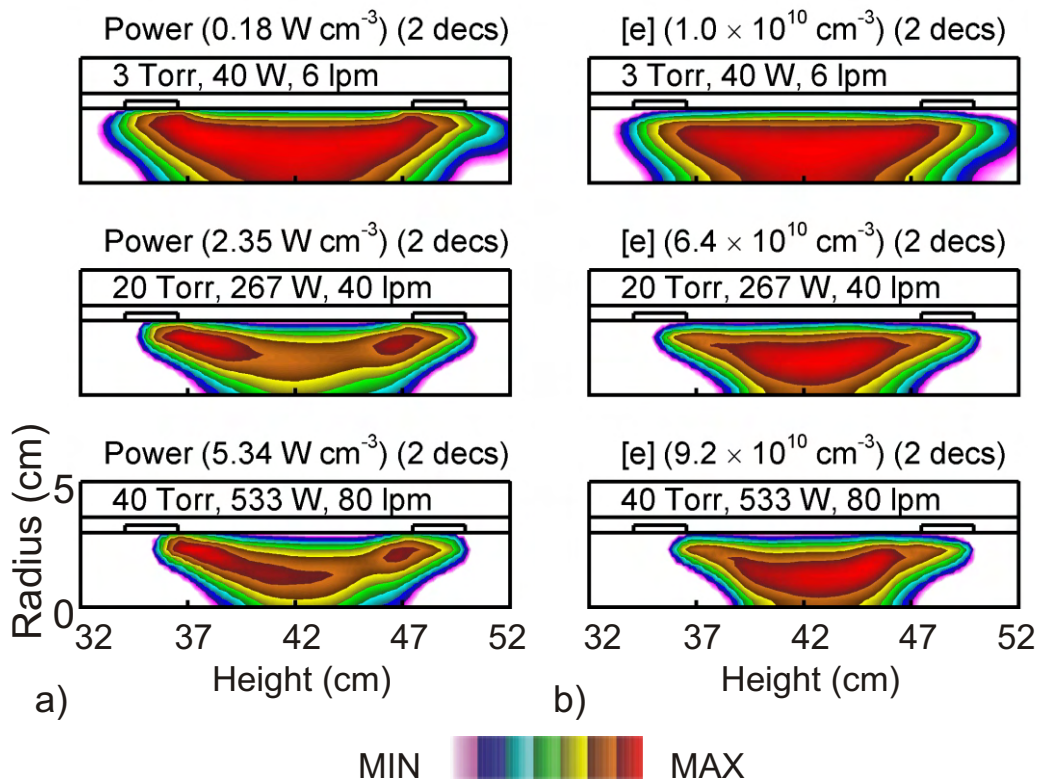


Fig. 3.16 Plasma characteristics such as: a) Power Deposition, and b) Density of e maintaining eV per molecule and residence time for CCP with a 70/30 He/O₂ mixture. The contours are plotted on a 2-decade log scale. Note that the flow is from left to right.

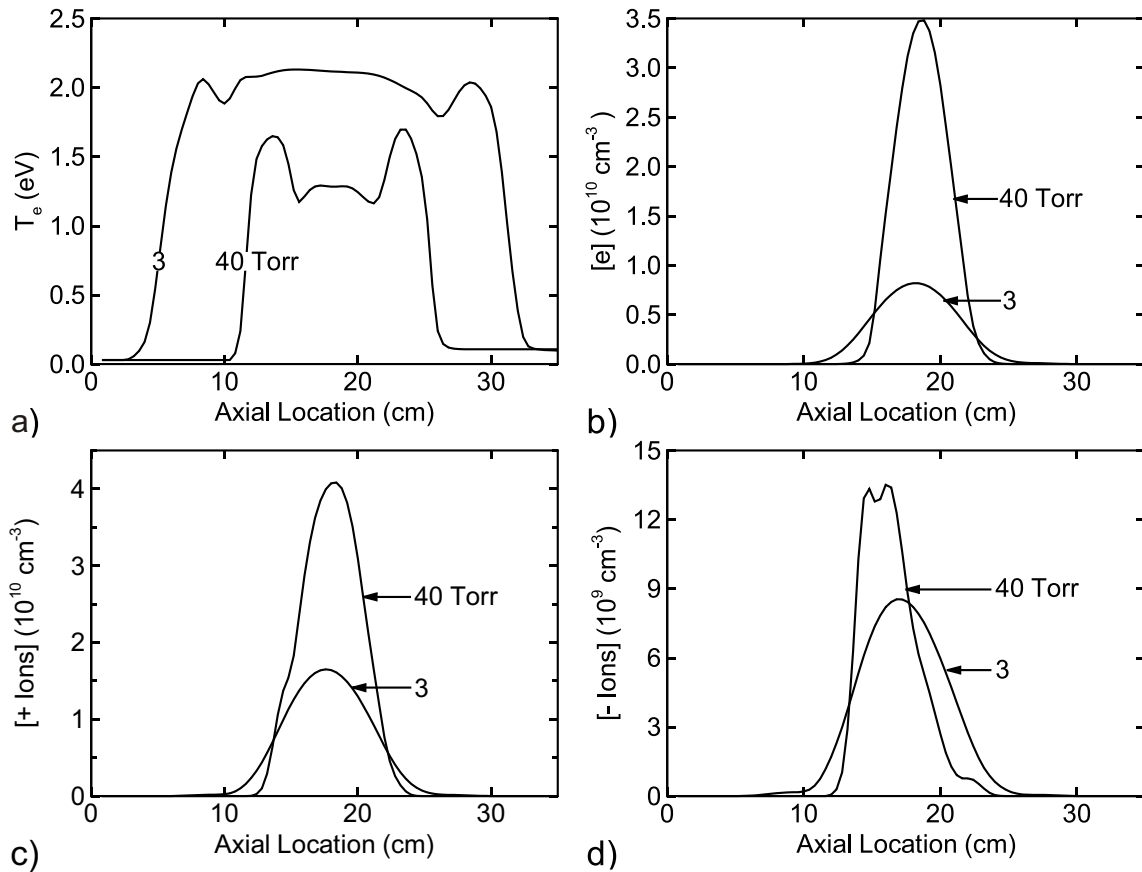


Fig. 3.17 Plasma characteristics along the axis: a) T_e , and b) Density of electrons, c) Positive Ion Density, and d) Negative Ion Density maintaining eV per molecule and residence time for CCP with a 70/30 He/O₂ mixture. Note that the flow is from left to right.

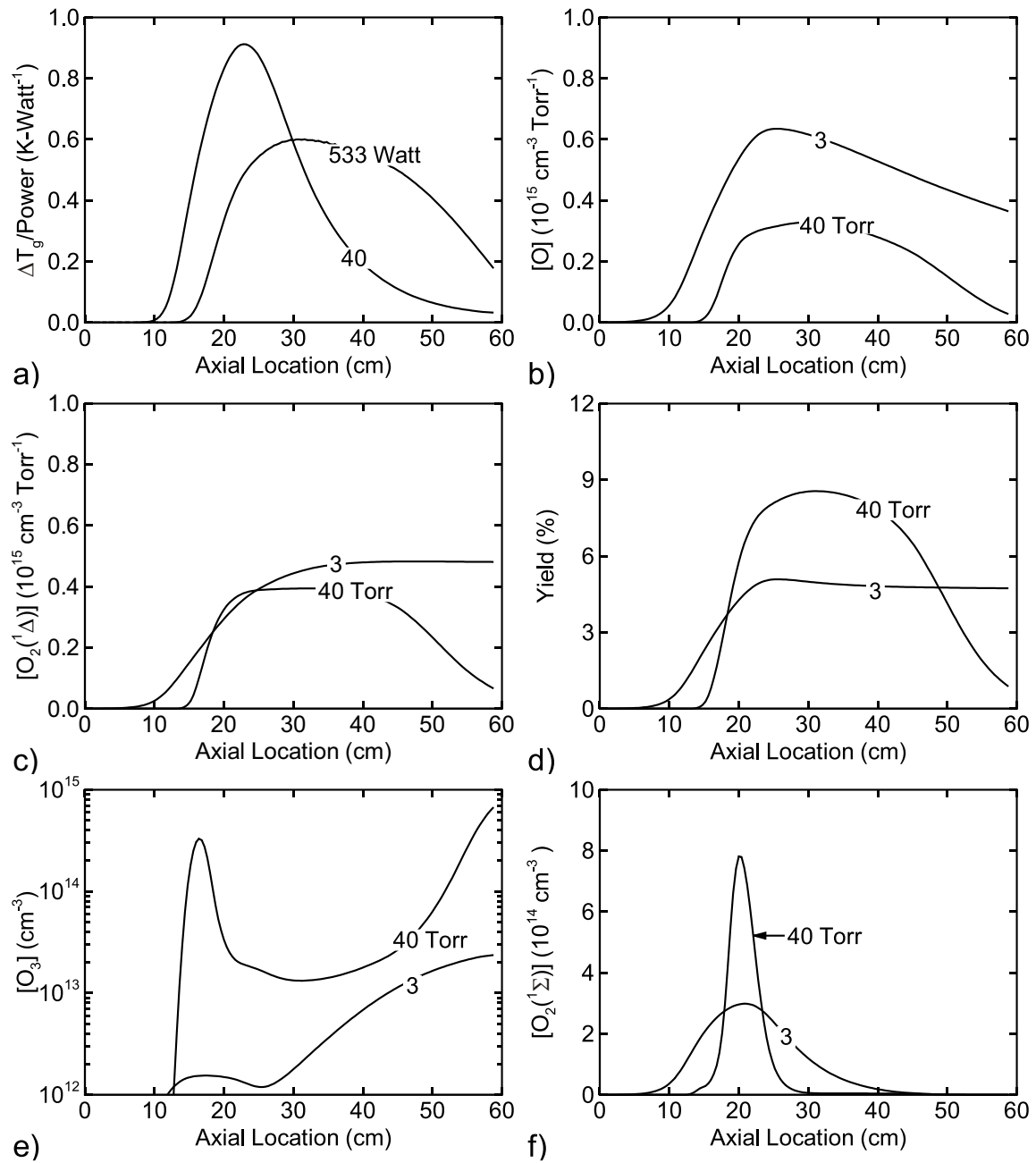


Fig. 3.18 Normalized fluid characteristics: a) Increase in T_g per unit power, b) Density of O, c) Density of $O_2(^1\Delta)$, d) Yield, e) Density of O_3 , and f) $O_2(^1\Sigma)$ for constant eV per molecule and residence time in the discharge.

3.9 References

1. W. E. McDermott, N. R. Pchelkin, D. J. Benard, and R. R. Bousek, *Appl. Phys. Lett.* **32**, 469 (1978).
2. H. Fujii, S. Yoshida, M. Iizuka, and T. Atsuta, *J. Appl. Phys.* **67**, 3948 (1990).
3. A. Elior, B. D. Barmashenko, E. Lebiush, and S. Rosenwaks, *Appl. Phys. B: Lasers Opt.* **B61**, 37 (1995).
4. M. Endo *et al.* *IEEE J. Quantum Electron.* **34**, 393 (1998).
5. D. Furman, E. Bruins, V. Rybalkin, B. D. Barmashenko, and S. Rosenwaks, *IEEE J. Quantum Electron.* **37**, 174 (2001).
6. J. Kodymová, O. Spalek, V. Jirasek, M. Censky, and G. D. Hager, *Appl. Phys. A* **77**, 331 (2003).
7. J. Kodymová, *COIL – Chemical Oxygen-Iodine Laser: Advances in development and applications*, *Proc. SPIE*, **5958**, 595818-1 (2005).
8. V. V. Ivanov, K. S. Klopovsky, D. V. Lopaev, A. T. Rakhimov and T. T. Rakhimova, *IEEE Trans. on Plasma Science*, **27**, 1279 (1999).
9. D. L. Carroll and W. C. Solomon, *ElectriCOIL: An Advanced Chemical Iodine Laser Concept*, *Proc. SPIE*, **4184**, 40 (2001).
10. J. Kodymová and O. Spalek, *Jpn. J. Appl. Phys.*, **37**, 117 (1998).
11. J. Hon *et al.*, *A Heuristic Method for Evaluating COIL Performance*, *AIAA Paper* 94-2422 (1994).
12. S. N. Foner and R. L. Hudson, **25**, 601 (1956).
13. T. J. Cook and T. A. Miller, *Chem. Phys. Lett.* **25**, 396 (1974).
14. D. J. Benard and N. R. Pchelkin, *Rev. Sci. Instrum.* **49**, 794 (1978).

15. A. Hill, *The next generation of controlled avalanche discharge gas lasers*, International Conference on Lasers, Albuquerque, NM (2000).
16. J. T. Verdeyen et al, "Diagnostic development for the ElectriCOIL flow system", Proc. SPIE. **4631**, 154 (2002).
17. A. A. Ionin et al, J. Phys. D: Appl. Phys. **36**, 982 (2003).
18. A. Hicks et al, J. Phys. D: Appl. Phys. **38**, 3812 (2005).
19. A. P. Napartovich, A. A. Deryugin and I. V. Kochetov, J. Phys. D: Appl. Phys. **34**, 1827 (2001).
20. D. S. Stafford and M. J. Kushner, J. Appl. Phys. **96**, 2451 (2004).
21. D. S. Stafford and M. J. Kushner, J. Appl. Phys. **98**, 073303 (2005).
22. J. A. Davidson and E. A. Ogryzlo, in *Chemiluminescence and Bioluminescence*, ed. M. J. Cornier, D. M. Hercules and J. Lee, p. 111 (Plenum, New York, 1973).

CHAPTER 4. O₂(¹Δ) PRODUCTION AND GAIN IN PLASMA PUMPED OXYGEN- IODINE LASERS: EFFECT OF NO AND NO₂ ADDITIVES

4.1. Introduction

In this chapter, we extend the work presented in Ch. 3 by looking at the effects of additives such as NO and NO₂ on the scaling of O₂(¹Δ) and optical gain. The chemical oxygen-iodine lasers (COILs) operate on the 1.315 μm [I(²P_{1/2}) → I(²P_{3/2})] transition of atomic iodine.[1-3] A series of collisional transfer reactions between O₂(¹Δ), and I₂ and ground state I(²P_{3/2}) (to be referred to as I) result in excitation of the upper laser level I(²P_{1/2}) (to be referred to as I^{*}). Typically O₂(¹Δ) is generated upstream of the laser cavity. I₂ is injected immediately prior to the cavity upon which the flow is supersonically expanded to lower the gas temperature as required to maximize the gain. Laser gain and oscillation have been demonstrated in electri-COILs (eCOILs) by Verdeyen et al [1] and Hicks et al [3].

A challenge in eCOILs is to produce sufficiently high yields of O₂(¹Δ) and the subsequent laser gain, to enable the laser transition to be saturated and produce high power.[4] In this regard, recent research has focused on tailoring the discharge parameters [5,6,7] and using additives such as CO, H₂, D₂ [8] and NO [9] to improve the excitation efficiency of O₂(¹Δ). NO and NO₂ are also used as additives to control the post-discharge chemistry [9]. In fact, all demonstrations of laser gain and oscillation to date have used flowing plasmas in He/O₂ mixtures with NO as an additive.

ECOILs differ from conventional COILs in that atomic oxygen is also produced in the electrical discharge by electron impact dissociation of O₂. The O atoms flow downstream where 3-body reactions produce O₃ and the remaining O atoms may react with the injected I₂.

Beneficial reactions of O with I₂ produce I atoms, thereby eliminating the expense of O₂(¹Δ) molecules for the initiating dissociating reactions. Detrimental reactions involving O atoms include quenching of I* by O which reduces gain. As such, management of the O atom density is important to optimize these opposing effects.

Injection of NO or NO₂ through or downstream of the discharge in eCOIL systems has two goals; improving the efficiency of direct production of O₂(¹Δ) in the discharge by electron impact and management of the O atom density downstream of the plasma. Including NO in the gas stream flowing through the discharge has, in part, the goal of improving production of O₂(¹Δ). NO, having a lower ionization potential (9.26 eV) than either O₂ or He, is likely to provide more rapid ionization with the possibility of lowering the operating E/N (electric field/gas number density) and electron temperature, *T_e*. Lowering *T_e* from the values typical of self-sustained He/O₂ mixtures is advantageous in more efficiently producing O₂(¹Δ) by direct electron impact.[5,8,10] Discharges in NO have also been known to produce O₂(¹Δ) in relatively large amounts even though O₂ may not be present as a feedstock gas, indicating the beneficial effect of NO.[11] However, when flowing NO through the discharge, some of the power that would otherwise be available to excite O₂ is dissipated by excitation and ionization of NO.

In addition to possibly improving the production of O₂(¹Δ), NO and NO₂ are effective in managing the inventory of O atoms through direct and cyclic reactions which have the effect of converting O atoms back into O₂. NO and NO₂ also have secondary effects in that they react with I atoms forming intermediary species such as INO, and INO₂ which further react with I to reform I₂. [12]

In this chapter, we report on results from a computational investigation of the consequences of NO and NO₂ additives on flowing He/O₂ plasmas and their afterglows with I₂ injection in the context of eCOIL systems. These investigations were conducted using plug-flow (*GlobalKIN*) and 2d (*nonPDPSIM*) plasma-hydrodynamics models. Although for most conditions the addition of NO to the inlet gas stream reduced the density of O₂(¹Δ), it ultimately increased the densities of I^{*} downstream of the discharge through management of the O atom density. The inlet NO mole fraction also typically increased extent of the region over which positive laser gain could be achieved. This can be particularly useful in high speed flows where mixing lengths are longer. Injection of NO₂ in the post-discharge flow can help in rapidly scavenging O atoms in two body reactions (as compared to scavenging by NO which proceeds by a 3-body mechanism). In general, addition of NO₂ in the post-discharge region improves laser gain.[9] The downside to NO₂ injection is a rise in gas temperature due to the exothermicity of the reactions between NO₂ and O.

4.2 Description of Reactor

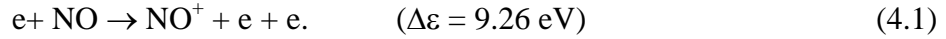
A schematic of the cylindrically symmetric, 6 cm diameter flow tube used in this study is shown in Fig. 4.1. Power is capacitively coupled using ring electrodes operating at 25 MHz. A mixture of He/O₂/NO at 3 Torr enters the discharge through the inlet at a flow rate of 6 slpm corresponding to an axial speed of $\approx 890 \text{ cm s}^{-1}$. The length of the tube is 90 cm and it captures the downstream kinetics in sufficient detail. The flow consists of 30% O₂ with the balance divided between He and NO. The NO mole fraction is varied from 0 – 10%. Two injection nozzles are located downstream. (In the 2d cylindrically symmetric geometry these nozzles appear to be rings.) The first nozzle at 51.5 cm is used to inject a mixture of

He/NO or He/NO₂. The second nozzle at 64.5 cm injected a mixture of He/I₂. At the outlet, axial gradients are assumed to be zero and the exit speeds are adjusted to maintain constant pressure and mass flux.

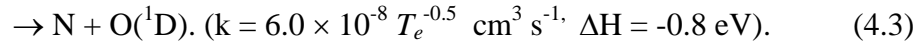
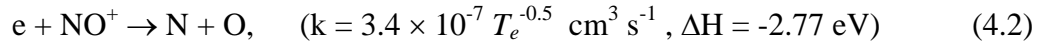
4.3 Reaction Mechanism

The reaction mechanism builds upon that previously developed for He/O₂ (Appendix A) discharges. The processes that were added to that reaction mechanism to account for the injection of NO, NO₂ and I₂ are listed in Appendix B. The species included in the reaction mechanism are e, He, He(²S), He⁺, O₂, O₂(v), O₂(¹Δ), O₂(¹Σ), O₂⁻, O₂⁺, O, O(¹D), O(¹S), O⁻, O⁺, O₃, O₃⁻, NO, NO⁺, NO₂, NO⁻, NO₂⁻, N, N₂, I₂, I₂^{*}, I(²P_{3/2}), I(²P_{1/2}), IO, INO, and INO₂. The vibrational levels of N₂ were not included as individual species in the reaction mechanism as N₂ densities were small and predominantly produced downstream of the discharge where electron impact processes are negligible. Excitation of the first five vibrational levels of NO ($\Delta\varepsilon = 0.23, 0.46, 0.69, 0.91, \text{ and } 1.13$) and the electronic states: NO(^aΣ) ($\Delta\varepsilon=5.48$ eV), NO(^cΠ) ($\Delta\varepsilon= 6.5$ eV), and NO(^bΣ) ($\Delta\varepsilon = 7.58$ eV) were included for purposes of energy loss collisions with ground state NO. The densities of these states were not explicitly tracked in the model. The negative ions NO⁻ and NO₂⁻ were included only in *GlobalKIN* after confirming that their exclusion does not make a significant change to the reaction kinetics in *nonPDPSIM* (2d). Their exclusion from *nonPDPSIM* was for the purpose of speeding the calculation.

An important motivation for flowing NO through the plasma zone is that it has a smaller ionization potential than O₂ and He, and so should produce more ionization at a lower T_e ,



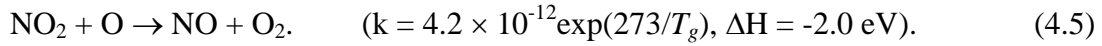
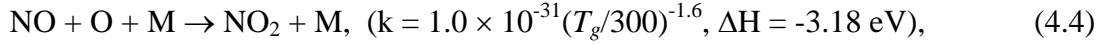
This ionization does, however, come at the cost of channeling discharge power into NO (e.g., vibrational excitation and dissociation), power that might otherwise be deposited into O₂. This power therefore does not directly lead to generation of O₂(¹Δ). Since NO⁺ has the smallest ionization potential among all the atoms and molecules in this mechanism, significant amounts of NO⁺ are formed by charge-exchange reactions with He⁺, O⁺, and O₂⁺. Dissociative recombination of NO⁺ with electrons can produce N, O and O(¹D), as well as contribute to gas heating through Frank-Condon processes,



where ΔH is the change in enthalpy of the recombination event.

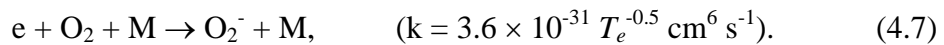
Electron impact dissociation of O₂ (Eqs. 3.3 and 3.4) is a significant source of O atoms and, in part, the motivation for injection of NO and NO₂ to manage the resulting flow of O atoms. For self sustaining discharges, roughly one O atom is generated for every O₂(¹Δ) produced in the plasma zone. The O atoms are useful in dissociating I₂, and are also a quencher of the upper level of the lasing species I^{*}, and hence the density of O needs to be managed. NO and NO₂ are useful in this regard as they are useful in managing of the O atom inventory. Much of this chemistry is cyclic and hence small amounts of NO or NO₂ can produce significant

effects in O atom densities. NO reacts with O to form NO₂ which then further reacts with O to regenerate O₂,

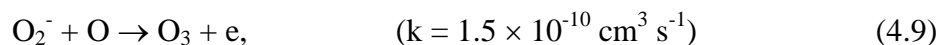
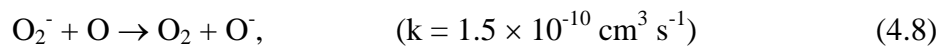


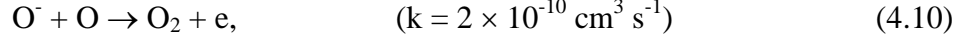
At low pressures where the third-body density is low, the rate of reaction of O with NO₂ occurs at a higher rate than with NO. Hence addition of NO₂ in the downstream region may be preferred over that of NO if the residence time in the flow tube is a limiting factor. These reactions are, however, exothermic and so can increase the gas temperature which is generally not beneficial.

The negative ion chemistry of He/O₂ mixtures is initiated by dissociative attachment and 3-body reactions,

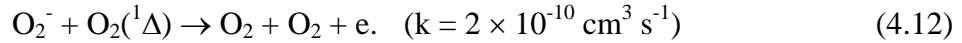
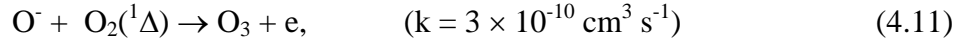


where M is a third body and k is the rate coefficient. O₂⁻ subsequently charge exchanges with O atoms to form O⁻ or associatively detaches to form O₃. A similar process occurs with O⁻ to reform O₂,

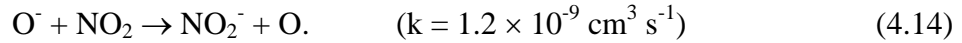
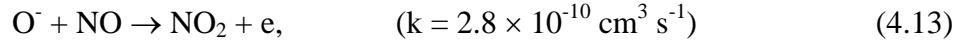




Through dissociative detachment reactions, Both O^- and O_2^- react with $\text{O}_2(^1\Delta)$ to form O_3 , and to quench $\text{O}_2(^1\Delta)$,



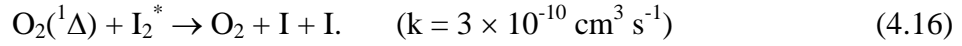
NO also intercepts the negative ion chemistry through charge exchange reactions and associative attachment,



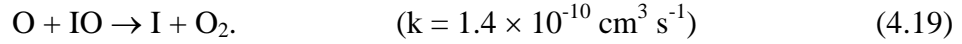
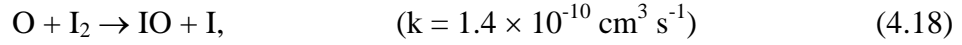
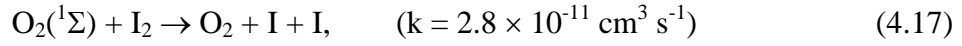
These reactions are potentially beneficial in two ways. They increase the electron density which can lower T_e into a more favorable range for exciting $\text{O}_2(^1\Delta)$ and they reduce the density of O^- which would otherwise quench $\text{O}_2(^1\Delta)$ to form O_3 . The negative ions NO^- and NO_2^- were not included in the 2d model (to increase computational speed), whereas they were included in the plug-flow model. Computational experiments were conducted using the plug-flow model to quantify the effects of the NO^- and NO_2^- and are discussed below.

Laser gain is ultimately achieved by injection of I_2 downstream of the plasma zone, and by its reacting with O , $\text{O}_2(^1\Delta)$, and $\text{O}_2(^1\Sigma)$ to create I atoms and to pump the upper laser

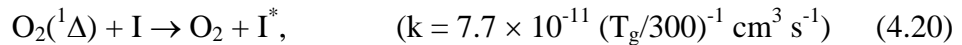
level. In a conventional COIL there is a negligible inventory of O atoms and $O_2(^1\Sigma)$, and so the dissociation of I_2 is dominantly by $O_2(^1\Delta)$ in a two-step process,



In eCOIL, the presence of $O_2(^1\Sigma)$ and O help in dissociating I_2 and producing I atoms. A reaction intermediate IO is also helpful in this regard,



The laser pumping reaction by $O_2(^1\Delta)$ in collisions with I is favored at lower temperatures over its endothermic back reaction,

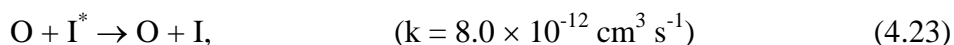


To suppress the back reaction, the laser cavity is typically placed in a supersonically expanded flow to lower the translational temperature. As such, the threshold yield, Y_{th} , of $O_2(^1\Delta)$ required for positive optical gain in an undissociated flow of O_2 is [13],

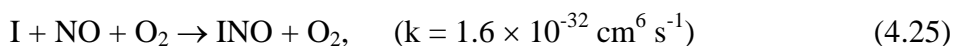
$$Y_{th} = \frac{[O_2(^1\Delta)]}{[O_2]} = \frac{1}{1+1.5\exp(401/T_g)}. \quad (4.22)$$

For example, in an undissociated flow of O₂, the threshold yield at room temperature is 15% whereas at 180 K the threshold yield is 6%.

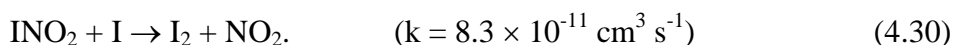
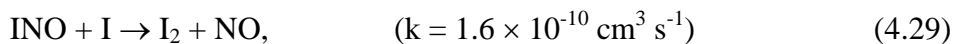
Quenching of I* occurs dominantly by reactions with O and O₂ (the backward reaction), and to a lesser extent with O₂(¹Δ) and NO,



NO and NO₂ also help in removing ground state I atoms and so aid in maintaining the inversion,



The INO_x species in turn abstract I atoms to release I₂ and NO_x back into the flow,



Typically, the injection of I₂ occurs during or following a supersonic expansion of the gas to velocities equivalent to Mach 2 or Mach 3 to lower T_g to decrease the yields of O₂(¹Δ) required to achieve positive gain. Accurately simulating a supersonic expansion is difficult in our modeling platform. In order to provide a best case estimate for laser gain we used for the temperature of the reactions in Eq. 4.20 and 4.21 a value appropriate for a Mach 2 flow. This temperature can be approximated from,

$$\frac{T_0}{T_g} = \left(1 + \frac{\gamma - 1}{2} M^2 \right), \quad (4.31)$$

where T_0 is the stagnation (or tank) temperature, γ is the ratio of specific heats and M is the Mach number. For $M = 2$ and $T_0 = 300$ K, this ratio is ≈ 2.18 , and would lead to a gas temperature of 137 K. This enables the simulation of experimental conditions from a kinetics viewpoint, without actually simulating the supersonic expansion.

The reaction mechanism was validated by comparing to experimental data from Carroll et al [14], as discussed below.

4.4 Consequences of NO in the Inlet Flow

Plasma characteristics (n_e , T_e , negative total negative ion density M^- , total positive ion density M^+ , and power density) obtained with the *nonPDPSIM* are shown in the vicinity of the electrodes in Fig. 4.2 for the base case having an inlet flow of He/O₂/NO = 67/30/3. T_e in the bulk of the discharge is 2.3 eV and the peak electron density is 9.0×10^9 cm⁻³. Since NO and O₂ are attaching species, the negative ion density (maximum of 1.1×10^{10} cm⁻³) is

commensurate with n_e . The n_e is fairly symmetric between the electrodes and relatively uniform. The power deposition is moderately higher near the upstream electrode due to gas heating which reduces the neutral densities downstream. This is not a general result as higher power deposition and more rarefaction can produce regions of locally intense power deposition near the downstream electrode.

The densities of the neutral species O, $O_2(^1\Delta)$, I and I^* , and T_g are shown for the base case in Fig. 4.3. A flow of 36 sccm of pure NO is injected through the first nozzle and a flow of 100 sccm of He/I₂ = 99/1 is injected through the second nozzle. Having few quenchers at these pressures, the $O_2(^1\Delta)$ accumulates as the gas flows through the discharge reaching a maximum value of $1.35 \times 10^{15} \text{ cm}^{-3}$. The $O_2(^1\Delta)$ density remains nearly constant thereafter until the injection point for I₂. Reactions of $O_2(^1\Delta)$ with I₂ and I (the latter being the laser pumping reaction producing I^*) reduce its density by a factor of five to $2.7 \times 10^{14} \text{ cm}^{-3}$.

Similar to $O_2(^1\Delta)$, the density of O atoms accumulate from electron impact dissociation of O₂ passing through the discharge (with a small amount of depletion of the O in forming O₃) until the injection point of NO at the first nozzle. The O densities decrease from a peak value of 1.4×10^{15} to $4.0 \times 10^{14} \text{ cm}^{-3}$ downstream of the NO injection due to its reaction with NO. The remaining O atoms flow to the injection point of I₂ where they are further depleted in dissociating reactions with I₂. The I₂ is nearly completely dissociated by reactions with the O atoms to form I. Pumping reactions between $O_2(^1\Delta)$ and I produce I^* . The region of positive gain (where the inversion density of $G = [I^*] - 1/2[I] > 0$) is a narrow band downstream of the I₂ injection point, with a peak value of $G = 2.6 \times 10^{11} \text{ cm}^{-3}$.

T_g has two local maxima. The first is due to discharge Joule heating, Frank Condon heating and exothermic reactions of NO with O reaching 340 K adjacent to the downstream

electrode. As the walls are held at 300 K, the gas rapidly cools by conduction. A second local maximum occurs downstream of the first injection nozzle (up to 348 K) due to additional exothermic reactions of O and the newly injected NO.

To investigate the consequences of NO in inlet flow over a wider parameter space, the plug-flow model was used. We first addressed the importance of NO^- and NO_2^- in the reaction mechanism and their effects on the densities of electrons, $\text{O}_2(^1\Delta)$ and $\text{O}_2(^1\Sigma)$. The densities of these species are shown along the axis of the discharge in Fig. 4.4 for a 3 Torr mixture of He/O₂/NO = 60/30/10 with 40 W power deposition. A high mole fraction of NO was used as an extreme case. When including NO^- and NO_2^- the peak electron density decreased approximately 10% from $1.4 \times 10^{10} \text{ cm}^{-3}$. The reduction in n_e results in large part from the attachment of electrons to NO through 3-body reactions similar to those for O_2^- formation (Eq. 4.7) and dissociative attachment to NO. The changes in densities of $\text{O}_2(^1\Delta)$ and $\text{O}_2(^1\Sigma)$ were relatively small (<5%) and could be attributed to the fact that n_e decreases and T_e increases modestly (0.05-0.1 eV from ≈ 2.0 eV) with the inclusion of NO^- and NO_2^- . (Recall that electron impact excitation of $\text{O}_2(^1\Delta)$ is maximum for $T_e = 1-1.5$ eV.) The density of O atoms was relatively independent on the inclusion of NO^- and NO_2^- . Based on these trends, we can expect results from *nonPDPSIM* (which do not include NO^- and NO_2^- in the reaction mechanism) to over-predict $\text{O}_2(^1\Delta)$ densities by a few percent.

The consequences of NO in the inlet flow on the maximum densities of charged species, T_g , T_e , and power deposition into different species by electron impact are shown in Fig. 4.5 for 3 Torr and 40 W. A modest increase in n_e , from $1.1 \times 10^{10} \text{ cm}^{-3}$ to $1.25 \times 10^{10} \text{ cm}^{-3}$, occurs as the NO mole fraction is increased from zero to 10% due to the higher rates of ionization with NO in spite of a decrease in the positive and negative ion densities. The

increase in n_e results from the density of negative ions decreasing more rapidly than the positive ions when increasing the mole fraction of NO. The positive ion density decreases from $2.3 \times 10^{10} \text{ cm}^{-3}$ to $2.0 \times 10^{10} \text{ cm}^{-3}$ while the decrease in negative ion density is $1.2 \times 10^{10} \text{ cm}^{-3}$ to $0.75 \times 10^{10} \text{ cm}^{-3}$. T_e decreases from 2.2 to 1.9 eV as the NO mole fraction is increased from 0 to 10%. The reduction in T_e is due to the additional power loss resulting from electron impact on NO when substituting NO for He and the reduction in the average ionization potential thereby enabling the discharge to be self sustained with a lower value of T_e . This trend is partially offset by the additional attachment probability represented by NO.

While the total ion densities gradually decrease with increasing NO mole fraction, the densities of individual ions show more variation. In the absence of NO, O_2^+ forms the majority (>99%) of the positive ions. However with as little as 1-2% of NO, the majority ion is NO^+ . This is due to exchange reactions between O_2^+ and NO. The dominant negative ion in the absence of NO is O^- , and as the NO mole fraction is increased, the density of NO_2^- ions increases, a result of charge exchange between O^- and NO_2 (Eq. 4.14).

T_g increases with NO mole fraction primarily due to the exothermicity of reactions between O, NO and NO_2 (Eqs. 4.4 and 4.5). In the absence of NO, the maximum value of T_g is 328 K (increasing from the inlet value of 300 K). This value increases to 362 K with 10% NO. The peak gas temperatures occur just downstream of the discharge region. With large NO mole fractions, the contribution of Frank-Condon gas heating due to dissociation of NO can be more than a few percent.

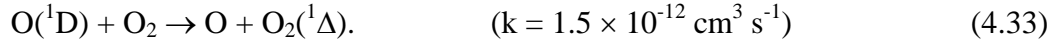
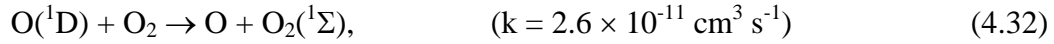
The fractional power deposited into NO by electron impact (Boltzmann calculation) increases nearly linearly with the NO mole fraction, increasing to 25% for an NO mole fraction of 10%. Note that these values were computed using the actual mole fractions of

species in the discharge and not the inlet conditions. Correspondingly, the power deposition into O_2 decreases, from more than 85% in the absence of NO to 66% for an NO mole fraction of 10%. (Little power is dissipated by He.) In spite of the fraction of discharge power dissipated in O_2 decreasing, the power expended in exciting $O_2(^1\Delta)$, α , was relatively unchanged, reaching a shallow maximum of 8.7% for a NO mole fraction of 5%. As the NO mole fraction increases, T_e decreases from 2.2 to 1.9 eV thereby increasing the efficiency of $O_2(^1\Delta)$ production by electron impact [10]. Fortuitously, a combination of decreasing power dissipated by O_2 and an increase in the efficiency of exciting of $O_2(^1\Delta)$ maintains the total power expended in exciting $O_2(^1\Delta)$ relatively constant. This is not necessarily a general result but lowering T_e is generally beneficial. Similar trends are seen for $O_2(^1\Sigma)$ as the fractional power expended in exciting $O_2(^1\Sigma)$ increases slightly from 3.2 to 3.9% as the NO mole fraction increases to 10%.

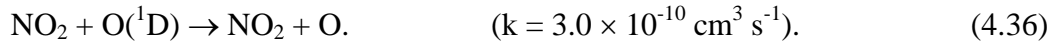
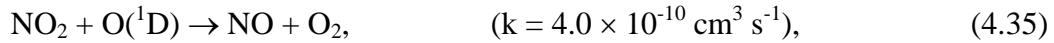
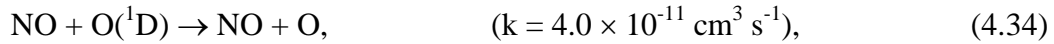
The consequences of NO mole fraction in the inlet flow on the densities of O, $O_2(^1\Delta)$ and $O_2(^1\Sigma)$, and the yield of $O_2(^1\Delta)$ along the axis of the discharge are shown in Fig. 4.6 for the base case of 3 Torr, 40 W and 30% O_2 . (Note that this yield is based on the mole fraction equivalent of O_2 for all oxygen species.[10]) A flow of 100 sccm of He/ $I_2 = 99/1$ is injected through the second nozzle. In the absence of NO, the density of $O_2(^1\Delta)$ increases to $1.2 \times 10^{15} \text{ cm}^{-3}$ due to electron impact excitation as the inlet flow passes through the plasma zone. The increase in the density of $O_2(^1\Delta)$ to $1.75 \times 10^{15} \text{ cm}^{-3}$ after the discharge zone results largely from quenching of a density of $0.4 \times 10^{15} \text{ cm}^{-3}$ of $O_2(^1\Sigma)$ by O atoms and excitation transfer from $O(^1D)$. The density of $O_2(^1\Delta)$ upstream of the I_2 injection point monotonically decreases with the addition of NO, from $1.75 \times 10^{15} \text{ cm}^{-3}$ without NO to $1.1 \times 10^{15} \text{ cm}^{-3}$ with

10% NO. A portion of this decrease results from an increase T_g when adding NO though the yield of $O_2(^1\Delta)$ also decreases from 5.9% when adding NO.

The production of $O_2(^1\Delta)$ is dominated by electron impact on O_2 and so is dependent on T_e and n_e . Since the power deposition producing $O_2(^1\Delta)$ is nearly constant, secondary processes must be responsible for the decrease in the yield of $O_2(^1\Delta)$ with increasing NO. One such secondary process is the production of $O_2(^1\Delta)$ by excitation transfer between $O(^1D)$ and O_2 . The majority of $O(^1D)$ is produced by dissociative excitation of O_2 (Eq. 3.12). Reactions of $O(^1D)$ with O_2 produced its excited states,



With the decrease in T_e with addition of NO, the production of $O(^1D)$ by electron impact dissociation of O_2 decreases and so these secondary sources of $O_2(^1\Delta)$ and $O_2(^1\Sigma)$ also decrease. Furthermore, both NO and NO_2 are quenchers of $O(^1D)$,



So the addition of NO reduces the production of $O(^1D)$ and increases its rate of quenching, thereby reducing the production of $O_2(^1\Delta)$ by excitation transfer. The importance of the quenching reactions of $O(^1D)$ is demonstrated by excluding the reactions in Eqs. 4.34 – 4.36

from the mechanism. For 10% NO in the flow, the yield of $O_2(^1\Delta)$ improved from 4.6% to 5.3% when quenching of $O(^1D)$ is eliminated. The quenching of $O_2(^1\Delta)$ by NO has a small rate coefficient ($3.5 \times 10^{-17} \text{ cm}^3 \text{ s}^{-1}$) and so does not significantly contribute to the loss of $O_2(^1\Delta)$.

However, experiments by Verdeyen et al [1] indicate that addition of NO results in increase in $O_2(^1\Delta)$ densities. The discrepancy between experiments and the model results could be due to a combination of the following. The rate constant for quenching of $O(^1D)$ used in the model could be larger than the real value, and the fact that the reactions between $NO(v)$ states and O_2 have not been included. As such, the 4th and 5th vibrational states of NO have sufficient energy to excite the O_2 to the $^1\Delta$ state.

The density of O atoms increases monotonically through the discharge zone to a maximum value of $2.5 \times 10^{15} \text{ cm}^{-3}$ in the absence of NO. (The small increase in the density of O after the discharge is mainly due to gas cooling.) With the addition of NO, the density of O atoms decreases throughout the flow-tube and, in particular, downstream of the discharge. This decrease is due both to the reduction in the rate of electron impact dissociation of O_2 by the decrease in T_e and by the formation of NO_2 in reactions with NO. In the post-discharge region in the absence of NO, the majority of $O_2(^1\Sigma)$ is converted to $O_2(^1\Delta)$ through collisions with O and O_3 . Due to the reduction of O atoms with increasing NO, the rates of quenching of $O_2(^1\Sigma)$ to $O_2(^1\Delta)$ are also smaller, leading to a higher densities of $O_2(^1\Sigma)$ in the afterglow. Higher $O_2(^1\Sigma)$ densities are not necessarily bad since they help in dissociating I_2 but maintaining those densities does result in lower densities of $O_2(^1\Delta)$ that directly pump I^* .

The densities of I and I^* , and the optical gain at $1.315 \mu\text{m}$ are shown in Fig. 4.7 for the conditions of Fig. 4.6 (1 sccm of I_2 injected in a 100 sccm, He/ I_2 = 99/1 flow). The gain was

obtained the inversion density G and the stimulated emission cross-section, $\text{gain} = \sigma([I^*] - 0.5[I])$ where σ is the stimulated emission cross-section. At pressures of less than tens of Torr, Doppler broadening dominates over pressure broadening, and so the stimulated emission cross-section can be approximated by,

$$\sigma = 1.33 \times 10^{-16} T_g^{-1/2} \text{ cm}^2. \quad [15] \quad (4.37)$$

In the absence of NO, the density of I increases from $1.75 \times 10^{13} \text{ cm}^{-3}$ at the I_2 injection point to $3.2 \times 10^{13} \text{ cm}^{-3}$ downstream due in large part to the reaction of O atoms with I_2 . The density of I^* is maximum at the injection point at $1.45 \times 10^{13} \text{ cm}^{-3}$ and decreases to negligible values by the end of the flow tube due to the depletion of $O_2(^1\Delta)$ (the species responsible for the pumping reaction) and quenching by O atoms. Since the lifetime of I^* (125 μs for quenching by O) is short compared to flow times, the density of I^* does not appreciably accumulate in the discharge and its density is a reflection of instantaneous production and quenching rates. The end result is a peak gain of $4.2 \times 10^{-5} \text{ cm}^{-1}$ within a centimeter of the I_2 injection point. Note that the rate of quenching of I^* by O is faster than that due to spontaneous emission (0.1 s). [16]

With injection of I_2 the density $O_2(^1\Delta)$ decreases by virtue of excitation transfer and dissociative excitation of I_2 , and reactions with I which pumps I^* . In the absence of NO, the density of $O_2(^1\Delta)$ is fully depleted by the reactions. In the absence of NO there is also a large density of O atoms at the injection point which react with I_2 producing IO and I. Since the rate of dissociation of I_2 by $O_2(^1\Delta)$ and $O_2(^1\Sigma)$ is slower than by O atoms there is a larger density of I available for $O_2(^1\Delta)$ to react with, and so the $O_2(^1\Delta)$ is rapidly depleted. As the

flow of NO is increased, the flow of O atoms decreases, resulting in a lower rate of dissociation of I₂ and fewer I atoms. With the lower density of I the reactivity of O₂(¹Δ) is lower; and so its density decreases less rapidly after injection of I₂.

The production of I* results from reactions of O₂(¹Δ) with I while the quenching of I* is largely due to collisions with O atoms. Increasing the NO mole fraction decreases the O atom density downstream thereby lowering the rates of quenching of I* and extending its plume beyond the I₂ injection point. However, having too large of an NO mole fraction results in too low rates of dissociation of I₂ and hence poor utilization of O₂(¹Δ). The end result is that the region over which positive gain can be sustained is maximum for an intermediate mole fraction of NO of 3 %.

The purpose of flowing NO (or injecting NO₂) is largely to manage the O atom density and so control the quenching of I* by O. A sensitivity study was conducted of the rate coefficient for this quenching reaction from the nominal value of $8 \times 10^{-12} \text{ cm}^3 \text{ s}^{-1}$. The densities of O₂(¹Δ) and I*, and gain are shown in Fig. 4.8 while varying this rate coefficient from 0 to $1.0 \times 10^{-11} \text{ cm}^3 \text{ s}^{-1}$. In the absence of quenching, the densities of I* and O₂(¹Δ) do not significantly decrease downstream of the I₂ injection point. In the absence of quenching by O, the predominant quencher of I* is O₂ and this quenching produces O₂(¹Δ). The forward and backward pumping reactions (Eqs. 4.20 and 4.21) reach an equilibrium where the I* and O₂(¹Δ) densities gradually decrease due to minor quenchers of I* [such as NO and O₂(¹Δ)] and radiative relaxation. When increasing the rate coefficient for quenching I*, the density of I* decreases proportionately. By removing I* in this manner the rate of the backward reaction with O₂ decreases and so does the density of O₂(¹Δ). The extent of positive gain is

progressively limited to the few cm beyond the I_2 injection point as the quenching of I^* increases, though the peak value of gain is not particularly sensitive to the rate coefficient.

The densities of $O_2(^1\Delta)$ and O, and T_g 2 cm upstream of the second nozzle are shown in Fig. 4.9 as a function of power deposition and NO mole fraction in the inlet flow. In general, T_g increases with power deposition and with NO addition reaching a maximum of 480 K with 400 W power deposition and 10% NO in the inlet flow. Increasing power deposition produces more electron impact dissociation of O_2 and NO, producing larger densities of O atoms. However, increasing NO mole fractions decrease the density of O atoms by virtue of scavenging by NO and NO_2 and decreasing T_e .

The density of $O_2(^1\Delta)$ decreases with NO addition, as discussed above, and increases with power deposition. The saturation in the density $O_2(^1\Delta)$ at $6.5 \times 10^{15} \text{ cm}^{-3}$ at higher powers is due in part to the depletion of O_2 by electron impact dissociation and in part to gas heating. For example, with 400 W and 0% NO, the fractional dissociation of O_2 is 68%. The addition of NO reduces the depletion of O_2 by both reducing the rate of O_2 dissociation and by recycling O atoms back to O_2 . For example, for 10% NO addition and 400 W, the fractional dissociation decreases to 36%. The yield of $O_2(^1\Delta)$ saturates with power at 18% due to the depletion of O_2 .

The densities of I and I^* , and gain as function of power deposition and NO mole fraction are shown in Fig. 4.10 at a location of 2 cm downstream from the I_2 injection point. This mixing length of 2 cm was chosen based on previous studies for similar flow conditions.[17] The inlet flow has 30% O_2 and the flow injected through the second nozzle is 1 sccm of I_2 in a 100 sccm flow of He/ $I_2 = 99/1$. At low power deposition, the density of I is large, $2.2 - 2.3 \times 10^{13} \text{ cm}^{-3}$, because the yields of $O_2(^1\Delta)$ are low enough that the pumping of I to I^* is slow. As

the yield of $O_2(^1\Delta)$ increases at higher powers, the pumping reactions reduce the density of I and increase that of I^* , leading to an increase in gain. However, at large power deposition, the density of O increases whereas that of $O_2(^1\Delta)$ saturates. This leads to an increased rate of quenching of I^* by O which reduces the density of I^* and increases that of I. The end result is a reduction in gain.

Increasing NO in the inlet flow reduces the density of O atoms at the injection point, thereby reducing the rate of dissociation of I_2 and the density of I atoms. The reduction in O by addition of NO also reduces the quenching of I^* by O, making the gain predominantly dependent on the yield of $O_2(^1\Delta)$. As a result, for 3% NO, the gain decreases from 6.0×10^{-5} to $4.3 \times 10^{-5} \text{ cm}^{-1}$ between 150 and 400 W, whereas in the absence of NO, the gain reduces by nearly a factor of 3.

The eCOIL system may operate in either power limited or iodine limited modes. In the iodine limited mode, the flow of $O_2(^1\Delta)$ and O generated by the discharge fully utilizes the injected flow of I_2 , and so gain saturates with increasing power. To some degree (quenching of I^* and depletion of O_2 aside), this is the mode that applies to the results shown in Fig. 4.10. In the power limited mode, the flow of $O_2(^1\Delta)$ and O is insufficient to fully utilize the injected flow of I_2 , and so gain saturates with flow if I_2 .

These modes of operation are demonstrated by varying power deposition and I_2 flow rate. The densities of I and I^* , and gain are shown 2 cm downstream of the I_2 injection point in Fig. 4.11 for a 6 slpm inlet flow of He/ O_2 /NO=67/30/3 while varying power and I_2 flow rate. The densities of I and I^* increase nearly linearly with the flow of I_2 and increase sub-linearly with power deposition. For example, with a flow of 3 sccm of I_2 , the density of I is $4.6 \times 10^{13} \text{ cm}^{-3}$ with 40 W and only $5.6 \times 10^{13} \text{ cm}^{-3}$ with 120 W. For these conditions the

production of I is limited by the availability of I₂ as the injected I₂ is nearly completely dissociated by reactions with O, O₂(¹Δ) and O₂(¹Σ) for all power depositions. The production of I* is limited by the yield of O₂(¹Δ) which does not scale linearly with power at higher power depositions. As a consequence the density of I* saturates with power deposition with large flows of I₂. This saturation is exacerbated at high power depositions (or low NO mole fractions) by large densities of O which quench I*.

With a power deposition of 40 W, gain increases with flow rate of I₂ [shown in Fig. 4.11(c)] saturating at 3 × 10⁻⁵ cm⁻¹ at 2 sccm, a consequence of being in a power limited regime. As the power increases the gain increases, and the flow rate at which the maximum gain is obtained also increases. For example, for 80 W, the gain saturates at 9 × 10⁻⁵ cm⁻¹ for an I₂ flow rate of 3 sccm. The higher power deposition is able to better utilize the increased flow of I₂. As the power further increases, the peak gain increases only moderately and decreases above 200 W as the system transitions to an I₂ limited regime and the densities of O₂(¹Δ) saturate.

The consequences of flow rates of NO and I₂ on gain are shown for 80 W in Fig. 4.11(d). For a fixed power, increasing the mole fraction of NO at the inlet reduces the density of O atoms which reduces the quenching of I*. Increasing the NO mole fraction increases the range of I₂ flow rates over which the positive gain can be achieved and increases the flow rate of I₂ at which the maximum gain is obtained. For example, the maximum gain in the absence of NO is 4.2 × 10⁻⁵ cm⁻¹ for an I₂ flow rate of 0.8 sccm. As the rate of quenching of I* decreases with increasing NO flow, gain increases to more than 1.2 × 10⁻⁴ cm⁻¹ for an inlet mole fraction of 5% NO and flow rate of 3 sccm of I₂.

The consequences of flow dynamics on the densities of $O_2(^1\Delta)$ and I^* are shown in Fig. 4.12 with results from *nonPDPSIM*. The densities of $O_2(^1\Delta)$ and I^* are shown for 80 W and a 6 slpm inlet flow of He/O₂/NO = 68/30/2. A 100 sccm flow of He/I₂ was injected from the second nozzle with the I₂ flow varied from 0.5 to 3 sccm. As the flow passes through the discharge zone, electron impact produces $O_2(^1\Delta)$ at large radius first where the plasma density is highest. Diffusion homogenizes the density of $2.5 \times 10^{15} \text{ cm}^{-3}$ across the radius by 10-12 cm downstream of the plasma zone. At and after the I₂ injection point, the densities of $O_2(^1\Delta)$ decrease due to excitation transfer to I₂ and pumping of I^* , first at the outer radius where the I₂ is injected and on axis 4-5 cm downstream. With low flow rates of I₂, (≤ 0.5 sccm) the $O_2(^1\Delta)$ is not significantly depleted where as flow rates ≥ 1 sccm, the flow $O_2(^1\Delta)$ is largely consumed by reaction with I₂ and I.

The densities of I^* are maximum adjacent to the second nozzle where densities of both $O_2(^1\Delta)$ and I₂ are largest. The I^* diffuses radially to the center of the discharge 4-5 cm downstream of the injection point. For small flow rates of I₂, the densities of I are smaller, and hence consumption of $O_2(^1\Delta)$ in pumping the I^* is gradual, leading to a longer distance over which significant amounts of I^* are present. At high flow rates of I₂, $O_2(^1\Delta)$ is largely consumed in the vicinity of the injection point and so I^* does not extend appreciably beyond that point.

The densities of I and I^* , and the gain obtained with *nonPDPSIM* at a radius of 1.5 cm are shown in Fig. 4.13 for the conditions of Fig. 4.12. Similar to the results obtained with *GlobalKIN*, the densities of I increase with increasing flow rate of I₂ indicating that the system is in an I₂ limited regime. The densities of I^* also increase with increasing I₂ mole fraction reaching a maximum 3-4 cm downstream of the injection point. I^* is rapidly

quenched by the O atoms whose densities are commensurate with $O_2(^1\Delta)$. At lower I_2 mole fractions, the densities of I^* do not decrease rapidly downstream of the injection point due to the availability of $O_2(^1\Delta)$ to continue to pump I to I^* .

The maximum gain (at a radius of 1.5 cm) is 10^{-4} cm^{-1} for an I_2 flow of 3 sccm. The axial extent of positive gain is limited by the depletion of $O_2(^1\Delta)$. Lower flow rates of I_2 produce lower gain but the axial extent of gain is greater. A comparison of maximum gain obtained with *GlobalKIN* and *nonPDPSIM* as a function of flow rate of I_2 is shown in Fig. 4.13(d). The predicted gains are commensurate except at large flow rates of I_2 where the gain with the *GlobalKIN* is significantly higher than with the 2d model. The lack of axial transport in the plug-flow model produces artificially high rates of reaction between O and $O_2(^1\Delta)$ with I and I_2 which increases predicted gain.

4.5 NO_2 Injection

In experimental demonstrations of laser oscillation and significant gain in eCOIL systems, NO_2 was usually injected downstream of the plasma zone and prior to the addition of I_2 . [9,14] Comparisons between predictions from *GlobalKIN* and experiments by Carroll et al [14] using this strategy are shown in Fig. 4.14. The conditions are a 10 Torr, 26.9 slpm (20 mmol s^{-1}) inlet flow of $He/O_2 = 80/20$ and 25 - 800 W followed by injection of 0 - 1344 sccm ($0 - 1 \text{ mmol s}^{-1}$) NO_2 and injection of 10.7 sccm ($0.008 \text{ mmol s}^{-1}$) of I_2 , equivalent to few percent of the $O_2(^1\Delta)$ flow rate. The diameter of the reactor is 4.9 cm and I_2 injection is 20 cm downstream of the NO_2 injection point. The power deposition spans nearly 25 cm due to a larger separation between electrodes in the experiment. The experimental measurements were made 10 cm downstream of the I_2 injection point in a subsonic (high gas temperature

flow) and so gains are negative. With the exception of low powers and low flow rates of NO_2 , the experimental trends are captured by *GlobalKIN*. Addition of NO_2 prior to injection of I_2 scavenges some of the O atoms in the flow and so reduces the quenching of I^* by O atoms. Higher powers produce larger flows of O atoms as well as more $\text{O}_2(^1\Delta)$ but the quenching of I^* dominates. Increasing the NO_2 flow rate increases the scavenging of O atoms and extends the power prior to transitioning to large negative gain.

Since NO_2 is more effective than NO in scavenging of O atoms, we investigated NO_2 injection through the first nozzle. The conditions are a 3 Torr, 6 slpm inlet flow of $\text{He}/\text{O}_2/\text{NO} = 67/30/3$ and discharge power of 40 W. A He/NO_2 flow of 36 sccm was injected through the first nozzle with the fraction of NO_2 being varied. As before a 100 sccm flow of $\text{He}/\text{I}_2 = 99/1$ was injected through the second nozzle. The consequences of NO_2 flow rate through the first nozzle on the densities of O and $\text{O}_2(^1\Delta)$, and yield of $\text{O}_2(^1\Delta)$ are shown in Fig. 4.15. These results are from *GlobalKIN* with a result from the *nonPDPSIM* without NO_2 injection for comparison. The injection of NO_2 produces a decrease in the O atom density due to the titration of O by NO_2 and the conversion of O to O_2 , respectively. As the NO_2 flow rate increases to 36 sccm the O atom densities decrease by a factor of 3 - 4 just downstream of the injection point due to the more rapid rate of reaction with O (compared to that of NO). The heat of reaction between NO_2 and O locally increases the gas temperature leading to a reduction in the density of $\text{O}_2(^1\Delta)$ near the first nozzle due to rarefaction. Note, however, that the yield of $\text{O}_2(^1\Delta)$ is not affected by NO_2 injection because NO_2 does not appreciably quench $\text{O}_2(^1\Delta)$. The reduction in the densities of O with NO_2 injection implies that the quenching of I^* by O is reduced. This produces a reduction in the amount of $\text{O}_2(^1\Delta)$ used in pumping the I^* . Hence, downstream of the second nozzle, the yield of $\text{O}_2(^1\Delta)$ is

higher for larger NO_2 mole fractions. Results from *GlobalKIN* and *nonPDPSIM* are in general agreement except downstream of the I_2 injection point due to the artificially higher rates of reaction upon injection of I_2 .

Gain is shown in Fig. 4.16 for 2 cm downstream from the second nozzle as a function of NO mole fraction in the inlet flow and flow rate of NO_2 through the second nozzle. The flow conditions are 3 Torr and 40 W power deposition. Having NO in the inlet flow affects the production of $\text{O}_2(^1\Delta)$ as discussed above as well as managing the O atoms density. Injection of NO_2 downstream of the discharge largely only affects the density of O atoms (and gas temperature). As such, at low values of NO flow, injection of NO_2 is effective in managing the O atom density and larger flow rates tend to maximize gain by reducing quenching of I^* by O atoms. At large flow rates of NO, the management of O atoms is dominated by reactions with NO, and so the injection of NO_2 is less effective. Since there is a deleterious effect on $\text{O}_2(^1\Delta)$ production by having large flows of NO through the discharge, managing the O atom density with injection of NO_2 is likely the optimum strategy

4.6 Concluding Remarks

The consequences of NO in the inlet flow of a He/ O_2 plasma and its flowing afterglow, and NO_2 and I_2 injection on the post-discharge kinetics of the eCOIL were investigated using plug-flow and 2d models. The addition of NO to the inlet flow through the discharge produces a reduction in T_e and a modest increase in n_e resulting in the densities and yields of $\text{O}_2(^1\Delta)$ being generally lower with NO. Including NO in the flow reduces the density of O atoms both by a reduction in the electron impact dissociation of O_2 and by exothermic reactions of O with NO. This proves beneficial to improving optical gain by

reducing the quenching of I^* by O atoms. At higher power deposition, the dissociation of O_2 saturates the yield of $O_2(^1\Delta)$. By virtue of adding NO to the inlet flow, the reduction in T_e reduces the rate of dissociation of O_2 . Even though the yields of $O_2(^1\Delta)$ were generally lower, the optical gain was generally higher when the NO mole inlet mole fraction was between 1-3%.

The eCOIL system can operate in power limited and I_2 limited regimes. At low flow rates, I_2 is nearly totally dissociated and so the densities of I depend largely on the I_2 flow rate. Upon increasing the flow rate of I_2 , the system transitions to a power limited regime and higher powers are required to optimize gain. Small flows of NO_2 in the post-discharge region can be used to fine tune the gain. The addition of NO_2 rapidly consumes O atoms without significantly changing other parameters (other than T_g) and so increases the optical gain. The injection of NO_2 was most effective at low flow rates of NO. In general, management of the O atom density is critical to optimizing gain due to its rapid rate of quenching of I^* .

4.7 Figures

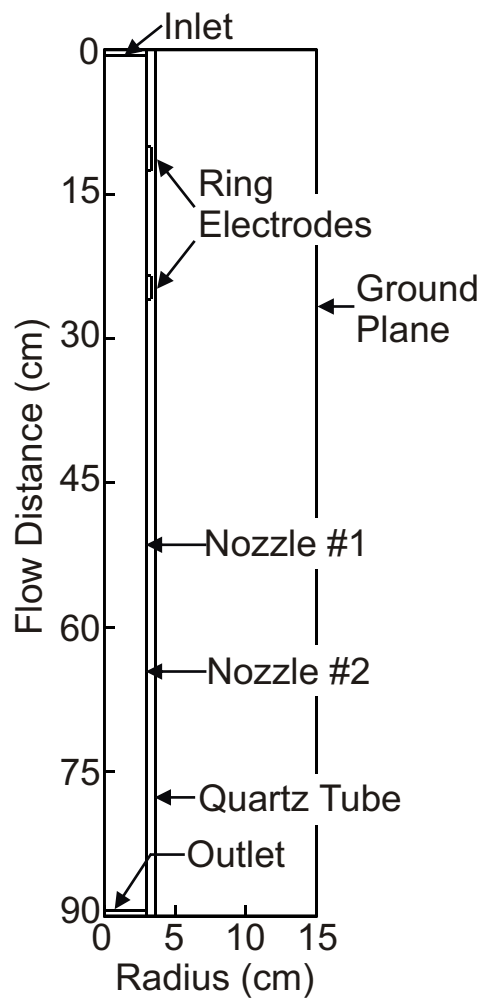


Fig. 4.1 Geometry of the reactor used.

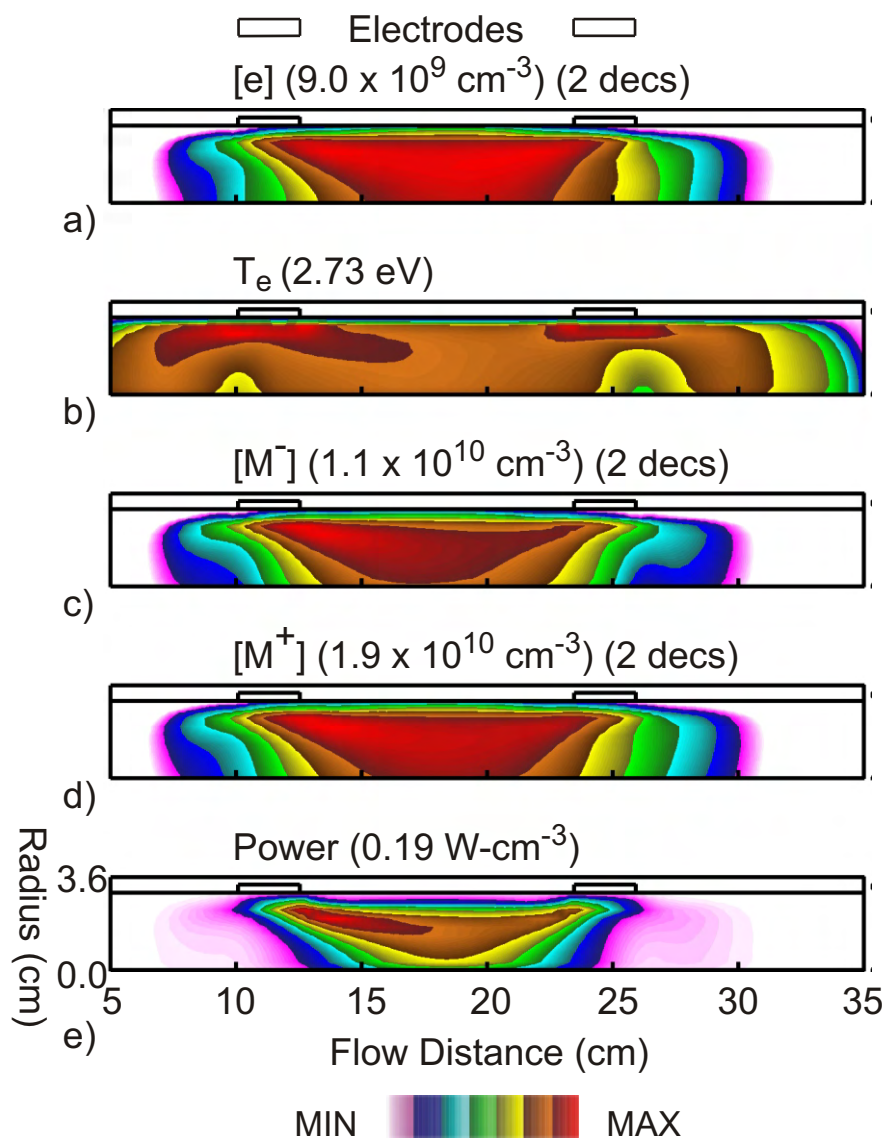


Fig. 4.2 Base case plasma characteristics from the 2d model for 3 Torr, 40 W, He/O₂/NO of 67/30/3 and a flow rate of 6 slpm. a) Electron density, b) electron temperature, c) sum of negative ion densities, d) sum of positive ion densities and e) power density.

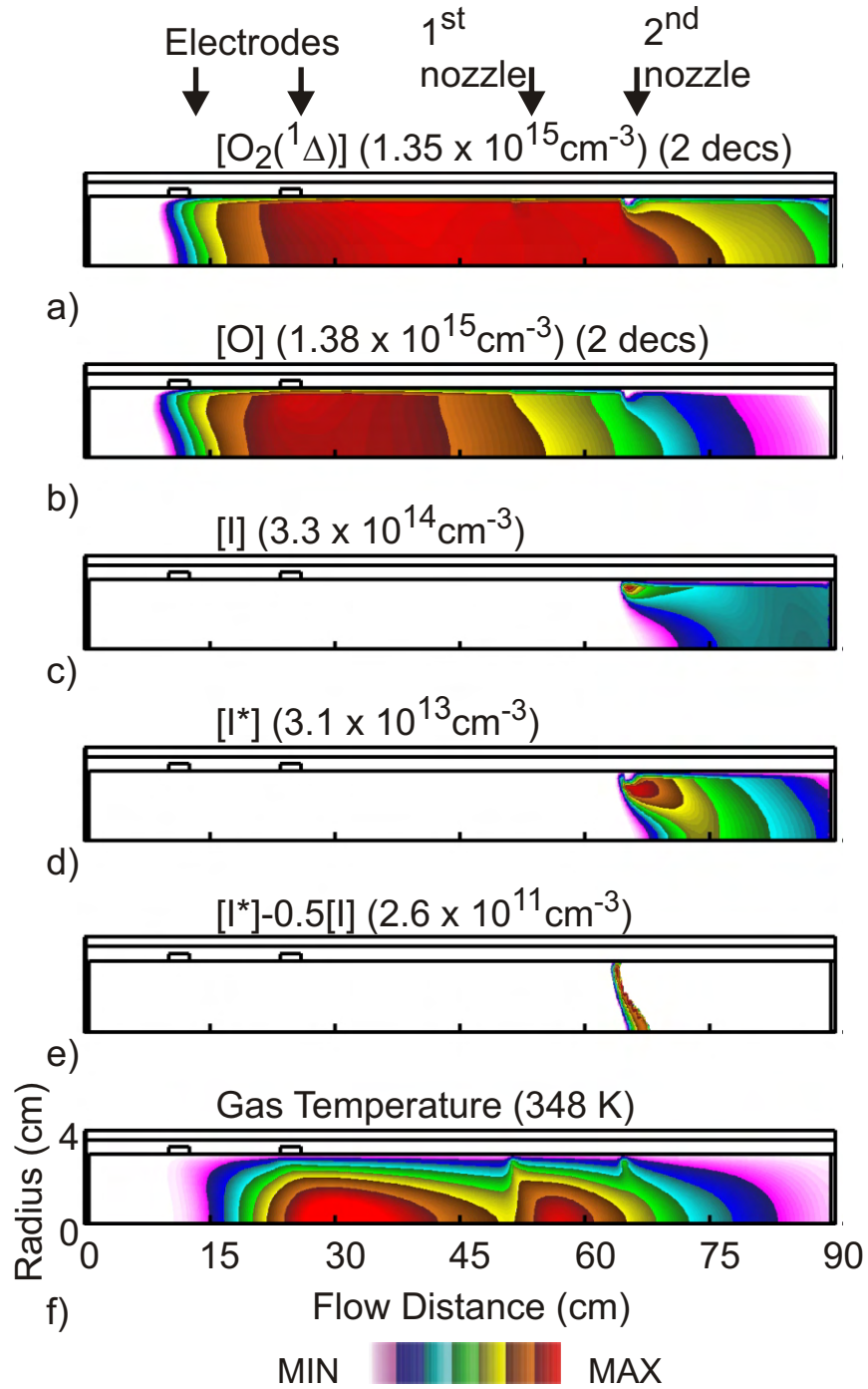


Fig. 4.3 Neutral species densities and T_g for the base case. 36 sccm of pure NO was injected through the first nozzle and 100 sccm of He/I₂ = 99/1 was injected through the 2nd nozzle. Densities of a) O₂(¹Δ), b) O, c) I, d) I*, e) inversion density ([I*]-0.5[I]), and f) gas temperature.

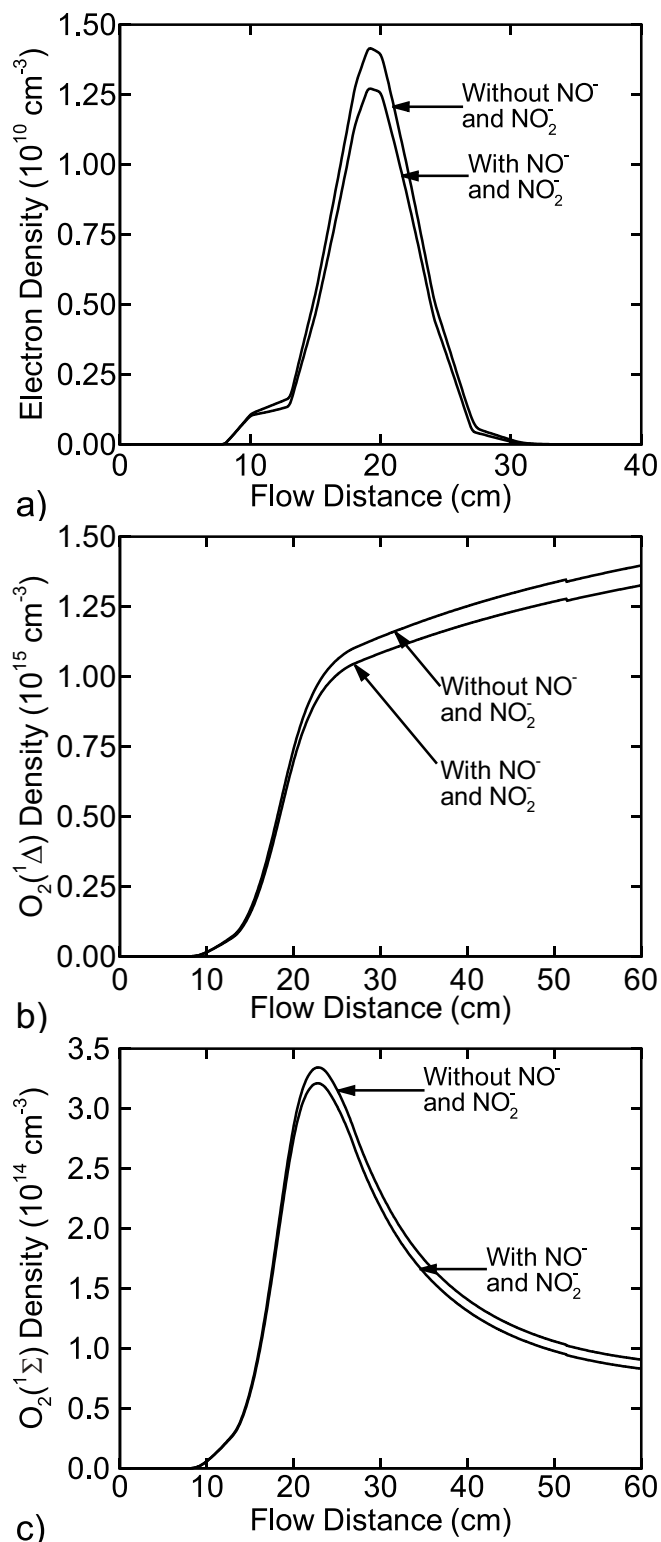


Fig. 4.4 Dependence of plasma characteristics on the inclusion of the NO^- and NO_2^- ions for 3 Torr, 40 W, He/ O_2 /NO = 60/30/10 and 6 slpm. Densities of a) electrons, b) $\text{O}_2(^1\Delta)$ and c) $\text{O}_2(^1\Sigma)$. The densities of O did not show any noticeable variation. These results are from the plug flow model.

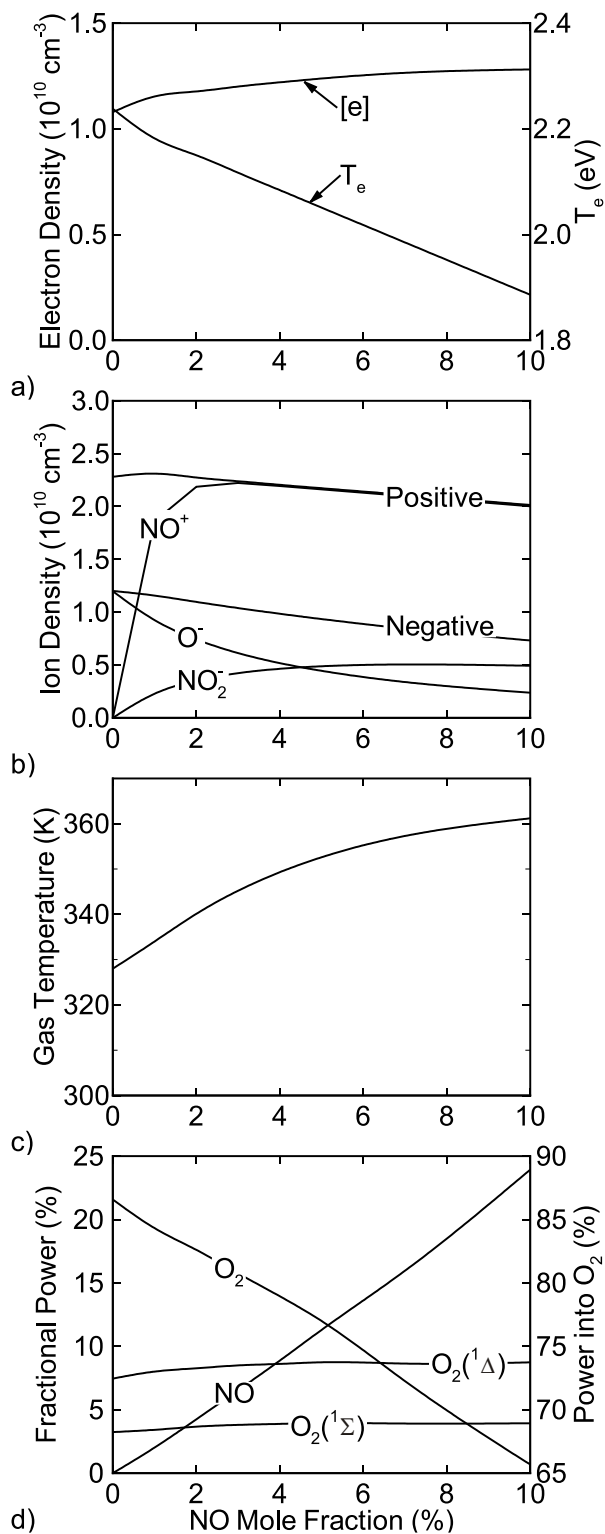


Fig. 4.5 Plasma and gas characteristics while varying the NO mole fraction for 3 Torr, 40 W and a 6 slpm flow of He/O₂/NO = 70-x/30/x. a) Maximum n_e , b) Maximum positive- and negative-ion densities, c) maximum T_g , and d) fractional power deposition into O₂ and NO, and in producing O₂(¹Δ) and O₂(¹Σ).

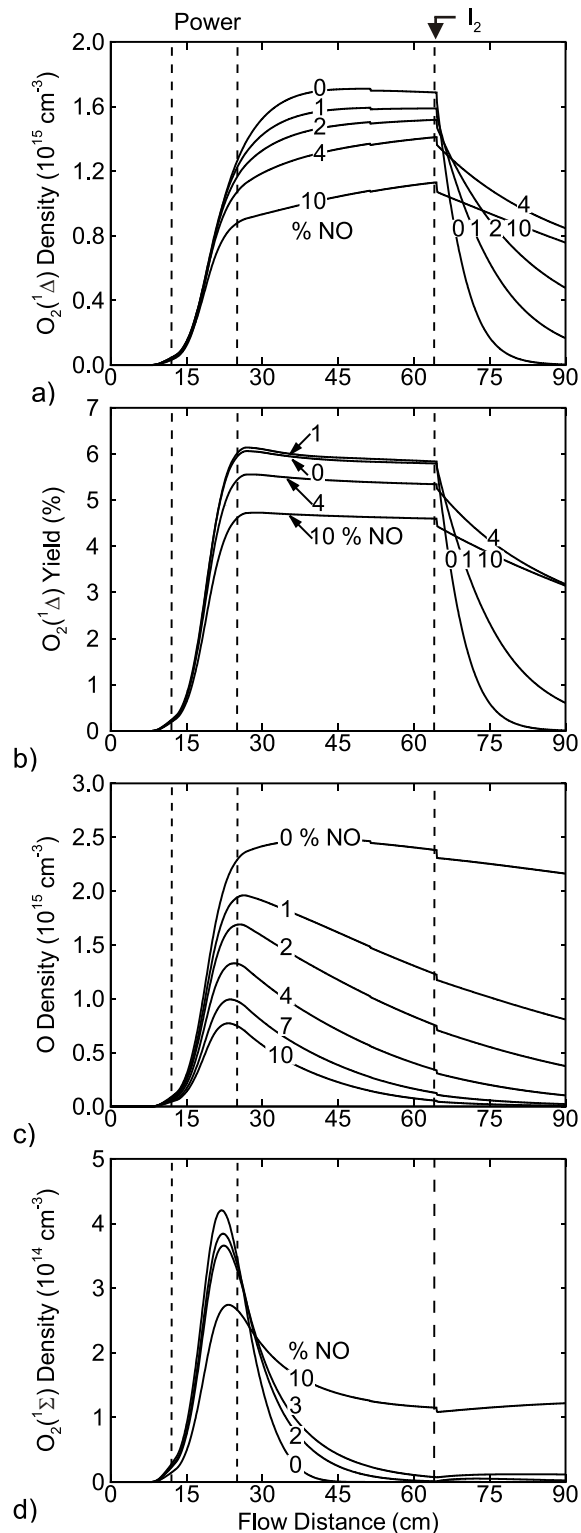


Fig. 4.6 Densities of oxygen species and yield of $O_2(^1\Delta)$ along the axis of the tube while varying NO mole fraction for 3 Torr and 40 W for a 6 slpm flow of He/ O_2 /NO of 70-x/30/x. 1 sccm of I_2 is injected through the second nozzle. a) $O_2(^1\Delta)$, b) yield of $O_2(^1\Delta)$, c) O, and d) $O_2(^1\Sigma)$. Results from the plug-flow.

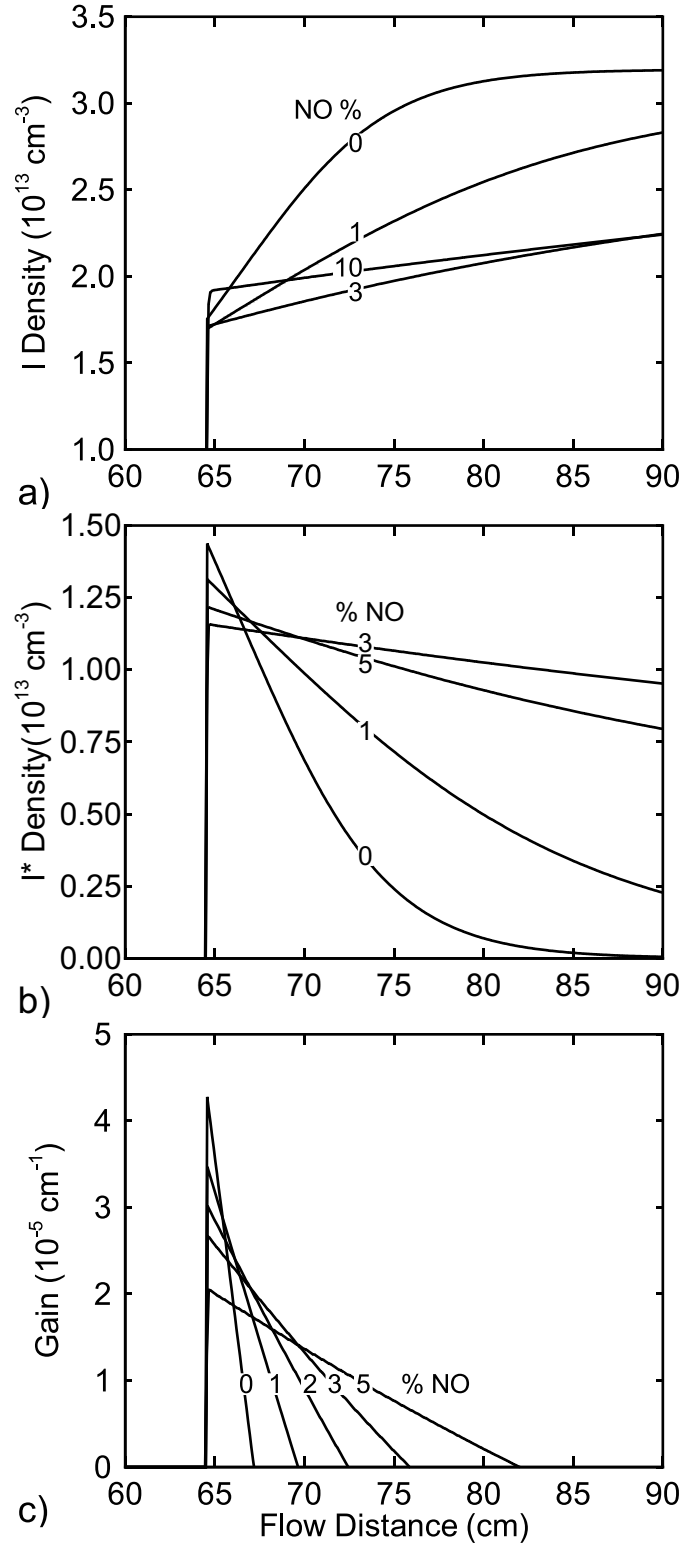


Fig. 4.7 Consequences of power deposition and NO mole fraction on iodine species and gain for 3 Torr, He/O₂/NO = 70-x/30/x and 6 slpm. Densities of a) I and b) I*, and c) optical gain. These results are from the plug flow model and the values are for 2 cm downstream of the second nozzle.

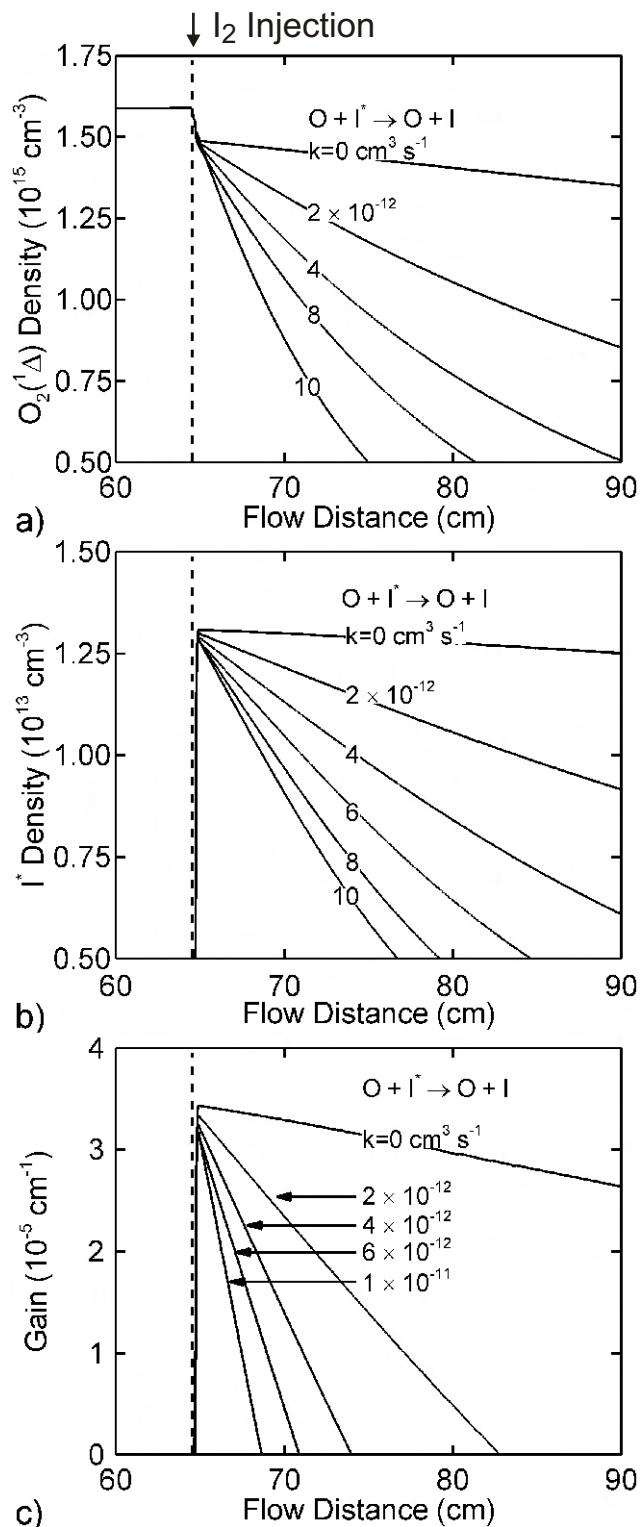


Fig. 4.8 Sensitivities of the value of the rate coefficient for the quenching reaction between O and I* on the post-discharge kinetics for 3 Torr, 40 W, He/O₂/NO=69/30/1, and 6 slpm. 1 sccm of I₂ is injected through the 2nd nozzle. Densities of a) O₂(¹Δ), b) I*, and c) optical gain. These results are from the plug flow model.

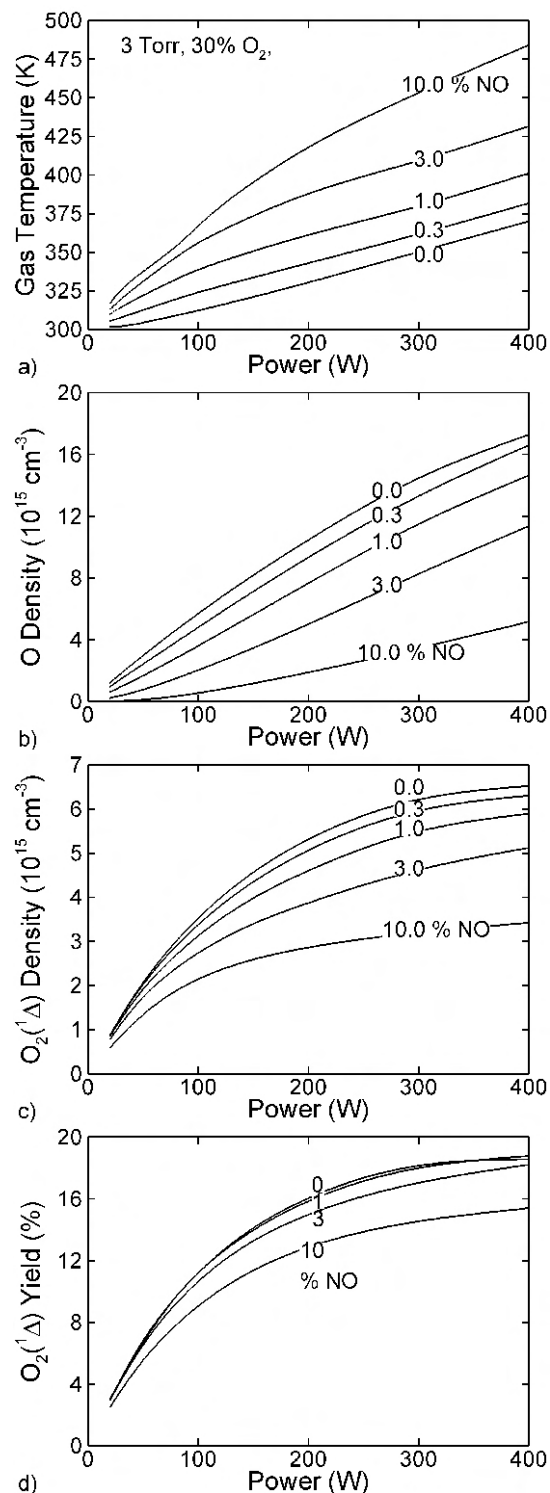


Fig. 4.9 Consequences of power deposition and NO mole fraction on the neutral gas properties for 3 Torr, He/O₂/NO = 70-x/30/x and 6 slpm. a) T_g , b) density of O, c) density of O₂(¹Δ) and d) yield of O₂(¹Δ). These results are from the plug flow model and the values are for 2 cm upstream of the second nozzle.

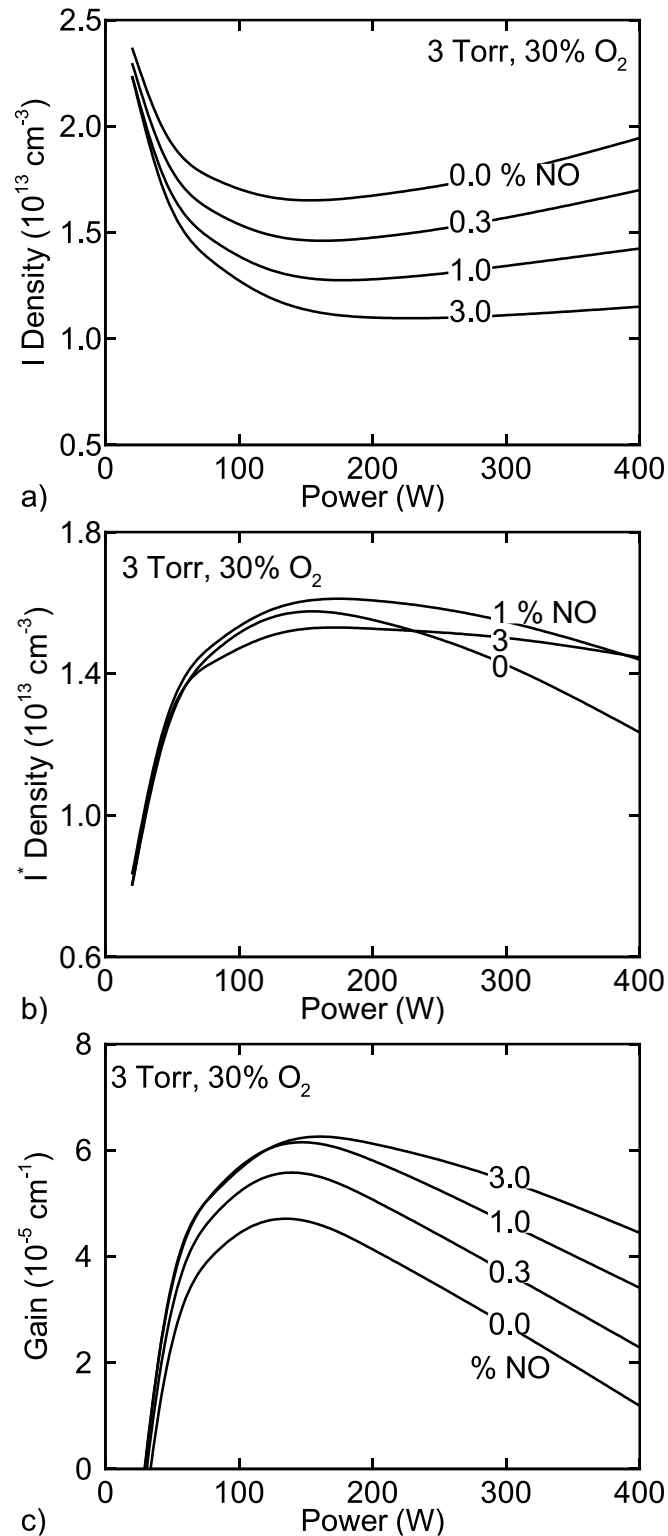


Fig. 4.10 Consequences of power deposition and NO mole fraction on iodine species and gain for 3 Torr, He/O₂/NO = 70-x/30/x and 6 slpm. Densities of a) I and b) I*, and c) optical gain. These results are from the plug flow model and the values are for 2 cm downstream of the second nozzle.

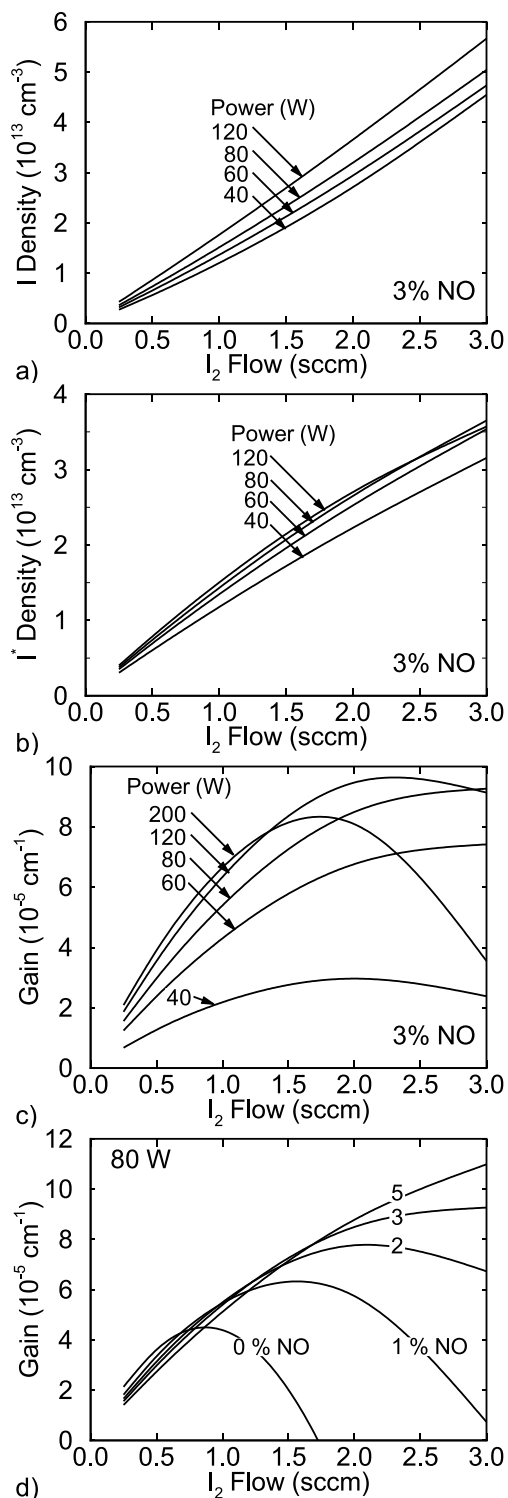


Fig. 4.11 Iodine species densities and gain while varying the I_2 flow rate through the 2nd nozzle. Densities of a) I and b) I^* , and c) optical gain for 3% NO in the inlet flow and d) gain for 80 W power deposition. These results are from the plug flow model and the values are for 2 cm downstream of the 2nd nozzle.

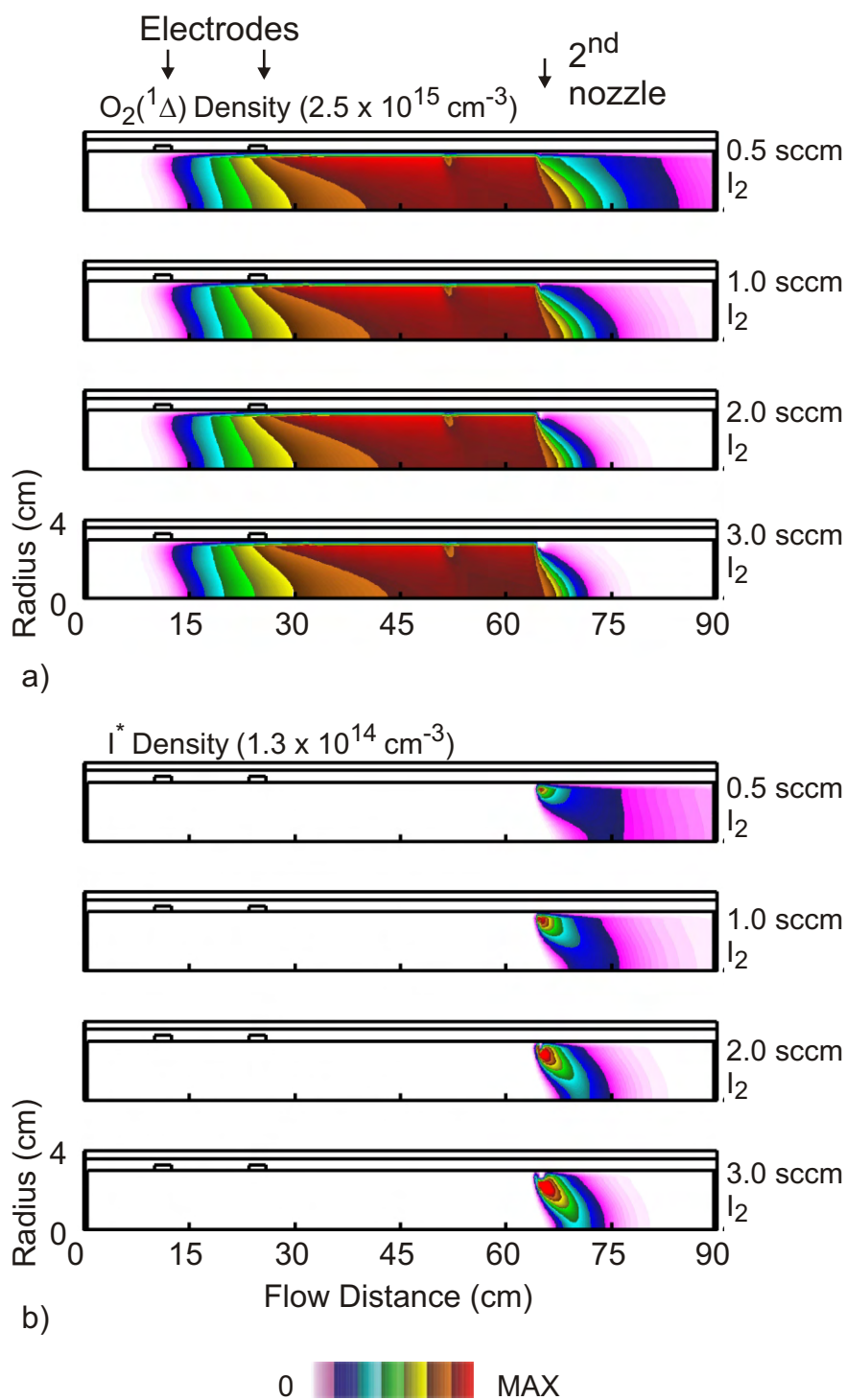


Fig. 4.12 Excited state densities while varying the I_2 flow rate through the 2nd nozzle. a) $O_2(^1\Delta)$ and b) I^* . These results, obtained with *nonPDPSIM*, are for 3 Torr, 80 W power deposition, and 6 slpm flow of $He/O_2/NO = 68/30/2$.

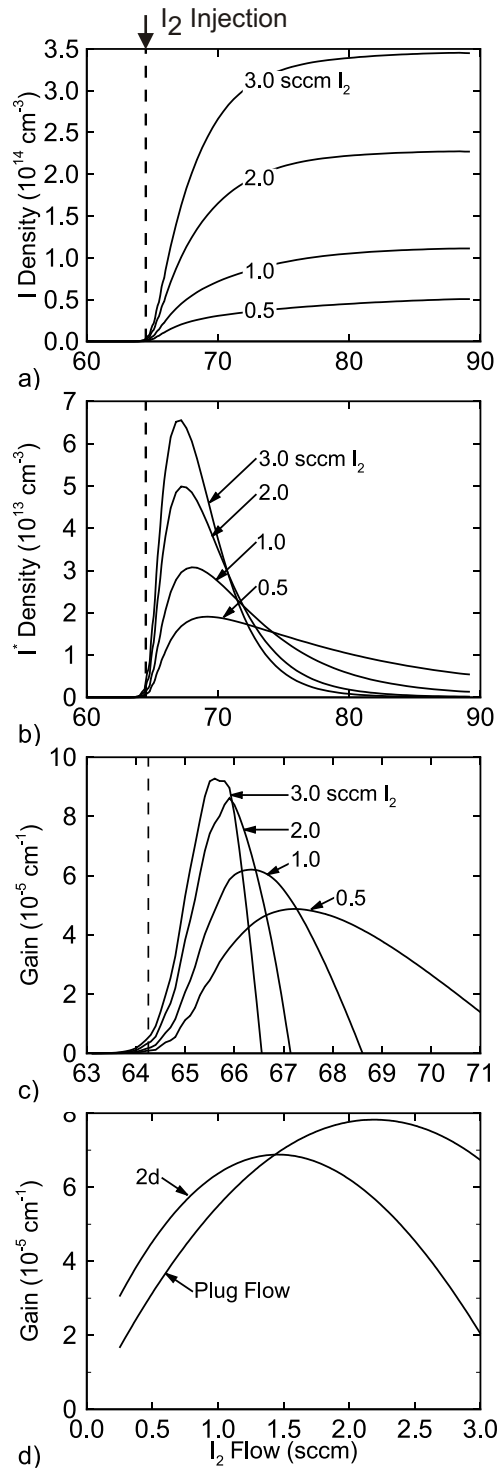


Fig. 4.13 Iodine species densities and gain at a radius of 1.5 cm as a function of the flow rate of I_2 through the 2nd nozzle. Densities of a) I and b) I^* , c) gain and d) comparison of the plug flow and 2d models for gain 2 cm downstream of the 2nd nozzle. Results from the 2d model for 3 Torr, 80 W power and 6 slpm flow of He/ O_2 /NO = 68/30/2.

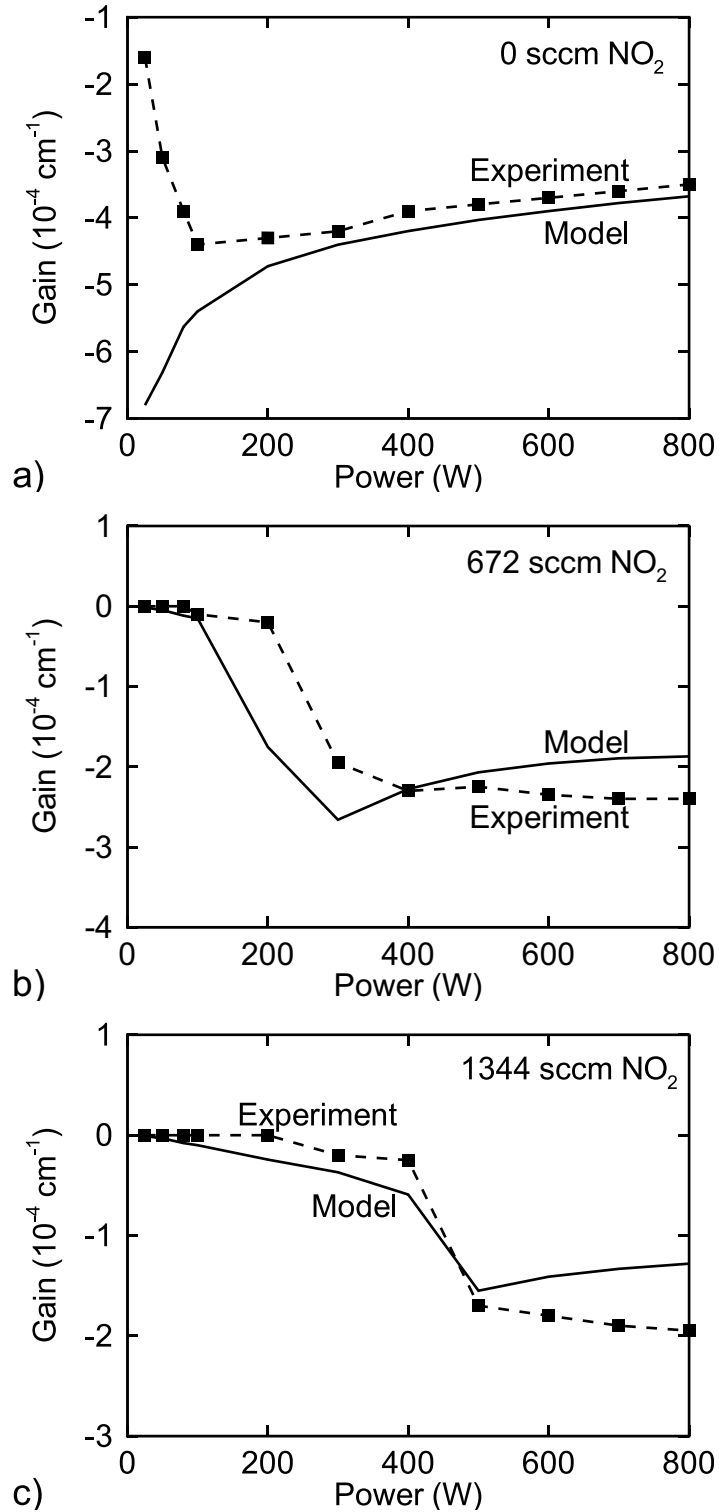


Fig. 4.14 Gain in a subsonic flow for 10 Torr, 26.9 slpm of $\text{He}/\text{O}_2 = 80/20$, 25–800 W, with 10.8 sccm of I_2 injected through the second nozzle. a) 0 NO_2 , b) 672 sccm NO_2 , and c) 1344 sccm NO_2 through the 1st nozzle. Experimental values are from [14].

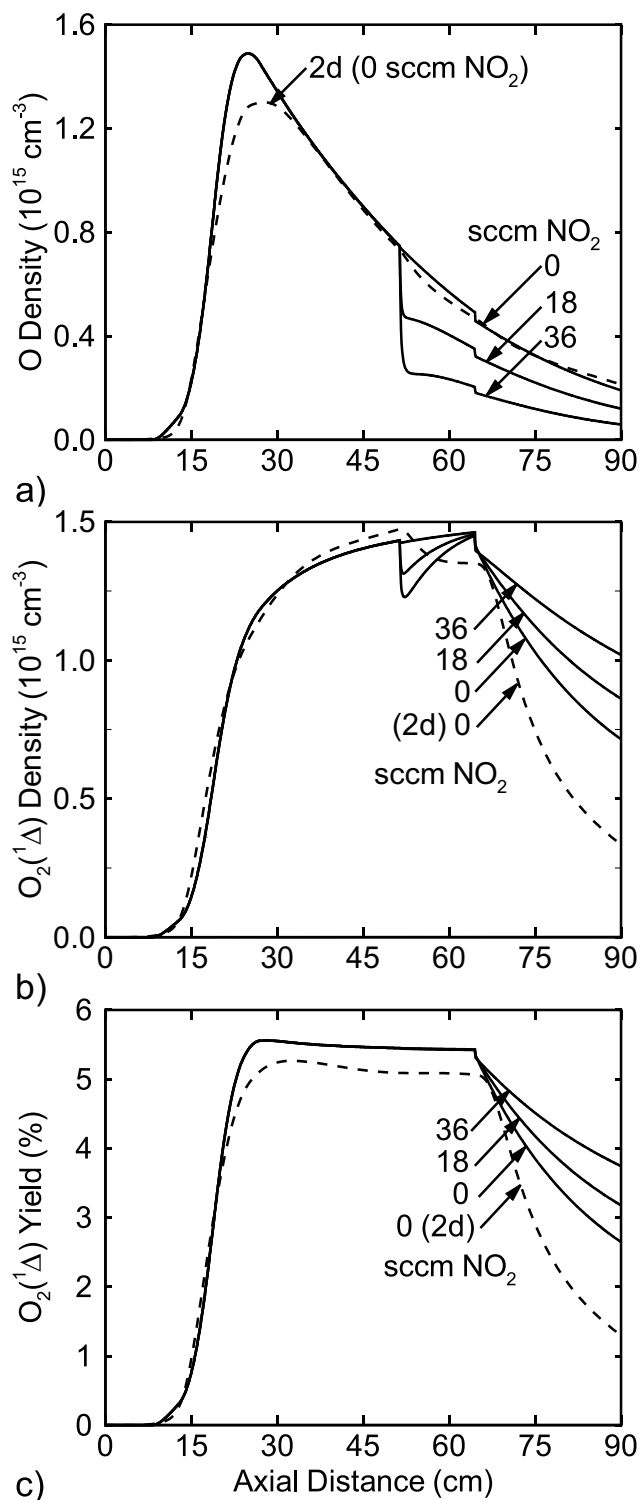


Fig. 4.15 Consequences of NO_2 injection through the 1st nozzle for 3 Torr, 40 W, $\text{He}/\text{O}_2/\text{NO} = 67/30/3$ and 6 slpm. 36 sccm of He/NO_2 is injected through the 1st nozzle. Densities of a) O and b) $\text{O}_2(^1\Delta)$, and c) yield of $\text{O}_2(^1\Delta)$. These results are from the plug-flow model. Values from the 2d *nonPDPSIM* are shown without NO_2 .

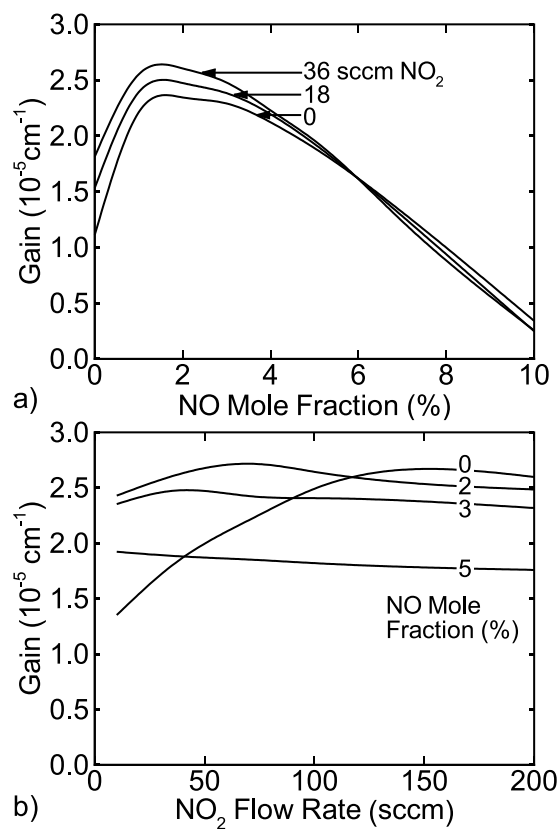


Fig. 4.16 Gain when including NO in the inlet flow and injecting NO_2 through the 1st nozzle for 3 Torr, 40 W, $\text{He}/\text{O}_2/\text{NO} = 70-x/30/x$ and 6 slpm. 100 sccm of 99/1 He/I_2 is injected through the 2nd nozzle. a) Gain as a function of NO mole fraction and b) gain as a function of NO_2 flow rate. These results are from the plug flow model.

4.8 References

1. J. T. Verdeyen et al, Appl. Phys. Lett. **89**, 101115 (2006).
2. O. V. Braginsky et al, J. Phys. D: Appl. Phys. **39**, 5183 (2006).
3. A. Hicks, Yu. G. Utkin, W. R. Lempert, J. W. Rich and I. V. Adamovich, Appl. Phys. Lett. **89**, 241131 (2006).
4. H. Fujii, S. Yoshida, M. Iizuka, and T. Atsuta, J. Appl. Phys. **67**, 3948 (1990).
5. A. Hill, *The next generation of controlled avalanche-discharge gas lasers*, International Conference on Lasers, Albuquerque, NM (2000).
6. A. Hicks et al, J. Phys. D: Appl. Phys. **38**, 3812 (2005).
7. A. N. Vasiljeva et al, J. Phys. D: Appl. Phys. **37**, 2455 (2004).
8. A. A. Ionin et al, J. Phys. D: Appl. Phys. **36**, 982 (2003).
9. A. D. Palla, D. L. Carroll, J. T. Verdeyen and W. C. Solomon, "Effects of mixing on post-discharge modeling of ElectricOIL experiments", Proc. SPIE. **6101**, 610125 (2006).
10. D. S. Stafford and M. J. Kushner, J. Appl. Phys. **98**, 073303 (2005).
11. T. J. Cook and T. A. Miller, Chem. Phys. Lett. **25**, 396 (1974).
12. R. Atkinson et al, J. Phys. Chem. Ref. Data **29**, 167 (2000).
13. J. Hon *et al*, *A Heuristic Method for Evaluating COIL Performance*, AIAA Paper 94-2422 (1994).
14. D. L. Carroll et al, IEEE J. Quantum Electron. **41**, 213 (2005).
15. M. V. Zagidullin, V. D. Nikolaev, M. I. Svistun, N. I. Khvatov and G. D. Hager, Appl. Phys. A: Materials and Processing **81**, 311 (2005).
16. D. Husain, N. K. H. Slater and J. R. Weisenfeld, Chem. Phys. Lett. **51**, 201 (1977).
17. T. M. Muruganandam et al, AIAA J. **40**, 1388 (2002).

CHAPTER 5. PRODUCTION OF H₂ IN Ar/NH₃ MICRODISCHARGES

5.1 Introduction

Fuel cells based on H₂ are gaining importance as alternative energy sources due to the increasing cost of non-renewable sources of energy. They also address environmental concerns such as global warming because the effluent of their power production is water vapor. Advances in fuel cell technology have led to efficient (>50%) conversion of thermal (H₂ + 1/2 O₂ → H₂O; ΔH = -2.5 eV) to electrical energy.[1]

Storage of H₂ for use in fuel cells is problematic as it liquefies only under extreme temperatures and pressure, and the highly combustible nature of H₂ requires caution. Due to the difficulty of H₂ storage, development of real time H₂ generators would be advantageous for portable fuel cells. Thus, it is worthy to investigate methods of in-situ production of molecular hydrogen for portable applications. In this study, we discuss results from computational investigations of the use of Ar/NH₃ mixtures for production of H₂ in micro-discharge devices. Although NH₃ is commercially produced by reactions between N₂ and H₂, it is also a by-product of natural biological processes and refineries. It has high H content (17% by mass), is easily liquefied and the end products are stable (N₂, H₂, some N_xH_y). Feedstock gases such as methane have higher H₂ content but they need to be partially oxidized to produce H₂ and the by-products include greenhouse gases such as CO₂.

NH₃ plasmas are used in various applications such as surface treatment to improve wettability and biocompatibility of polymer surfaces [2], and surface nitridation for semiconductor applications [3]. Van den Oever et al [4,5] investigated the production of NH and NH₂ in expanding Ar/NH₃ plasmas for possible use in ultrahigh-rate deposition of Si₃N₄ films. Recent interest in NH₃ plasmas include high pressure (0.1 – 1 atm.) dielectric barrier

discharges (DBDs), and micro-hollow cathode discharges for conversion of NH_3 to H_2 .

Experiments by Qiu et al [6] demonstrated a 20% conversion of H atoms in NH_3 to H_2 in atmospheric pressure microdischarges. Pulsing of the discharge improved the efficiency of conversion, as did using an array of microdischarges.

Hsu and Graves [7] investigated the decomposition of ammonia in microdischarges at 100s Torr at power levels of 1-5 W. They demonstrated a strong dependence of the conversion rate on the residence time (or flow rates) as a means to vary the eV/ NH_3 -molecule. They also showed that thermal as well as electron impact dissociation could be important in the conversion process. By fitting their data to a plug-flow model, they predicted the gas temperature to be as high as 2000 K.

Fateev et al [8] investigated Ar/ NH_3 plasma chemistry in a dielectric barrier discharge and modeled the chemical kinetics. They observed that the discharge produced stable species such as N_2 , H_2 , and N_2H_4 . At power densities of 1.2 W/cm^3 , they found that the leading source of NH_3 decomposition (to NH and NH_2) was collisions of NH_3 with Ar metastables.

Miller and Baird [9] studied the decomposition of NH_3 in radio frequency plasmas at pressures of few to 40 Torr. They found that the conversion of NH_3 to H_2 to be between 4.2 – 30 molecules/100 eV of deposited energy in inductively coupled plasmas, a value higher than that observed in capacitively coupled plasmas. At pressures above 20 Torr, they were unable to completely dissociate the NH_3 .

In this study, the real time production of H_2 using microdischarge devices is discussed with results from a computational investigation. Ar/ NH_3 mixtures were studied using plug-flow (*GlobalKIN*) and 2d (*nonPDPSIM*) models. The plug-flow model was useful to investigate scaling laws over a large parameter space. The 2-d model was used to address

flow issues, the non-equilibrium nature of the discharge near the cathode, and the spatial variation of the plasma characteristics such as power density, electron temperature, and plasma potential. We will focus on ways to produce H₂ with efficient utilization of the feedstock gas NH₃, and to maximize the production for a given power deposition into the plasma.

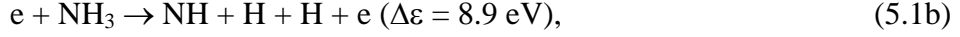
Typically, dissociation of NH₃ by electron-impact and thermal processes produce H atoms which then recombine to form H₂. We found that for sandwich type microdischarges with a diameter of 300 μm, the dissociation of NH₃ is largely (> 90%) and the rest is due to thermal processes. Efficiency of conversion of NH₃ to H₂ is dependent on residence time of the gas in the discharge, mole fraction of NH₃, and geometry. These properties typically determine the eV/molecule deposited into NH₃ molecules.

5.2 Reaction Mechanism

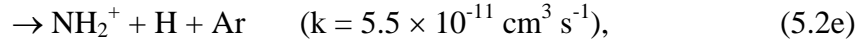
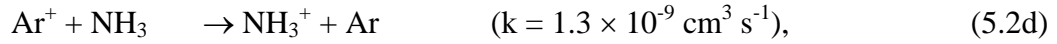
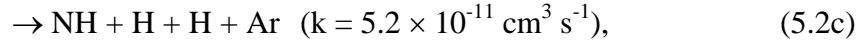
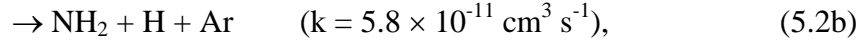
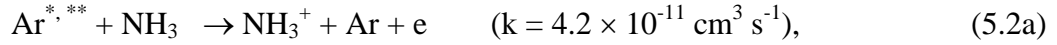
The reaction mechanism for the plasma chemistry of Ar/NH₃ mixture used in this study is listed in Appendix C. In this section we discuss the Ar/NH₃ chemistry with an emphasis on the H and H₂ production mechanisms. The species included in the mechanism are: e, Ar, Ar(4s) (referred to as Ar^{*}), Ar(4p) (referred to as Ar^{**}), Ar₂^{*}, Ar⁺, Ar₂⁺, ArH⁺, NH₃, NH₃⁺, NH₄⁺, NH₃(v), NH₂, NH₂⁺, NH₂⁻, NH, NH⁺, N, N⁺, N₂, H, H⁺, H⁻, H₂, H₂⁺, H₃⁺, N₂H₂, N₂H₃, and N₂H₄.

The primary source of H production in the discharge is by electron-impact dissociation of NH₃,





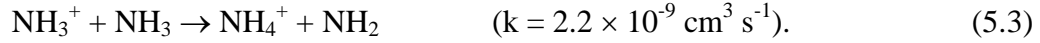
where $\Delta\varepsilon$ is the threshold energy. Ar^* , Ar^{**} , and Ar^+ , with energies of 11.6, 13.1, and 16 eV respectively, have enough energy to charge-exchange or Penning ionize, and so dissociate NH_3 ,



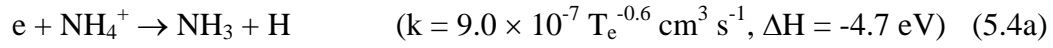
where k is the rate coefficient at room temperature unless noted otherwise. The branching ratio of Eq. (5.2(d)) to form ArH^+ and NH_2 is small ($< 3\%$) and so the presence of ArH^+ is not a major factor in the production of H_2 . This is because dissociative recombination and other charge exchange reactions can quickly consume the ArH^+ , releasing the H back into the discharge. The results discussed here from the plug-flow model include the ArH^+ in the reaction mechanism. Test cases were run using the plug-flow model with and without ArH^+ in the mechanism. The results yielded H_2 densities that were within 0.3% of each other. Based on the insensitivity of the reaction mechanism to the presence of ArH^+ and the need to speed the more extensive 2-d calculations, ArH^+ was excluded from the 2d parameterizations.

Charge exchange between Ar^+ and NH , NH_2 , and NH_3 produces the respective NH_x^+

ions. Further charge exchange between various NH_x^+ ions leads to formation of NH_4^+ which has the smallest ionization potential among all the ions in the mechanism,

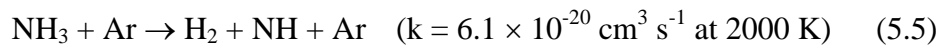


As such, the density of NH_4^+ tends to be large if NH_x species are not significantly depleted. Dissociative recombination of NH_x^+ produces NH_{x-1} and H as the dominant channels. These reactions also produce thermal energy by Frank-Condon heating, whereby potential energy in the dissociative electronic states is converted to translational energy and contributes to the change in enthalpy, ΔH , of the gas mixture,



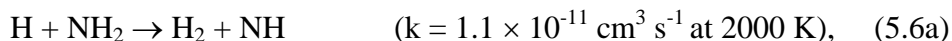
where the electron temperature T_e is in eV.

The gas temperature can increase by many 100s K to reach over 1000 K [7] while flowing through the discharge and so thermal dissociation processes can also contribute significantly to H production. For example, although the thermal dissociation of NH_3 by argon,

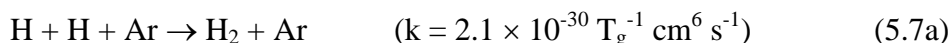


has a small rate coefficient, the total rate of the reaction can be large as the pressure

increases. As the temperature increases, other endothermic reactions also begin to become important. One such process is the abstraction of H from NH₂ and NH₃ by H atoms, directly producing H₂,



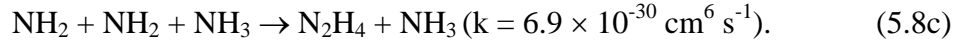
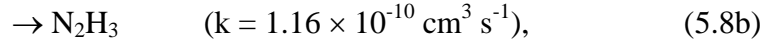
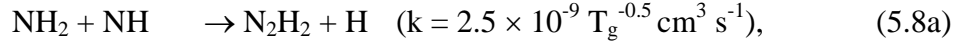
In the afterglow and downstream of the discharge region, neutral chemistry is most important. At this time the bulk of the dissociated NH₃ is in the form of N, H and NH₂. At pressures of ≥ 100 Torr, and as the gas cools, 3-body reactions begin to dominate the mechanism. A large fraction of H₂ is formed downstream by 3-body association reactions. For example, the reactions:



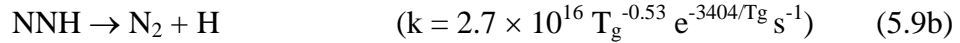
produce H₂ within a few ms at pressures ≥ 100 Torr. The fractional contribution from these (and similar) processes depends on the mole fractions of the third body and the fractional dissociation of the NH₃.

Loss of H by 3-body re-association with NH₂ to form NH₃ can be important as the rate coefficient for this reaction is large, particularly with NH₃ as the third body ($k = 6.0 \times 10^{-30} \text{ cm}^6 \text{ s}^{-1}$). The loss of H by this mechanism is rate limited by the density of NH₂ which is typically not large. Formation of N₂H_x (x=2,3,4) by 2 and 3-body reactions tend to deplete

NH₂. The primary pathways for producing N₂H_x (x=2,3,4) are,



Although NNH is potentially an important intermediate species, its density is typically low due to its high reactivity. The density of NNH was not explicitly included in the mechanism as the rate coefficient for decomposition to N₂ and H is much higher than for production from N₂H₂,



To simplify the reaction mechanism and to reduce the mathematical stiffness of the mechanism, the above reactions were combined to,



with the rate coefficient being that of the slower reaction, Eq. (5.9(a)).

The surface-to-volume ratio in microdischarges is high due to the small dimensions of the reactor, and so the interaction of radicals with surfaces is potentially important. To this effect a simple surface reaction mechanism was included. Ions and excited states striking the

surfaces were returned to the plasma with unit probability after being neutralized or quenched by the walls. The reaction of H on the walls to form H₂ can be important especially in low pressure discharges where 3-body recombination rates are small.[10] Jackson and Pearson[11] investigated the recombination of atomic hydrogen to yield H₂ on metallic surfaces such as Cu and W. They found reaction probabilities to be between 0.3 – 0.6 for Cu and ≈0.9 for W at incident energies < 1.5 eV. In this work, 10% (probability = 0.1) of H striking the surfaces was returned to the plasma as H₂ as a worst case scenario. The probability for H recombination on surfaces was varied in the model to determine the sensitivity of the results to our choice for this parameter. Increasing the probability for recombination from 0.1 to 0.5 increased the exit H₂ densities by not more than 7%.

5.3. Scaling of Microdischarge Production of H₂: Plug Flow Modeling

To characterize the production of H₂ in microdischarges, the following parameters are used;

$$\eta = \frac{2}{3} \frac{[H_2]v_e A_e}{[NH_3]v_i A_i}, \quad (5.11a)$$

$$\gamma(H_2) = \frac{P}{[H_2]A_e v_e}, \quad (5.11b)$$

$$\gamma(NH_3) = \frac{P}{[NH_3]A_i v_i}, \quad (5.11c)$$

where [H₂], and [NH₃] are the densities of H₂, and NH₃ at the exit and inlet respectively; and v_i, and v_e are the inlet and exit speeds. A_e and A_i are the cross sectional areas at the exit and

inlet of the reactor, and P is the power deposition. η , the conversion efficiency, is the fraction of H entering the discharge in the form of NH_3 that exits in the form of H_2 . $\gamma(\text{H}_2)$, the H_2 energy efficiency, is the energy required to produce an H_2 molecule at the exit. $\gamma(\text{NH}_3)$, the NH_3 energy deposition, is the energy deposited per inlet NH_3 molecule.

Fractional power dissipation by electron impact as a function of T_e in pure NH_3 discharges based on rate coefficients produced from solutions of Boltzmann's equation is shown in Fig 5.2(a). At low T_e , most of the power is dissipated in vibrational excitation of NH_3 ($\Delta\varepsilon = 0.11$ eV). Power loss to momentum transfer is typically small ($< 1\%$) at low temperatures (< 2 eV), and is negligible at higher T_e . Power dissipated in attachment to form H is also small (at most few percent). Fractional power dissipation into dissociative excitation forming NH_2 and H has a peak value of 0.7 at $T_e = 2.2$ eV. Production of NH and 2H has a peak fractional dissipation of 0.32 at $T_e = 8.5$ eV. Electron impact ionization to form NH_3^+ and NH_2^+ with thresholds of 10.2, and 16.0 eV respectively, account for 10-20% of power dissipation for $T_e > 6$ eV. This is not unexpected. Based on solutions of Boltzmann's equation for Electron Energy Distributions (EED) in pure NH_3 , for $T_e = 3.6$ eV, 10% of electrons have energies ≥ 10.2 eV, and for $T_e = 5$ eV, 25% of electrons have energies above 10.2 eV. Thus, for moderate T_e (2-3 eV) the dominant form of power dissipation is by neutral dissociation of NH_3 , whereas at higher T_e , ionization reactions gain prominence.

The effect of dilution of NH_3 by Ar on the fractional power dissipation by electron impact processes is shown in Fig. 5.2(b) for $\text{Ar}/\text{NH}_3 = 90/10$. For $T_e > 2.5 - 3$ eV, most of the power is dissipated in exciting and ionizing Ar. The fractional dissipation by dissociation of NH_3 into $\text{NH}_2 + \text{H}$ is half that of pure NH_3 for $T_e < 2$ eV, and this reaction is the dominant

source of H production for this mixture. Excitation and ionization of Ar are not total losses with respect to H production as Penning and charge exchange reactions can recoup H atoms. The net energy efficiency of those processes is, however, smaller.

The rates of production of H as a function of T_e for Ar/NH₃ mixtures at 100 Torr are shown in Fig. 5.2(c). This rate is $[\text{NH}_3] \sum_i k_i n_i$ where k_i is the rate coefficient for the i^{th} reaction and n_i is the number of H atoms produced. This value can be interpreted as the rate of production of H atoms per electron from a distribution having temperature T_e . As the NH₃ mole fraction decreases from 1 to 0.1, the optimum T_e for H atom production decreases from 3 to 1.6 eV, and the peak production rates of H decrease from $9.7 \times 10^{17} \text{ s}^{-1}$ to $5.8 \times 10^{17} \text{ s}^{-1}$. These estimates ignore the production of H by dissociative recombination of NH₃⁺ and NH₂⁺, which is not terribly important since production of H is generally dominated by neutral dissociation at low T_e . The presence of Ar shifts the optimum T_e for H production not only to a lower value but also into a narrower range of T_e due to the cut-off of the tail of the EED resulting from electronic excitation of Ar (11.6 eV). This effect could be mitigated by electron-electron collisions which thermalizes the EED towards a Maxwellian at high fractional ionizations. These results do not necessarily imply that H production must decrease due to increasing dilution with Ar. This is because the electron density could increase (due to increase in ionizing reactions) at a higher rate than the reduction in NH₃ density. The results do, however, indicate that as the Ar mole fraction is increased, T_e should be lower to preferentially dissociate NH₃ rather than excite Ar. They also indicate that the optimum operating conditions lie in a narrower range of T_e and so operation of a device may need to be more carefully controlled.

The simplified geometry used for the plug-flow modeling is shown in Fig. 5.1(b).

The flow enters into a cylindrical tube 300 μm in diameter and 1 cm long. Power deposition is specified to occur over a 0.4 mm length (the discharge region). Using the plug-flow model, the electron density (n_e) and T_e are shown in Fig. 5.3 as a function of NH_3 fraction for a pressure of 100 Torr, inlet flow speed of $10 \text{ m}\cdot\text{s}^{-1}$ (corresponding to 5.6 sccm) and a power density $2.5 \text{ kW}\cdot\text{cm}^{-3}$ (in the discharge region). The total power deposition is 0.1 W. Increasing the NH_3 mole fraction increases the power dissipation per electron by dissociative excitation (rather than ionization) and so, for fixed power deposition, the electron density decreases. From 1% to 20% NH_3 , the electron density decrease by a factor of 20. (The reduction of electron density by dissociative attachment is small.) Note that n_e increases in traversing the discharge, a result of depletion of NH_3 and decrease in gas density due to gas heating. T_e did not show a marked difference in the range of NH_3 mole fractions considered. The increase in NH_3 mole fractions increases the rate of inelastic electron impact reactions having lower threshold energies and so lowers T_e . This fortuitously lowers T_e from an above optimum value ($> 3 \text{ eV}$) into a regime where H production is larger.

The densities of H and H_2 are shown in Fig. 5.4 along the axis of the discharge for different NH_3 fractions between 1 and 20% with a flow speed of $10 \text{ m}\cdot\text{s}^{-1}$ (5.6 sccm). The density of H increases at the leading edge of the discharge as electron impact dissociation of NH_3 begins. At high NH_3 fractions, H densities peak at the edge of the discharge ($2\text{-}3 \times 10^{16} \text{ cm}^{-3}$) before decreasing due to re-association. At NH_3 mole fractions exceeding 10%, there is a rapid decrease in H atom density beginning immediately at the edge of the discharge region. This is due to the more rapid rate of recombination with NH_2 to form NH_3 , and with H to form H_2 with NH_3 as the third body. (Recall that the 3-body rate coefficient for re-association of H is larger with NH_3 as the third body compared to Ar.) With low mole

fractions of NH_3 ($< 5\text{-}6\%$), the H atom density continues to increase downstream of the discharge (to $5\text{-}6 \times 10^{16} \text{ cm}^{-3}$). This is in large part due to the cooling of the gas which increases the density of H atoms and the fact that with the low mole fractions of NH_3 , H is not rapidly consumed by the 3-body processes (e.g., recombination with NH_2 and NH_3) that would otherwise decrease its density.

H_2 production, shown in Fig. 5.4(b) increases with increasing NH_3 mole fraction but saturates at densities of $5\text{-}6 \times 10^{16} \text{ cm}^{-3}$ with NH_3 mole fractions of $\geq 10\%$. This trend results from at least two factors. The first is that there is a decrease in n_e as the fraction of NH_3 increases (as shown in Fig. 5.3(a)). This decrease in n_e offsets the increase in rate of production of H atoms per electron obtained when increasing the NH_3 mole fraction (as shown in Fig. 5.2(c)). The second factor is based on energy utilization. For a fixed power deposition, as the NH_3 mole fraction increases, the fractional energy deposition into NH_3 , β , increases, as shown in Fig. 5.4(c). β is large for low T_e ($< 2 \text{ eV}$) for all NH_3 mole fractions above 10% but this energy is expended in pathways such as vibrational excitation, which do not produce H atoms. As T_e increases, the fraction of energy deposition is expended in dissociative pathways increases, but so does the energy deposition into argon. When T_e is large enough ($> 4\text{-}5 \text{ eV}$) that inelastic electronic excitation and ionization of both Ar and NH_3 are important, β increases directly with the NH_3 mole fraction. In the intermediate regime and for the range of T_e in the main part of the discharge (2.5-3 eV), the proportion of power deposition into NH_3 and its distribution into dissociative modes are sensitive functions of the NH_3 mole fraction.

The density and flux of H_2 at the exit of the flow tube and η , the efficiency of H conversion, for various flow speeds (sccm at the inlet) as a function of NH_3 mole fraction are

shown in Fig. 5.5. (Note that flow speed of $1 \text{ m}\cdot\text{s}^{-1}$ corresponds to $\approx 0.56 \text{ sccm}$.) The H_2 density, the efficiency of conversion of NH_3 to H_2 , η , and the eV per H_2 molecule produced, $\gamma(\text{H}_2)$, are also shown as a function of eV per inlet NH_3 molecule, $\gamma(\text{NH}_3)$, in Fig. 5.6. The pressure was 100 Torr and the power in the discharge region was $2.5 \text{ kW}\cdot\text{cm}^{-3}$ (total power 0.1 W).

At flow speeds of $2.5 - 40 \text{ m}\cdot\text{s}^{-1}$ ($1.4 - 22.4 \text{ sccm}$) the time spent in the discharge region ranged from $160 - 10 \mu\text{s}$. For a fixed inlet mole fraction of NH_3 , low flow rates result in larger $\gamma(\text{NH}_3)$ and so produce larger rates of dissociation. Larger densities and fluxes of H_2 at the exit are therefore produced. At high flow rates, the residence time of NH_3 in the discharge region is short enough (and $\gamma(\text{NH}_3)$ low enough) that there is not significant fractional dissociation of the NH_3 . As the flow rate decreases and $\gamma(\text{NH}_3)$ increases, there is significant fractional dissociation, and so there is an advantage in increasing the NH_3 mole fraction to capture more energy into dissociative modes. A secondary effect of the increase in fractional dissociation is the increase in flow speeds to maintain a constant pressure.

Conversion efficiencies generally decrease with increasing flow rate and mole fraction. Maximum conversion efficiencies are obtained when dissociation rates are large which occurs when $\gamma(\text{NH}_3)$ is large, which in turn occurs when the NH_3 mole fraction and inlet speed (sccm) are both low. These conditions unfortunately do not produce a high H_2 output flux. Conversely, although the efficiency of conversion is low for higher NH_3 mole fractions, the outlet flux of H_2 is higher.

From an application standpoint, there is a tradeoff between conversion of NH_3 to H_2 (fuel utilization) and net output flux of H_2 . A measure of the latter is the energy required to produce an H_2 molecule, $\gamma(\text{H}_2)$, which is important because the maximum energy recovered

from a H₂ molecule in a fuel cell is 2.5 eV. This tradeoff is shown in Fig. 5.6c where $\gamma(\text{H}_2)$ is shown as a function of energy deposition per feedstock NH₃, $\gamma(\text{NH}_3)$. For a constant power deposition, $\gamma(\text{NH}_3)$ decreases with either increasing mole fraction (energy distributed over more NH₃ molecules) or increase in inlet speed (smaller residence time). At high flow speeds, $\gamma(\text{H}_2)$ is too large (few 10s eV) to be useful in producing feedstock for a fuel cell. At the lowest flow speed (2.5 m s⁻¹) and highest NH₃ mole fraction (20 %) investigated, $\gamma(\text{H}_2)$ was 3.3 eV per H₂ created, and η was 0.9, values that begin to become interesting for local H₂ production. Further reduction in flow speed to 1.25 m·s⁻¹ (not shown in the figure) caused a reduction in H₂ flux and increase in $\gamma(\text{H}_2)$. At a flow speed of 2.5 m·s⁻¹, the conversion efficiency, η , was high (0.8 – 0.9) for all mole fractions, implying that the H₂ density was unlikely to improve significantly at flow speeds lower than 2.5 m·s⁻¹. Lower flow speeds results in sufficiently long residence times that power was expended in dissociating the product H₂. As a result, the reduction of $\gamma(\text{H}_2)$ to lower than 3.3 would require optimizing other parameters in the system. Most such parameters have to do with more efficiently utilizing the thermal energy of the discharge to dissociate the NH₃. Once the discharge energy is expended to heat the gas, utilizing that heat to further thermally dissociate the feedstock gas can only improve efficiency. For a given total power deposition, increasing the power density will increase the local gas temperature. Since thermal dissociation has an exponential temperature dependence, more dissociation will likely be obtained even though the volume is smaller. This strategy is discussed below. Another strategy is to thermally engineer the device to minimize heat transfer out of the discharge and so reduce cooling rates.

The consequences of varying the power density (kW·cm⁻³) while keeping total power

constant (0.1 W) on plasma characteristics are shown in Fig. 5.7. The pressure was 100 Torr, the NH_3 mole fraction was 0.1, and the inlet flow speed was $10 \text{ m}\cdot\text{s}^{-1}$ (5.6 sccm). The axial power densities, shown in Fig. 5.7(a), maintain the total energy deposition per unit volume a constant for a given flow rate. The maximum T_g (shown in Fig. 5.7(b)) increased from 800 K to 1,100 K as the power density was increased from 1.25 to $10 \text{ kW}\cdot\text{cm}^{-3}$. The maximum value of n_e (shown in Fig. 5.7(c)) increased nearly linearly from $1.0 \times 10^{13} \text{ cm}^{-3}$ to $3.8 \times 10^{13} \text{ cm}^{-3}$ as the power density was increased from 1.25 to $10 \text{ kW}\cdot\text{cm}^{-3}$.

If H_2 production was purely a function of energy deposition, then the rate of production would be independent of the variation in the spatial distribution of power deposition examined here. We found that not to be the case. For example, the density of H_2 and the conversion efficiency η at the exit as a function of NH_3 mole fraction are shown in Fig. 5.8 for different power densities and constant total energy deposition. In principle, η should be independent of power density. The H_2 densities (Fig. 5.8(a)) increased with increasing power densities, and the effect was more pronounced at higher NH_3 mole fractions. At higher power densities, T_g increases thereby increasing the contribution of thermal decomposition of NH_3 to the production of H atoms and other endothermic processes such as H abstraction. As a result, η increased with increasing power deposition (as shown in Fig. 5.8(b)) while $\gamma(\text{H}_2)$ was reduced by nearly 60% by increasing the power density from 1.25 – 10 kW cm^{-3} (as shown in Fig. 5.8(c)).

5.4 Scaling of Microdischarge Production of H_2 : 2-D Modeling

Results from the plug-flow model provide trends and scaling but are not able to accurately capture the consequences of spatial variations in, for example, power deposition or

the emission of secondary electrons from the cathode. To provide insights to the consequences of spatial variations in plasma and flow properties, we used our 2-dimensional model to investigate microdischarges within a similar parameter space as that for the plug-flow modeling. The pressure, and power for all the results reported in this section are 100 Torr and 1 W, respectively.

The geometry used for this study is shown in Fig. 5.1(a) and was discussed previously. In analogy to the plug-flow model, the discharge region is between the centers of the electrodes (0.15 to 0.25 cm along the vertical axis). The electrons and the ions were initialized to have small densities (10^9 cm^{-3}) in a Gaussian distribution of width 200 μm in the center of the reactor adjacent to the cathode. The velocity and density of the gas at the inlet was set based on the specified flow rate and the pressure. T_g was initialized to 300 K throughout the domain. The outlets were sufficiently far away from the discharge region that the normal gradients (along the flow direction) of flow quantities were assumed to be zero. A no-slip condition was imposed on all other surfaces in contact with the plasma.

The plasma potential, T_e , and n_e for the base case (10 sccm, Ar/NH₃= 95/5) are shown in Fig. 5.9. Power deposition and ionization sources are shown in Fig. 5.10. The steep gradients of the plasma potential near the cathode represents the cathode fall. The potential drop across the cathode fall is -330 V over a 100 μm distance producing an average electric field of 3.3 kV-cm⁻¹. Ionization occurs from collisions of bulk electrons and the secondary beam electrons produced at the cathode as a result of ion bombardment. The maximum value of ionization from these two sources are within a factor of two ($1.5 \times 10^{22} \text{ cm}^{-3}\text{s}^{-1}$ for bulk ionization and $7 \times 10^{21} \text{ cm}^{-3}\text{s}^{-1}$ for beam ionization). The plasma is segmented into a portion that appears hollow cathode-like (that is, dominantly negative glow) within the ring cathode

and a portion that is positive column-like, extending along the axis towards the anode.

The ionization by beam electrons in the negative glow region contributes towards producing a local maximum in electron density of $1.1 \times 10^{14} \text{ cm}^{-3}$. Ionization by bulk electrons also is also a maximum in this region. As such, vast majority of the power expended by electrons in the positive column portion of the discharge goes into non-ionizing dissociation reactions. Power deposition is dominated by ion acceleration and secondary electron emission within the hollow cathode, and by conventional resistive heating in the positive column.

The gas temperature and densities of the neutral fluid, NH_2 , H, and H_2 are shown in Fig. 5.11. The densities of the neutral fluid, NH_2 , H, and H_2 as they convect out of the reactor channel are shown in Fig. 5.12. T_g increases from 300 K at the inlet to 2,050 K in discharge region. The skew in the high temperature region to the right represents the convection of the gas by the flow. This peak in gas temperature is likely a lower limit as the boundary condition for the material temperatures was 300 K, which may artificially constrain the maximum T_g by having high rates of thermal conduction to the walls. Rarefaction of the gas occurs due to gas heating and reduces the fluid density within the cathode ring. This reduction in gas density lengthens the range of beam electrons emitted from the cathode and contributes to the hollow-cathode like behavior. On the other hand, the reduction in density reduces the density of collision partners for the electron and heavy particles, resulting in plasma chemistry occurring dominantly in the positive column region of the discharge. The rates of formation of NH_2 and the H by electron impact have a maximum in the positive column portion of the plasma where T_e , at 3 eV, is close to the value that optimizes energy dissipation by dissociative excitation of NH_3 . The production of H_2 is maximum in the

hottest regions within the cathode due to abstraction of H from NH₂ (Eq. 5.6(a)), and from NH₃ (Eq. 5.6(b)) to a smaller degree. The contribution to H production from direct decomposition of NH₃ is not more than a few percent of the total.

Downstream of the discharge, densities increase due to cooling of the gas. The H₂ production in the afterglow is dominated by volumetric 3-body recombination with a small contribution (< 10%) from wall recombination. The recombination of H and NH₂ with NH₃ as the third body to form NH₃ ($k = 6 \times 10^{-30} \text{ cm}^6 \text{ s}^{-1}$) competes with that of H₂ production (Eq. 5.7(b), $k = 1.4 \times 10^{-31} \text{ cm}^6 \text{ s}^{-1}$). The fraction of NH₃ production to H₂ production by these 3-body reactions is determined by the product of the ratio of the rate constants (≈ 40) and [NH₂]/[H]. While this can be a large fraction ($\approx 90\%$ in this case), the amount of H in this region is already <10 % of the H in the discharge region, and hence the loss of H is not alarmingly large.

The conversion of NH₂ into N₂H₄ (Eq. 5.8(c)) can also consume NH₂ when NH₂ densities are comparable to those of H. This is, in principal, advantages because it eliminates a channel for H consumption, re-association of H with NH₂ to reform NH₃. It is disadvantageous because the reservoir of H in NH₂ is made that much more distant from H₂ formation. These tradeoffs place a large premium on fully dissociating the NH₂ and NH fragments of NH₃ to minimize the re-association reactions. Downstream of the plasma channel, the densities of all product species decrease in the expanding plume. However the more rapid decrease in the H atom density indicates its consumption in re-association reactions.

The densities of selected ions and neutral species along the axis of the 2-d reactor are shown in Fig. 5.13. Ion densities extended significantly further upstream and downstream

than shown in the plug-flow model due to ambipolar diffusion (upstream) and convection (downstream). In the positive column region NH_4^+ is the most abundant ion as predicted by the global model. The lower thresholds for ionization of NH_x compared to Ar preferentially produce their ions in the positive column where T_e is low. Within the hollow cathode region, the major ion is Ar^+ . This results from ionization being dominated by beam electrons which do not so clearly discriminate between species having differences in threshold energies of 5-10 eV. The low gas density in this region due to gas heating, and the resulting lower rate of charge exchange reactions, result in NH_3^+ being the dominant NH_x ion. Only downstream after gas densities rebound with cooling does charge exchange enable NH_4^+ to become the dominant ion again.

The dominant neutral species apart from NH_3 and Ar are H_2 , N_2 , N_2H_4 , NH_2 , and H. The reduction in densities of the H_2 , and N_2 starting at the end of the plasma tube is due in large part to the expansion of the plume. These are stable end products, and the gas temperature is not high enough in the downstream region for additional endothermic reactions to occur. The reduction in densities in the cathode region is due to gas heating. Note that the H_2 density decreased by a factor of only 2 in the cathode region even though the gas temperature increased by a factor of nearly 7 to 2,050 K. This indicates a large source of H_2 , which is H abstraction by H from NH_3 and NH_2 (Eqs. 5.6(a) and 5.6(b)). Direct thermal decomposition of NH_3 plays a smaller role.

The densities and flow rates at the exit of the plasma tube will be used as the basis of commenting on efficiencies and conversion rates. The density of H_2 at the exit of the plasma tube is $4.6 \times 10^{16} \text{ cm}^{-3}$, and the efficiency of H conversion is $\eta = 0.41$ resulting in a total dissociation of NH_3 of 0.31. The rate of production of H_2 molecules is $1.6 \times 10^{17} \text{ s}^{-1}$ which

for a power deposition of 1 W corresponds to $\gamma(\text{H}_2) = 39$ eV.

The consequences of NH_3 mole fraction on n_e , T_g and H_2 production are shown in Fig. 5.14. The values of n_e and T_g are on axis of the reactor at the center of the cathode, and the values of $[\text{H}_2]$ are at the end of the plasma tube. n_e decreases with increasing NH_3 mole fraction, as predicted by the plug-flow, model due to more rapid rates of power dissipation per electron. The plasma becomes more resistive when increasing the NH_3 mole fraction as indicated by the increase in voltage required to dissipate 1 W. The general trend is for T_g to increase with increasing NH_3 mole fraction. The sources of gas heating are largely Joule heating (including ion acceleration in the pre-sheath and sheath) and dissociation reactions (Frank-Condon effects). At lower NH_3 mole fractions Joule heating from Ar^+ near the cathode was the primary source of gas heating, whereas, at higher NH_3 mole fractions, the dissociation of NH_3 and Frank-Condon relaxation provided the major source of heating. The exit $[\text{H}_2]$ increased from $2.3 - 12.8 \times 10^{16} \text{ cm}^{-3}$ when increasing the NH_3 mole fraction from 1 to 15% for the same power deposition. This resulted in $\gamma(\text{H}_2)$ decreasing from 242 – 38. These trends are in-line with predictions from the plug-flow model.

5.5 Concluding Remarks

The production of H_2 in microdischarges sustained in Ar/NH_3 mixtures was computationally investigated using plug-flow and 2-dimensional models using an extensive plasma chemistry mechanism. We found that the efficiency of H production by electron impact dissociation of NH_3 is a sensitive function of electron temperature (T_e), optimizing at 3 eV for pure NH_3 , and < 1.6 eV for $\text{Ar}/\text{NH}_3=90/10$. H_2 densities of 10^{16} cm^{-3} were obtained with power densities of 2.5 kW-cm^{-3} and a NH_3 mole fraction of 0.1 at 100 Torr.

For constant power, an increase in NH_3 mole fraction reduced the electron density and hence reduced the plasma conductivity. This resistive plasma causes gas heating due to dissociation of the NH_3 molecules. The 2-d model suggests that the gas heating is maximum near the cathode surfaces. Significant rarefaction of the gas occurs due to gas temperatures exceeding 1000 K, giving a fillip to thermal decomposition and abstraction reactions that generate H_2 .

Results from both models suggest that high conversion rates of NH_3 to H_2 (η) occur at low NH_3 mole fractions and low flow speeds (or high residence times) both of which maximize the eV/ NH_3 molecule deposited, $\gamma(\text{NH}_3)$. However, at very low flowrates, the flux of H_2 molecules can be lower even though the conversion rates are high due to saturation of the conversion efficiency, η . η as high as 0.9 are predicted based on the quasi-one dimensional model. These conditions usually correspond to higher energy deposition per H_2 molecule exiting the discharge, $\gamma(\text{H}_2)$. A higher η implies a better utilization of the incoming feedstock gas (NH_3). A lower $\gamma(\text{H}_2)$ implies an efficient utilization of the power deposited in the plasma. These two factors will ultimately determine whether this process could be practically used to locally generate H_2 for technological purposes.

Results from the plug-flow model also suggest that higher power densities in the discharge (for a given total power) can lead to more efficient production of H_2 . This could be used to decrease the $\gamma(\text{H}_2)$ to a value below 2.5 eV which would then make these devices commercially feasible.

5.6 Figures

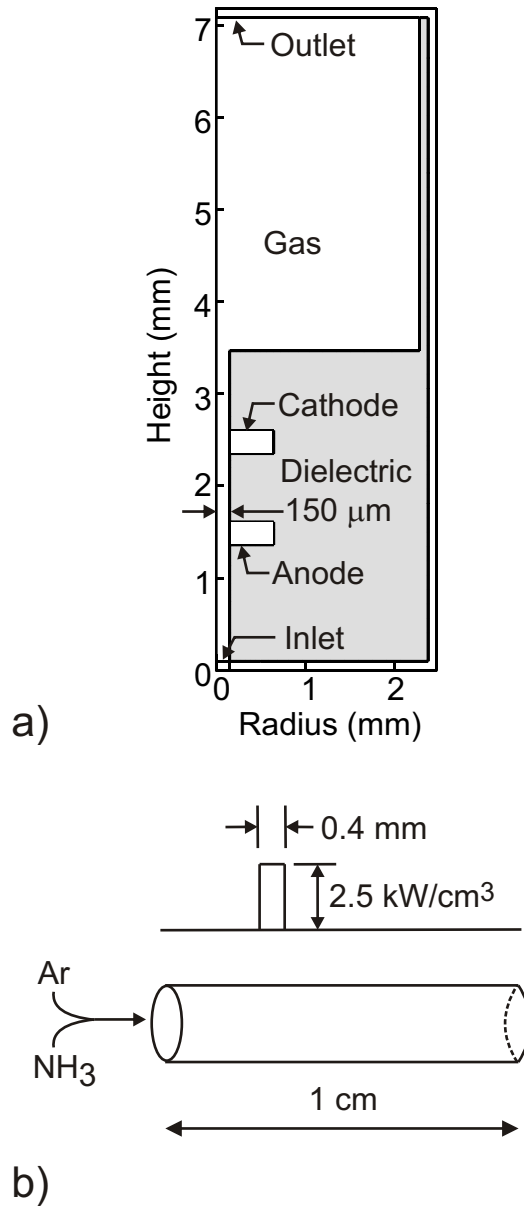


Fig. 5.1: Geometry of the reactors: a) Structure of the cylindrically symmetric discharge used for the 2-d model and b) schematic of plug flow model.

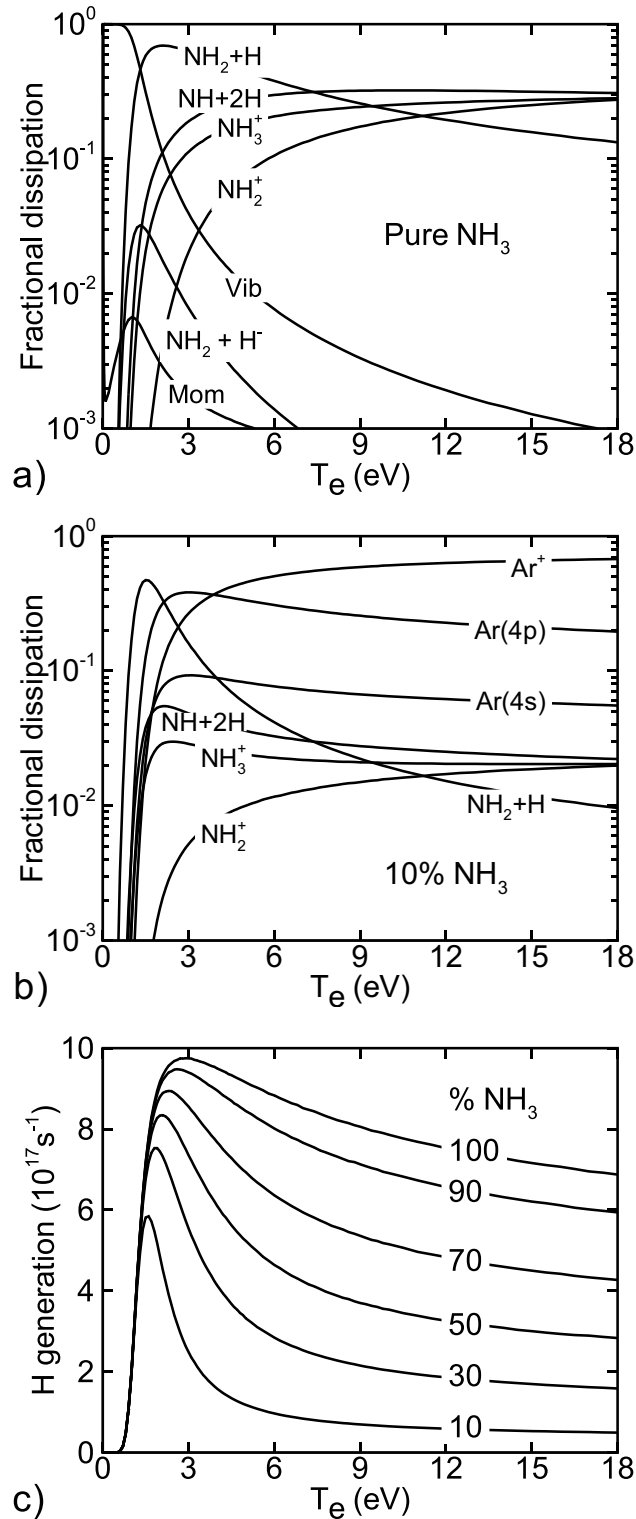


Fig. 5.2: Discharge parameters obtained from electron impact rate coefficients as a function of T_e . a) Fractional Power Deposition by e- impact in pure NH_3 , b) Fractional Power Deposition in $\text{Ar}/\text{NH}_3=90/10$, and c) Total H generation by e- impact on NH_3 per unit power for different NH_3 mole fractions.

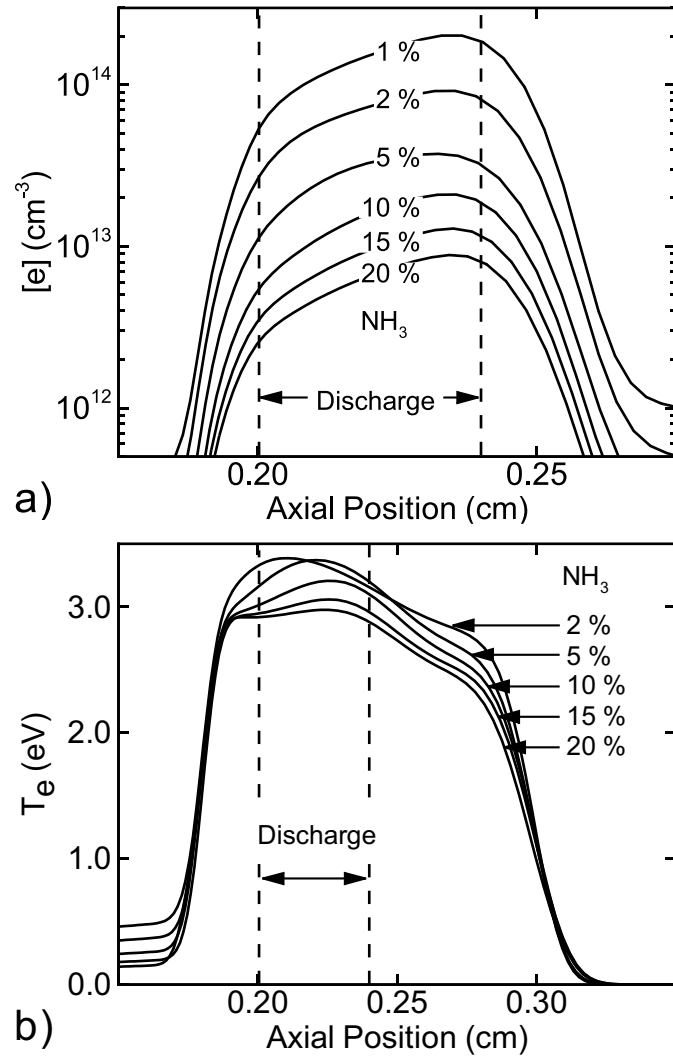


Fig. 5.3: Plasma characteristics along the axis of the discharge with varying NH_3 mole fractions and constant flow speed of $10 \text{ m}\cdot\text{s}^{-1}$. a) Electron Density and b) Electron Temperature.

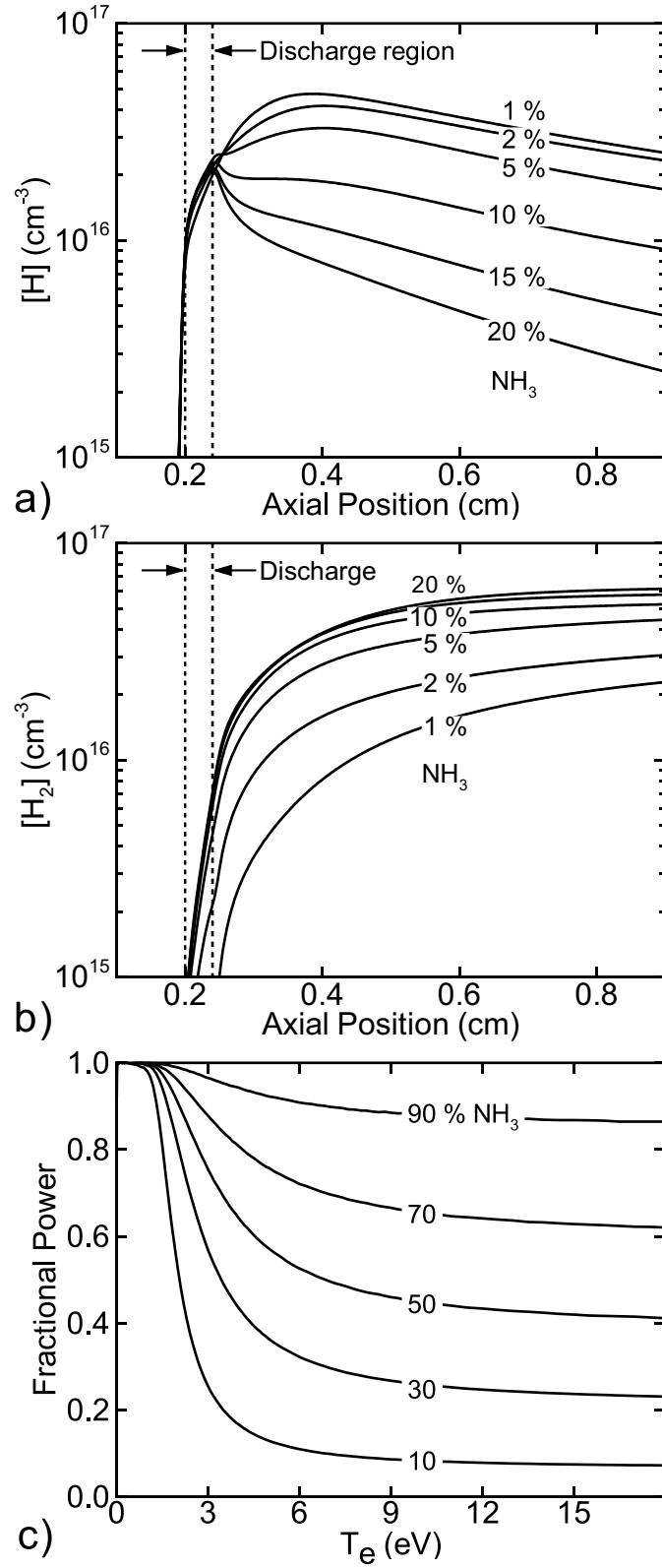


Fig. 5.4: Plasma parameters while varying NH₃ mole fractions for a constant flow speed of 10 m·s⁻¹. a) Density of H, b) Density of H₂ and c) Fractional Power Deposition into NH₃.

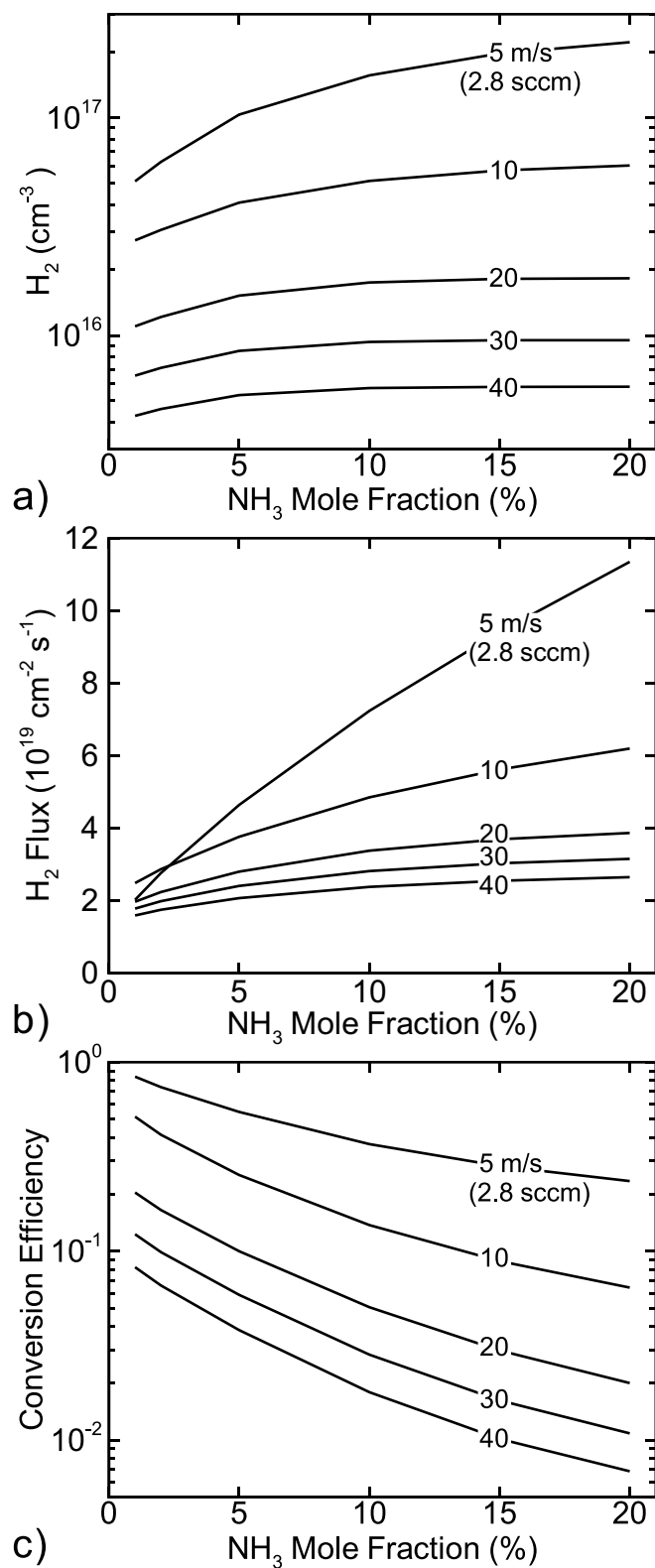


Fig. 5.5: Hydrogen production at the exit of the reactor as a function of NH₃ mole fraction and flow speed. a) H₂ density, b) H₂ flux and c) , hydrogen conversion efficiency.

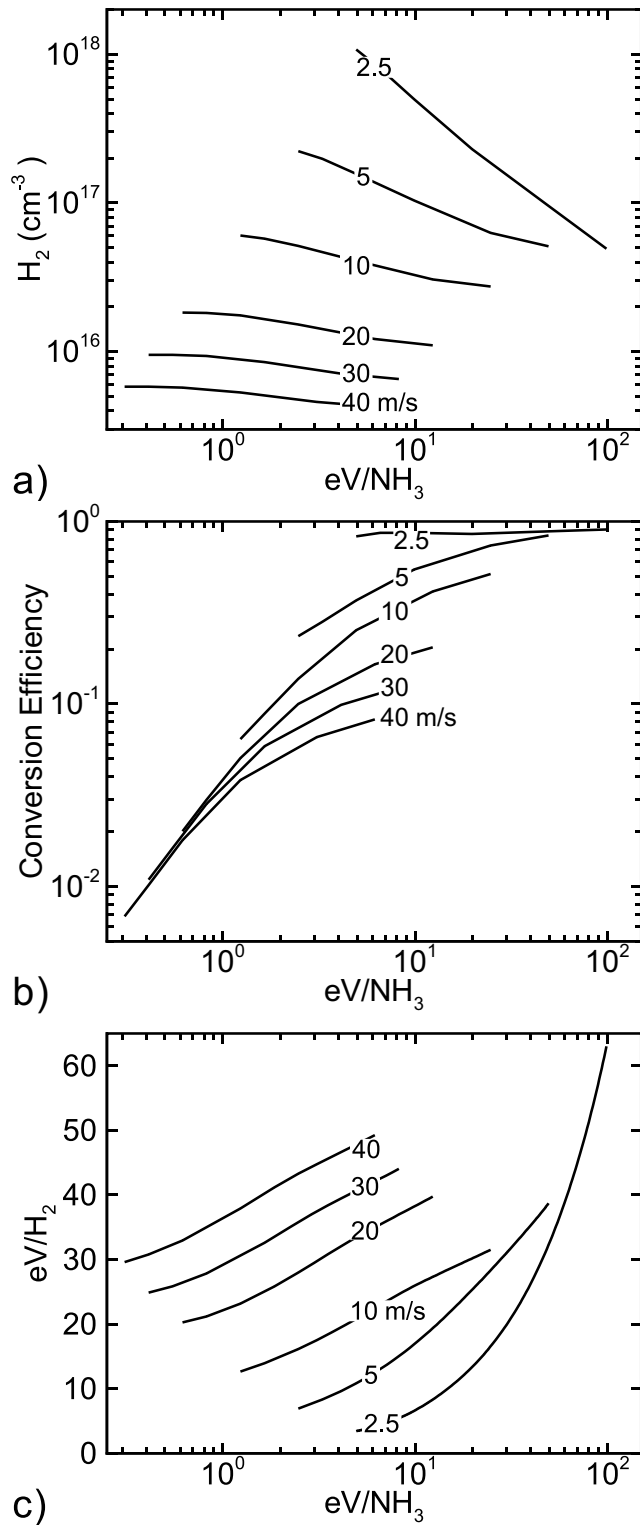


Fig. 5.6: Hydrogen production at the exit of the reactor as a function of NH_3 energy deposition efficiency, $\gamma(\text{NH}_3)$ and flow speed. a) Density of H_2 , b) , Hydrogen Conversion Efficiency, and c) $\gamma(\text{H}_2)$, Hydrogen Power Efficiency.

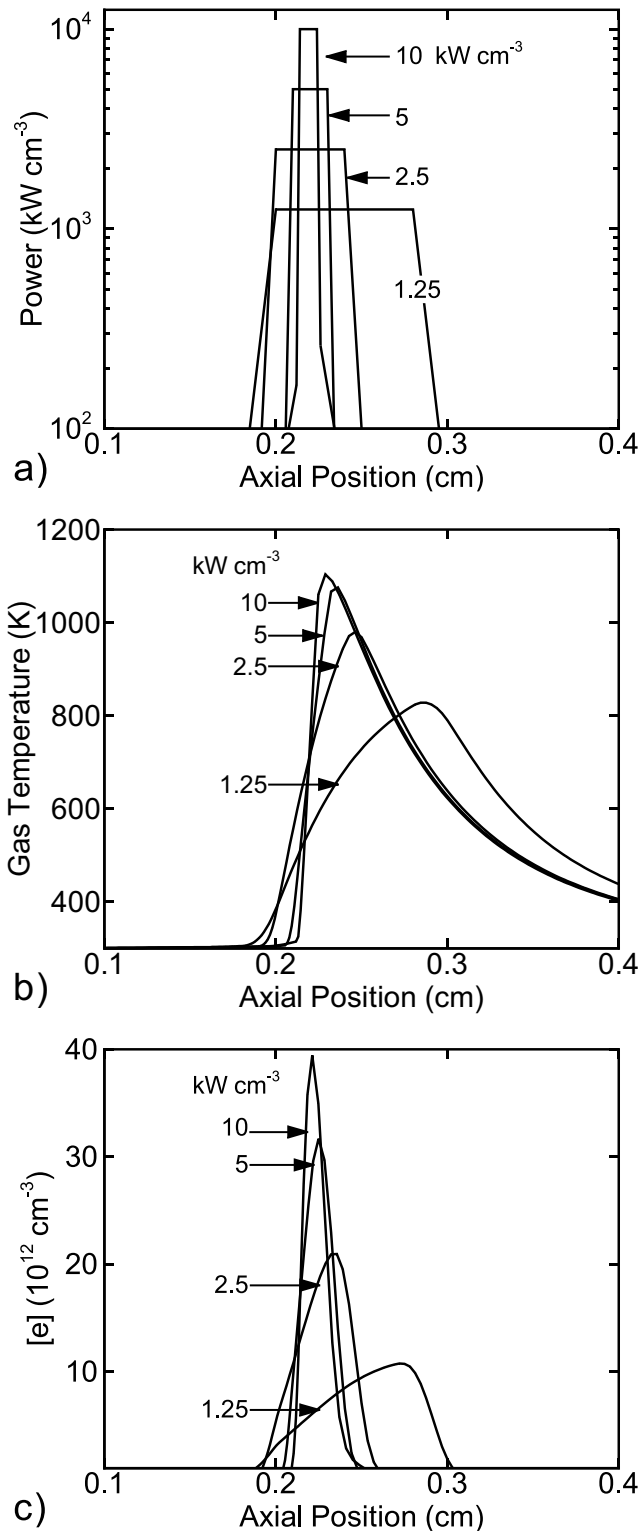


Fig. 5.7: Plasma parameters along the axis for constant total power deposition (0.1 W) while varying the peak power deposition. a) Specified Power Deposition, b) Gas Temperature and c) Electron Density.

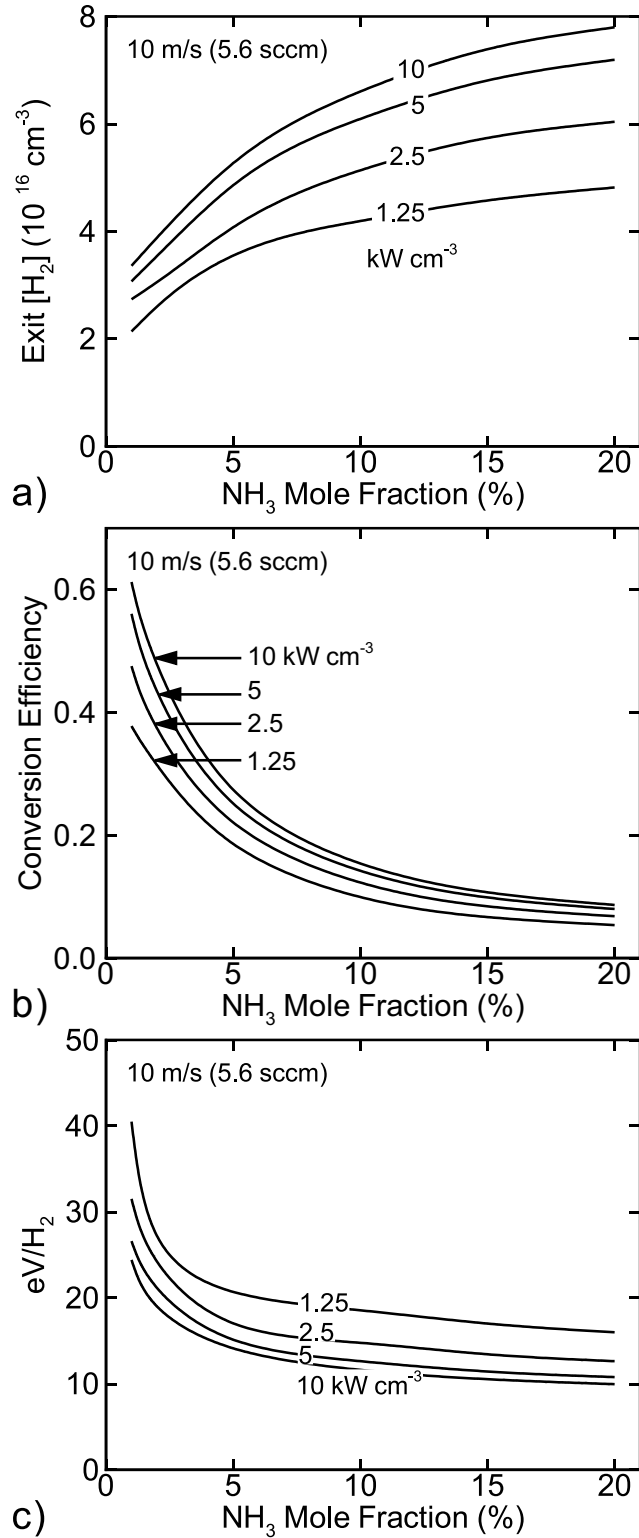


Fig. 5.8: Plasma parameters as a function of NH_3 mole fraction for constant total power (0.1 W) while varying the peak power deposition. a) Density of H_2 , b) Hydrogen Conversion Efficiency (η) and c) Hydrogen Power Efficiency, $\gamma(\text{H}_2)$.

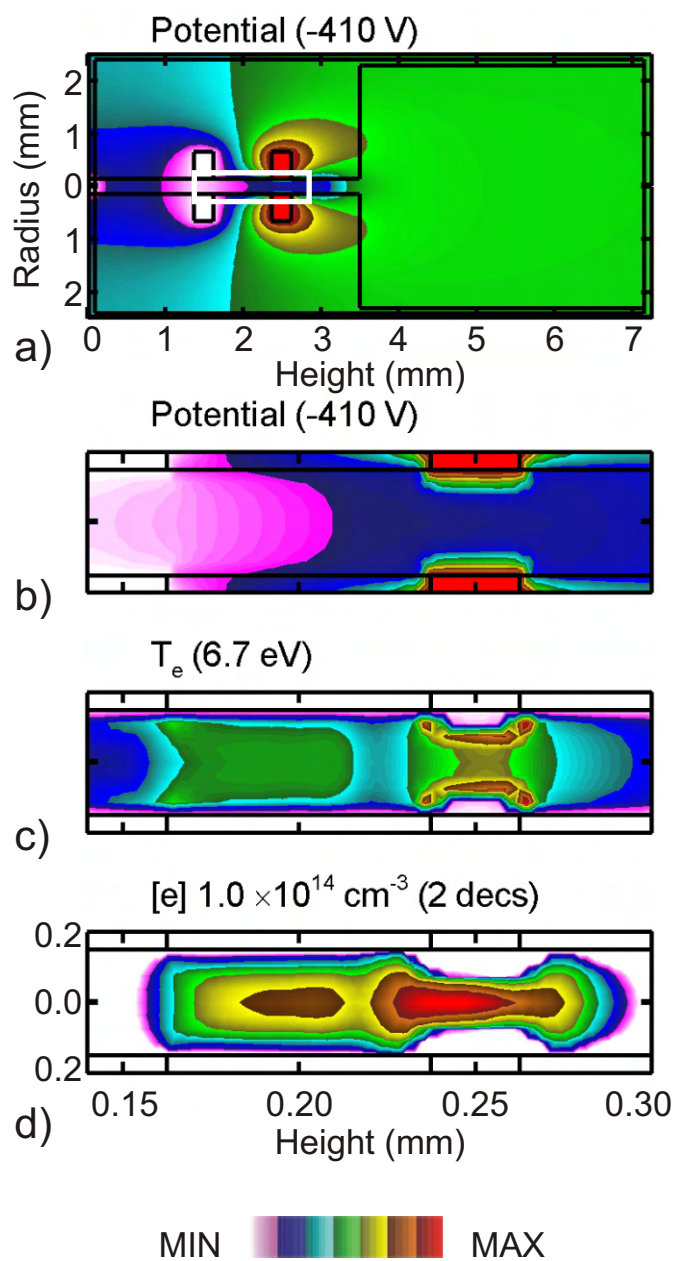


Fig. 5.9: Plasma characteristics for the 2-d model for a power deposition of 1 W, Ar/NH₃ of 90/10 and flowrate of 10 sccm (18 m·s⁻¹). a) Plasma Potential for the entire reactor, b) Plasma Potential in the enlarged region designated by the white outline above, c) Electron Temperature, and d) Electron Density. The scales are linear except for electron density that is plotted on a 2-decade log scale.

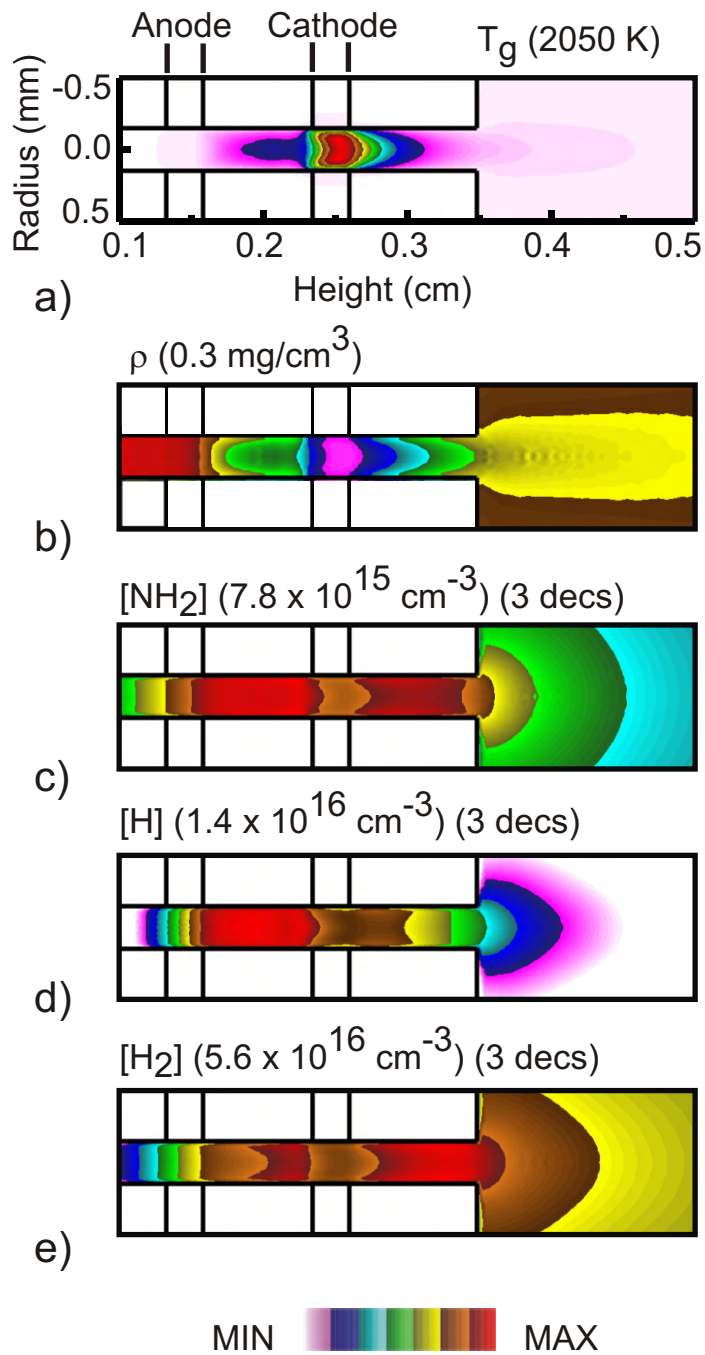


Fig. 5.11: Neutral flow properties in the discharge region for the base case. a) Gas Temperature, b) Gas Density, c) Density of NH_2 , d) H, and e) H_2 .

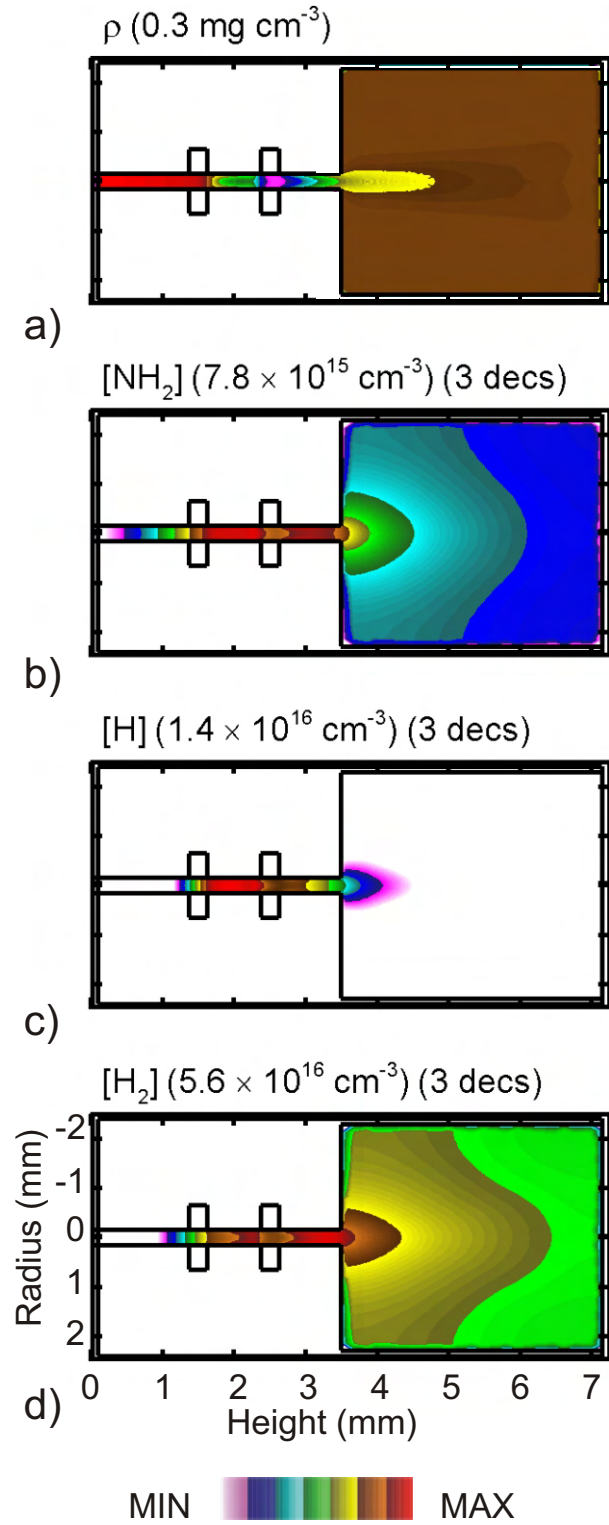


Fig. 5.12: Neutral flow properties for the entire reactor for 1 W power deposition, 100 sccm of Ar. a) Gas Density, b) Density of NH_2 , c) Density of H, and d) Density of H_2 .

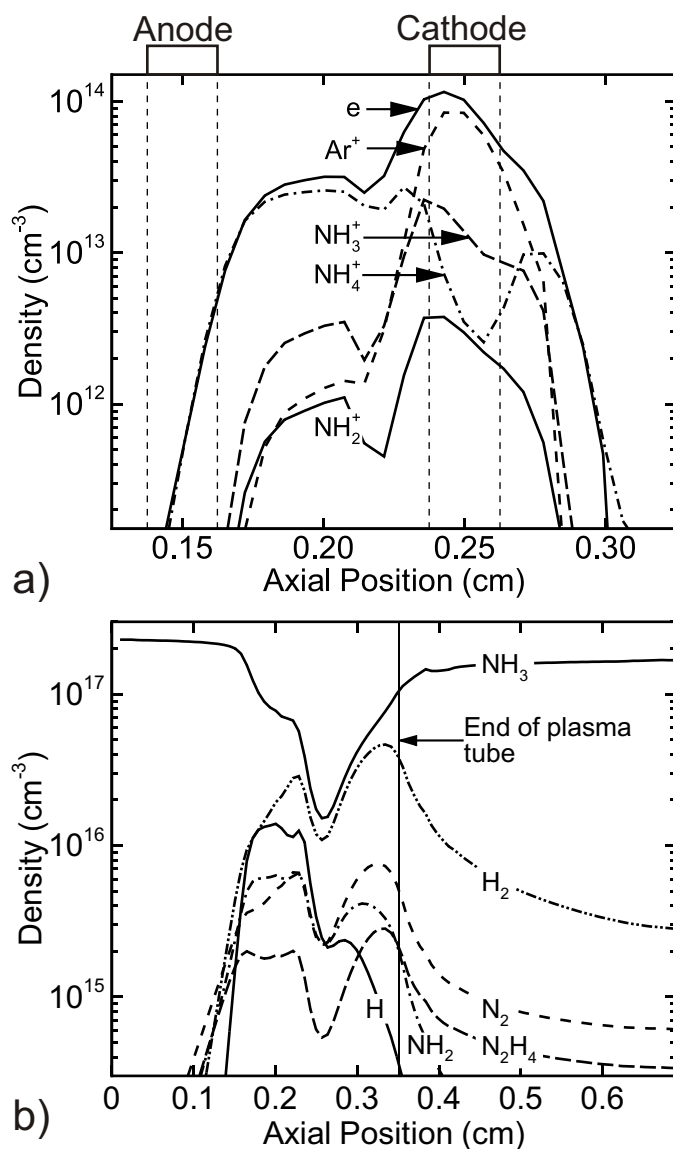


Fig. 5.13: Densities of selected ions and neutral species along the axis of the discharge for 1 W power deposition, 10 sccm of Ar flow. a) Densities of Charged Species, and b) Densities of Neutral Species.

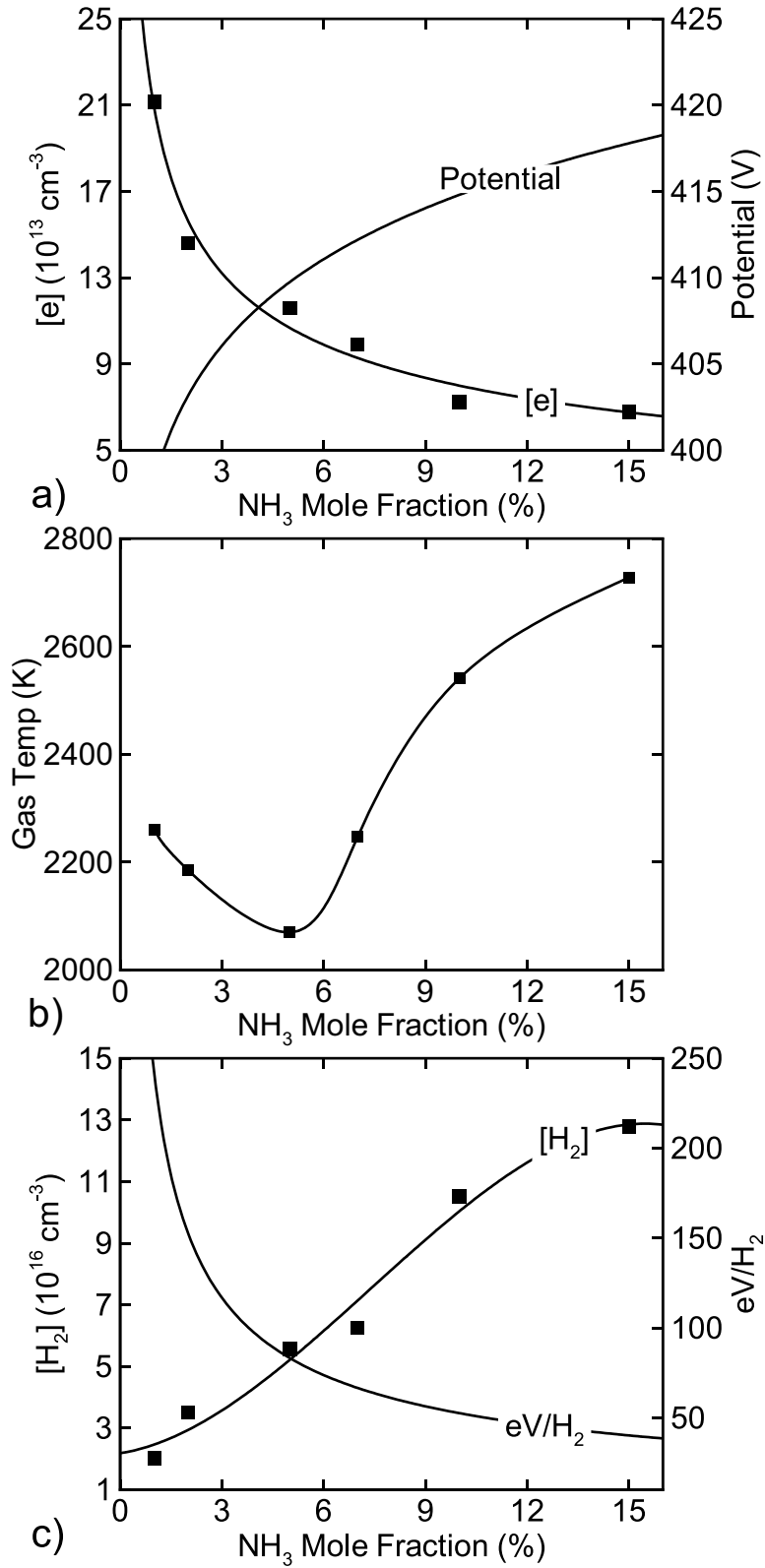


Fig. 5.14: Variation of discharge and flow properties with NH_3 mole fraction for 1 W and 10 sccm ($18 \text{ m}\cdot\text{s}^{-1}$). a) Electron Density and Cathode Potential, b) Gas Temperature and c) Density of H_2 , and Hydrogen Power Efficiency, $\gamma(\text{H}_2)$.

5.7 References

1. F. Barbir and T. Gómez, *Int. J. Hydrogen Eng.*, **22**, 1027 (1997).
2. J. E. Klemberg-Sapieha, O. M. Küttel, L. Martinu and M. R. Wertheimer, *J. Vac. Sci. Tech. A*, **9**, 2975 (1991).
3. M. Losurdo, P. Capezzuto, G. Bruno and E. A. Irene, *Phys. Rev. B*, **58**, 878 (1998).
4. P. J. van den Oever et al, *J. Appl. Phys.* **98**, 093301 (2005).
5. P. J. van den Oever et al, *Plasma Sources Sci. Tech.* **15**, 546 (2006).
6. H. Qiu, K. Martus, W. Y. Lee and K. Becker, *Int. J. Mass Spect.* **233**, 19 (2004).
7. D. D. Hsu and D. B. Graves, *Plasma Chem. Plasma Proc.* **25**, 1 (2005).
8. A. Fateev et al, *Plasma Proc. Polymers* **2**, 193 (2005).
9. G. P. Miller and J. K. Baird, *J. Phys. Chem.* **97**, 10984 (1993).
10. P. Vankan, R. Engeln and D. C. Schram, *Appl. Phys. Lett.* **86**, 101501 (2005).
11. B. Jackson and M. Pearson, *J. Chem. Phys.* **96**, 2378 (1992).

CHAPTER 6. MICRODISCHARGES AS SOURCES OF THRUST FOR MICROTHRUSTERS

6.1 Introduction

Small satellites with masses of few to tens of kg are being developed for phased-array radars and satellite networks.[1] Apart from the advantages of scalability and robustness, these systems also have a reduced risk of mission failure due to the redundancy available with large fleet of micro-spacecraft. Efficient, non-contaminating and reliable thrusters are required for these small spacecraft to enable attitude and orbit control to increase their operational lifespan.[2] A variety of electrostatic and electromagnetic thrusters, such as Hall thrusters and Pulsed Plasma Thrusters (PPTs), are now used in satellites for attitude control orbit maneuvers, station keeping and de-orbiting.[3-5] Depending on size and mission, these micro-satellites require mN to a few N of thrust, which in turn requires tens to hundreds of watts to operate. Scaling these devices down in power and size to suit the need of micro-satellites is a continuing challenge. For example, Hall thrusters make use of magneto-static fields to increase the residence times of electrons in an annular region and the required strength of the magnetic fields scales inversely with the characteristic length. Micro-discharge (MD) devices are also being developed as thrusters for micro-satellites.

MDs based on cathode boundary layer [6] or hollow cathode excitation [7,8] leverage pd (pressure \times distance) scaling to operate as dc discharges in inert gas mixtures at relatively high pressures and characteristic dimensions of hundreds of μm . They are being investigated for possible applications as excimer lighting sources [6], hydrogen production [7,8], and diamond deposition [9]. Radio frequency (rf) excited MDs are also being studied for use in surface modification processes such as etching and deposition [10-12]. Eden et al [13]

demonstrated the operation of large-arrays of rf MD sources operating at 5 – 20 kHz based on rare gas and Ar/N₂ mixtures in Si-based substrates. Arrays as large as 40,000 pixels were shown to have uniform optical and electrical uniformity, which could potentially be used in photonic applications.

MDs have also recently been investigated for use as microthrusters (MTs). Horisawa and Kimura [14] studied the feasibility of 2-20 W dc plasma jets as MTs using both gaseous (N₂) and solid propellants (Teflon). They generated mNs of thrust at N₂ flow rates of a few mg-s⁻¹ and found that increasing anode-cathode separation improved the thrust efficiency (incremental thrust per unit power). Slough et al [15] investigated the feasibility of dc MDs (300 μm aperture at back pressures of 10s Torr in Ar consuming 1-5 W) as thrusters. They measured a specific impulse (I_{sp} , defined as thrust per unit mass flow divided by gravity on earth's surface) of up to 220 s for 1 mg-s⁻¹ of Ar resulting in a total thrust of 2.2 mN. Kothnur and Raja [16] computationally investigated MDs (200 μm diameter) in 300 - 1000 Torr He and found them to operate in an abnormal glow regime. They also predicted high gas temperatures (>1000 K) and high plasma densities (>10¹⁴ cm⁻³). Takao and Ono [17] computationally investigated a miniature electro-thermal thruster using microwave excitation in Ar. They estimated a total thrust of 4.3 mN at 3 W. They also conducted preliminary experiments obtained a steady discharge at powers as low as 1 W.

MDs sustained in small volumes and high power densities (many to tens of kW/cm³) result in significant gas heating (gas temperature $T_g > 1000$ K). The change in gas temperature occurs over small distances (100 μm) in the vicinity of the discharge leading to steep thermal gradients. These gradients produce a change in the velocity of the gas thereby generating an incremental change in thrust (ΔF) above that produced by expansion of a cold-

gas flow. In general, ΔF is a function of the power deposition, flow rate and upstream (or back) gas pressure. As such, placement of the electrodes and the shape of the nozzle impact the location of the discharge and gas heating, and so affect the flow properties.

In this chapter, we discuss results from a computational investigation of the properties of MDs configured for MT applications. The consequences of discharge configurations, power, pressure and flow rates on thrust are discussed. For example, for a cylindrically symmetric discharge sustained in Ar with diameter 600 μm and electrode separation of 210 μm (cathode located upstream in the gas flow) we predict $\Delta F = 100 - 150 \mu\text{N}$ for power depositions of 0.5 – 2 W. (The upstream pressure of 50 Torr exhausts into 40 Torr.) The specific thrust (thrust per unit power deposition) ranged from 0.2 – 0.07 N kW⁻¹ which is commensurate with electro-thermal propulsion devices.

The incremental thrust produced by the discharge, ΔF , and incremental thrust per unit power, T_s , are defined as,

$$\Delta F = \left[\int_0^R (\rho v^2(r) + p(r)) (2\pi r) dr \right]_d - \left[\int_0^R (\rho v^2(r) + p(r)) 2\pi r dr \right]_0 \quad (6.1)$$

$$T_s = \frac{\Delta F}{P} \quad (6.2)$$

where P is the power, ρ is the neutral gas density, $v(r)$ is the axial speed at radius r , $p(r)$ is the pressure, and the integration is carried out over the exit plane of the nozzle. The subscripts d and 0 represent the powered and cold gas flow, respectively. T_s is a measure of efficiency.

In real devices the downstream is near vacuum, leading to supersonic and rarefied gas flows. However, due to complexities involving supersonic flows the downstream pressure is

maintained high and the flows encountered in this work are all supersonic. Hence, these results do not necessarily conform to conditions existing in space, although they provide considerable insight into the problem.

For the lowest pressures considered in this study (25 Torr), the Knudsen number (Kn) is ≈ 0.15 and the no-slip boundary conditions ($\vec{v} = 0$ at the boundary) used in this study are not accurate. [23] The slip-flow boundary condition is given by:

$$V_w = \lambda \frac{2 - \sigma}{\sigma} \frac{\partial v}{\partial y} \quad (6.3)$$

where V_w is the wall slip velocity, λ is the mean free path, σ is the transverse momentum accommodation coefficient (≈ 1), and $\partial v/\partial y$ is the gradient of axial velocity along the axial direction. Using the slip-flow boundary conditions, the wall velocity was ≈ 7 -10 m/s for flow rates of 8 sccm (mean flow = 100 – 200 m/s), and the error in our thrust calculations was ≈ 3 % compared to the results using no-slip boundary conditions.

In these flows, the Reynolds number ($\rho v D/\mu$) ranges from 40 – 500, and as such, the viscous losses are high, and were included while solving for the momentum equations.

6.2 Sandwich Microdischarge

The sandwich microdischarge configuration used in this investigation is shown in Fig. 6.1. The plasma channel has a diameter of 300 μm and the nozzle divergence angle is 3.8° . The diameter of the nozzle at the exit is 500 μm at the top of the downstream electrode. The thickness of the dielectric on top of the downstream electrode was varied from 0 to 750 μm . The metal electrodes are 125 μm thick and the cathode is connected to the power supply

through a 10 k Ω ballast resistor. The outer boundaries are electrically grounded and a layer of dielectric insulates the plasma from the boundary on the outer radius. This latter condition was for computational convenience to shield the ground plane.

For the base case, the inlet (back) Ar gas pressure is 30 Torr and the outlet pressure is 10 Torr. As such, there is a pressure gradient through the channel even with cold gas flow (no power deposition) which in turn produces cold gas flow thrust. The gas flow rate was varied from 8 to 30 sccm ($\approx 0.25 - 0.89 \text{ mg s}^{-1}$) and the power deposition was varied from 0.25 to 1 W.

The plasma potential, electron temperature (T_e) and ionization sources by bulk and beam electrons are shown in Fig. 6.2 for base case conditions of 30 Torr, 30 sccm and 0.5 W. The anode is upstream and the cathode is downstream. There is no dielectric on top of the cathode. The electron density (n_e), power deposition, and density of Ar* are shown in Fig. 6.3. The gas speed, Ar density, and T_g are shown in Fig. 4. The cathode voltage required to dissipate 0.5 W is -256 V.

The conductivity of the channel is high enough that the anode potential is pulled well into the cylindrical channel creating a hollow cathode-like configuration of electric potential. In the resulting cathode fall, the potential changes by nearly 240 V over $\approx 100 \text{ }\mu\text{m}$ producing an electric field in excess of 24 kV cm $^{-1}$ and E/N (electric field/gas number density) of greater than $4 \times 10^{-14} \text{ V cm}^2$. T_e in the pre-sheath leading to the cathode is 6-7 eV (in volumes where n_e is greater than 10^{-3} of it's maximum) whereas in the bulk plasma $T_e \approx 4.0$ eV. Ionization sources by electron impact have similar contributions from bulk electrons and from the beam electrons emitted from the cathode, both peaking at $5 \times 10^{20} \text{ cm}^{-3} \text{ s}^{-1}$. The ionization sources are larger inside the nozzle because the neutral gas density is higher and

there is a hollow-cathode effect from electrons emitted from the inside surfaces of the cathode. Downstream of the cathode, the ionization sources are lower and diffuse due to the lower gas density. The secondary electrons from the top cathode surface (facing the outlet) are accelerated in a lower electric field due to the thicker sheath thickness in a direction of lower gas density and so undergo fewer collisions per unit volume. The lack of a hollow cathode effect on the front surface also reduces the rate of ionization. T_e is a few eV downstream of the cathode due to the lower electric field and so these electrons produce fewer ionizations. Power deposition has two contributions, from bulk electrons and from secondary electrons accelerated by the cathode fall, the latter contributing <10% of the total in this case. A significant fraction ($\approx 30\%$) of the power is dissipated outside of the nozzle and so any gas heating produced by this power does not contribute to thrust.

The electron density has two peaks. The first is on the axis inside the nozzle ($3.0 \times 10^{13} \text{ cm}^{-3}$) adjacent to the cathode. Here the ionization by beam electrons is large by virtue of a hollow-cathode effect and the gas density is large enough to slow beam electrons. The excited state density is also high ($7 \times 10^{13} \text{ cm}^{-3}$) so that multi-step ionization is rapid, by both beam and bulk electrons. The second peak in electron density is downstream of the cathode ($2 \times 10^{13} \text{ cm}^{-3}$). Here, the effective diffusion length is longer thereby decreasing rates of loss by diffusion so that the lower ionization rates produce commensurate electron densities to that in the nozzle. Although T_e is lower in this regions (3 eV) ionization by Penning collisions ($3 \times 10^{17} \text{ cm}^{-3}\text{s}^{-1}$) produces about 10% of the total and helps sustain the plasma. The pinching of the electron density between the two peaks is due to the extension of the cathode fall from the vertex of the cathode which excludes bulk electrons. The peak of electron density downstream is augmented by the advective flow of the gas which entrains

the ions and, through ambipolar forces, drags along electrons.

The Ar^* density is the sum of the densities of $\text{Ar}(4s)$ and $\text{Ar}(4p)$ which, due to the short lifetime of, $\text{Ar}(4p)$ is dominated by $\text{Ar}(4s)$. The $\text{Ar}(4s)$ is consumed by Penning reactions (with lifetime of $\approx 10 \mu\text{s}$), by 3-body reactions with Ar atoms producing Ar_2^* (lifetime $\approx 90 \mu\text{s}$) and, downstream where T_e is small, by super-elastic electron collisions (lifetime $\approx 20 \mu\text{s}$). These processes dominate over losses due to diffusion.. The fractional power dissipated by radiation is typically $< 0.5 \%$.

Gas heating in large part results from Joule heating by ion collisions (e.g., elastic collisions and symmetric charge exchange) and secondarily by elastic collisions with electrons. Net momentum transfer from the electric field through ions and electrons is only important in non-neutral regions such as the cathode fall. For this geometry, this momentum transfer opposes the direction of net thrust though the fractional contribution is small ($< 1\%$). Typically, the momentum transfer from ion-neutral collisions is important only when the degree of ionization is large ($> 10^{-3}$). Energy transfer processes increase T_g from 300 K at the inlet to 765 K adjacent to the cathode where the drift of ions back towards the cathode produces a maximum in Joule heating. The plume of hot gas downstream results from the advective flow of the heated gas. As the gas cools further downstream, the resulting expansion leads to an increase in neutral gas speed from a cold thrust value of 310 m/s to a peak value of 480 m/s. Due to the high surface-to-volume ratio in this device and the fact that the walls have a large thermal mass, the heat transfer to the walls is significant. For example, Williams et al [24] predicted that the thermal loss to the walls to be $\approx 60\text{-}70\%$ of the input power at pressures of 45 – 60 Torr in an electrothermal microthruster having similar dimensions. In devices where the temperature of the walls significantly increases, the

heating is not necessarily all bad as the energy lost to the walls is recouped by the incoming gas which gets pre-heated as it enters the discharge region.

The neutral gas density is highest near the inlet and decreases steadily as the gas flows through the nozzle. During this expansion, the Ar density decreases from $2.4 \times 10^{18} \text{ cm}^{-3}$ at the inlet to $1.5 \times 10^{17} \text{ cm}^{-3}$ 0.5 mm downstream of the cathode. The reduction in gas density at the outlet is due to a combination of the initial condition (a pressure gradient across the device producing cold gas thrust) and gas heating by the discharge. With a constant mass flow rate, the change in gas speed due to heating by the discharge produces an increase in thrust over the cold gas value.

The consequences of power deposition (0.2-1 W) on plasma properties (cathode fall voltage, n_e and T_e) and flow speed are shown in Fig. 6.5. T_e is measured at the center of the channel in bulk plasma near the cathode (height = 3 mm) and n_e is the maximum value. The cathode voltage and n_e increase nearly linearly with power indicating the MD is operating in an abnormal glow regime. T_e decreases by 0.45 eV (4.25 eV to 3.8 eV) with power deposition over this range. This decrease is in part attributable to an increase in Ar^* densities thereby increasing the rate of multi-step ionization and an increase in the contributions to ionization by beam-electrons due to the higher cathode voltage, both of which allow the self sustaining T_e to decrease. As the cathode potential increases with power (becomes more negative) and the gas rarefies due to more gas heating, E/N in the pre-sheath increases. The larger E/N and larger ion density N_i with power increases the ion flux to the walls and to the cathode in particular. The ions recombine on surfaces and dissipate an energy at least equal to its ionization potential (16 eV). This is a power loss which might otherwise be used in gas heating. Over the range of power investigated, this loss is not more than a few percent of the

total. This low loss is due, in part, to increasing power deposition by secondary electrons (secondary electron emission coefficient of 0.15) produced by ion collisions with the cathode.

The increase in gas temperature above the inlet value of 300 K, (ΔT), and the gas speed at the throat of the nozzle are shown in Fig. 6.5(c). These values are the maximum in each case and occur ≈ 100 -150 μm downstream of the cathode. ΔT and the increase in speed are nearly linear with the power deposition at lower powers and begin to saturate near 1 W. The maximum ΔT is ≈ 700 K and the speed increases from 415 to 610 m/s as the power is increased from 0.0 to 1.0 W. The saturation in ΔT and speed is not unexpected. At higher power deposition and greater rarefaction, the mean free paths of secondary electrons are longer and so beam ionization and ion production occurs over a larger volume. Since gas heating is dominated by ion Joule heating which has a diminishing specific rate, ΔT saturates

The consequences of flow rate and power deposition on ΔT and gas speed 150 μm downstream of the nozzle exit are shown in Fig. 6.6. The residence-time of gas between the electrodes decreases with increasing flow rate, thereby decreasing the specific energy deposition per atom for a given power. For example, from 7.5 sccm to 30 sccm, the specific energy deposition decreases from 1.8 to 0.44 eV/atom. As a result ΔT decreases with increasing flow rate. The speeds at the nozzle exit increase with power for a given flow rate (more gas heating) and increase with flow rate for a given power (increase of the cold gas contribution to thrust). To isolate the contributions of the cold gas flow, the increase in axial speed relative to the cold gas value is shown in Fig. 6(c). The MT is most efficient at low flow rates and high powers, where the ΔV is large in comparison to the cold gas speed V . This is not unexpected because at low flow velocities, the kinetic energy in the flow, $\rho V^2/2$,

is small compared to the power from the discharge, and so the discharge has a larger influence on ΔV .

The consequences of nozzle design on the discharge and flow properties were investigated by adding a layer of dielectric insulation on top (downstream) of the cathode and varying its thickness up to 750 μm . (See Fig. 6.1.) The plasma properties for a 500 μm thick dielectric are shown in Fig. 6.7 for 1 W and 30 sccm Ar flow with an inlet pressure of 30 Torr. Power deposition is concentrated in a smaller volume near the cathode producing a higher peak value ($60 \text{ kW}\cdot\text{cm}^{-3}$) than with an exposed cathode. With roughly the same current, secondary electrons are emitted from only the inner surface of the cathode and so the current density of ionizing beam electrons is higher. As a result, the ionization sources are restricted to a small volume spanning 400 μm upstream of the cathode, with nearly no ionization sources downstream. The curvature of the cathode fall results from there being a higher plasma density upstream producing a smaller sheath thickness. This curvature orients trajectories of beam electrons upstream in spite of the slant of the face of the cathode which faces the other direction.

The consequences of dielectric thickness on the electron density are shown in Fig. 6.8 for 30 sccm Ar at 30 Torr back-pressure and 1 W. The peak electron density is $8.7 \times 10^{13} \text{ cm}^{-3}$ with an exposed cathode when the top surface emits secondary electrons [Fig. 6.8(a)]. The secondary maximum downstream is $8.7 \times 10^{13} \text{ cm}^{-3}$. With the addition of the dielectric [Figs 6.8(c-d)], large ionization sources are restricted to the volume between the electrodes producing higher peak n_e of $2.4 \times 10^{14} \text{ cm}^{-3}$ which is not a sensitive function of dielectric thickness. The electrons downstream of the nozzle diffuse in an almost electric field free region with little additional ionization and so their density is low (10^{11} cm^{-3}). The shift in

location of the plasma when covering the top dielectric is due, in part, to negative charging of the dielectric walls downstream of the cathode which confines the plasma. However the majority of the effect is due current and secondary electrons being emitted from only the inner-walls of the cathode, producing a higher current density and larger specific ionization source. As such, the increase in peak n_e is a consequence of the maximum power deposition increasing from 14 kW/cm³ with the exposed cathode to 60 kW/cm³ with the covered cathode, tempered by increased rates of loss by recombination and diffusion with the more confined plasma.

Changing the thickness of the dielectric did not significantly affect the plasma properties once the top surface of the cathode is covered and secondary electron emission from the top surface is curtailed. To demonstrate this effect, the secondary electron emission coefficient on the top surface of the exposed cathode (no dielectric layer) was set to zero so that only the inner surfaces of the cathode emitted secondary electrons. In this case [Fig. 6.8(b)], the plasma is not as confined as with a dielectric cap due to the lack of negative charging of the walls, although the peak n_e increases from 8.7×10^{13} to 1.1×10^{14} cm⁻³. With only secondary emission from the inner surface, the peak power density increases (≈ 14 to 28 kW/cm³) compared to when the entire cathode emits secondary electrons and the secondary peak in electron density downstream is eliminated indicating that the ionization produced by beam electrons from the top surface is significant. Management of the location of secondary electron emission is important to the confinement of the plasma.

The increase in specific power deposition resulting from confinement of the plasma with the dielectric covered cathode results in higher gas temperatures and exit speeds of the gas flow. For example, ΔT and the increase in gas speed relative to cold gas flow, ΔV , and

the incremental thrust ΔF are shown in Fig. 6.9 at the nozzle exit plane for different dielectric thicknesses. ΔT increases from 625 K without the dielectric to 1,185 K with a 750 μm dielectric. In the absence of the dielectric thickness, the gas heats nearest the cathode and cools as the gas transits outside the discharge, and so ΔV is also highest at large radius. By confining the discharge with the dielectric over-layer, the peak power deposition and gas heating are higher, thereby producing higher local ΔT and ΔV . A relatively thin dielectric cap, 250 - 500 μm , optimizes ΔT and ΔV . With thicker caps, the heated gas travels a longer distance beyond the volume peak power deposition before reaching the exit of the nozzle, and hence has more opportunity to cool thereby lowering exit speeds. This effect is likely exaggerated here as the wall temperatures are close to 300 K.

The incremental speed, ΔV , is an indication of the increase in thrust due to the discharge. The larger the ΔV , the larger the recoverable thrust. For this particular geometry and power, the incremental thrust is highest when the dielectric thickness above the cathode surface is 500 μm . The thermal losses to the wall and the viscous losses in the boundary layer are dependent on the length of the nozzle. If the nozzle length is too short, then the thermal energy in the gas is diffused in the downstream volume and so is underutilized. If the nozzle is too long, then thermal losses to the walls and viscous losses in the afterglow are large. Hence, for optimal nozzle lengths, the ΔF is maximum for a given power. For example, as an extreme case of nozzle length, the polarities of the anode and cathode were reversed so that the discharge took place deep inside the nozzle. In this case, the ΔV at the nozzle exit was nearly zero and the gas had cooled to nearly 300 K before reaching the exit plane.

6.3 Annular Microdischarges: Scaling with Power and Flow

In the sandwich-type microdischarges, power deposition is close to the side-walls of the nozzle which can lead to substantial loss power by heat conduction. To position the discharge at the center of the flow and so reduce these losses, an annular MD was considered, as shown in Fig. 6.10. In this geometry (referred to as a micro-arc), a cathode (400 μm diameter) is inserted into the middle of the flow producing an annular inlet flow of 200 μm around the wire. The anode is part of the nozzle and the separation between the electrodes is ≈ 210 μm . As experimentally [25] the cathode heats to high temperatures, the initial temperature of the cathode was set to 800 K, a value lower than that expected for gas temperature near the cathode. The boundary and initial conditions for the flow and the plasma are otherwise similar to those described above.

The plasma characteristics for the micro-arc are shown in Fig. 6.11 for base case conditions of 25 Torr exhausting into 20 Torr, 1 W and 25 sccm of Ar. The plasma spreads over the entire face of the nozzle and diffuses >1 mm downstream whereas significant power deposition is confined to 150-200 μm downstream of the cathode. With the cathode fall facing the direction of gas flow, secondary electrons emitted from cathode produce ionizations along the flow direction. Ionization is dominated by beam electrons near the cathode fall by a factor of 1.4 above that by bulk electrons. However, the volume in which bulk electrons produce significant ionization is more extended, extending upstream into the annular region. The peak n_e occurs in the center of the discharge at the throat of the nozzle, and extends in the downstream direction. A well-developed sheath near the cathode leads to a considerable net-positive space charge in the sheath producing a net acceleration by ion

collisions opposite that of the flow. However, the absolute magnitude of ion-drag caused by this space charge is small.

The neutral gas density, T_g , and axial speed in the micro-arc are shown for the base case in Fig. 6.12. In this geometry, a stagnation point ($\vec{V} = 0$) occurs at the tip of the cathode. As a result, the forced convection of gas from this location is small and so the gas temperature is higher (1,940 K) compared to the sandwich discharge. The conduction of heat through the cathode wire leads to preheating of gas as it flows around the cathode in the annular flow space into the cylindrical discharge region in front of the cathode. The peak flow speed is 206 m/s.

Gas heating produces rarefaction in the discharge and so influences the E/N and ionization sources. For example, beam ionization sources and n_e are shown in Fig. 6.13 and 6.14 as a function of power for 25 Torr upstream pressure and 25 sccm of Ar. With an increase in power, T_g increases and the gas density decreases due to rarefaction. Hence the secondary electrons undergo fewer collisions and extend further downstream of the cathode. Also, due to there being fewer collisions there is a greater loss of secondary electrons which are directly collected by the anode before they are slowed in the gas. The end result is that at higher powers, the ionization region is larger, extends further downstream and is dominated by beam electrons. At lower powers, the ionization sources are diffusive and relatively concentrated in the narrow gap between the electrodes. The ionization sources due to bulk electrons behave similarly with power deposition. The end result is an extension of n_e downstream with increasing power deposition.

The consequences of upstream pressure (25 -75 Torr) on n_e are shown in Fig. 6.15 for 1 W. The sccm is scaled with pressure to keep the cold-gas residence time constant. The

electron collision frequency increases with pressure, and so ionization sources and power deposition are confined to a smaller volume within the nozzle as the pressure increases. Consequently, n_e increases with pressure, from $6.9 \times 10^{13} \text{ cm}^{-3}$ to $7.9 \times 10^{14} \text{ cm}^{-3}$ from 25 to 75 Torr.

The consequences of power deposition on the maximum values of n_e and ΔT are shown in Fig. 6.16 for different pressures. For the micro-arc geometry, n_e increased with pressure for a given power but weakly depended on power at low pressures. An increase in power deposition increases the ionization sources but does so over a larger volume while reducing the gas density due to an increase in T_g . The diffusion of electrons is more rapid at lower neutral densities with there being a lower specific power deposition, which leads to a reduction in the peak n_e . As a consequence, n_e may decrease with power in spite of there being a larger eV/atom deposited in the flow and so larger ΔT . The peak gas temperature occurs near the tip of the cathode where the power deposition is high, and the convection is low. The ΔT increases almost linearly with power deposition as expected, and has a weaker dependence on pressure.

The incremental thrust at a height of 1.9 mm and the specific thrust as a function of power are shown in Fig. 6.17 for different pressures. ΔF increases to 225 μN for 75 Torr and 1 W. ΔF increases rapidly with small power and saturates at higher powers for all pressures. As a result, the specific thrust T_s decreases with power. The saturation with power is due to increases in power losses (conduction to a larger area of walls with a larger ΔT), and to a smaller degree sheath losses and expansion of the plasma. However, for a given power, T_s is higher at higher pressures.

A comparison of flow properties for a constant energy deposition per atom (0.14

eV/atom) and constant residence time (13 μ s) is shown in Fig. 6.18. Since the flow-rate is increased in proportion to pressure, the velocity profiles for cold flow are essentially the same. With power deposition, ΔT is higher at higher pressures due to concentration of the plasma in a smaller volume and so axial speeds are higher at higher pressure. The incremental thrust ΔF increases almost linearly with pressure whereas the T_s is almost a constant with pressure due to the eV per atom being constant.

In this configuration of the micro-arc, the peak gas temperature occurs in a stagnation region at the tip of the cathode which may not be optimum with respect to creating thrust. Since power deposition occurs dominantly adjacent to the cathode, increasing the cathode surface area reduces the specific power density but also may place gas heating more optimally in the flow path. To investigate these issues, the geometry shown in Fig. 6.19 was used with the downstream electrode being the cathode and the on axis cylindrical electrode being the anode. A layer of dielectric is added around the anode to prevent plasma formation inside the annulus. The angle of the nozzle is 45°.

Plasma and flow properties for 100 Torr, 100 sccm, and 1 W are shown in Fig. 6.20. Power deposition and ionization sources extend over the cathode surface and as a result, the plasma also extends over the entire surface of the cathode. Although the peak in specific power deposition occurs in front of the anode due to geometrical electric field enhancement and electron acceleration, the absolute magnitude of power deposition near the anode is small due to the small volume. The power deposition heats the gas adjacent to the cathode leading to a peak T_g of 485 K, a lower than in the previous geometries because the specific power deposition is lower. For example, for a comparable energy deposition per atom, $\Delta T = 300$ K in the micro-arc whereas it is 185 K in this case. Due to a large divergence angle of the

nozzle, the gas flow out of the throat is separated from the cathode and so is not well coupled to the heated gas near its surface. As a result of a low ΔT and separation of flow from the heated volume, there is not a significant enhancement of the thrust above the cold gas value.

Gas temperature and ΔF as a function of cathode divergence angle (5-45°) are shown in Fig. 6.21 for 100 Torr, 1 W, and 100 sccm. T_g is a function of the power density and its coupling to the flowfield. For a nozzle angle is 45°, the major heating occurs in a region of low flow that is separated from the flow emerging from the nozzle. As the nozzle angle decreases, the flow separation is less severe and the flow is closer to the cathode surface. This allows for better mixing which results in a lower T_g but higher ΔF . However, as the nozzle divergence angle is reduced to 5°, the peak power density increases as the volume of the discharge is lower, leading to an increase in peak gas temperatures in spite of mixing of the flow. The ΔF as a function of the nozzle divergence angle is shown in Fig. 6.22. The divergence angle influences the incremental thrust due to the interplay between the flowfield and the power deposition regions. For large divergence angles, the flow is separated from the cathode surface, and due to formation of re-circulation zones, the performance of the thruster is negative. For very small angles, the flow is parallel to the surface of the cathode, and since the length of the nozzle is significantly high in these cases, there is considerable loss due to heat transfer and viscous dissipation of momentum leading to a lower performance of the thruster. For this case (5° divergence), the ΔF is 65 μN near the throat of the nozzle and -7 μN at the exit plane. Thus, in this case, the addition of nozzle is actually detrimental from the viewpoint of flow. This is also in agreement with the findings of Ivanov et al.[26] However, the nozzle cannot be avoided in this case as it forms the cathode. In general, the performance of the anode-wire geometry is worse than the micro-arc

geometry due to lower temperatures and large surface areas in contact with the plasma.

6.4 Concluding Remarks

A computational investigation was performed of cylindrically-symmetric dc MDs with an emphasis on their ability to convert discharge power into thermal power for use as micro-thrusters. A variety of discharge configurations were used to study the coupling of discharge power and flow to optimize thrust. In these MDs, the plasma is sustained by ionization by both bulk and secondary electrons. The power deposition is typically concentrated near the cathode surface, leading to high power densities and high gas temperatures, and so geometries which optimize the overlap between gas flow and peak power deposition tend to maximize thrust. In general, discharges that were confined inside the nozzle (by, for example, the location of the electrodes, shape of the nozzle or by operating conditions such as pressure, power) produced higher gas heating and larger incremental thrusts ranging from 50 – 200 μN for power deposition of 0.25 – 2 W. In this regard, the nozzle divergence angle is an important consideration since flow separation can decouple volumes where gas heating is large from the flow that produces thrust. ΔF generally scales sub-linearly with power for a given pressure, producing lower values of specific thrust, T_s , due to rarefaction which reduces the specific power deposition.

6.5 Figures

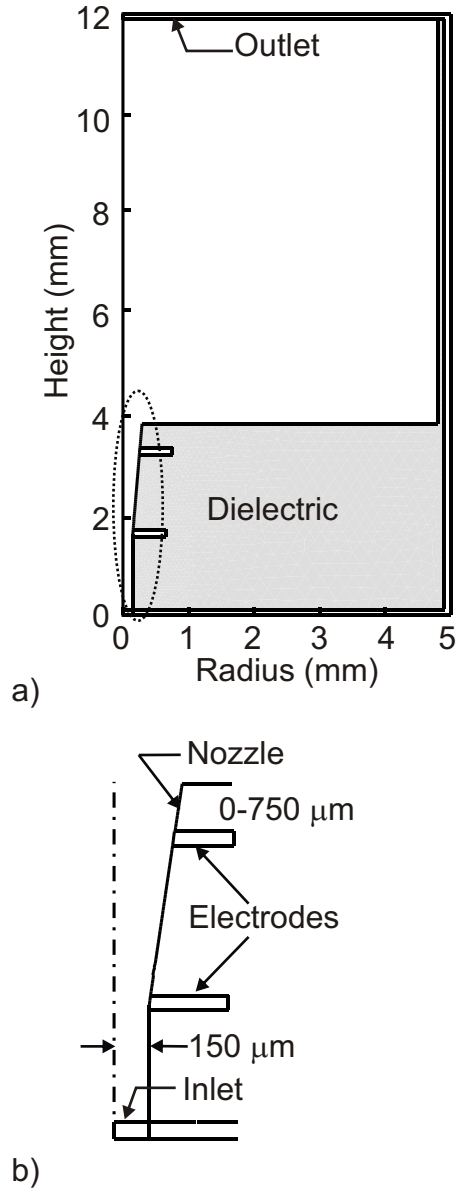


Fig. 6.1: Geometry of the sandwich type microdischarge: a) Entire geometry, b) Zoomed portion.

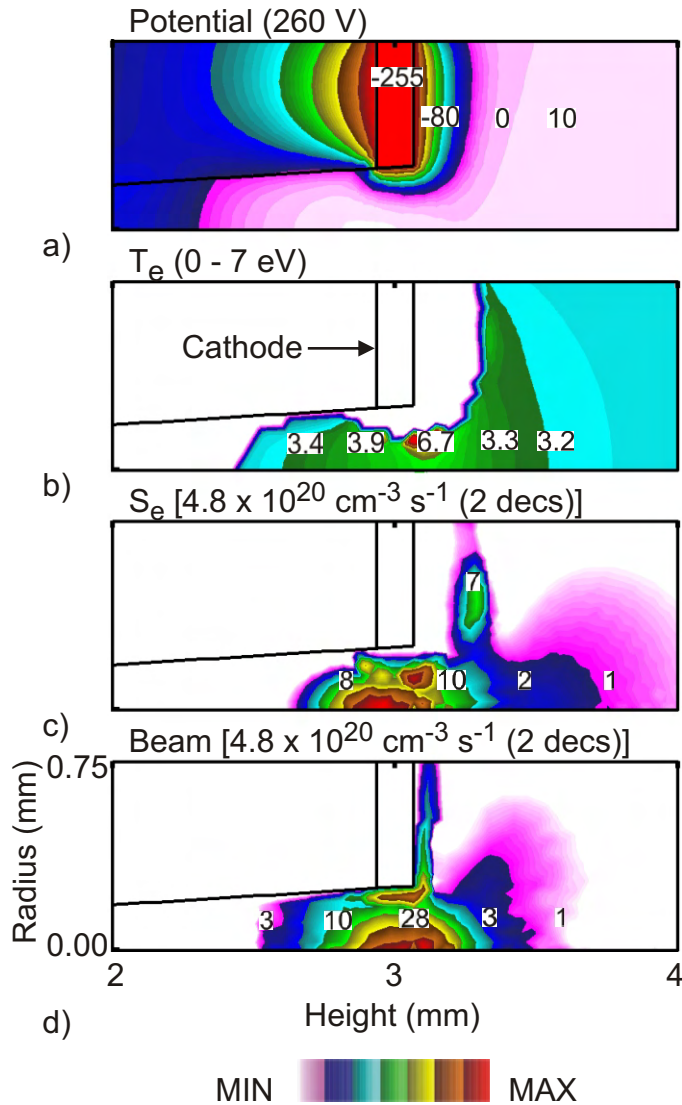


Fig. 6.2: Plasma characteristics of the microdischarge geometry for a power deposition of 1.0 W, 30 sccm of Ar flow at 30 Torr inlet pressure. a) Plasma potential, b) electron temperature (only where $n_e > 10^{-3}$ of peak values, c) ionization due to bulk electrons, and d) ionization by beam electrons. The ionization sources are plotted on a 2-decade log scale.

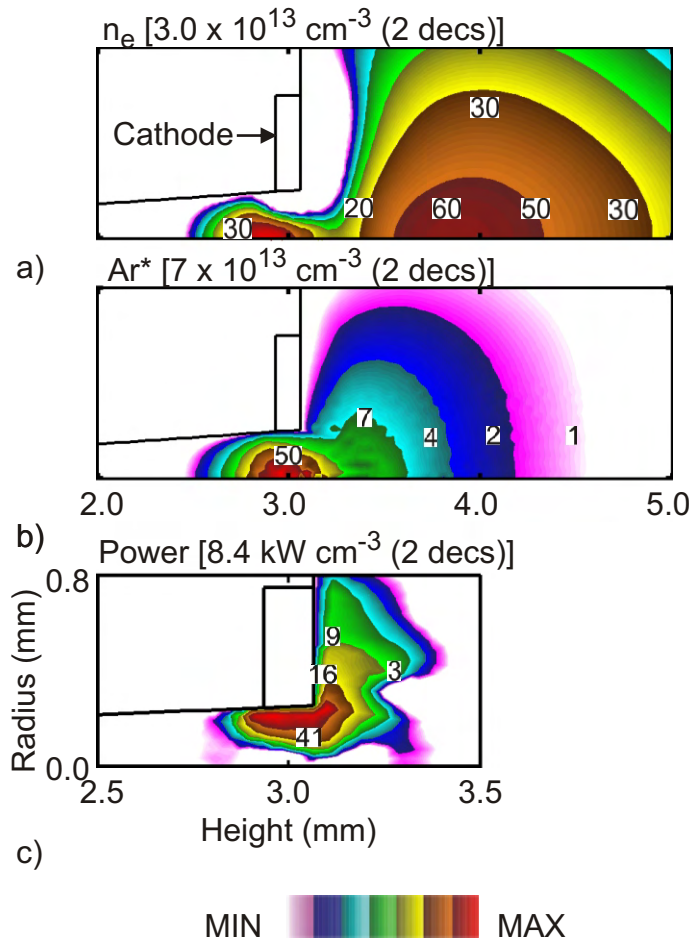


Fig. 6.3: a) Electron density, b) Ar^* density, and c) power deposition for base case conditions of 1.0 W, 30 sccm of Ar flow at 30 Torr inlet pressure. All plots are on a 2-decade log scale.

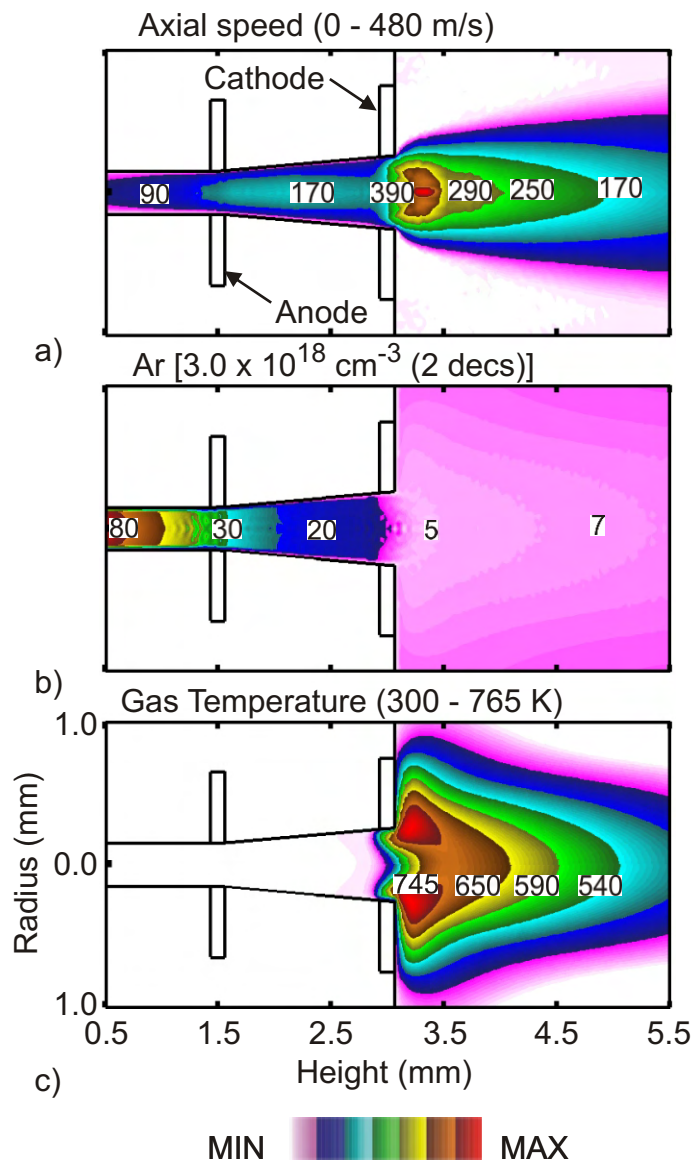


Fig. 6.4: Neutral flow characteristics for the microdischarge geometry for a power deposition of 1.0 W, 30 sccm of Ar flow at 30 Torr inlet pressure. a) Axial speed, b) Ar density, and c) T_g .

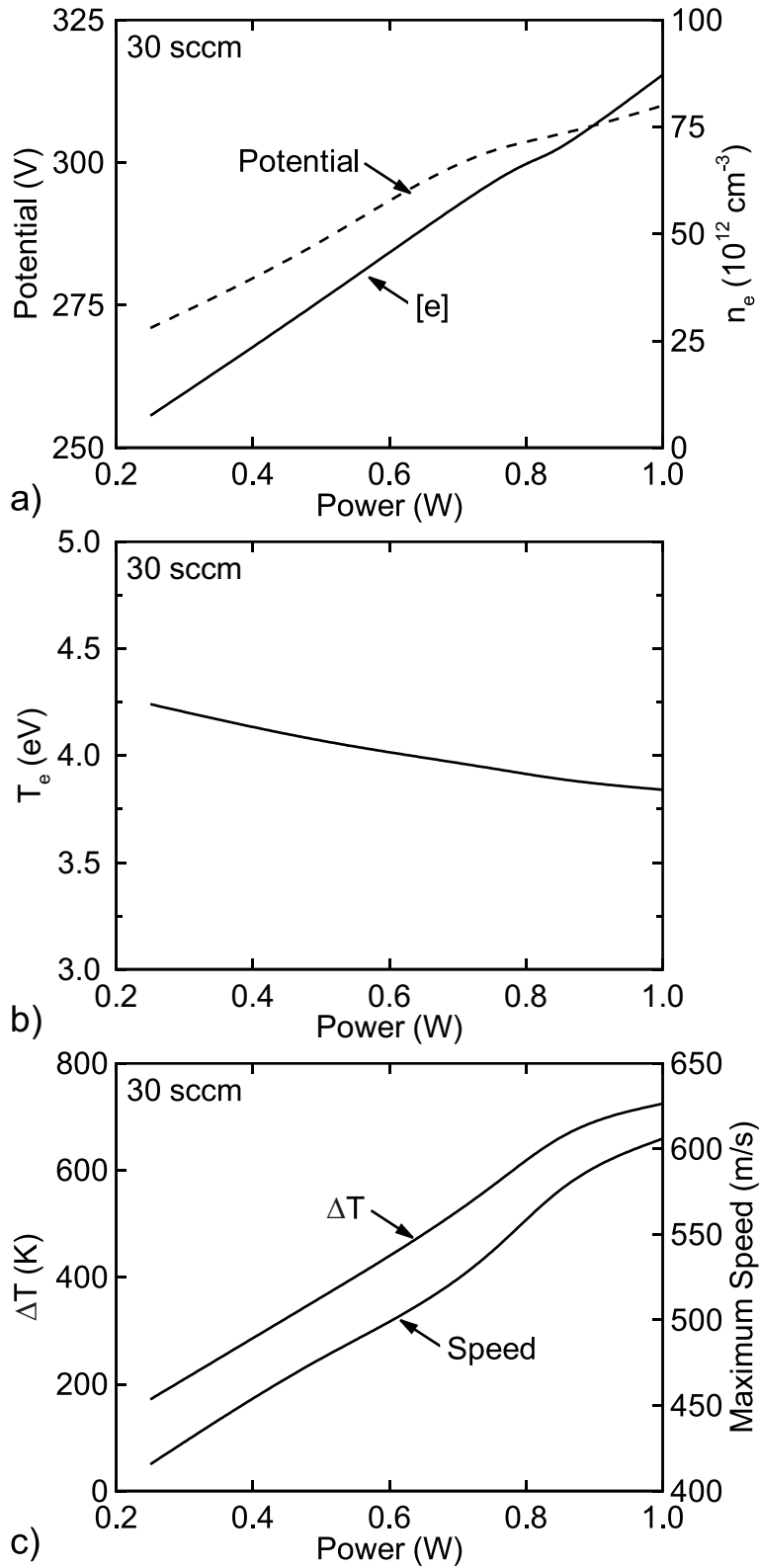


Fig. 6.5: Plasma and flow characteristics while varying power for 30 Torr, 30 sccm of Ar. a) Plasma potential and $[e]$, b) T_e and c) ΔT and axial speed.

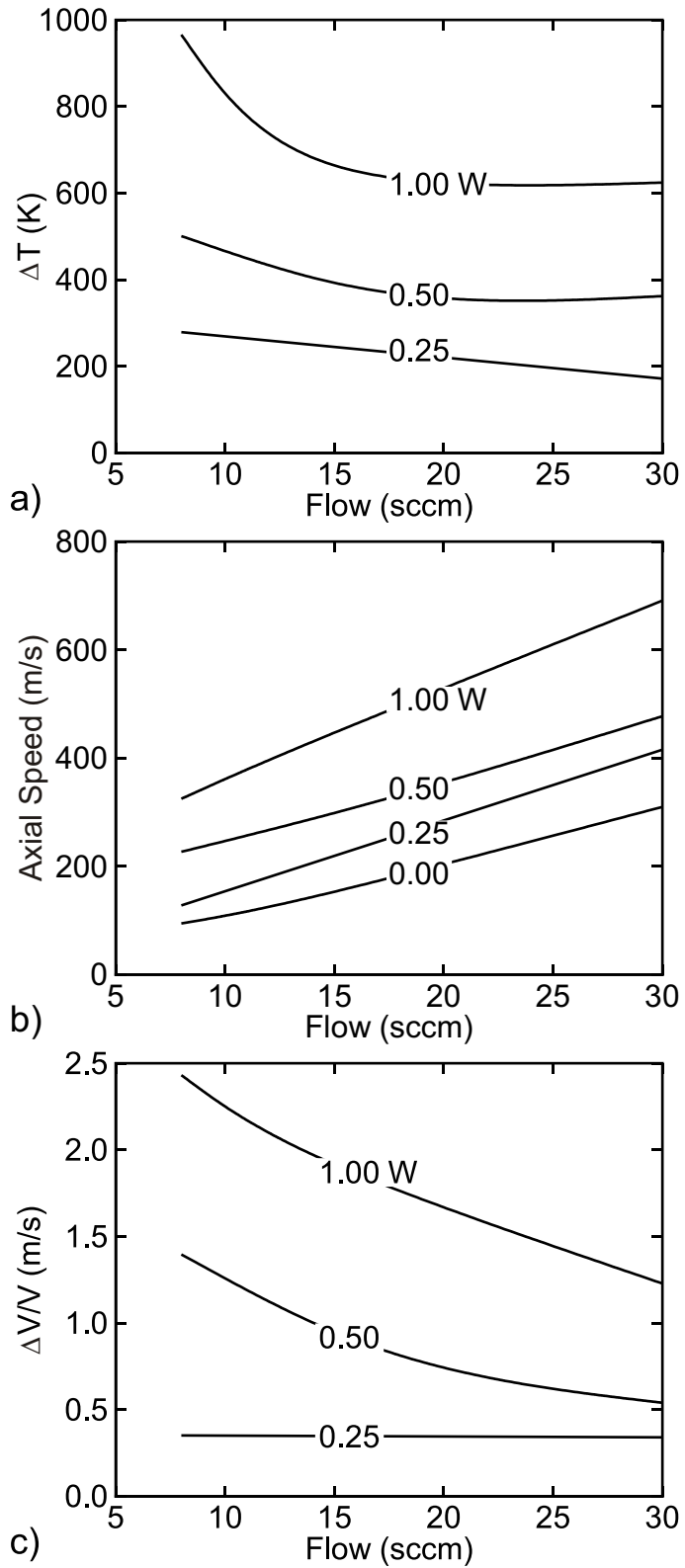


Fig. 6.6: Plasma and flow properties as a function of flow rate for different power deposition at 30 Torr inlet pressure. a) ΔT , b) axial velocity, and c) relative incremental velocity ($\Delta V/V$).

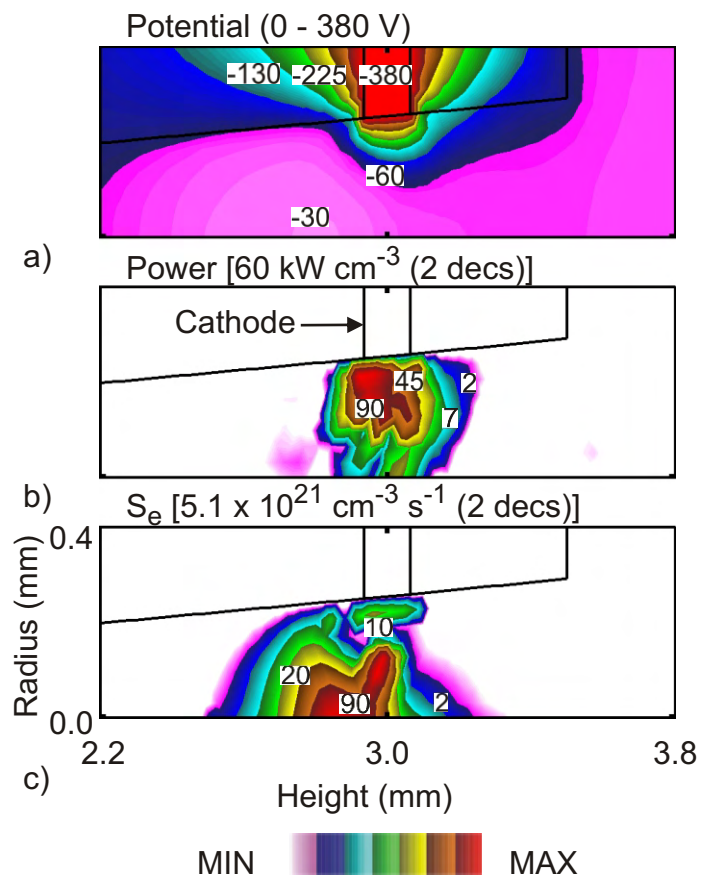


Fig. 6.7: Plasma properties for the sandwich-type discharge with a $500 \mu\text{m}$ dielectric layer over the cathode. a) Potential, b) power density, and c) ionization sources.

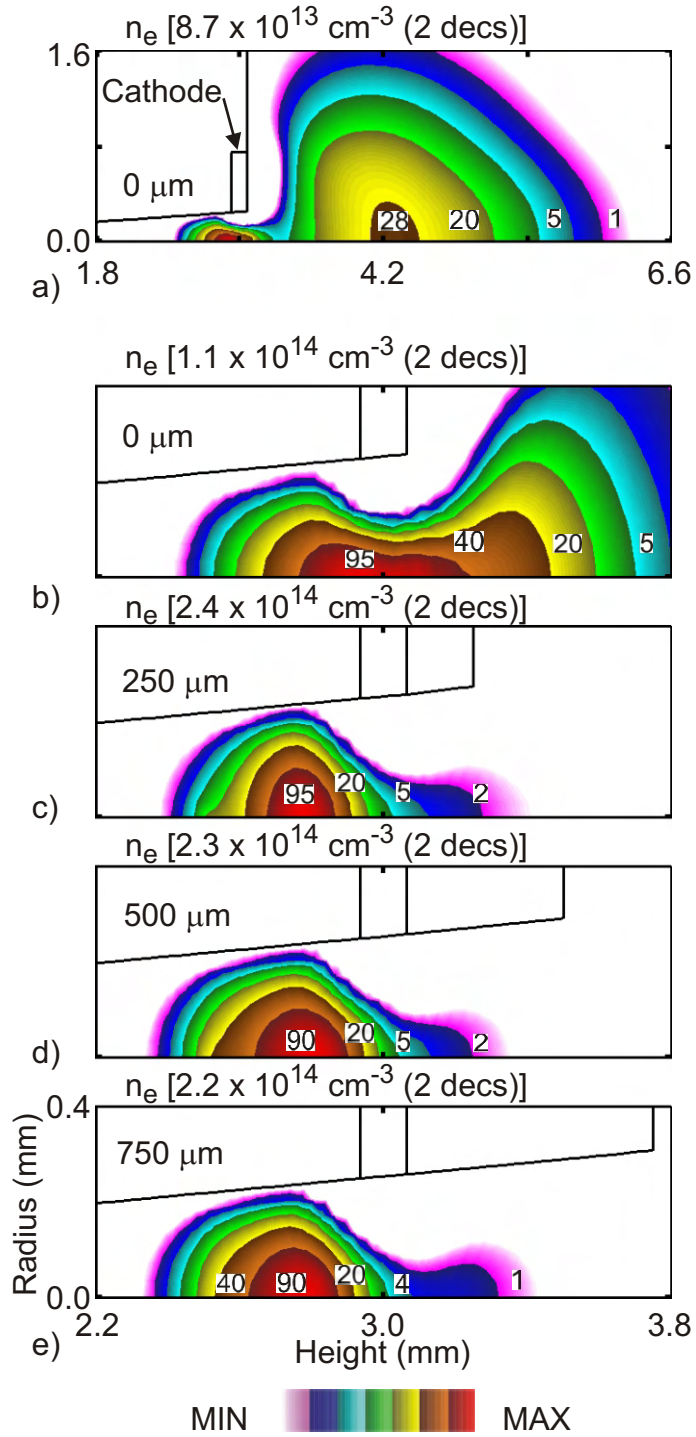


Fig. 6.8: Effect of geometry on plasma density for 30 Torr, 30 sccm, 1 W power deposition. The thickness of dielectric layer on top of the cathode is varied from 0 - 750 μm . a) 0 μm , b) 0 μm with no secondary emission from top surface, c) 250 μm , d) 500 μm , and e) 750 μm . The contours are plotted on a 2-decade log scale.

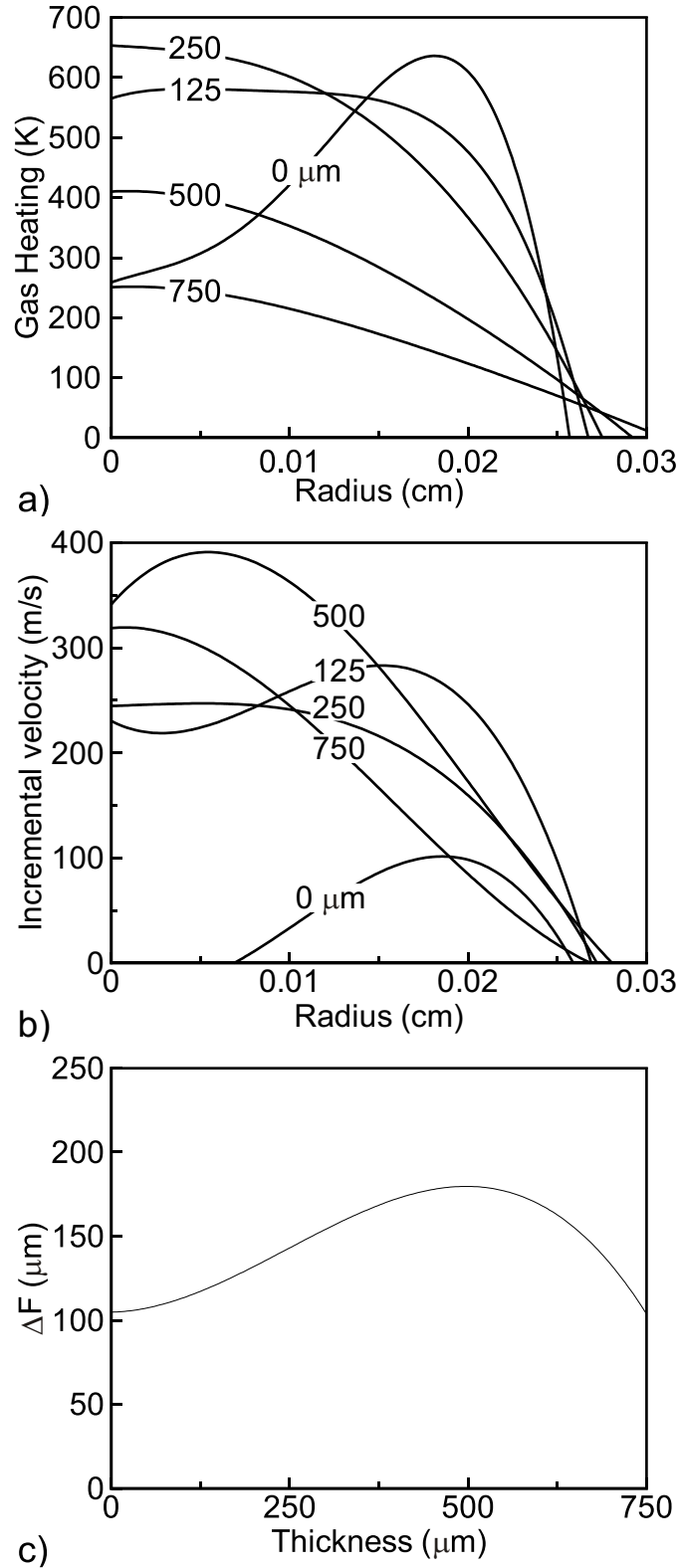


Fig. 6.9: Effect of the dielectric thickness on neutral flow properties at the exit of the nozzle for 30 Torr, 30 sccm, 1.0 W power deposition. a) ΔT , b) ΔV (from the cold flow), and c) ΔF . Note that the exit plane is different for different geometries.

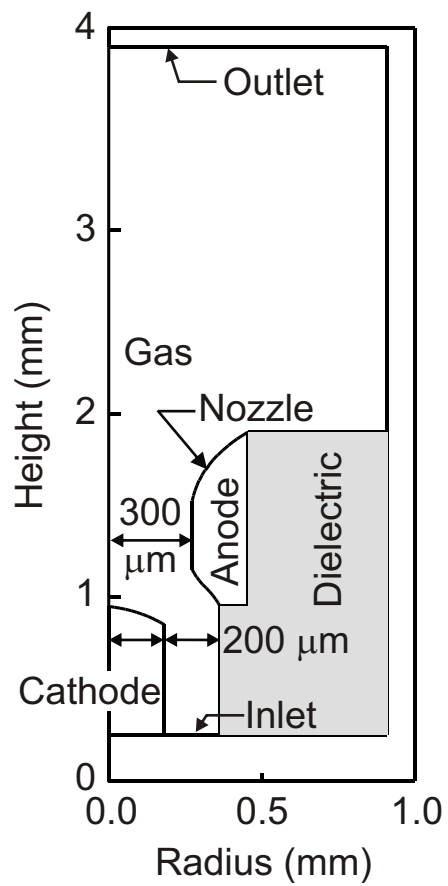


Fig. 6.10: Schematic of the reactor with co-axial flow and axial separation of the electrodes (micro-arc geometry).

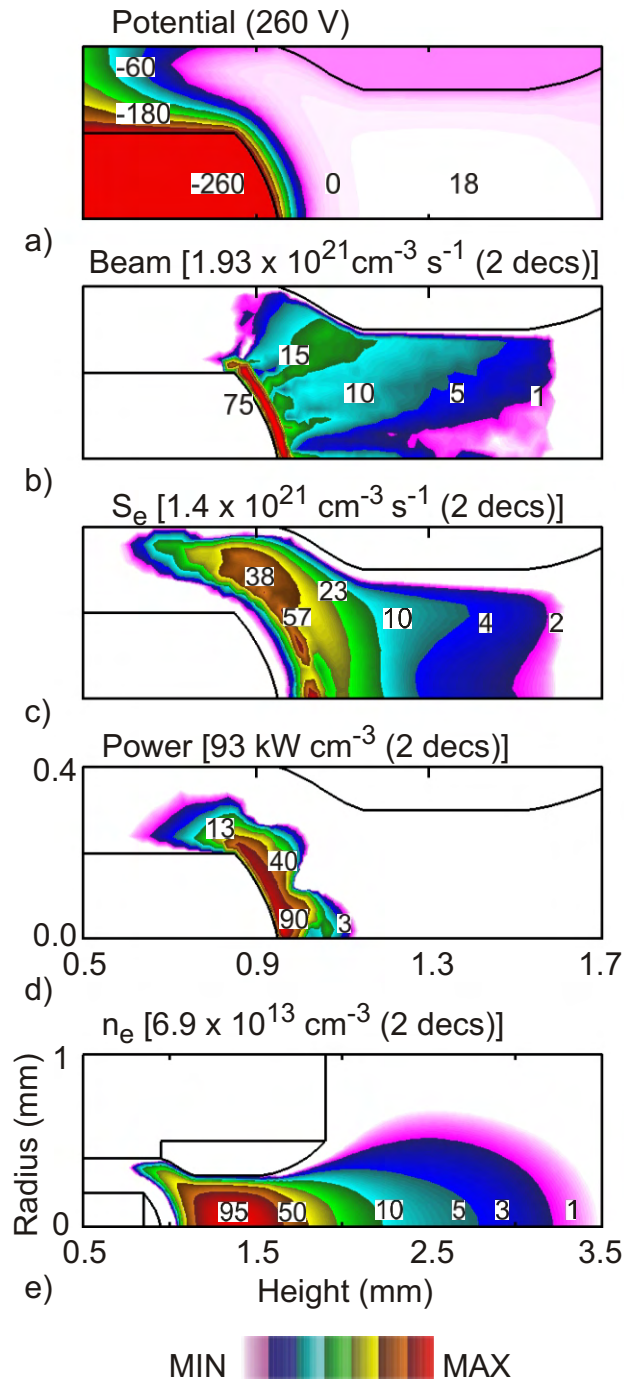


Fig. 6.11: Plasma characteristics for the micro-arc geometry for 1 W power deposition, 25 sccm of Ar at 25 Torr inlet pressure. a) Plasma potential, b) ionization by beam electrons, c) ionization by bulk electrons, d) power deposition, and e) n_e . All contours except the potential are on a 2-decade log scale.

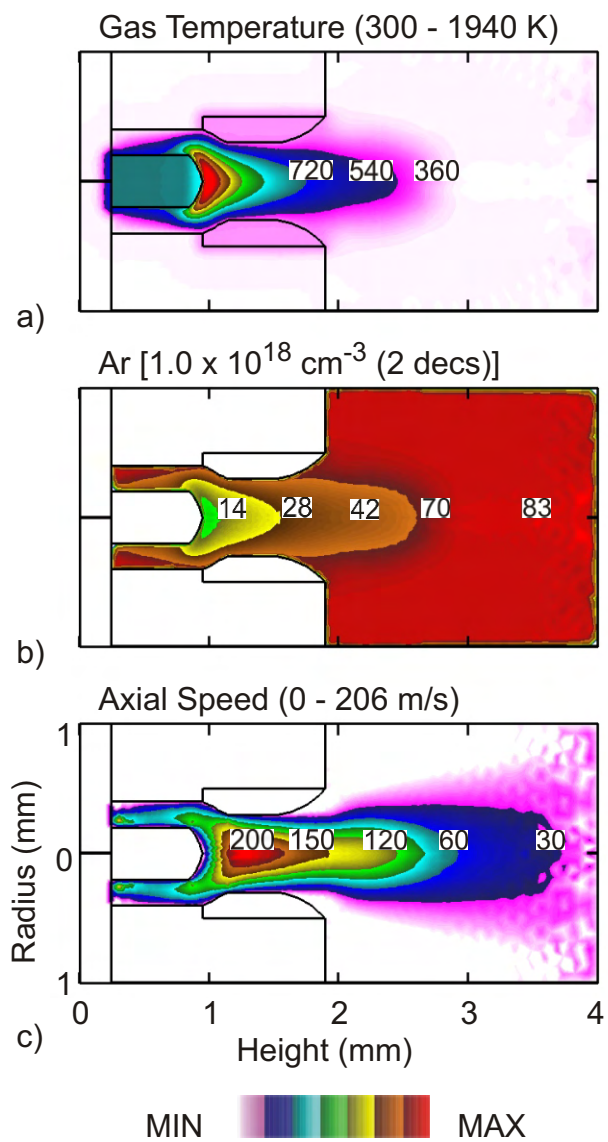


Fig. 6.12: Flow characteristics for the micro-arc geometry for 1.0 W power deposition, 25 sccm of Ar at 25 Torr inlet pressure. a) T_g , b) Ar density, and c) axial speed. Argon density is plotted on a 2-decade log scale.

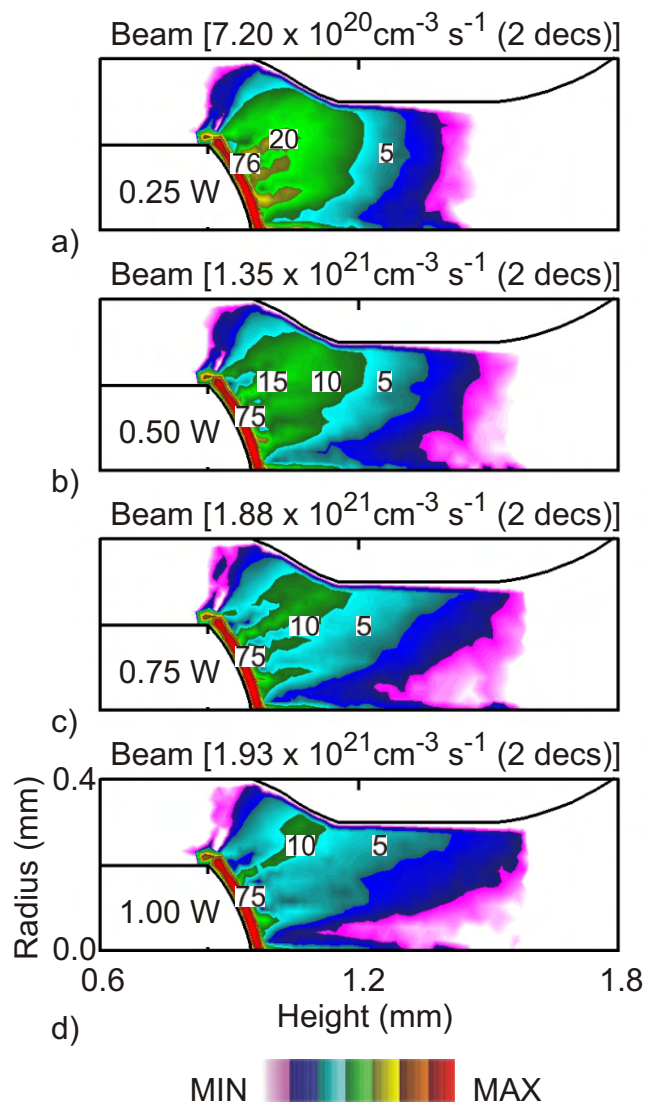


Fig. 6.13: Beam ionization sources while varying power deposition for 25 sccm of Ar at 25 Torr pressure. a) 0.25 W, b) 0.50 W, c) 0.75 W, and d) 1.00 W. The contours are plotted on a 2-decade log scale.

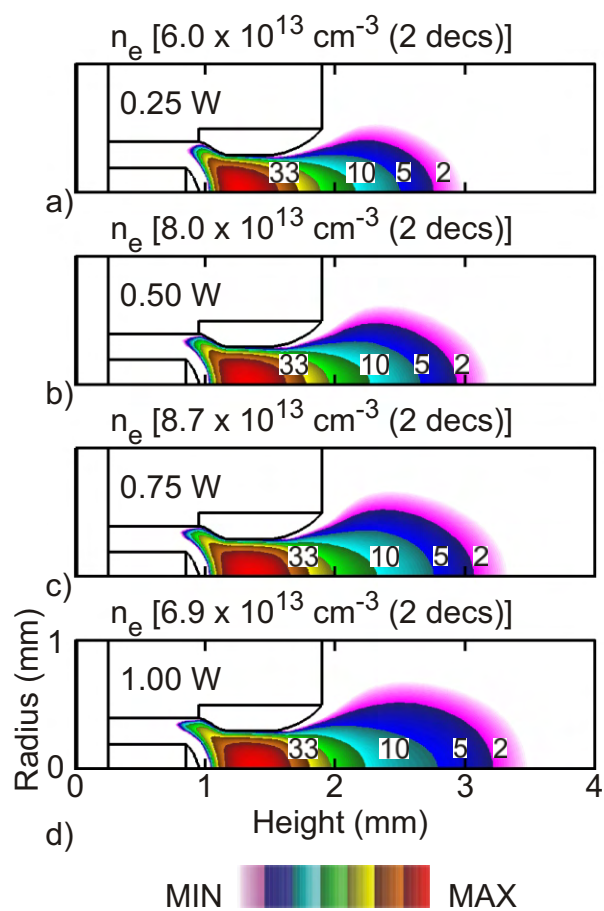


Fig. 6.14: Electron density as a function of power for 25 Torr, 25 sccm Ar. a) 0.25 W, b) 0.50 W, c) 0.75 W, and d) 1.00 W. The contours are plotted on a 2-decade log scale.

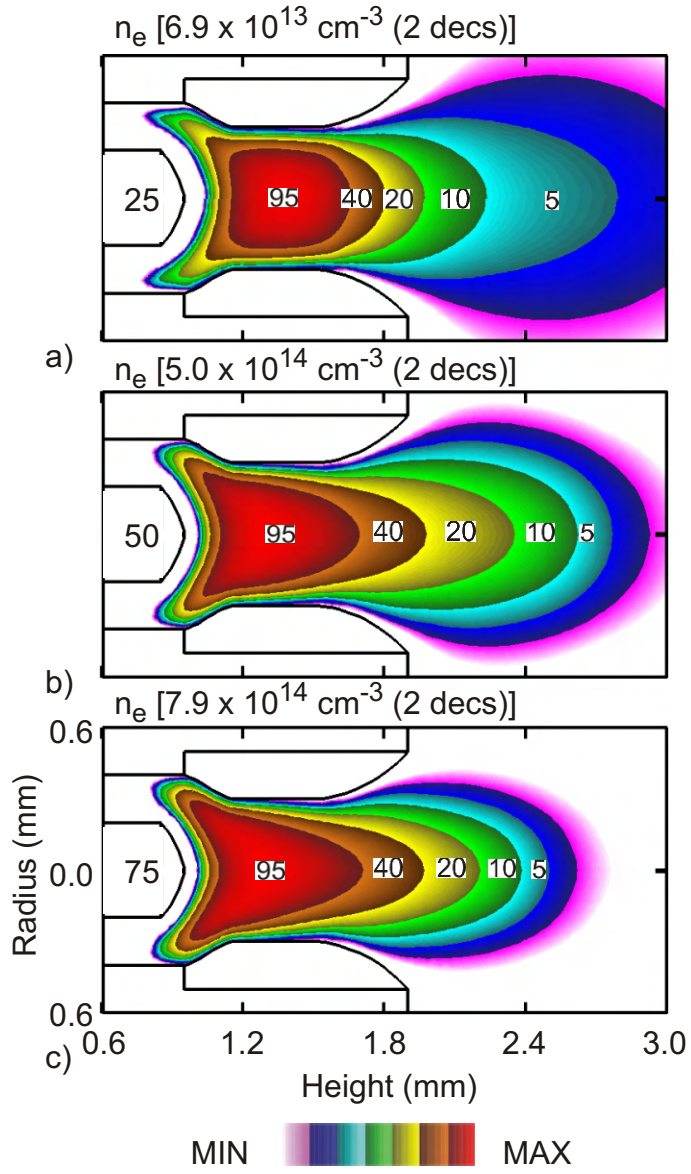


Fig. 6.15: N_e as a function of pressure for a 1 W power deposition. a) 25 Torr, b) 50 Torr, and c) 75 Torr.

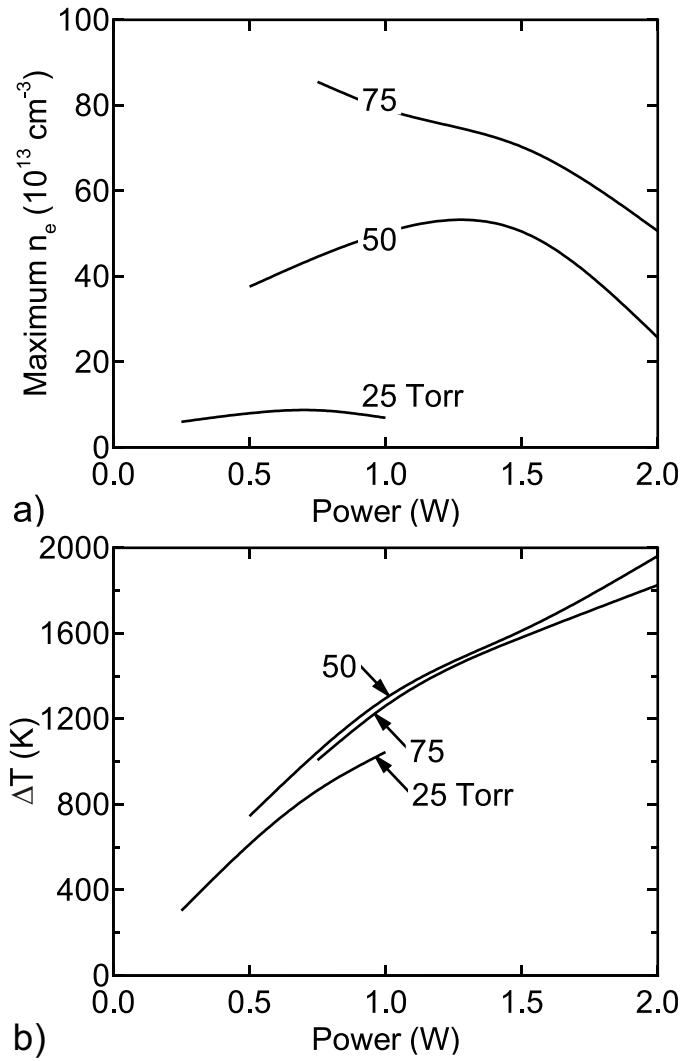


Fig. 6.16: Plasma and flow characteristics as a function of power and pressure for the micro-arc geometry. a) Maximum n_e , and b) ΔT .

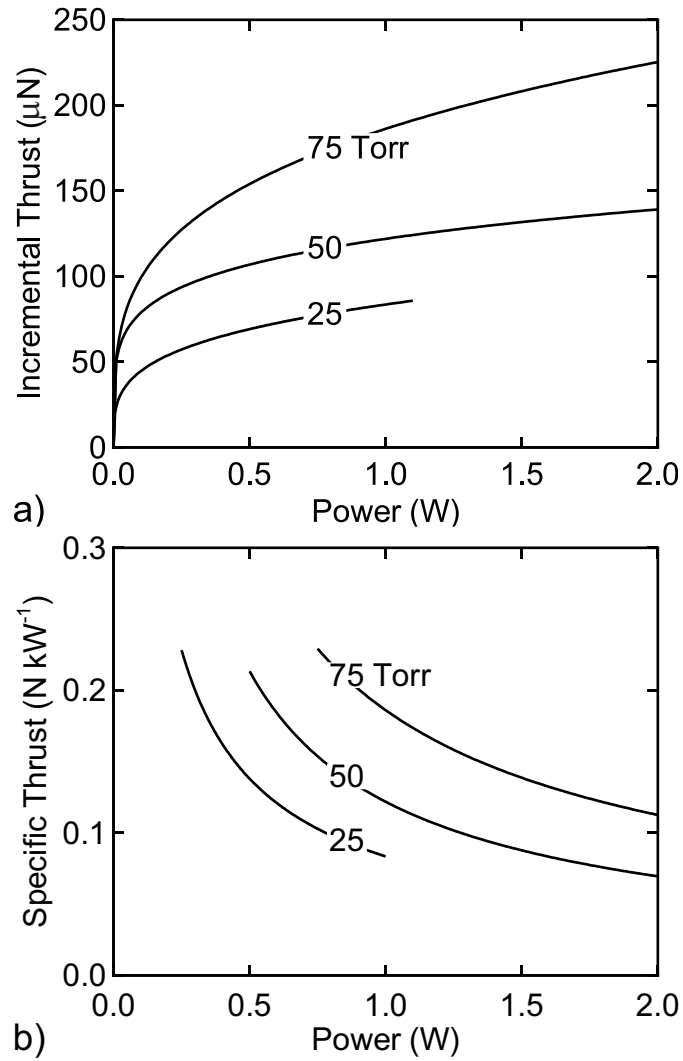


Fig. 6.17: Incremental thrust and specific thrust (Thrust per unit power) as a function of power for different pressures. a) Incremental thrust, b) Specific thrust.

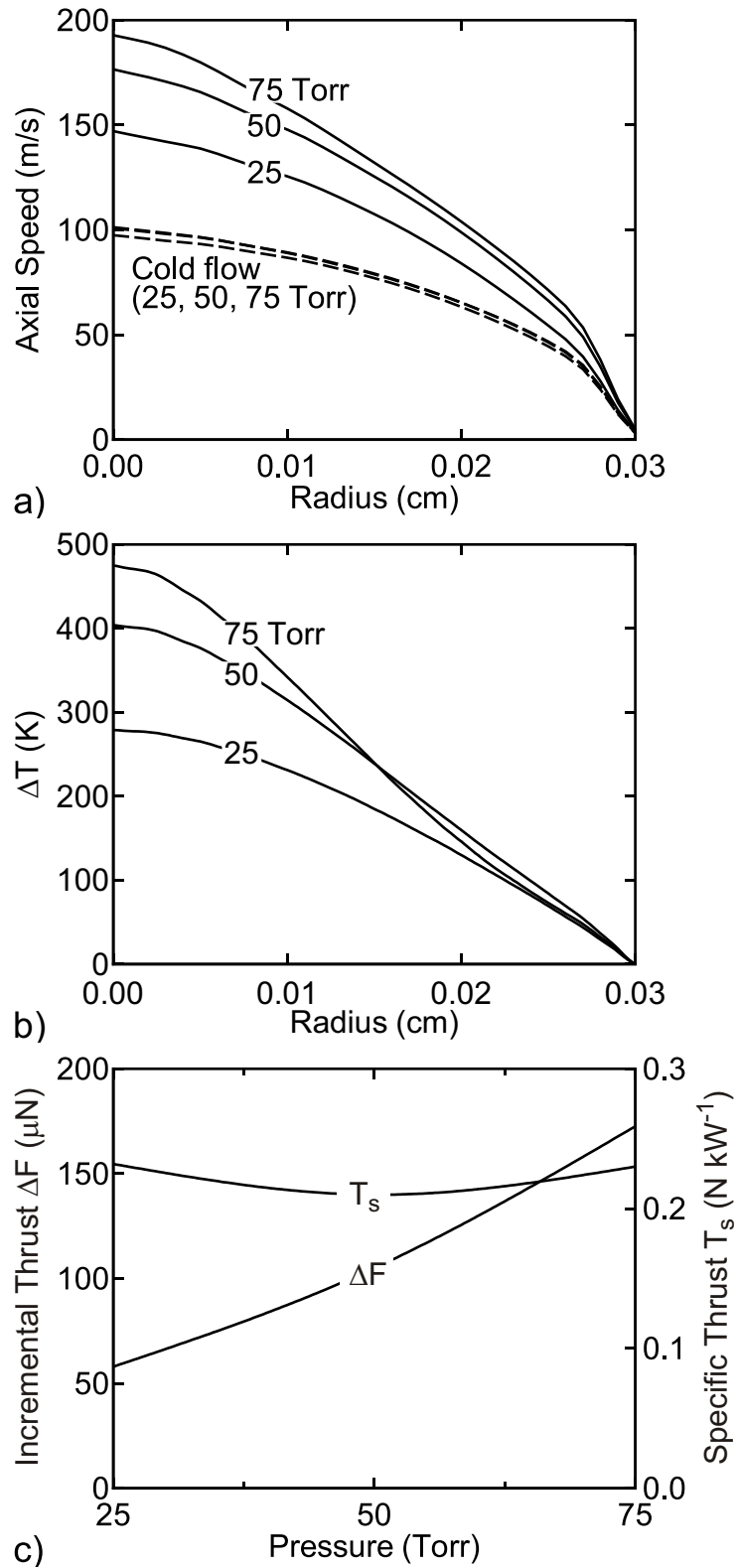
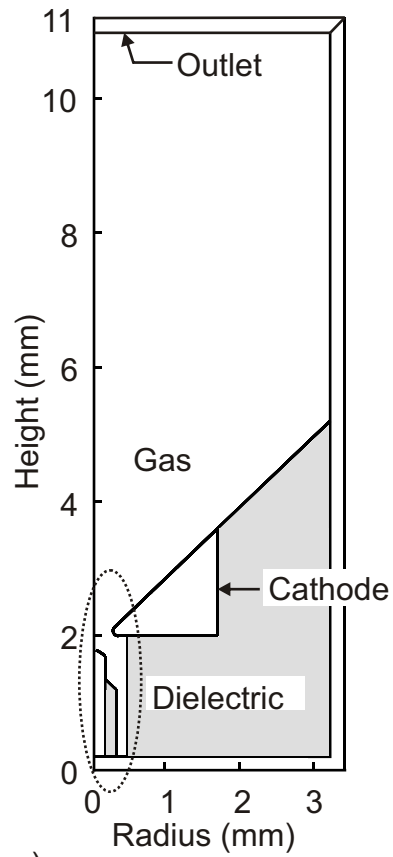
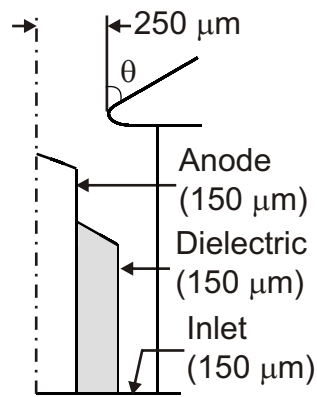


Fig. 6.18: Flow properties as a function of pressure for the same eV per Ar atom. a) Axial Speed profile, b) ΔT and c) Incremental thrust and specific thrust.



a)



b)

Fig. 6.19: Anode-wire geometry with the downstream electrode as the cathode. Dielectric coating added to the anode wire to prevent discharge inside the tube. Nozzle divergence angle varied from 5- 45°.

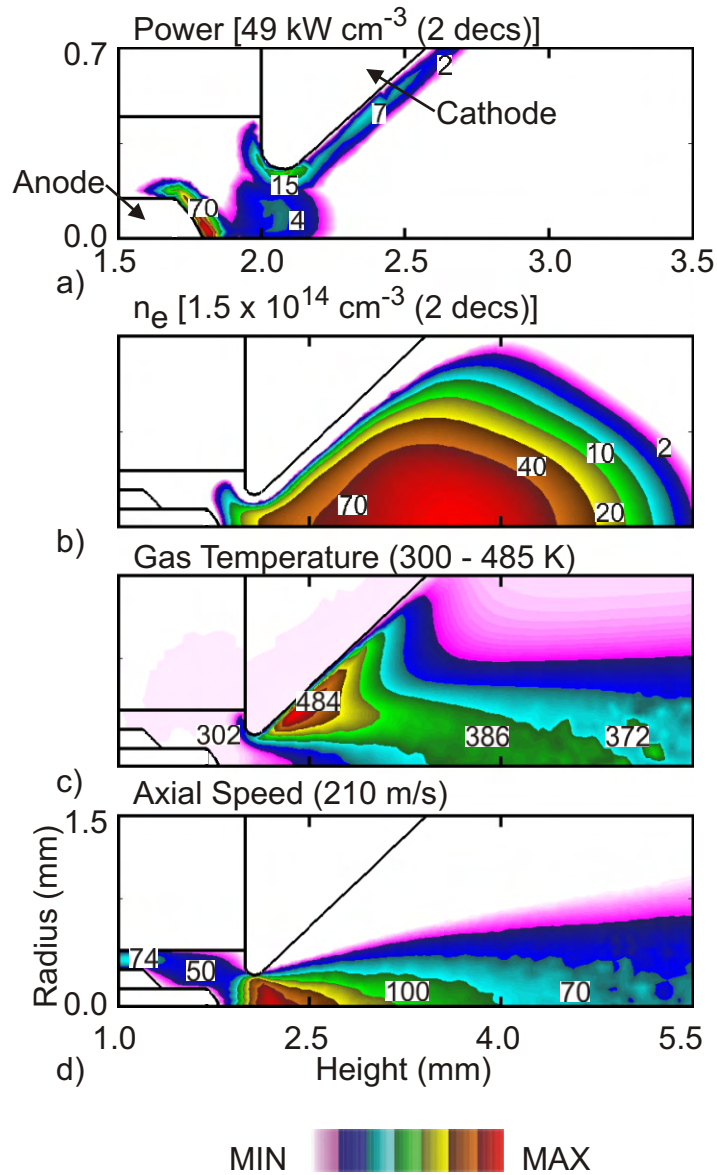


Fig. 6.20: Plasma and flow properties for the anode-wire geometry with 45° nozzle divergence for 100 sccm Ar, 100 Torr, and 1 W power deposition. a) Power, b) n_e , c) T_g , and d) axial speed.

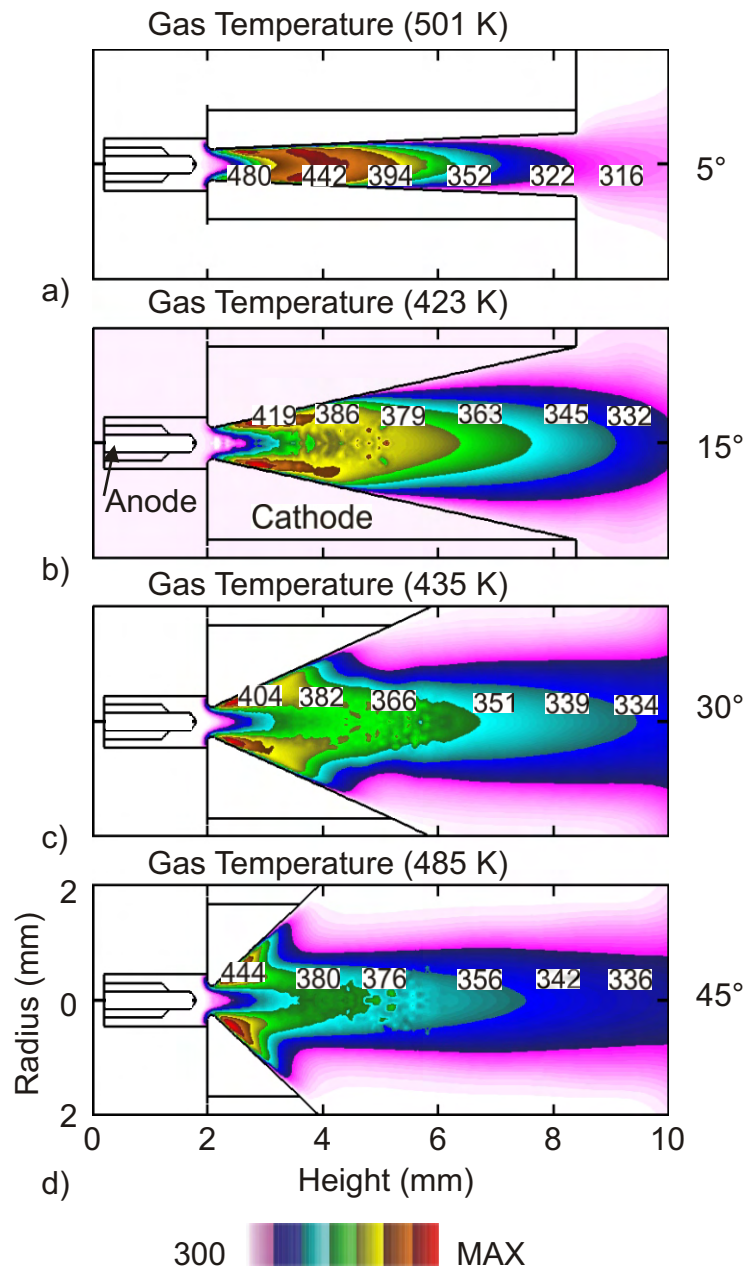


Fig. 6.21: Gas temperature for different nozzle divergence angles. a) 5° b) 15°, c) 30°, and d) 45°.

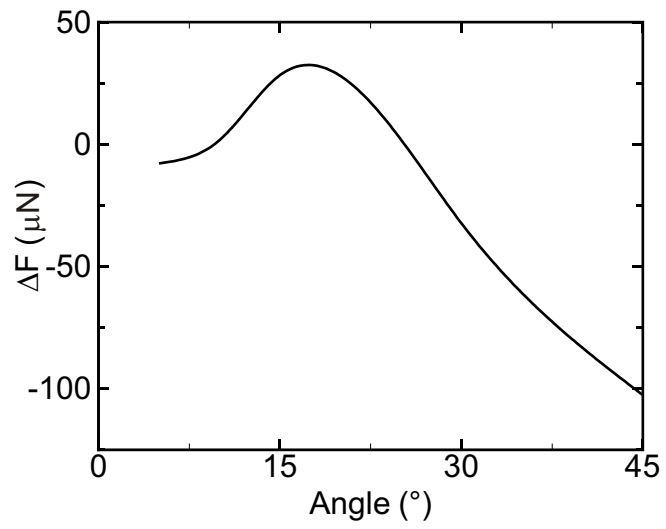


Fig. 6.22: ΔF as a function of nozzle divergence angle for the anode-wire geometry.

6.6 References

1. S. W. Janson, H. Helvajian, W. W. Hansen and Lt. J. Lodmell, AIAA, 99-2722.
2. J. Mueller, “Thruster Options for Microspacecraft: A Review and Evaluation of State-of-the-Art and Emerging Technologies”, in *Micropropulsion for Small Spacecraft*, ed. M. M. Micci and A. D. Ketsdever, (AIAA, Reston, VA, 2000).
3. M. Martinez-Sanchez and J. E. Pollard, *J. Prop. Power* **5**, 688 (1998).
4. R. L. Burton and P. J. Turchi, *J. Prop. Power* **5**, 716 (1998).
5. R. G. Jahn, *Physics of Electric Propulsion*, McGraw-Hill, NY (1989).
6. Moselhy and Schoenbach, *J. Appl. Phys.* **95**, 1642 (2004).
7. H. Qiu, K. Martus, W. Y. Lee and K. Becker, *Intl. J. Mass Spect.* **233**, 19 (2004).
8. D. D. Hsu and D. B. Graves, *Plasma Chem. Plasma Proc.* **25**, 1 (2005).
9. R. M. Sankaran and K. P. Giapis, *J. Appl. Phys.* **92**, 2406 (2002).
10. J. L. Lauer et al, *J. Appl. Phys.* **96**, 4539 (2004).
11. T. Kikuchi, Y. Hasegawa and H. Shirai, *J. Phys. D: Appl. Phys.* **37**, 1537 (2004).
12. T. Ichiki, R Taura, and Y Horiike, *J Appl. Phys.* **95**, 35 (2004).
13. J. G. Eden, S. –J. Park, N. P. Ostrom and K. –F. Chen, *J. Phys. D: Appl. Phys.* **38**, 1644 (2005).
14. H. Horisawa and I. Kimura, AIAA 2001-3791.
15. J. Slough, S. Andreason, T. Ziemba and J. J. Ewing, AIAA 2005-4074.
16. P. S. Kothnur and L. L. Raja, *J. Appl. Phys.* **97**, 043305 (2005).
17. Y. Takao and K. Ono, AIAA 2004-3621.
18. M J Kushner, *J. Appl. Phys.* **95** 846 (2004).

19. R. A. Arakoni, D. S. Stafford, N. Y. Babaeva and M. J. Kushner, *J. Appl. Phys.* **98** 073304 (2005).
20. D. L. Scharfetter and H. K. Gummel, *IEEE Trans. Electron Dev.* **16**, 64 (1969).
21. S. D. Rockwood, *Phys. Rev. A* **8**, 2348 (1973).
22. A. N. Bhoj and M. J. Kushner, *J. Phys. D.* **37**, 2510 (2004).
23. S. A. Schaaf and P. L. Chambre, “Flow of Rarefied Gases”, Princeton University Press, NJ, USA (1961).
24. K. L. Williams et al, *J. Micromech. Microeng.* **16**, 1154 (2006).
25. J. Slough and J. J. Ewing, AIAA 2007-5181.
26. M. Ivanov, G. Markelov, A. Ketsdever and D. Wadsworth, AIAA 1999-0166.

APPENDIX A. LIST OF REACTIONS FOR He/O₂ PLASMAS

<u>List of Species</u>		
e	He	O [*]
He ⁺	He [*]	O ¹ S
O ₂ ⁺	He ^{**}	O
O ₂ ⁻	O ₂	O ₃
O ⁺	O ₂ (v)	
O ⁻	O ₂ [*]	
O ₃ ⁻	O ₂ ^{*1} S	
<u>Reactions</u>	<u>Rate Coefficient^a</u>	<u>Reference</u>
$e + \text{He} \rightarrow \text{He}^* + e$	b	1
$e + \text{He} \rightarrow \text{He}^{**} + e$	b	1
$e + \text{He} \rightarrow \text{He}^+ + e + e$	b	2
$e + \text{He}^* \rightarrow \text{He}^+ + e + e$	b	3
$e + \text{He}^* \rightarrow \text{He} + e$	b	c
$e + \text{He}^+ \rightarrow \text{He}^*$	$6.76 \times 10^{-13} T_e^{-0.5}$	4
$e + e + \text{He}^+ \rightarrow \text{He}^* + e$	$5.12 \times 10^{-27} T_e^{-4.5}$	4
$e + \text{O}_2 \rightarrow \text{O}^- + \text{O}$	b	5
$e + \text{O}_2 \rightarrow \text{O}_2(\text{v}) + e$	b	5
$e + \text{O}_2 \rightarrow \text{O}_2(\text{v}) + e$	b	5

$e + O_2 \rightarrow O_2(v) + e$	b	5
$e + O_2 \rightarrow O_2(v) + e$	b	5
$e + O_2 \rightarrow O_2^* + e$	b	5
$e + O_2 \rightarrow O_2^{*1}S + e$	b	5
$e + O_2 \rightarrow O + O + e$	b	5
$e + O_2 \rightarrow O^* + O + e$	b	5
$e + O_2 \rightarrow O_2^+ + e + e$	b	5
$e + O_2 \rightarrow O^+ + O + e + e$	b	5
$e + O_2(v) \rightarrow O^- + O$	b	d
$e + O_2(v) \rightarrow O_2 + e$	b	c
$e + O_2(v) \rightarrow O_2^* + e$	b	e
$e + O_2(v) \rightarrow O_2^{*1}S + e$	b	e
$e + O_2(v) \rightarrow O + O + e$	b	e
$e + O_2(v) \rightarrow O^* + O + e$	b	e
$e + O_2(v) \rightarrow O_2^+ + e + e$	b	e
$e + O_2(v) \rightarrow O^+ + O + e + e$	b	e
$e + O_2^* \rightarrow O^- + O$	b	6
$e + O_2^* \rightarrow O_2(v) + e$	b	c
$e + O_2^* \rightarrow O_2^{*1}S + e$	b	7
$e + O_2^* \rightarrow O_2 + e$	b	c
$e + O_2^* \rightarrow O + O + e$	b	e

$e + O_2^* \rightarrow O^* + O + e$	b	e
$e + O_2^* \rightarrow O_2^+ + e + e$	b	e
$e + O_2^* \rightarrow O^+ + O + e + e$	b	e
$e + O_2^{*1}S \rightarrow O^- + O$	b	f
$e + O_2^{*1}S \rightarrow O_2(v) + e$	b	g
$e + O_2^{*1}S \rightarrow O_2^* + e$	b	g
$e + O_2^{*1}S \rightarrow O_2 + e$	b	c
$e + O_2^{*1}S \rightarrow O + O + e$	b	e
$e + O_2^{*1}S \rightarrow O^* + O + e$	b	e
$e + O_2^{*1}S \rightarrow O_2^+ + e + e$	b	e
$e + O_2^{*1}S \rightarrow O^+ + O + e + e$	b	e
$e + O_2 + M \rightarrow O_2^- + M^h$	$3.6 \times 10^{-31} T_e^{-0.5}$	8
$e + O_2(v) + M \rightarrow O_2^- + M^h$	$3.6 \times 10^{-31} T_e^{-0.5}$	8, e
$e + O_2^+ \rightarrow O + O$	$1.2 \times 10^{-8} T_e^{-0.7}$	9
$e + O_2^+ \rightarrow O^* + O$	$8.88 \times 10^{-9} T_e^{-0.7}$	9
$e + O_3 \rightarrow O^- + O_2$	b	10
$e + O_3 \rightarrow O_2^- + O$	b	10
$e + O \rightarrow O^* + e$	b	11
$e + O \rightarrow O^1S + e$	b	11
$e + O \rightarrow O^+ + e + e$	b	11
$e + O^* \rightarrow O + e$	b	c

$e + O^* \rightarrow O^+ + e + e$	b	e
$e + O^1S \rightarrow O + e$	b	c
$e + O^1S \rightarrow O^+ + e + e$	$6.6 \times 10^{-9} T_e 0.6 e^{-9.43/T_e}$	e
$e + O^- \rightarrow O + e + e$	$1.95 \times 10^{-12} T_e^{0.5} e^{-3.4/T_e}$	12
$e + O^+ \rightarrow O^*$	$5.3 \times 10^{-13} T_e^{-0.5}$	4
$e + e + O^+ \rightarrow O^* + e$	$5.12 \times 10^{-27} T_e^{-4.5}$	4
$O^- + O_2^+ \rightarrow O + O_2$	$2 \times 10^{-7} T_g^{-1.0}$	9
$O^- + O_2^+ \rightarrow O + O + O$	1×10^{-7}	9
$O^- + O^+ \rightarrow O + O$	$2 \times 10^{-7} T_g^{-1.0}$	9
$O^- + He^+ \rightarrow O + He$	$2 \times 10^{-7} T_g^{-1.0}$	9
$O_2^- + O_2^+ \rightarrow O_2 + O_2$	$2 \times 10^{-7} T_g^{-1.0}$	9
$O_2^- + O_2^+ \rightarrow O_2 + O + O$	1×10^{-7}	9
$O_2^- + O^+ \rightarrow O_2 + O$	$2 \times 10^{-7} T_g^{-1.0}$	9
$O_2^- + He^+ \rightarrow O_2 + He$	$2 \times 10^{-7} T_g^{-1.0}$	9
$O_3^- + O_2^+ \rightarrow O_3 + O_2$	$2 \times 10^{-7} T_g^{-1.0}$	9
$O_3^- + O_2^+ \rightarrow O_3 + O + O$	1×10^{-7}	9
$O_3^- + O^+ \rightarrow O_3 + O$	$2 \times 10^{-7} T_g^{-1.0}$	9
$O_3^- + He^+ \rightarrow O_3 + He$	$2 \times 10^{-7} T_g^{-1.0}$	9
$O^- + O_2^+ + M \rightarrow O + O_2 + M^h$	$2 \times 10^{-25} T_g^{-2.5}$	9
$O^- + O^+ + M \rightarrow O + O + M^h$	$2 \times 10^{-25} T_g^{-2.5}$	9
$O^- + He^+ + M \rightarrow O + He + M^h$	$2 \times 10^{-25} T_g^{-2.5}$	9

$O^- + O \rightarrow O_2 + e$	$2 \times 10^{-10} T_g^{0.5}$	13
$O^- + O_2^* \rightarrow O_3 + e$	$3 \times 10^{-10} T_g^{0.5}$	13
$O^- + O_2^* S \rightarrow O + O_2 + e$	$6.9 \times 10^{-10} T_g^{0.5}$	9
$O^- + O_2 \rightarrow O_3 + e$	$5 \times 10^{-15} T_g^{0.5}$	9
$O^- + O_2(v) \rightarrow O_3 + e$	$5 \times 10^{-15} T_g^{0.5}$	9, i
$O^- + O_3 \rightarrow O_2 + O_2 + e$	$3 \times 10^{-10} T_g^{0.5}$	13
$O^- + O_3 \rightarrow O_3^- + O$	$2 \times 10^{-10} T_g^{0.5}$	13
$O^- + O_3 \rightarrow O_2^- + O_2$	$1 \times 10^{-10} T_g^{0.5}$	13
$O_2^- + O \rightarrow O^- + O_2$	$1.5 \times 10^{-10} T_g^{0.5}$	13
$O_2^- + O \rightarrow O_3 + e$	$1.5 \times 10^{-10} T_g^{0.5}$	13
$O_2^- + O_2^* \rightarrow e + O_2 + O_2$	$2 \times 10^{-10} T_g^{0.5}$	13
$O_2^- + O_3 \rightarrow O_3^- + O_2$	$6 \times 10^{-10} T_g^{0.5}$	13
$O_3^- + O \rightarrow O_2^- + O_2$	$2.5 \times 10^{-10} T_g^{0.5}$	13
$O + O^+ + M \rightarrow O_2^+ + M^h$	$1 \times 10^{-29} T_g^{0.5}$	9
$O^+ + O_2 \rightarrow O_2^+ + O$	$2 \times 10^{-11} T_g^{-0.4}$	13
$O^+ + O_3 \rightarrow O_2^+ + O_2$	1.00×10^{-10}	9
$O^* + O \rightarrow O + O$	8.00×10^{-12}	9
$O^* + O_2 \rightarrow O + O_2^* S$	$2.56 \times 10^{-11} e^{67/Tg}$	14
$O^* + O_2 \rightarrow O + O_2^*$	$1.6 \times 10^{-12} e^{67/Tg}$	14
$O^* + O_2 \rightarrow O + O_2$	$4.8 \times 10^{-12} e^{67/Tg}$	14
$O^* + O_3 \rightarrow O_2 + O + O$	1.20×10^{-10}	15

$O^* + O_3 \rightarrow O_2 + O_2$	1.20×10^{-10}	16
$O^* + He \rightarrow O + He$	1.00×10^{-13}	17
$O^1S + O_2 \rightarrow O^* + O_2$	$3.2 \times 10^{-12} e^{-850/Tg}$	16
$O^1S + O_2 \rightarrow O + O_2$	$1.6 \times 10^{-12} e^{-850/Tg}$	16
$O^1S + O_2(v) \rightarrow O^* + O_2(v)$	$3.2 \times 10^{-12} e^{-850/Tg}$	16, i
$O^1S + O_2(v) \rightarrow O + O_2(v)$	$1.6 \times 10^{-12} e^{-850/Tg}$	16, i
$O^1S + O_2^* \rightarrow O + O_2$	1.10×10^{-10}	9, j
$O^1S + O_2^* \rightarrow O^* + O_2^*1S$	2.90×10^{-11}	9
$O^1S + O_2^* \rightarrow O + O + O$	3.20×10^{-11}	9
$O^1S + O \rightarrow O^* + O$	$1.67 \times 10^{-11} e^{-300/Tg}$	16
$O^1S + O \rightarrow O + O$	$3.33 \times 10^{-11} e^{-300/Tg}$	16
$O^1S + O_3 \rightarrow O_2 + O_2$	5.80×10^{-10}	16, k
$O_2^* + O \rightarrow O_2 + O$	2.00×10^{-16}	16
$O_2^* + O_2 \rightarrow O_2 + O_2$	$3 \times 10^{-18} e^{-200/Tg}$	14
$O_2^* + O_2(v) \rightarrow O_2 + O_2(v)$	$3 \times 10^{-18} e^{-200/Tg}$	14, i
$O_2^* + O_2^* \rightarrow O_2 + O_2$	$9 \times 10^{-17} e^{-560/Tg}$	16, l
$O_2^* + O_2^* \rightarrow O_2^*1S + O_2$	$9 \times 10^{-17} e^{-560/Tg}$	1
$O_2^* + O_2^* + O_2 \rightarrow O_3 + O_3$	$9 \times 10^{-32} e^{-560/Tg}$	9
$O_2^* + O_2 \rightarrow O + O_3$	$2.95 \times 10^{-21} T_g^{0.5}$	18
$O_2^* + O_2(v) \rightarrow O + O_3$	$2.95 \times 10^{-21} T_g^{0.5}$	18, i
$O_2^* + O_3 \rightarrow O_2 + O_2 + O$	$5.2 \times 10^{-11} e^{-2840/Tg}$	15

$O_2^* + He \rightarrow O_2 + He$	$8 \times 10^{-21} T_g^{0.5}$	19
$O_2^{*1}S + O_2^{*1}S \rightarrow O_2^* + O_2$	$3.6 \times 10^{-17} T_g^{0.5}$	14, i
$O_2^{*1}S + O_2 \rightarrow O_2^* + O_2$	$3.6 \times 10^{-17} T_g^{0.5}$	14
$O_2^{*1}S + O_2 \rightarrow O_2 + O_2$	$4 \times 10^{-18} T_g^{0.5}$	14
$O_2^{*1}S + O_2(v) \rightarrow O_2^* + O_2(v)$	$3.6 \times 10^{-17} T_g^{0.5}$	14, i
$O_2^{*1}S + O_2(v) \rightarrow O_2 + O_2(v)$	$4 \times 10^{-18} T_g^{0.5}$	14, i
$O_2^{*1}S + O \rightarrow O_2^* + O$	$7.2 \times 10^{-14} T_g^{0.5}$	14
$O_2^{*1}S + O \rightarrow O_2 + O$	$8 \times 10^{-15} T_g^{0.5}$	14
$O_2^{*1}S + O_3 \rightarrow O + O_2 + O_2$	$7.3 \times 10^{-12} T_g^{0.5}$	20
$O_2^{*1}S + O_3 \rightarrow O_2^* + O_3$	$7.3 \times 10^{-12} T_g^{0.5}$	20
$O_2^{*1}S + O_3 \rightarrow O_2 + O_3$	$7.3 \times 10^{-12} T_g^{0.5}$	20
$O_2^{*1}S + He \rightarrow O_2^* + He$	$1 \times 10^{-17} T_g^{0.5}$	m
$O_2(v) + M \rightarrow O_2 + M^h$	$1 \times 10^{-14} T_g^{0.5}$	14, m
$O + O + O_2 \rightarrow O_2 + O_2$	$2.6 \times 10^{-34} T_g^{-0.63}$	9
$O + O + O_2(v) \rightarrow O_2 + O_2(v)$	$2.6 \times 10^{-34} T_g^{-0.63}$	9
$O + O + O \rightarrow O_2 + O$	$9.2 \times 10^{-34} T_g^{-0.63}$	9
$O + O + He \rightarrow O_2 + He$	1.20×10^{-33}	9, 19
$O + O + O_2 \rightarrow O_2^* + O_2$	$1.9 \times 10^{-35} T_g^{-0.63}$	9
$O + O + O_2(v) \rightarrow O_2^* + O_2(v)$	$1.9 \times 10^{-35} T_g^{-0.63}$	9, i
$O + O + O \rightarrow O_2^* + O$	$6.9 \times 10^{-35} T_g^{-0.63}$	9
$O + O + He \rightarrow O_2^* + He$	9.90×10^{-35}	9, 19

$O + O_2 + O_2 \rightarrow O_3 + O_2$	$6 \times 10^{-34} T_g^{-2.8}$	14
$O + O_2 + O_2(v) \rightarrow O_3 + O_2(v)$	$6 \times 10^{-34} T_g^{-2.8}$	14, i
$O + O_2 + He \rightarrow O_3 + He$	$3.4 \times 10^{-24} T_g^{-1.2}$	19
$O + O_2 + O \rightarrow O_3 + O$	$3.4 \times 10^{-24} T_g^{-1.2}$	m
$O + O_3 \rightarrow O_2 + O_2$	$8 \times 10^{-12} e^{-2060/Tg}$	14
$O_3 + M \rightarrow O_2 + O + M^h$	$1.6 \times 10^{-9} e^{-11490/Tg}$	21, m
$He^* + He^* \rightarrow He + He^+ + e$	$1.6 \times 10^{-9} T_g^{0.5}$	22
$He^* + O_2 \rightarrow O_2^+ + He + e$	$2.54 \times 10^{-10} T_g^{0.5}$	23
$He^* + O_2(v) \rightarrow O_2^+ + He + e$	$2.54 \times 10^{-10} T_g^{0.5}$	23, i
$He^* + O_3 \rightarrow O_2^+ + O + He + e$	$2.54 \times 10^{-10} T_g^{0.5}$	23, i
$He^* + O_2^* S \rightarrow O_2^+ + He + e$	$2.54 \times 10^{-10} T_g^{0.5}$	23, i
$He^* + O \rightarrow O^+ + He + e$	$2.54 \times 10^{-10} T_g^{0.5}$	23, i
$He^* + O^* \rightarrow O^+ + He + e$	$2.54 \times 10^{-10} T_g^{0.5}$	23, i
$He^* + O^1S \rightarrow O^+ + He + e$	$2.54 \times 10^{-10} T_g^{0.5}$	23, i
$He^+ + O_2 \rightarrow O^+ + O + He$	$1.07 \times 10^{-9} T_g^{0.5}$	13
$He^+ + O_2(v) \rightarrow O^+ + O + He$	$1.07 \times 10^{-9} T_g^{0.5}$	13, i
$He^+ + O_3 \rightarrow O^+ + O_2 + He$	$1.07 \times 10^{-9} T_g^{0.5}$	13, m
$He^+ + O_2 \rightarrow O_2^+ + He$	$3.3 \times 10^{-11} T_g^{-0.5}$	13
$He^+ + O_2^* \rightarrow O^+ + O + He$	$1.07 \times 10^{-9} T_g^{0.5}$	13, i
$He^+ + O_2^* \rightarrow O_2^+ + He$	$3.3 \times 10^{-11} T_g^{-0.5}$	13, i
$He^+ + O \rightarrow O^+ + He$	$5 \times 10^{-11} T_g^{0.5}$	m

$\text{He}^+ + \text{O}^* \rightarrow \text{O}^+ + \text{He}$	$5 \times 10^{-11} T_g^{0.5}$	m
$\text{He}^+ + \text{O}^1\text{S} \rightarrow \text{O}^+ + \text{He}$	$5 \times 10^{-11} T_g^{0.5}$	m
$\text{He} + \text{He}^+ \rightarrow \text{He} + \text{He}^+$	$5 \times 10^{-11} T_g^{0.5}$	m

- a. Rate coefficient in $\text{cm}^3 \text{s}^{-1}$ for 2-body reactions, and $\text{cm}^6 \text{s}^{-1}$ for 3-body reactions.
- b. Rate coefficients calculated using cross-section data from the indicated reference.
- c. Super elastic collision rates calculated by detailed balance.
- d. Estimated to have the same cross section as the ground state.
- e. Cross section estimated by shifting and scaling the ground state cross section by the excitation threshold.
- f. Cross section estimated by shifting and scaling the $\text{O}_2(^1\Delta)$ cross section by the excitation threshold.
- g. Superelastic collision rates calculated by detailed balance for excitation from $\text{O}_2(^1\Delta)$.
- h. for all neutral species.
- i. Analogous to reaction with the ground state O_2 .
- j. Assuming branching to ground state.
- k. Rate given by Ref. 16 with branching given by Ref. 9.
- l. Rate given by Ref. 16; assumed 50% branching to O_2 , and 50% to $\text{O}_2(^1\Delta)$.
- m. Estimated.

A.1 References

1. J. P. Boeuf and E. Marode, *J. Phys. D* **15**, 2169 (1982).
2. D. Rapp and P. Englander-Golden, *J. Chem. Phys.* **43**, 1464 (1965).
3. L. Vriens, *Phys. Lett.* **8**, 260 (1964).
4. G. Bekefi, *Radiation Processes in Plasmas* (Wiley, New York, 1966).
5. A. V. Phelps, JILA Information Center Report No. 28, 1985.
6. P. D. Burrow, *J. Chem. Phys.* **59**, 4922 (1973).
7. R. I. Hall and S. Trajmar, *J. Phys. B* **8**, L293 (1975).
8. Y. Itikawa *et al.*, *J. Phys. Chem. Ref. Data* **18**, 23 (1989).
9. B. F. Gordiets *et al.*, *IEEE Trans. Plasma Sci.* **23**, 750 (1995).
10. S. Matejcek *et al.*, *Plasma Sources Sci. Technol.* **6**, 140 (1997).
11. R. R. Laher and F. R. Gilmore, *J. Phys. Chem. Ref. Data* **19**, 277 (1990).
12. E. Meeks *et al.*, *J. Vac. Sci. Technol. A* **16**, 544 (1998).
13. Y. Ikezoe, S. Matsuoka, M. Takebe, and A. Viggiano, *Gas Phase Ion-Molecule Reaction Rate Constants Through 1986* (Ion Reaction Research Group of the Mass Spectroscopy Society of Japan, Tokyo, Japan, 1987).
14. R. Atkinson, *et al.*, *J. Phys. Chem. Ref. Data* **26**, 521 (1997).
15. R. Atkinson *et al.*, *J. Phys. Chem. Ref. Data* **26**, 1329 (1997).
16. J. T. Herron and D. S. Green, *Plasma Chem. Plasma Process.* **21**, 459 (2001).
17. J. Shi and J. R. Barker, *Int. J. Chem. Kinet.* **22**, 1283 (1990).
18. R. K. Datta and K. N. Rao, *Indian J. Chem. A.* **18A**, 102 (1979).
19. *NIST Standard Reference Database 17-2Q98* (National Institute of Standards and Technology, Gaithersburg, MD, 1998).

20. K. W. Choo and M. T. Leu, *Int. J. Chem. Kinet.* **17**, 1155 (1985).
21. B. Eliasson and U. Kogelschatz, *Brown Boveri Technical Report LKR 86-11 C*, (1986).
22. R. Deloche, P. Monchicourt, M. Cheret, and F. Lambert, *Phys. Rev. A* **13**, 1140 (1976).
23. J. M. Pouvesle *et al.*, *J. Chem. Phys.* **88**, 3061 (1988).

APPENDIX B. LIST OF REACTIONS FOR He/O₂/NO PLASMAS

<u>List of species</u>		
He	NO	e
He*	NO ₂	He ⁺
O	N	O ₂ ⁺
O(¹ D)	N ₂	O ₂ ⁻
O(¹ S)	I ₂	O ⁺
O ₂	I	O ⁻
O ₂ (v)	I*	O ₃ ⁻
O ₂ (¹ Δ)	IO	NO ⁺
O ₂ (¹ Σ)	INO	NO ⁻
O ₃	INO ₂	NO ₂ ⁻
<u>Reaction</u>	<u>Rate Coefficient</u> ^a	<u>Reference</u>
$e + NO \rightarrow N + O^-$	b	1
$e + NO \rightarrow N + O + e$	b	2
$e + NO \rightarrow NO^+ + e + e$	b	3
$e + NO \rightarrow N + O^+ + e + e$	b	3
$e + NO^+ \rightarrow N + O$	$3.4 \times 10^{-7} T_e^{-0.5}$	4
$e + NO^+ \rightarrow N + O(^1D)$	$6.0 \times 10^{-7} T_e^{-0.5}$	4

$e + NO + He \rightarrow NO^- + He$	$1.0 \times 10^{-32} T_e^{-0.5}$	5
$e + NO + NO \rightarrow NO^- + NO$	$6.5 \times 10^{-31} T_e^{-0.5}$	5
$He^* + NO \rightarrow He + NO^+ + e$	2.5×10^{-10}	c
$He^+ + NO \rightarrow He + NO^+$	1.6×10^{-9}	6
$He^+ + NO \rightarrow He + N + O^+$	4.2×10^{-10}	6
$O^+ + NO \rightarrow O + NO^+$	1.7×10^{-12}	6
$O_2^+ + NO \rightarrow O_2 + NO^+$	4.5×10^{-10}	6
$O_2^+ + N \rightarrow NO^+ + O$	1.2×10^{-10}	6
$NO^-, NO_2^- + M^+ \rightarrow NO, NO_2 + M^d$	$2.0 \times 10^{-7} (T_g/300)^{-1}$	c
$NO^+ + M^- \rightarrow NO + M^e$	$2.0 \times 10^{-7} (T_g/300)^{-1}$	c
$O^- + NO \rightarrow NO_2 + e$	$2.8 \times 10^{-10} (T_g/300)^{0.5}$	6
$O^- + N \rightarrow NO + e$	$2.2 \times 10^{-10} (T_g/300)^{0.5}$	6
$O^- + NO_2 \rightarrow NO_2^- + e$	$1.2 \times 10^{-9} (T_g/300)^{0.5}$	6
$O_2^- + N \rightarrow NO_2 + e$	$4.0 \times 10^{-10} (T_g/300)^{0.5}$	6
$O_2^- + NO_2 \rightarrow NO_2^- + O_2$	$7.0 \times 10^{-10} (T_g/300)^{0.5}$	6
$O_3^- + NO \rightarrow NO_2^- + O_2$	$2.2 \times 10^{-12} (T_g/300)^{0.5}$	6
$NO^- + NO \rightarrow NO + NO + e$	$5.0 \times 10^{-12} (T_g/300)^{0.5}$	6
$NO^- + He \rightarrow NO + He + e$	$2.4 \times 10^{-13} (T_g/300)^{0.5}$	6
$NO^- + NO_2 \rightarrow NO + NO_2^-$	$7.4 \times 10^{-10} (T_g/300)^{0.5}$	6
$NO^- + O_2 \rightarrow NO + O_2^-$	$5.0 \times 10^{-10} (T_g/300)^{0.5}$	6
$NO_2^- + O_3 \rightarrow O_3^- + NO_2$	$9.4 \times 10^{-12} (T_g/300)^{0.5}$	6

$\text{NO} + \text{O}_3 \rightarrow \text{NO}_2 + \text{O}_2$	$1.4 \times 10^{-12} e^{-1,310/T_g}$	7
$\text{NO} + \text{O}_2(^1\Delta) \rightarrow \text{NO} + \text{O}_2$	3.5×10^{-17}	8
$\text{NO} + \text{O}(^1\text{D}) \rightarrow \text{N} + \text{O}_2$	5.0×10^{-15}	9
$\text{NO} + \text{O}(^1\text{D}) \rightarrow \text{NO} + \text{O}$	4.0×10^{-11}	10
$\text{NO} + \text{O} + \text{M} \rightarrow \text{NO}_2 + \text{M}^f$	$1.0 \times 10^{-31} (T_g/300)^{-1.6}$	7
$\text{NO}_2 + \text{O} \rightarrow \text{NO} + \text{O}_2$	$4.2 \times 10^{-12} e^{273/T_g}$	7
$\text{NO}_2 + \text{O}(^1\text{D}) \rightarrow \text{NO}_2 + \text{O}$	3.2×10^{-10}	11
$\text{NO}_2 + \text{O}(^1\text{D}) \rightarrow \text{NO} + \text{O}_2$	3.0×10^{-10}	11
$\text{N} + \text{O}_2 \rightarrow \text{NO} + \text{O}$	$2.4 \times 10^{-11} e^{-5,320/T_g}$	12
$\text{N} + \text{NO}_2 \rightarrow \text{NO} + \text{NO}$	6.1×10^{-12}	13
$\text{N} + \text{NO}_2 \rightarrow \text{N}_2 + \text{O} + \text{O}$	2.4×10^{-12}	13
$\text{N} + \text{NO}_2 \rightarrow \text{N}_2 + \text{O}_2$	1.8×10^{-12}	13
$\text{N} + \text{O} + \text{M} \rightarrow \text{NO} + \text{M}^f$	$5.5 \times 10^{-33} e^{155/T_g}$	14
$\text{O}_2(^1\Delta) + \text{O}_2 + \text{O} \rightarrow \text{O}_2 + \text{O}_2 + \text{O}$	1.0×10^{-32}	15
$\text{O}_2(^1\Sigma) + \text{I}_2 \rightarrow \text{O}_2 + \text{I} + \text{I}$	2.8×10^{-11}	16
$\text{O}_2(^1\Sigma) + \text{I}_2 \rightarrow \text{O}_2(^1\Delta) + \text{I}_2$	2.3×10^{-11}	16
$\text{O}_2(^1\Sigma) + \text{I}_2 \rightarrow \text{O}_2 + \text{I}_2$	6.0×10^{-12}	16
$\text{O}_2(^1\Delta) + \text{I}_2 \rightarrow \text{O}_2 + \text{I}_2^*$	7.0×10^{-15}	16
$\text{O}_2(^1\Delta) + \text{I}_2 \rightarrow \text{O}_2 + \text{I}_2$	5.0×10^{-16}	16
$\text{O} + \text{I}_2 \rightarrow \text{IO} + \text{I}$	1.4×10^{-10}	16
$\text{He} + \text{I}_2^* \rightarrow \text{He} + \text{I}_2$	9.8×10^{-12}	16

$O_2 + I_2^* \rightarrow O_2 + I_2$	4.9×10^{-12}	16
$O_2(^1\Delta) + I_2^* \rightarrow O_2 + I + I$	3.0×10^{-10}	16
$O_2(^1\Delta) + I \rightarrow O_2 + I^*$	$7.7 \times 10^{-11} (T_g/300)^{-1.0}$	16
$O_2(^1\Delta) + I \rightarrow O_2 + I$	1.0×10^{-15}	16
$O_3 + I \rightarrow O_2 + IO$	$2.0 \times 10^{-11} e^{-890/T_g}$	16
$He + I^* \rightarrow He + I$	5.0×10^{-18}	16
$O_2(^1\Delta) + I^* \rightarrow O_2(^1\Sigma) + I$	$8.4 \times 10^{-15} (T_g/300)^{3.8} e^{700/T_g}$	16
$O_2(^1\Delta) + I^* \rightarrow O_2 + I$	1.10×10^{-13}	16
$O_2 + I^* \rightarrow O_2^* + I$	$1.0 \times 10^{-10} (T_g/300)^{-1.0} e^{-403/T_g}$	16
$O + I^* \rightarrow O + I$	8.0×10^{-12}	16
$NO + I^* \rightarrow NO + I$	1.2×10^{-13}	16
$NO_2 + I^* \rightarrow NO_2 + I$	8.5×10^{-14}	16
$I_2 + I^* \rightarrow I_2^* + I$	$1.40 \times 10^{-13} e^{1,600/T_g}$	16
$IO + IO \rightarrow O_2 + I + I$	8.2×10^{-11}	16
$NO + IO \rightarrow NO_2 + I$	$4.3 \times 10^{-12} e^{-397/T_g}$	17
$O + IO \rightarrow O_2 + I$	1.4×10^{-10}	16
$O + IO \rightarrow O_2(^1\Delta) + I$	1.5×10^{-11}	16
$I + INO \rightarrow I_2 + NO$	1.6×10^{-10}	18
$I + INO_2 \rightarrow I_2 + NO_2$	8.3×10^{-11}	18
$INO + INO \rightarrow I_2 + NO + NO$	$8.4 \times 10^{-11} e^{-2,620/T_g}$	18

$\text{INO}_2 + \text{INO}_2 \rightarrow \text{I}_2 + \text{NO}_2 + \text{NO}_2$	$2.9 \times 10^{-11} e^{-2.600/T_g}$	18
$\text{I} + \text{I} + \text{I}_2 \rightarrow \text{I}_2 + \text{I}_2$	3.6×10^{-30}	16
$\text{I} + \text{I} + \text{He} \rightarrow \text{I}_2 + \text{He}$	3.8×10^{-33}	16
$\text{I} + \text{I} + \text{O}_2 \rightarrow \text{I}_2 + \text{O}_2$	3.3×10^{-32}	16
$\text{I} + \text{I}^* + \text{I}_2 \rightarrow \text{I} + \text{I} + \text{I}_2$	3.6×10^{-30}	16
$\text{I} + \text{I} + \text{O}_2 \rightarrow \text{I}_2 + \text{O}_2(^1\Delta)$	3.7×10^{-33}	16
$\text{I} + \text{NO} + \text{He} \rightarrow \text{INO} + \text{He}$	$6.0 \times 10^{-33} (T_g/300)^{-1.0}$	18
$\text{I} + \text{NO} + \text{O}_2 \rightarrow \text{INO} + \text{O}_2$	1.6×10^{-32}	18
$\text{I} + \text{NO}_2 + \text{He} \rightarrow \text{INO}_2 + \text{He}$	$1.5 \times 10^{-31} (T_g/300)^{-1.0}$	18
$\text{I} + \text{NO}_2 + \text{O}_2 \rightarrow \text{INO}_2 + \text{O}_2$	2.6×10^{-31}	18
$\text{I}^* \rightarrow \text{I}$	10	19

a. Rate coefficient in $\text{cm}^3 \text{ s}^{-1}$ for 2-body reactions, and $\text{cm}^6 \text{ s}^{-1}$ for 3-body reactions, and s^{-1} for radiation reactions.

b. Rate coefficients calculated using cross-section data from the indicated reference.

c. Estimated.

d. Where M is one of the cations O^+ , O_2^+ , He^+ , or NO^+ .

e. Where M is one of the anions O^- , O_2^- , or O_3^- .

f. Where M is one of the major neutral species He, O_2 , $\text{O}_2(\text{v})$, $\text{O}_2(^1\Delta)$, O, or O_3 .

B.1 References

1. D. Rapp and D. D. Briglia, *J. Chem. Phys.* **43**, 1480 (1965).
2. L. Josic, T. Wroblewski, Z. Lj. Petrovic, J. Mechlinska-Drewko and G. P. Karwasz, *Chem. Phys. Lett.* **350**, 318 (2001).
3. B. G. Lindsay, M. A. Mangan, H. C. Straub and R. F. Stebbings, *J. Chem. Phys.* **112**, 9404 (2000).
4. L. Vejby-Christensen, D. Kella, H. B. Pedersen and L. H. Andersen, *Phys. Rev. A* **57**, 3627 (1998).
5. H. Shimamori and H. Hotta, *J. Chem. Phys.* **89**, 2938 (1988).
6. Y. Ikezoe, S. Matsuoka, M. Takebe and A. Viggiano, *Gas Phase Ion-Molecule Reaction Rate Constants Through 1986* (Ion Reaction Research Group of the Mass Spectroscopy Society of Japan, Tokyo, Japan 1987).
7. R. Atkinson et al, *Atmos. Chem. Phys.* **4**, 1461 (2004).
8. R. B. Boodaghians, P. M. Borrell and P. Borrell, *Chem. Phys. Lett.* **97**, 193 (1983).
9. N. C. Blais, *J. Phys. Chem.* **89**, 4156 (1985).
10. V. M. Doroshenko, V. M. Kudryavtsev and V. V. Smetanin, *High Energy Chem.* **26**, 227 (1992).
11. M. J. E. Gauthier and D. R. Snelling, *J. Photochem.* **4**, 27 (1975).
12. G. S. Valli, R. Orru, E. Clementi, A. Lagana and S. Crocchianti, *J. Chem. Phys.* **102**, 2825 (1995).
13. L. F. Phillips and H. I. Schiff, *J. Chem. Phys.* **42**, 3171 (1965).
14. I. M. Campbell and C. N. Gray, *Chem. Phys. Lett.* **18**, 607 (1973).
15. A. N. Vasiljeva et al, *J. Phys. D: Appl. Phys.* **37**, 2455 (2004).

16. A. D. Palla, D. L. Carroll, J. T. Verdeyen and W. C. Solomon, "Effects of mixing on post-discharge modeling fo ElectricOIL experiments", Proc. SPIE. **6101**, 610125 (2006).
17. D. Holscher and R. Zellner, Phys. Chem. Chem. Phys. **4**, 1839 (2002).
18. R. Atkinson et al, J. Phys. Chem. Ref. Data **29**, 167 (2000).
19. D. Husain, N. K. H. Slater and J. R. Weisenfeld, Chem. Phys. Lett. **51**, 201 (1977).

APPENDIX C. LIST OF SPECIES AND REACTIONS IN Ar/NH₃ PLASMAS

<u>Species</u>		
e	NH ₃	NH ₄ ⁺
Ar	NH ₃ (v)	NH ₃ ⁺
Ar [*] (4s)	NH ₂	NH ₂ ⁺
Ar ^{**} (4p)	NH	NH ⁺
Ar ₂ [*]	N	N ⁺
Ar ⁺	N ₂	H ₃ ⁺
Ar ₂ ⁺	N ₂ H ₂	H ₂ ⁺
ArH ⁺	N ₂ H ₃	H ⁺
	N ₂ H ₄	NH ₂ ⁻
	H	H ⁻
	H ₂	
<u>Reaction</u>	<u>Rate Coefficient</u> ^a	<u>Reference</u>
$e + Ar \rightarrow Ar + e$	b	1
$e + Ar \leftrightarrow Ar^* + e$	b	2, c
$e + Ar \leftrightarrow Ar^{**} + e$	b	2, c
$e + Ar \rightarrow Ar^+ + e + e$	b	3
$e + Ar^* \leftrightarrow Ar^{**} + e$	b	4, c
$e + Ar^* \rightarrow Ar^+ + e + e$	b	5
$e + Ar^{**} \rightarrow Ar^+ + e + e$	b	6

$e + \text{Ar}_2^* \rightarrow \text{Ar}_2^+ + e + e$	$9 \times 10^{-8} T_e^{0.7} e^{-3.66/T_e}$	7
$e + \text{Ar}_2^* \rightarrow \text{Ar} + \text{Ar} + e$	1×10^{-7}	7
$e + \text{Ar}_2^+ \rightarrow \text{Ar}^{**} + \text{Ar}$	$5.4 \times 10^{-8} T_e^{-0.66}$	7
$e + \text{Ar}^+ \rightarrow \text{Ar}^{**}$	$4 \times 10^{-13} T_e^{-0.5}$	8
$e + e + \text{Ar}^+ \rightarrow \text{Ar}^{**} + e$	$5 \times 10^{-27} T_e^{-4.5}$	8
$e + \text{NH}_3 \rightarrow \text{NH}_3 + e$	b	9
$e + \text{NH}_3 \leftrightarrow \text{NH}_3(\text{v}) + e$	b	9, c
$e + \text{NH}_3 \rightarrow \text{NH}_2 + \text{H}^\cdot$	b	9
$e + \text{NH}_3 \rightarrow \text{NH}_2 + \text{H} + e$	b	9
$e + \text{NH}_3 \rightarrow \text{NH} + \text{H} + \text{H} + e$	b	9
$e + \text{NH}_3 \rightarrow \text{NH}_3^+ + e + e$	b	9
$e + \text{NH}_3 \rightarrow \text{NH}_2^+ + \text{H} + e + e$	b	10
$e + \text{NH}_3(\text{v}) \rightarrow \text{NH}_3(\text{v}) + e$	b	9
$e + \text{NH}_3(\text{v}) \rightarrow \text{NH}_2 + \text{H}^\cdot$	b	9, d
$e + \text{NH}_3(\text{v}) \rightarrow \text{NH}_2 + \text{H} + e$	b	9, e
$e + \text{NH}_3(\text{v}) \rightarrow \text{NH} + \text{H} + \text{H} + e$	b	9, e
$e + \text{NH}_3(\text{v}) \rightarrow \text{NH}_3^+ + e + e$	b	10, e
$e + \text{NH}_3(\text{v}) \rightarrow \text{NH}_2^+ + \text{H} + e + e$	b	10, e
$e + \text{NH}_2 \rightarrow \text{NH}_2 + e$	b	9, f
$e + \text{NH}_2 \rightarrow \text{NH} + \text{H}^\cdot$	b	9
$e + \text{NH}_2 \rightarrow \text{NH} + \text{H} + e$	b	9

$e + \text{NH}_2 \rightarrow \text{N} + \text{H} + \text{H} + e$	b	9
$e + \text{NH}_2 \rightarrow \text{NH}_2^+ + e + e$	b	11
$e + \text{NH}_2 \rightarrow \text{NH}^+ + \text{H} + e + e$	b	11
$e + \text{NH} \rightarrow \text{NH} + e$	b	9, f
$e + \text{NH} \rightarrow \text{N} + \text{H} + e$	b	9
$e + \text{NH} \rightarrow \text{N}^+ + \text{H} + e + e$	b	11
$e + \text{NH} \rightarrow \text{NH}^+ + e + e$	b	11
$e + \text{N} \rightarrow \text{N} + e$	b	12
$e + \text{N} \rightarrow e + \text{N}^*$	b, g	13
$e + \text{N} \rightarrow \text{N}^+ + e + e$	b	14
$e + \text{N}_2 \rightarrow \text{N}_2 + e$	b	15
$e + \text{N}_2 \rightarrow \text{N}_2(\text{v}) + e$	b, g	15
$e + \text{N}_2 \rightarrow \text{N}_2^* + e$	b, g	15
$e + \text{N}_2 \rightarrow \text{N} + \text{N} + e$	b	16
$e + \text{N}_2 \rightarrow \text{N}_2^+ + e + e$	b	15
$e + \text{H} \rightarrow \text{H} + e$	b	17
$e + \text{H} \rightarrow \text{H}^* + e$	b, g	18
$e + \text{H} \rightarrow \text{H}^+ + e + e$	b	18
$e + \text{H}_2 \rightarrow \text{H}_2 + e$	b	19
$e + \text{H}_2 \rightarrow \text{H}_2(\text{v}) + e$	b, g	19
$e + \text{H}_2 \rightarrow \text{H}_2^* + e$	b, g	19

$e + H_2 \rightarrow H_2^+ + e + e$	b	19
$e + H_2 \rightarrow H + H + e$	b	20
$e + H^+ \rightarrow H$	$4 \times 10^{-13} T_e^{-0.5}$	8
$e + H_2^+ \rightarrow H^+ + H + e$	b	21
$e + H_2^+ \rightarrow H + H$	$1 \times 10^{-7} T_e^{-0.4}$	22
$e + H_3^+ \rightarrow H^+ + H_2$	b	21
$e + H_3^+ \rightarrow H + H_2$	b	23
$e + ArH^+ \rightarrow Ar + H$	b	23
$e + N^+ \rightarrow N$	$4 \times 10^{-13} T_e^{-0.5}$	8
$e + NH^+ \rightarrow N + H$	$1 \times 10^{-7} T_e^{-0.5}$	23
$e + NH_2^+ \rightarrow NH + H$	$1 \times 10^{-7} T_e^{-0.5}$	23
$e + NH_3^+ \rightarrow NH_2 + H$	$1 \times 10^{-7} T_e^{-0.5}$	23
$e + NH_4^+ \rightarrow NH_3 + H$	$9 \times 10^{-7} T_e^{-0.6}$	24
$e + M^+ \rightarrow M^+ + e$	b	25
$Ar^+ + Ar \rightarrow Ar + Ar^+$	4.6×10^{-10}	26
$Ar^+ + Ar + M \rightarrow Ar_2^+ + M$	2.5×10^{-31}	7,h,i
$Ar^+ + NH_3, NH_3(v) \rightarrow NH_2^+ + H + Ar$	5.5×10^{-11}	27
$Ar^+ + M \rightarrow Ar + M^+$	1.3×10^{-9}	27,j
$Ar^+ + NH_3, NH_3(v) \rightarrow ArH^+ + NH_2$	9.2×10^{-11}	27
$Ar^+ + NH_2 \rightarrow NH^+ + H + Ar$	5.5×10^{-11}	27,h
$Ar^+ + H_2 \rightarrow H_2^+ + Ar$	1×10^{-9}	27

$\text{Ar}^+ + \text{H}_2 \rightarrow \text{H}^+ + \text{H} + \text{Ar}$	1×10^{-9}	27
$\text{Ar}^+ + \text{H}_2 \rightarrow \text{ArH}^+ + \text{H}$	1×10^{-9}	27
$\text{Ar}^+ + \text{N} \rightarrow \text{N}^+ + \text{Ar}$	1×10^{-11}	27
$\text{Ar}^+ + \text{N}_2 \rightarrow \text{N}^+ + \text{N} + \text{Ar}$	5×10^{-12}	27,h
$\text{Ar}^+ + \text{H} \rightarrow \text{H}^+ + \text{Ar}$	1×10^{-10}	27
$\text{H}_2^+ + \text{N} \rightarrow \text{N}^+ + \text{H}_2$	5×10^{-10}	27,h
$\text{H}_2^+ + \text{H} \rightarrow \text{H}^+ + \text{H}_2$	6.4×10^{-10}	27
$\text{H}_2^+ + \text{H}_2 \rightarrow \text{H}_3^+ + \text{H}$	2.1×10^{-9}	27
$\text{H}_2^+ + \text{M} \rightarrow \text{H}_2 + \text{M}^+$	5×10^{-10}	27,h,j
$\text{H}_2^+ + \text{NH}_x \rightarrow \text{NH}_{x+1}^+ + \text{H} \text{ (x=1,2,3)}$	5×10^{-11}	27,h
$\text{N}^+ + \text{H} \rightarrow \text{N} + \text{H}^+$	2×10^{-9}	27,h
$\text{N}^+ + \text{H}_2 \rightarrow \text{NH}^+ + \text{H}$	5.6×10^{-10}	27
$\text{N}^+ + \text{M} \rightarrow \text{N} + \text{M}^+$	2.4×10^{-9}	27,h,j
$\text{Ar}_2^+ + \text{M} \rightarrow \text{Ar} + \text{Ar} + \text{M}^+$	4.5×10^{-10}	27,j
$\text{Ar}_2^+ + \text{H} \rightarrow \text{H}^+ + \text{Ar} + \text{Ar}$	5×10^{-11}	27,h
$\text{Ar}_2^+ + \text{H}_2 \rightarrow \text{ArH}^+ + \text{Ar} + \text{H}$	4.7×10^{-10}	27
$\text{H}^+ + \text{M} \rightarrow \text{H} + \text{M}^+$	5×10^{-11}	j,k
$\text{NH}^+ + \text{NH}_3, \text{NH}_3(\text{v}) \rightarrow \text{NH}_3^+ + \text{NH}$	1.8×10^{-9}	27
$\text{NH}^+ + \text{NH}_3, \text{NH}_3(\text{v}) \rightarrow \text{NH}_4^+ + \text{N}$	6×10^{-10}	27,h
$\text{NH}^+ + \text{NH}_2 \rightarrow \text{NH} + \text{NH}_2^+$	1.8×10^{-9}	27,k
$\text{NH}^+ + \text{H}_2 \rightarrow \text{NH}_2^+ + \text{H}$	1×10^{-9}	27

$\text{NH}_2^+ + \text{NH}_3, \text{NH}_3(\text{v}) \rightarrow \text{NH}_3^+ + \text{NH}_2$	1.1×10^{-9}	27,h
$\text{NH}_2^+ + \text{NH}_3, \text{NH}_3(\text{v}) \rightarrow \text{NH}_4^+ + \text{NH}$	1.1×10^{-9}	27,h
$\text{NH}_2^+ + \text{H}_2 \rightarrow \text{NH}_3^+ + \text{H}$	1×10^{-9}	27
$\text{ArH}^+ + \text{H}_2 \rightarrow \text{H}_3^+ + \text{Ar}$	5×10^{-10}	27
$\text{H}_3^+ + \text{NH}_3 \rightarrow \text{NH}_4^+ + \text{H}_2$	4.4×10^{-9}	27
$\text{NH}_3^+ + \text{NH}_3, \text{NH}_3(\text{v}) \rightarrow \text{NH}_3^+ + \text{NH}_2$	2.0×10^{-10}	27
$\text{NH}_3^+ + \text{NH}_3, \text{NH}_3(\text{v}) \rightarrow \text{NH}_4^+ + \text{NH}_2$	2.2×10^{-9}	27
$\text{NH}_3^+ + \text{H}_2 \rightarrow \text{NH}_4^+ + \text{H}$	4×10^{-13}	27
$\text{NH}_2^- + \text{H}_2 \rightarrow \text{H}^- + \text{NH}_3$	2.3×10^{-11}	27
$\text{H}^- + \text{H} \rightarrow \text{H}_2 + \text{e}$	1.8×10^{-9}	27
$\text{H}^- + \text{NH}_3, \text{NH}_3(\text{v}) \rightarrow \text{NH}_2^- + \text{H}_2$	8.8×10^{-13}	27
$\text{H}^- + \text{M}^+ \rightarrow \text{H} + \text{M}$	3×10^{-6}	k,l
$\text{H}^- + \text{M}^+ \rightarrow \text{H} + \text{M}$	2×10^{-7}	k,m
$\text{H}^- + \text{Ar}_2^+ \rightarrow \text{H} + \text{Ar} + \text{Ar}$	2×10^{-7}	k
$\text{H}^- + \text{ArH}^+ \rightarrow \text{Ar} + \text{H} + \text{H}$	2×10^{-7}	k
$\text{H}^- + \text{H}_3^+ \rightarrow \text{H}_2 + \text{H}_2$	1×10^{-7}	k
$\text{H}^- + \text{H}_3^+ \rightarrow \text{H}_2 + \text{H} + \text{H}$	1×10^{-7}	k
$\text{NH}_2^- + \text{M}^+ \rightarrow \text{NH}_2 + \text{M}$	2×10^{-7}	k,n
$\text{NH}_2^- + \text{NH}_4^+ \rightarrow \text{NH}_2 + \text{NH}_3 + \text{H}$	2×10^{-7}	k
$\text{NH}_2^- + \text{Ar}_2^+ \rightarrow \text{NH}_2 + \text{Ar} + \text{Ar}$	2×10^{-7}	k
$\text{NH}_2^- + \text{ArH}^+ \rightarrow \text{NH}_3 + \text{Ar}$	1×10^{-7}	k

$\text{NH}_2^- + \text{ArH}^+ \rightarrow \text{NH}_2 + \text{Ar} + \text{H}$	1×10^{-7}	k
$\text{NH}_2^- + \text{H}_3^+ \rightarrow \text{NH}_3 + \text{H}_2$	1×10^{-7}	k
$\text{NH}_2^- + \text{H}_3^+ \rightarrow \text{NH}_2 + \text{H}_2 + \text{H}$	1×10^{-7}	k
$\text{Ar}^* + \text{Ar}^* \rightarrow \text{Ar}^+ + \text{Ar} + \text{e}$	1×10^{-9}	7
$\text{Ar}^* + \text{Ar}^{**} \rightarrow \text{Ar}^+ + \text{Ar} + \text{e}$	1×10^{-9}	7
$\text{Ar}^{**} + \text{Ar}^{**} \rightarrow \text{Ar}^+ + \text{Ar} + \text{e}$	1×10^{-9}	7
$\text{Ar}_2^* + \text{Ar}_2^* \rightarrow \text{Ar}_2^+ + \text{Ar} + \text{Ar} + \text{e}$	5×10^{-10}	7
$\text{Ar}^* + \text{Ar} + \text{Ar} \rightarrow \text{Ar}_2^* + \text{Ar}$	1.1×10^{-32}	7
$\text{Ar}^{**} + \text{Ar} + \text{Ar} \rightarrow \text{Ar}_2^* + \text{Ar}$	1.1×10^{-32}	7
$\text{Ar}_2^* \rightarrow \text{Ar} + \text{Ar}$	6×10^7	7
$\text{Ar}^{**} \rightarrow \text{Ar}^*$	2×10^6	k
$\text{Ar}^* \rightarrow \text{Ar}$	1×10^1	28,o
$\text{Ar}^{***} + \text{NH}_3, \text{NH}_3(\text{v}) \rightarrow \text{Ar} + \text{NH}_3^+ + \text{e}$	4.2×10^{-11}	29
$\text{Ar}^{***} + \text{NH}_3, \text{NH}_3(\text{v}) \rightarrow \text{Ar} + \text{NH}_2 + \text{H}$	5.8×10^{-11}	29
$\text{Ar}^{***} + \text{NH}_3, \text{NH}_3(\text{v}) \rightarrow \text{Ar} + \text{NH} + 2\text{H}$	5.2×10^{-11}	30
$\text{Ar}^{***} + \text{NH}_3, \text{NH}_3(\text{v}) \rightarrow \text{Ar} + \text{NH} + \text{H}_2$	5.8×10^{-12}	30
$\text{NH}_3, \text{NH}_3(\text{v}) + \text{Ar} \rightarrow \text{H}_2 + \text{NH} + \text{Ar}$	$1.1 \times 10^{-9} e^{-47,032/T_g}$	31
$\text{N}_2\text{H}_4 + \text{Ar} \rightarrow \text{NH}_2 + \text{NH}_2 + \text{Ar}$	$6.6 \times 10^{-9} e^{-20,615/T_g}$	32
$\text{NH}_2 + \text{Ar} \rightarrow \text{H} + \text{NH} + \text{Ar}$	$2.2 \times 10^{-9} e^{-38,224/T_g}$	33
$\text{NH} + \text{Ar} \rightarrow \text{H} + \text{N} + \text{Ar}$	$3 \times 10^{-10} e^{-37,615/T_g}$	33
$\text{N}_2 + \text{Ar} \rightarrow \text{N} + \text{N} + \text{Ar}$	$4.3 \times 10^{-10} e^{-86,460/T_g}$	34

$\text{N}_2 + \text{N}_2 \rightarrow \text{N} + \text{N} + \text{N}_2$	$4.3 \times 10^{-10} e^{-86,460/T_g}$	34
$\text{NH}_3 + \text{H} \rightarrow \text{H}_2 + \text{NH}_2$	$6.5 \times 10^{-13} (T_g/300)^{2.76} e^{-5,135/T_g}$	35
$\text{NH}_3(\text{v}) + \text{H} \rightarrow \text{H}_2 + \text{NH}_2$	$6.5 \times 10^{-13} (T_g/300)^{2.76} e^{-5,135/T_g}$	35
$\text{NH}_2 + \text{H} \rightarrow \text{NH} + \text{H}_2$	$1.1 \times 10^{-10} e^{-4,451/T_g}$	36
$\text{NH}_2 + \text{H}_2 \rightarrow \text{H} + \text{NH}_3$	$2.1 \times 10^{-12} e^{-4,277/T_g}$	29
$\text{NH}_2 + \text{NH}_2 \rightarrow \text{N}_2\text{H}_2 + \text{H}_2$	1.3×10^{-12}	37
$\text{NH}_2 + \text{NH}_2 \rightarrow \text{NH}_3 + \text{NH}$	$1.8 \times 10^{-14} (T_g/300)^{2.79} e^{-660/T_g}$	38
$\text{NH}_2 + \text{N} \rightarrow \text{N}_2 + \text{H} + \text{H}$	1.2×10^{-10}	29
$\text{NH}_2 + \text{NH} \rightarrow \text{N}_2\text{H}_2 + \text{H}$	$2.5 \times 10^{-9} (T_g/300)^{-0.5}$	29
$\text{NH}_2 + \text{NH} \rightarrow \text{N}_2\text{H}_3$	1.2×10^{-10}	39
$\text{NH} + \text{N} \rightarrow \text{N}_2 + \text{H}$	2.5×10^{-11}	40
$\text{NH} + \text{H} \rightarrow \text{H}_2 + \text{N}$	$6 \times 10^{-11} e^{-166/T_g}$	29
$\text{NH} + \text{NH} \rightarrow \text{N}_2 + \text{H} + \text{H}$	1.2×10^{-9}	41
$\text{NH} + \text{NH} \rightarrow \text{N}_2\text{H}_2$	3.5×10^{-12}	42
$\text{NH} + \text{NH} \rightarrow \text{NH}_2 + \text{N}$	$1.4 \times 10^{-14} (T_g/300)^{2.89} e^{1,015/T_g}$	43
$\text{N} + \text{H}_2 \rightarrow \text{H} + \text{NH}$	$2.7 \times 10^{-10} e^{-12,609/T_g}$	44
$\text{N}_2\text{H}_2 + \text{H} \rightarrow \text{N}_2 + \text{H}_2 + \text{H}$	$4.5 \times 10^{-13} (T_g/300)^{2.63} e^{115/T_g}$	45
$\text{H} + \text{H} + \text{M} \rightarrow \text{H}_2 + \text{M}$	1.4×10^{-31}	46,h,i
$\text{H} + \text{H} + \text{Ar} \rightarrow \text{H}_2 + \text{Ar}$	$6.4 \times 10^{-33} (T_g/300)^{-1}$	47
$\text{H} + \text{H} + \text{H}_2 \rightarrow \text{H}_2 + \text{H}_2$	$8.9 \times 10^{-33} (T_g/300)^{-0.6}$	47
$\text{H} + \text{H} + \text{H} \rightarrow \text{H}_2 + \text{H}$	8.9×10^{-33}	48

$\text{H} + \text{N} + \text{M} \rightarrow \text{NH} + \text{M}$	5×10^{-32}	29,h,i
$\text{H} + \text{NH}_2 + \text{M} \rightarrow \text{NH}_3 + \text{M}$	6×10^{-30}	29,h,i
$\text{H}_2 + \text{N} + \text{NH}_3 \rightarrow \text{NH}_2 + \text{NH}_3$	1×10^{-36}	49
$\text{N} + \text{N} + \text{Ar} \rightarrow \text{N}_2 + \text{Ar}$	2.3×10^{-32}	50
$\text{N} + \text{N} + \text{M} \rightarrow \text{N}_2 + \text{M}$	7.2×10^{-33}	51,p
$\text{NH} + \text{NH}_3, \text{NH}_3(\text{v}) + \text{M} \rightarrow \text{N}_2\text{H}_4 + \text{M}^{\text{m}}$	4×10^{-35}	52,i
$\text{NH} + \text{NH}_3 + \text{NH}_3 \rightarrow \text{N}_2\text{H}_4 + \text{NH}_3$	1×10^{-33}	52
$\text{NH}_2 + \text{NH}_2 + \text{Ar} \rightarrow \text{N}_2\text{H}_4 + \text{Ar}$	2.9×10^{-30}	53
$\text{NH}_2 + \text{NH}_2 + \text{NH}_3 \rightarrow \text{N}_2\text{H}_4 + \text{NH}_3$	6.9×10^{-30}	29
$\text{N}_2\text{H}_2 + \text{NH}_2 \rightarrow \text{N}_2 + \text{H} + \text{NH}_3$	$1.5 \times 10^{-13} (\text{T}_g/300)^{4.05} e^{810/\text{T}_g}$	45
$\text{N}_2\text{H}_3 + \text{H} \rightarrow \text{NH}_2 + \text{NH}_2$	2.7×10^{-12}	54
$\text{N}_2\text{H}_3 + \text{N}_2\text{H}_3 \rightarrow \text{NH}_3 + \text{NH}_3 + \text{N}_2$	5×10^{-12}	55
$\text{N}_2\text{H}_3 + \text{N}_2\text{H}_3 \rightarrow \text{N}_2\text{H}_4 + \text{N}_2\text{H}_2$	2×10^{-11}	56
$\text{N}_2\text{H}_4 + \text{N} \rightarrow \text{N}_2\text{H}_2 + \text{NH}_2$	1.3×10^{-13}	54
$\text{N}_2\text{H}_4 + \text{H} \rightarrow \text{N}_2\text{H}_3 + \text{H}_2$	$1.2 \times 10^{-11} e^{-1260/\text{T}_g}$	57
$\text{N}_2\text{H}_4 + \text{NH}_2 \rightarrow \text{NH}_3 + \text{N}_2\text{H}_3$	5.2×10^{-13}	54

- ^a Rate constant in $\text{cm}^3 \text{s}^{-1}$ for 2-body reactions, and $\text{cm}^6 \text{s}^{-1}$ for 3-body reactions. For radiation reactions, units are in s^{-1} .
- ^b Rate constant calculated by using cross-section data from the indicated reference.
- ^c Superelastic collision cross-section calculated using detailed balance.
- ^d Cross-section is the same as the reaction for the ground state, with the threshold shifted by

- the excitation threshold of $\text{NH}_3(\text{v})$.
- ^e Cross-section estimated by shifting and scaling the ground state cross-section by the excitation threshold.
 - ^f Estimated to have the same cross-section as NH_3 .
 - ^g Reaction is included for energy loss, but the excited state is not tracked.
 - ^h Rate constant estimated by analogy.
 - ⁱ M is all major neutral species unless otherwise specified.
 - ^j M is one of NH_3 , $\text{NH}_3(\text{v})$, NH_2 or NH .
 - ^k Estimated.
 - ^l M is one of N^+ , NH^+ , NH_2^+ , NH_3^+ , NH_4^+ . In case of NH_4^+ , the products are NH_3 and H_2 .
 - ^m M is one of Ar, H, or H_2 .
 - ⁿ M is one of N^+ , NH^+ , NH_2^+ , or NH_3^+ .
 - ^o Trapped rate for the radiation reaction.
 - ^p M is one of N, H, H_2 , N_2 , NH_3 , $\text{NH}_3(\text{v})$.

C.1 References

1. M. Hayashi, Nagoya Inst. Tech. Report No: IPPJ-AM-19 (1991).
2. K. Tachibana, Phys. Rev. A **34**, 1007 (1986).
3. D. Rapp and P. Englander-Golden, J. Chem. Phys. **43**, 1464 (1965).
4. I. P. Zapesochnyi, and L. L. Shimon, Opt. Spect. **11**, 155 (1966).
5. R. H. McFarland and J. D. Kinney, Phys. Rev. A **137**, 1058 (1965).
6. L. Vriens, Phys. Lett. **8**, 260 (1964).
7. F. Kannari, A. Suda, M. Obara and T. Fujioka, IEEE. J. Quant. Elec. **QE-19**, 1587 (1983).
8. M. A. Biondi, *Principles of Laser Plasmas* (Wiley, New York, 1976).
9. M. Hayashi, "Electron collision cross-sections determined from beam and swarm data by Boltzmann analysis" in *Non-equilibrium Processes in Partially Ionized Gases*, ed. M. Capitelli and J. Norman Bardsley (Plenum, New York, 1990).
10. T. D. Märk and G. H. Dunn, *Electron impact ionization* (Springer, Vienna, 1985).
11. V. Tarnovsky, H. Deutsch and K. Becker, Intl. J. Mass. Spect. Ion. Proc. **167/168**, 69 (1997).
12. S. Geltman, J. Quant. Spect. Rad. Transfer, **13**, 601 (1973).
13. R. J. W. Henry, P. G. Burke and A. –L. Sinfailam, Phys. Rev. **178**, 218 (1969).
14. A. C. H. Smith, Phys. Rev. **127**, 1647 (1962).
15. Y. Itikawa *et al*, J. Phys. Chem. Ref. Data, **15**, 985 (1986).
16. A.V. Phelps and L.C. Pitchford, Phys. Rev. **31**, 2932 (1985).
17. P. Banks, Planet. Space Sci. **14**, 1085 (1966).

18. R. K. Janev, W. d. Langer, D. Evans, Jr. and D. E. Post, *Elementary Processes in Hydrogen and Helium Containing Plasmas* (Springer-Verlag, Berlin, 1987)
19. M. Hayashi, *J. de Physique*, **40**, C7/45-46 (1979).
20. S. J. B. Corrigan, *J. Chem. Phys.* **43**, 4381 (1965).
21. C. F. Chan, "Reaction cross sections and rate coefficients related to production of positive ions", *Lawrence Berkeley Laboratory Report* No LBID-632 (1983).
22. W. L. Morgan, *Adv. At. Mol. Opt. Phys.* **43**, 79 (2000).
23. A. I. Florescu and J. B. A. Mitchell, *Phys. Rep.* **430**, 277 (2006).
24. J. Öjekull et al, *J. Chem. Phys.* **120**, 7391 (2004).
25. M. Mitchner and C. H. Kruger Jr., *Partially Ionized Gases* (Wiley, New York, 1992).
26. H. W. Ellis, R. Y. Pai, E. W. McDaniel, E. A. Mason and L. A. Viehland, *At. Data. Nucl. Data Tab.* **17**, 177 (1976).
27. Y. Ikezoe, S. Matsuoka, M. Takebe and A. Viggiano, *Gas Phase Ion-Molecule Reaction Rate Constants Through 1986* (Ion Reaction Research Group of the Mass Spectroscopy Society of Japan, Tokyo, Japan 1987).
28. T. Holstein, *Phys. Rev.* **83**, 1159 (1951).
29. M. J. Kushner, *J. Appl. Phys.* **71**, 4173 (1992).
30. J. Balamuta, M. F. Golde and Y. Ho, *J. Chem. Phys.* **79**, 2822 (1983).
31. R. K. Hanson and S. Salimian, "Survey of rate constants in the N/H/O system" in *Combustion Chemistry*, ed. W. C. Gardiner (Springer-Verlag, New York 1984).
32. E. Meyer, H. A. Olschewski, J. Troe and H. Gg. Wagner, *Investigation of N₂H₄ and H₂O₂ decomposition in low and high pressure shock waves*, Proceedings of the 12th International Symposium on Combustion, pp. 345-355 (1969).

33. J. Deppe, G. Friedrichs, A. Ibrahim, H.-J. Romming and H. Gg. Wagner, Ber. Bunsenges. Phys. Chem. **102**, 1474 (1998).
34. K. Thielen and P. Roth, AIAA J. **24**, 1102 (1986).
35. J. C. Corchado and J. Espiona-Garcia, J. Chem. Phys. **106**, 4013 (1997).
36. M. Rohrig and H. G. Wagner, *The reactions of $NH(X^3\Sigma)$ with the water gas components CO_2 , H_2O , and H_2* , Proceedings of the 25th International Symposium on Combustion, pp. 975-981 (1994).
37. N. Stothard, R. Humpfer and H-H. Grotheer, Chem. Phys. Lett. **240**, 474 (1995).
38. Z-F. Xu, D-C. Fang and X-Y Fu, Intl. J. Quant. Chem. **70**, 321 (1998).
39. P. B. Pagsberg, J. Eriksen and H. C. Christensen, J. Phys. Chem. **83**, 582 (1979).
40. W. Hack, H. Gg. Wagner and A. Zaspypkin, Ber. Bunsenges. Phys. Chem. **98**, 156 (1994).
41. G. M. Meaburn and S. Gordon, J. Phys. Chem. **72**, 1592 (1968).
42. J. E. Nicholas, A. I. Spiers and N. A. Matin, Plasma Chem. Plasma Proc. **6**, 39 (1986).
43. Z-F Xu, D-C Fang, X-Y Fu, Chem. Phys. Lett. **275**, 386 (1997).
44. R. F. Davidson and R. K. Hanson, Int. J. Chem. Kinet. **22**, 843 (1990).
45. D. P. Linder, X. Duan and M. Page, J. Chem. Phys. **104**, 6298 (1996).
46. L. Teng, C. A. Winkler, Can. J. Chem. **51**, 3771 (1973).
47. D. L. Baulch et al, J. Phys. Chem. Ref. Data **21**, 411 (1992).
48. N. Cohen and K. R. Westberg, J. Phys. Chem. Ref. Data **12**, 531 (1983).
49. V. A. Petrishchev and A. Yu. Sapozhkov, Kin. Catal. **22**, 771 (1981).
50. V. A. Emel'kin and V. V. Marusin, Kin. Catalysis **19**, 1118 (1978).
51. T. Yamashita, J. Chem. Phys. **70**, 4248 (1979).

52. C. Zetsch and F. Stuhl, *Ber. Bunsenges, Phys. Chem.* **85**, 564 (1981).
53. V. A. Lozovskii, V. A. Nadtochenko, O. M. Sarkisov and S. G. Cheskis, *Kin. Catal.* **20**, 918 (1979).
54. M. Gehring, K. Hoyer mann, H. Gg. Wagner and J. Wolfrum, *Ber. Bunsenges, Phys. Chem.* **75**, 1287 (1971).
55. M. Schiavello and G. G. Volpi, *J. Chem. Phys.* **37**, 1510 (1962).
56. L. J. Stief, *J. Chem. Phys.* **52**, 4841 (1970).
57. G. L. Vaghjiani, *Intl. J. Chem. Kin.* **27**, 777 (1995).

AUTHOR'S BIOGRAPHY

Ramesh Ananthanarayanan Arakoni was born in Cochin, India, and grew up in Chennai, India. He finished schooling in 1996 at the P.S. Senior Secondary School in Chennai, and subsequently obtained a B.Tech in Aerospace Engineering from the Indian Institute of Technology, Madras in 2000. He obtained his M.S. in 2003 where he worked on icing effects on airfoils under guidance of Dr. Michael B. Bragg at the University of Illinois Urbana-Champaign. He joined the Ph.D. program in Aerospace Engineering and has been working with Dr. Mark J. Kushner on modeling of low-temperature plasmas with applications to microdischarges and electrical Oxygen-Iodine Lasers. His Ph.D. work has resulted in 10 conference presentations and 4 publications in refereed journals. After graduation in October 2007, he will start working at Intel as a software engineer in the process technology modeling group in Portland, OR.